Probing Heavy Neutral Leptons in Direct Searches, Double Beta Decay and Cosmology

Zhong Zhang

A dissertation submitted in partial fulfillment

of the requirements for the degree of

Doctor of Philosophy

of

University College London.

Department of Physics & Astronomy

University College London

January 7, 2025

I, Zhong Zhang, confirm that the work presented in this thesis is my own. Where information has been derived from other sources, I confirm that this has been indicated in the work.

Abstract

Heavy Neutral Leptons (HNLs) are a popular extension of the Standard Model (SM) to explain the lightness of neutrino masses and the matter-antimatter asymmetry through leptogenesis. This work studies the phenomenology of low scale Seesaw HNLs with their mass between 1 MeV and 1 GeV in direct searches, neutrinoless double beta decay and cosmology.

Future direct searches, such as fixed target setups like DUNE, and neutrinoless double beta decay, such as LEGEND-1000, are both expected to probe the regime of the standard Seesaw scenario of neutrino mass generation for HNL masses around $m_N \lesssim 1$ GeV. We analyse the complementarity between the two experiments to probe the nature of HNLs, i.e., the Majorana nature and CP-violating phases in the HNL sector. Following an analytic discussion of the complementarity, a statistical analysis is performed in the combined search for HNLs.

HNLs in the MeV-scale mass range, are very constrained by Big Bang Nucleosynthesis (BBN) as their decays significantly impact the formation of the primordial elements. We propose here a model where the primary decay channel for the HNLs is to an axion-like particle (ALP) and a neutrino. Consequently HNLs decay much earlier and can evade the BBN bound for much lower masses, provided the ALPs themselves decay considerably later. Further cosmological and astrophysical constraints limit severely the range of validity of the ALP properties. We find that a new parameter region opens for HNLs with masses between 1 MeV and 1 GeV, and active-sterile mixing between $10^{-9} - 10^{-6}$ that is consistent with observations. In such a scenario, current HNL bounds, as well as sensitivities of future direct HNL searches such as at DUNE or PIONEER, will be affected.

Acknowledgements

First, I want to express my sincere gratitude to my supervisor, Professor Frank Deppisch, for his unwavering kindness, tolerance, and patience throughout my PhD. This work would not have been possible without his guidance and support.

I also would like to thank my collaborators: Drs. Patrick Bolton, Tomas Gonzalo, Chayan Majumdar and Mudit Rai. This thesis could not be done without their important contributions.

I thank Professors Jonathan Tennyson, Gavin Hesketh, Stuart Mangles, Zhongfeng Xu, Yongtao Zhao, Jieru Ren, Samjid Mannan, Chris Lorentz, Yongchao Zhang, Guijun Ding, Wei Liu, Jessica Turner, and Drs. Alexander Jenkins, Di Zhang, Xin Wang, and Yikun Gu for their valuable suggestions during my PhD studies and beyond. I also wish to thank my UCL colleagues: Drs. Graham Van Goffrier, James Canning, Matt Reader, Tom Meltzer and Wenna Pei, Noor Boudjema, Alex Wilkinson, Luzhan Yue, Yuwen Zhang, for their support to my PhD.

I also want to thank my friends: Howard Chen, Wanxiang Fan, Yunqi Gao, Haoyang Fu, Hurst He, Changlin Li, Haolin Li, Xianglong Li, Chiho Lau, Vincent Lin, Yang Liu, Zhaolin Liu, Yujian Long, Louise Mak, Yingtong Shao, Enhua Shi, Dr. Wenqing Xiao, Yifei Zhao, Dr. Zelong Zhao, Zehao Zhu, Chenkai Zhou, Lotus Zhang, Yifan Zhou, Yuhui Zhang, Dulcea Zhong, and many others, for their help.

Finally, I want to give special thanks to my grandmother Chunmin Li, my grandfather Sheng Long, and my second aunt Xiuhua Zhang. They sadly passed away during my PhD studies, but they have irreplaceable places in my life. Last but not least, I thank my parents for giving me the opportunity to pursue my PhD and for their unwavering support throughout my life.

Impact Statement

This work represents a comprehensive study of heavy neutral leptons (HNLs) under non-standard seesaw scenarios. It summaries results from nuclear decays, fixed target experiments, cosmology and astrophysical observations to give constraints on heavy neutral lepton parameters.

The neutrino mass is inconsistent with the standard model of particle physics. HNLs, as one of the most popular extensions to the standard model, can explain the mass origin of neutrinos. Therefore, the study of the nature of HNLs can help to develop our understanding of neutrinos and their position in physics.

Neutrinoless double beta decay ($0\nu\beta\beta$) has been one of the most promising approaches to probe lepton number violation, which specifically indicates that neutrinos are their own anti-particles, or in another word, if they are Majorana particles. The complementary study between $0\nu\beta\beta$ experiments and beam dump experiments can be used to probe the Majorana nature of neutrinos and existence of HNLs.

Neutrinos and HNLs can likewise be a portal to the dark matter problem. Dark matter particles may be interacting with the neutrino sector in the very early Universe. A better understanding of the nature of dark matter can be achieved by studying interactions between the neutrino sector and dark matter.

This work focuses on the theoretical extensions of neutrino sector which are experimentally testable. It attempts to explain the Majorana nature, the mass origin of neutrinos and the nature of dark matter. It is hoped that the work will be a useful reference to the relevant researchers and will be inspiring to young people who are interested in fundamental sciences.

Contents

List of Figures

List of Tables

Chapter 1

Introduction

There exists Taiji,
it gives birth to dipoles.

Yijing

Particle Physics is a branch of physics which studies the most fundamental building blocks in nature. The understanding of elementary particles not only helps us to gain knowledge of the microscopic world, but it is also the key to describe how the Universe evolves. The standard model (SM) [1–3] is currently the best theory to explain most of the observed phenomena in particle physics with a remarkable precision. It therefore becomes one of the most successful theories in physics.

Neutrinos are an important part of the SM which have not been fully understood. The concept of the neutrino was proposed by Wolfgang Pauli in 1930 in order to explain the electron energy spectrum in beta decay processes. Neutrinos are predicted to be electrically neutral and light in order to satisfy the conservation laws. It was estimated by Enrico Fermi [4] that a neutrino-nucleus scattering cross-section per neutrino energy is of the order $10^{-38}\mathrm{cm}^2/\mathrm{GeV}$. The small scattering cross-section makes neutrinos hardly interact with ordinary matter and extremely difficult to be detected. However, Reines and Cowan [5] successfully observed the first event only in 1956. As suggested by Pontecorvo and Wang [6, 7], the experiment is based on the inverse beta decay process where an anti-electron neutrino from a reactor interacts with a proton in the detector to produce a neutrino and a

positron such as

$$p + \bar{\nu}_e \rightarrow n + e^+. \tag{1.1}$$

The detector contains two large water tanks to increase the interaction possibility of the electron neutrino. The gamma rays produced from positron-electron annihilation in water can be seen by the liquid scintillator between the water tanks.

After the discovery of the electron neutrino, the other flavours of neutrinos were not known until 1962, when Lederman, Schwartz and Steinberger [8] discovered the muon neutrino. Finally, the tau neutrino was discovered in 2000 by the DONUT collaboration [9].

One of the key things to learn about the properties of neutrinos is to understand weak interactions which were not fully understood before the 1950s. It was suggested by Yang and Lee [10] that parity is violated in weak interactions and neutrinos were assumed to be massless due to the absence of the right-handed partners. The theory was proved by Wu's experiment [11] that beat decay indeed violates parity. However, the discovery of neutrino oscillations [12], which were initially proposed to explain the electron deficit in solar neutrino observation [13, 14] shows, that the three types of neutrinos should have at least two massive states. The reason why oscillations require massive neutrinos is the misalignment between the mass states (ν_1, ν_2, ν_3) and flavour states (ν_e, ν_μ, ν_τ) of the neutrinos. Based on the work of Maki, Nakagawa and Sakata [15], Pontecorvo and Gribov [16] developed the model of neutrino mixing which describes how neutrinos change their flavours during propagation, i.e., oscillations.

Six parameters control neutrino oscillations, namely, the three neutrino mixing angles ($\theta_{12}, \theta_{13}, \theta_{23}$), the neutrino mass squared differences ($\Delta m^2_{12}, \Delta m^2_{23}$) and a CP-violating phase δ. These parameters are probed by different types of neutrino experiments. Long baseline accelerator experiments such as MINOS, K2K, NOvA and T2K [17–20] measure the oscillation pattern of the propagation of the neutrinos produced from the collision between an accelerated proton beam and a target over a long distance. Atmospheric neutrino experiments such as Super-Kamiokande and IceCube [21–23] look for neutrinos produced in the upper atmosphere. Super-

Kamiokande gave measurements of $\Delta m^2_{23} \sim 2.5 \times 10^{-3}\text{eV}^2$ and the mixing angle $\theta_{23} \sim 45^\circ$. Solar neutrino experiment such as Borexino [24] looks for neutrinos produced from the sun and they measure $\Delta m^2_{12} \sim 7.5 \times 10^{-5}\text{eV}^2$ and the mixing angle $\theta_{12} \sim 33^\circ$. Short baseline reactor neutrino experiments, such as Double CHOOZ, Reno and Daya Bay [25–27], measure the $\theta_{13} \sim 8.5^\circ$ mixing angle using neutrinos produced from nuclear reactors. IceCube is also looking for cosmic TeV-PeV high energy neutrinos, which cannot be produced artificially on Earth [28].

From oscillation experiments, the mass splittings can be measured precisely, but the absolute neutrino masses are still not known. The current best result for the absolute neutrino mass bound is from the KATRIN experiment. It puts an upper bound of the neutrino mass of $m_\beta < 0.45$ eV [29] through the measurement of the spectrum of the electron produced from tritium decays. The absolute neutrino mass is also constrained by cosmology, the mass of the neutrinos will have an impact on CMB and structure formation of the Universe. Combining data from the PLANCK satellite, such considerations give an upper mass bound of $\sum_i m_{\nu_i} < 0.1$ eV [30].

The neutrino mass can be the Dirac, Majorana or a combination of the two types. If neutrinos are of Dirac type, they will have similar properties as the other SM fermions. If neutrinos are Majorana, they are their own anti-particles and they can have a bare mass disconnected form electroweak symmetry breaking. The see-saw mechanism [31–34] is one of the most popular models to explain neutrino masses. It requires heavy right-handed partners to the active neutrinos. These heavy partners should be sterile in all known SM interactions in order to fits into the SM gauge structure, they are often called heavy neutral leptons (HNLs).

Majorana neutrinos will induce lepton number violating (LNV) processes. Neutrinoless double beta decay ($0\nu\beta\beta$) is one of them. Since $0\nu\beta\beta$ produces two electrons without neutrino emission, lepton number is violated by two units. $0\nu\beta\beta$ is induced by new physics (NP) beyond the SM. It is also proven that no matter what mechanism induces $0\nu\beta\beta$, the active neutrinos have Majorana character [35–37]. HNLs can also induce $0\nu\beta\beta$ and this implies that neutrinos are Majorana.

The Universe is an excellent laboratory for probing BSM theories and the na-

ture of neutrinos. Neutrinos were originally in equilibrium with other particles in the thermal plasma very shortly after the Big Bang. As the Universe expands, the thermal energy ($T \sim 1$ MeV) becomes insufficient to support weak interactions between neutrinos and other SM particles [38]. Neutrinos are therefore decoupled from the thermal bath and the neutrino temperature starts to evolve differently from the photon temperature. Primordial light elements such as ^{4}He and ^{7}Li can give information about the Big Bang Nucleosythesis (BBN), shortly after neutrino decoupling [39]. BBN constrains BSM theories by constraining the proton, neutron and light nuclei abundances in the early Universe and the effective number of relativistic species at the time. After recombination, electrons combine with protons to form neutral atoms and photons decouple from matter in the Universe. The light degrees of freedom (N_{eff}) can probe all light species in the Universe including the three types of neutrinos in the SM. The measurements of N_{eff} put a bound on BSM theories with light exotic particles.

This thesis summaries the author's work related to neutrinos and HNLs. It is organised as follows. Chapter 2 reviews the fundamentals of particle physics which includes the particle content, SM symmetries, the Higgs mechanism and its relation to fermion mass. This chapter ends with a brief discussion of BSM phenomena such as neutrino masses, the matter-antimatter asymmetry and dark matter. In Chapter 3, we start with the three-neutrino mixing theory and oscillation experiments. The neutrino mass problem will be discussed following a brief introduction to neutrino mixing, after which the most popular theories explaining neutrino masses will be presented, namely the seesaw mechanism. After that, a short introduction to double beta decay is given. Single beta decay and double beta decay are mentioned briefly and we pay most of our attention to the basic theory and current experimental status of neutrinoless double beta decay. At the end of this chapter, we will talk about the basics of cosmology and the impact of neutrinos on the evolution of the Universe from early times (neutrino decoupling and BBN) to late periods (CMB). Chapter 4 demonstrates one of the main works of this thesis. In this chapter, we will see how to probe the nature of $\simeq$1 GeV mass HNLs complementarily in fixed

target and neutrinoless double beta decay experiments. The chapter starts with the phenomenological model for a simplified 1-active neutrino plus 2-HNLs scenario and also a more complete 3+2 scenario, followed by a pheomenological study of LEGEND-1000 and DUNE experiments. Finally, we perform a combined analysis for signals observed in both experiments. Chapter 5 demonstrates the other work in this thesis which is about how a HNL-ALP (axion-like particle) coupling impacts the evolution of the Universe. HNLs in the mass range of MeV to GeV are studied together with 10 eV to 1 keV mass ALPs. The history of HNLs, ALPs and neutrino abundance is computed and the impact on cosmology is illustrated. At the end of this thesis, Chapter 6 summarises the two works and gives an outlook for future research in these directions.

Chapter 2

The Standard Model & Beyond

Before a discussion of the three types of neutrinos in the SM of elementary particles, this chapter reviews of the structure and content of the SM with an emphasis of the leptonic sector. I will then discuss the need to extend the SM to deal neutrino oscillation and finally give some insights of the seesaw mechanism to the neutrino mass problem.

2.1 The Standard Model of Elementary Particles

The SM of elementary particles preserves a $SU(3)_c \times SU(2)_L \times U(1)_Y$ symmetry [1–3] and it contains 6 types of quarks, 6 types of leptons, 4 gauge bosons and 1 scalar boson. The $SU(3)_c$ non-abelian group is responsible for the interactions between coloured quarks and gluons, as discussed in quantum chromo dynamics (QCD) [40–42]. The rest of the symmetry group, $SU(2)_L \times U(1)_Y$, gives us the electroweak (EW) sector. The weak and electromagnetic interactions emerge through the spontaneous EW symmetry breaking via the Higgs mechanism [43–45]. Apart from giving masses to the gauge bosons, the Higgs also gives masses to most of the fermion fields in the SM.

Table 2.1 shows the field content and the corresponding charge under each symmetry. All the fermion fields stand for the three generations of particles: e, μ, τ for leptons, u, c, t for $u_{L/R}$ and d, s, d for $d_{L/R}$. In the QCD and quark sector, the quark fields (Q, u_R, d_R) transform as colour triplets under the $SU(3)_c$ group associated with gluons and the representation $\bar{3}$ stands for the conjugated triplets for the

Fields	$SU(3)_c$	$SU(2)_L$	$U(1)_Y$
$L \equiv \begin{pmatrix} \nu_L \\ \ell_L \end{pmatrix}$	1	2	-1/2
$Q \equiv \begin{pmatrix} u_L \\ d_L \end{pmatrix}$	3	2	1/6
ℓ_R	1	1	1
u_R	$\bar{3}$	1	2/3
d_R	$\bar{3}$	1	-1/3
W	1	3	0
B	1	1	0
G	8	1	0
$H \equiv \begin{pmatrix} h^+ \\ h^0 \end{pmatrix}$	1	2	1/2

Table 2.1: Particle content in the SM and representations under the SM gauge group stands for. The left hand lepton doublet is for all three generations of charged leptons $\ell_L = (e_L, \mu_L, \tau_L)$ and the three corresponding neutrinos. The left-handed quark doublet is for all three generations $u_L = (u_L, c_L, t_L)$ and $d_L = (d_L, s_L, b_L)$ and all colour states (r, g, b). The weak hypercharge is given by $Y = Q - T_3$ with Q as the electric charge and T_3 is the third component of the weak isospin.

right-handed components. The gluon field G contains 8 fundamental representation generators of the $SU(3)_c$ group. The left-handed components of the fermion fields transform as doublets under the $SU(2)_L$ group, whereas the right-handed components transform as singlets. The relevant bosons for the $SU(2)_L$ and $U(1)_Y$ are the $W^{\pm}$ bosons and the B boson respectively. The W field also transforms as a triplet and the B field is a singlet under $SU(2)_L$. W and B do not carry any weak hypercharge for $U(1)_Y$.

The SM Lagrangian can be written as,

$$\mathscr{L}_{\text{SM}} = \mathscr{L}_{\text{Gauge}} + \mathscr{L}_{\text{Fermion}} + \mathscr{L}_{\text{Higgs}} + \mathscr{L}_{\text{Yukawa}} \,. \tag{2.1}$$

The gauge part $\mathscr{L}_{\text{Gauge}}$ describes the photon, weak boson and gluon dynamics.

$$\mathscr{L}_{\text{Gauge}} = -\frac{1}{4} B_{\mu\nu} B^{\mu\nu} - \frac{1}{4} W^i_{\mu\nu} W^{i\mu\nu} - \frac{1}{4} G^a_{\mu\nu} G^{a\mu\nu}. \tag{2.2}$$

The fermion part $\mathscr{L}_{\text{Fermion}}$ gives the details for the dynamics of the fermionic

fields and their interactions with the gauge fields, it can be shown in the Eq. (2.3).,

$$\begin{aligned}\mathscr{L}_{\text{Fermion}} = & \sum_{\ell=e,\mu,\tau} i\bar{L}^{\ell}\gamma^{\mu}\left(\partial_{\mu} - ig_1 Y_L^{\ell} B_{\mu} - ig_2 \frac{\tau^i}{2} W_{\mu}^i\right) L^{\ell} \\ & + \sum_{q=d,s,b} i\bar{Q}^{q}\gamma^{\mu}\left(\partial_{\mu} - ig_1 Y_L^{q} B_{\mu} - ig_2 \frac{\tau^i}{2} W_{\mu}^i - ig_s \frac{t^a}{2} G_{\mu}^a\right) Q^{q} \\ & + \sum_{\ell=e,\mu,\tau} i\bar{\ell}_R\gamma^{\mu}\left(\partial_{\mu} - iY_R^{\ell} g_1 B_{\mu}\right)\ell_R \\ & + \sum_{u'=u,c,t} i\overline{u_R}\gamma^{\mu}\left(\partial_{\mu} - iY_R^{q} g_1 B_{\mu}\right) u'_R \\ & + \sum_{d'=d,s,b} i\overline{d_R}\gamma^{\mu}\left(\partial_{\mu} - iY_R^{q} g_1 B_{\mu}\right) d'_R,\end{aligned} \tag{2.3}$$

here Y_L is the weak hypercharge and g_1 is the B field coupling strength. τ^i is the normalised $SU(2)_L$ group generators and g_2 is the W field coupling strength. g_2 is gluon field coupling strength. It can also be seen from the Lagrangian that the right-handed fermion fields only interact with the B field, whereas the left-handed leptons also interact with the W and the left-handed quarks interact with all three gauge fields. The G field only interacts with the quark sector and t^a is the normalised group generators for $SU(3)_c$.

The Yukawa sector $\mathscr{L}_{\text{Yukawa}}$ shows how fermionic masses can be generated via Higgs boson.

$$\begin{aligned}\mathscr{L}_{\text{Yukawa}} = & -\sum_{\ell=e,\mu,\tau} \mathrm{y}_{\ell}\bar{L}^{\ell} H \ell_R - \sum_{\substack{q=d,s,b \\ d'=d,s,b}} \mathrm{y}^{d}_{qu}\bar{Q}^{q} H d'_R \\ & - \sum_{\substack{q=d,s,b \\ u'=u,c,t}} \mathrm{y}^{u}_{qu'}\bar{Q}^{q}\tilde{H} u'_R + \text{ h.c. },\end{aligned} \tag{2.4}$$

$\tilde{H}$ stands for the conjugate Higgs field. The Yukawa term shows how the Higgs gives mass to the fermionic fields. This type of mass is called the Dirac mass for fermion which will be discussed in the later section.

The final part $\mathscr{L}_{\text{Higgs}}$ gives the properties of Higgs itself and its interaction

with itself and the gauge bosons.

$$\begin{aligned}\mathscr{L}_{\text{Higgs}} =& H^\dagger \left(\partial_\mu + \frac{i}{2} g_1 B_\mu + i g_2 W_\mu^a \frac{\tau^a}{2}\right)\left(\partial^\mu - \frac{i}{2} g_1 B^\mu - i g_2 W^{b\mu} \frac{\tau^b}{2}\right) H \\ & - \lambda \left(H^\dagger H - \frac{v^2}{2}\right)^2,\end{aligned} \tag{2.5}$$

v in the Lagrangian is the Higgs vacuum expectation value and it usually has a value of 246 GeV. The first line describes the interactions between the Higgs and the gauge bosons and the second line contains the Higgs kinetic, self-interaction and mass terms. The interaction between the Higgs and the gauge bosons will be discussed in the spontaneous symmetry breaking section.

2.2 Particle Symmetry

Fermionic fields given in Eq. (2.3) are elementary particles that contribute to ordinary matter formation. All fermions in the SM satisfy Dirac's equation,

$$i\gamma^\mu \partial_\mu \psi - m\psi = 0. \tag{2.6}$$

The field ψ in this equation form a spinor, which is a 4-component object transforming differently from scalars or vectors under Lorentz transformations and m defined as the bare mass of the field ψ. Correspondingly, the gamma matrices γ^μ are 4×4 matrices satisfying

$$\frac{1}{2}\{\gamma^\mu, \gamma^\nu\} = \eta^{\mu\nu}\mathbf{1}. \tag{2.7}$$

The Dirac Lagrangian can be expressed from Dirac's Equation,

$$\mathscr{L}_{\text{Dirac}} = \bar{\psi}\left(i\gamma^\mu \partial_\mu - m\right)\psi = \bar{\psi}(i\not{\partial} - m)\psi, \tag{2.8}$$

with the conjugate field $\bar{\psi} = \psi^\dagger \gamma_0$, also called the Dirac adjoint. The equation of motion for this Lagrangian is just the Dirac equation.

A fifth gamma matrix is defined as,

$$\gamma^5 = i\gamma^0\gamma^1\gamma^2\gamma^3. \tag{2.9}$$

It has the properties $(\gamma^5)^2 = \mathbf{1}$, $(\gamma^5)^\dagger = \gamma^5$ and $\{\gamma^5, \gamma^\mu\} = 0$. The left and right chiral projection operators for spinors can be defined correspondingly,

$$\begin{aligned} P_L &= \frac{1}{2}\left(\mathbf{1} - \gamma^5\right), \\ P_R &= \frac{1}{2}\left(\mathbf{1} + \gamma^5\right). \end{aligned} \tag{2.10}$$

These hermitian projection operators can act on the spinors and give the left and right components ψ_L and ψ_R of a field repectively. These 2-component spinors are called Weyl spinors. The two parts add up to the whole fermionic field ψ. The Dirac Lagrangian can be therefore rewritten as

$$\mathscr{L} = \bar{\psi}_L i \not{\partial} \psi_L + \bar{\psi}_R i \not{\partial} \psi_R - m(\bar{\psi}_L \psi_R + \bar{\psi}_R \psi_L). \tag{2.11}$$

If the field is massless, the left and right components will decouple and the fermion field will have an additional global U(1) axial symmetry. There will be opposite global phases between the left and right chiral fields. The purpose of introducing the Weyl spinors ψ_L and ψ_R is for theoretical simplification in weak interaction. Parity operation reverse the spatial coordinates. It was found that there is only left-handed weak current and no matter how to reverse the coordinates. It was also observed in Wu's experiment [11] that parity is not conserved in weak interaction. The effective 4-point weak Lagrangian which describes beta decay process($n \to p\bar{\nu}_e e$) is written as

$$\mathscr{L}_{\text{weak}} = -\frac{G_F}{\sqrt{2}} J^\mu J^\dagger_\mu, \tag{2.12}$$

with G_F defined as the Fermi constant for weak interaction and the effective charged current J_μ is defined as

$$J_\mu = \overline{\nu_e}\gamma_\mu (1 - \gamma_5) e + \bar{u}\gamma_\mu (1 - \gamma_5) d. \tag{2.13}$$

Parity violation gives different properties to the left-handed fermions and right-handed fermions. It can also be noticed from Eq. (2.3) that the left-handed fermions transform differently from the right-handed fermions due to different symmetry groups. Theoretically, a fermion mass term $m\bar{\psi}\psi$ should always exist in its Lagrangian, such a mass term is forbidden in the SM since this mass is not invariant under gauge transformation.

For the lepton sector, the kinetic term goes with the covariant derivative for $SU(2)$ as given in Eq. (2.23). It can also be extended to the quark sector by adding the $SU(3)_c$ components into the derivative, so for any elementary fermion field ψ,

$$\mathscr{L}_{\text{Fermion}} = \bar{\psi}_L i \not{D} \psi_L + \bar{\psi}_R i \not{D} \psi_R, \tag{2.14}$$

the covariant derivative for fermions is defined as

$$D_\mu = \partial_\mu + i g_s G^a_\mu t^a + i g_1 B_\mu Y + i g_2 W^i_\mu \tau^i. \tag{2.15}$$

It is clear that the kinetic term in Eq. (2.14) describes both the kinetic motion of the SM fermionic fields and their interaction with to the SM gauge fields.

For the SM gauge bosons, a general gauge boson Lagrangian is

$$\mathscr{L}_{\text{Proca}} = -\frac{1}{4} F_{\mu\nu} F^{\mu\nu} + \frac{1}{2} m^2 A_\mu A^\mu, \tag{2.16}$$

with $F_{\mu\nu} = \partial_\mu A_\nu - \partial_\nu A_\mu$ is the field strength tensor and A_μ is the vector field. For different SM gauge fields $(G^a_\mu, W^i_\mu, B_\mu)$, the kinetic terms are gauge invariant under different symmetries $(SU(3)_c, SU(2)_L, U(1)_Y)$. By fixing the gauge $\partial_\mu A^\mu = 0$, one of the degrees of freedom of the gauge field is removed. The massive gauge field with three polarisations is therefore not invariant under a gauge transformation. Proca field is a historical version of massive gauge bosons. It can be seen in the following section that gauge bosons can acquire their masses via interactions with a scalar field.

2.3 Spontaneous Symmetry Breaking

It was discovered in spontaneous symmetry breaking of Abelian fields that every broken generator gives a massless Goldstone boson [46]. This prediction contradicts with experimental observation of massive weak gauge bosons [47–51].

In the SM, the $SU(2)_L$ group is non-Abelian and the Lagrangian becomes,

$$\mathscr{L}_{\text{Gauge}} = -\frac{1}{2}\operatorname{Tr} F_{\mu\nu}F^{\mu\nu} + \frac{1}{2}\left(D_\mu\phi\right)_i\left(D^\mu\phi\right)_i - V(\phi). \tag{2.17}$$

The field ϕ is now a two component scalar with a non-zero vacuum expectation value $\phi = \phi_0 + \varphi$. The scalar potential is $V(\phi) = \frac{1}{2}\lambda\phi_i^4 - \mu^2\phi_i^2$ with the mass term $\mu^2 > 0$. By defining a set of generators $\hat{T}$ which makes $\hat{T}\phi_0 = 0$, the corresponding vector is $\hat{\phi}^a = i\hat{T}^a\phi_0$ and gauge field $A_\mu = A_\mu^a\hat{T}^a$. The covariant derivative can be written as

$$\left(D_\mu\phi\right)_i = \partial_\mu\varphi_i + gA_\mu^a\hat{\phi}_i^a + igA_\mu^a\hat{T}_{ij}^a\varphi_j. \tag{2.18}$$

Therefore the kinetic term of the Lagrangian is

$$\begin{aligned}\frac{1}{2}\left(D_\mu\phi\right)_i\left(D^\mu\phi\right)_i = \frac{1}{2}\left(\partial_\mu\varphi_i\right)\partial^\mu\varphi_i + g\left(\partial_\mu\varphi_i\right)A^{\mu,a}\hat{\phi}_i^a \\ + \frac{1}{2}g^2\lambda_a A_\mu^a A^{\mu,a} + \mathscr{O}(A^4),\end{aligned} \tag{2.19}$$

where λ_a is the eigenvalue of the ϕ^2 operator or the so-called symmetry breaking operator S in kinetic term,

$$\begin{aligned}\hat{\phi}_i^a\hat{\phi}_i^b &= \left(\hat{\phi}^a\right)^T\hat{\phi}^b = -\phi_0^T\left(\hat{T}^a\right)^T\hat{T}^b\phi_0 = -\left(c^a\right)^\alpha\phi_0^T\left(T^\alpha\right)^T T^\beta\phi_0(c^b)^\beta \\ &= (c^a)^\alpha S^{\alpha\beta}(c^b)^\beta = \lambda_b(c^a)^\alpha(c^b)^\alpha = \lambda_b\delta_{ab}.\end{aligned} \tag{2.20}$$

The mixing term here again can be removed by choosing a new gauge for the infinitesimal transformation of $\varphi_i \to \varphi_i + \theta^a\phi_i^a$,

$$\theta^a = -\frac{1}{\lambda_a}\left(\varphi^T\hat{\phi}^a\right), \tag{2.21}$$

where θ^a is defined as an infinitesimal transformation of the gauge group $M =$

$\mathbf{1} + i\theta^a \hat{T}^a$. A similar unitary gauge $\varphi^T \hat{\phi}^a = 0$ can be derived as it is done for the Abelian scenario. The final Lagrangian computed is

$$\begin{aligned}\mathscr{L} = &-\frac{1}{4}\left(\partial_\mu A^a_\nu - \partial_\nu A^a_\mu\right)\left(\partial^\mu A^{\nu,a} - \partial^\nu A^{\mu,a}\right) + \frac{1}{2}g^2\lambda_a A^a_\mu A^{\mu,a} \\ &+ \frac{1}{2}\partial_\mu \varphi_i \partial^\mu \varphi_i - \frac{1}{2}m^2_{ij}\varphi_i\varphi_j.\end{aligned} \tag{2.22}$$

The mass $m^a = g\sqrt{\lambda_a}$ for each gauge field in the theory and one scalar field is removed by the unitary gauge.

In the $SU(2)_L$ symmetry, the symmetry breaking operator will give three degenerate massive states which corresponds to three weak bosons and one massless state which is the photon. There are two different coupling strengths g_1 and g_2 for the gauge bosons respectively,

$$D_\mu \phi = \partial_\mu \phi + i g_2 A_\mu \phi + i(g_1/2) B_\mu \phi, \tag{2.23}$$

with $A_\mu = A^a_\mu t^a$ is the $SU(2)_L$ gauge field and the forth component $B_\mu \equiv A^4_\mu$ is under $U(1)_Y$. This gives rise to the Weinberg mixing angle θ_W with

$$\sin\theta_W = \frac{g_1}{\sqrt{g_1^2 + g_2^2}}, \quad \cos\theta_W = \frac{g_2}{\sqrt{g_1^2 + g_2^2}}. \tag{2.24}$$

The symmetry breaking pattern for this scenario is $SU(2)_L \times U(1)_Y \to U(1)_{\text{em}}$. The residual symmetry $U(1)_{\text{em}}$ is a linear combination of $U(1)_Y$ and the $U(1)$ subgroup of $SU(2)_L$. A new set of generators $\hat{A}^a_\mu T^a = A^a_\mu t^a$ is given in the symmetry breaking basis, the fields are

$$\begin{aligned} A_\mu &= \hat{A}^1_\mu = \cos\theta_W B_\mu + \sin\theta_W A^3_\mu, \\ W^\pm_\mu &= \frac{1}{\sqrt{2}}\left(\hat{A}^2_\mu \mp i\hat{A}^3_\mu\right) = \frac{1}{\sqrt{2}}\left(A^1_\mu \mp iA^2_\mu\right), \\ Z_\mu &= \hat{A}^4_\mu = \cos\theta_W A^3_\mu - \sin\theta_W B_\mu. \end{aligned} \tag{2.25}$$

The covariant derivative can be rewritten correspondingly as

$$\begin{aligned} D_\mu = \partial_\mu + i\frac{g_1 g_2}{\sqrt{g_1^2+g_2^2}}\left(T^3+Y\right)\mathscr{A}_\mu \\ + i\frac{\left(g_2^2 T^3 - g_1^2 Y\right)}{\sqrt{g_1^2+g_2^2}} Z_\mu + \frac{ig_2}{\sqrt{2}}\left(W_\mu^+ T^+ + W_\mu^- T^-\right). \end{aligned} \tag{2.26}$$

The masses of the weak bosons are therefore $m_\gamma = 0$ for the A field, $m_W = g_2 v/2$ and $m_Z = v\sqrt{g_1^2+g_2^2}/2$. Weinberg angle can be calculated from the gauge boson masses, $\cos\theta_W = \frac{m_W}{m_Z} = 0.88153$ at tree level and there will also be higher order corrections. The vacuum expectation value is $v = \frac{2m_w}{g_2} = 246$ GeV. This covariant derivative is the same as Eq. (2.26). By rearranging the basis of the covariant derivative, $T^\pm = T^1 \pm iT^2$, the coupling for the residual $U(1)_{\text{em}}$ symmetry can be obtained,

$$e = \frac{g_1 g_2}{\sqrt{g_1^2+g_2^2}} = g_2 \sin\theta_W, \tag{2.27}$$

and the electric charge can be expressed in terms of the weak isospin and weak hypercharge,

$$Q = T^3 + Y. \tag{2.28}$$

2.4 Fermion Mass

As mentioned in previous section, the SM fermions cannot have mass terms due to the different gauge transformations of the left-handed and right-handed fields. The Higgs boson will also be needed in order to generate the masses for fermions via a different way from the gauge fields, namely, the Yukawa coupling.

The Higgs doublet needs to couple with the left-handed doublet and right-handed singlet in order to generate Yukawa type of coupling for fermion mass term in the SM. By defining the Higgs field H non-zero vev $\phi_0 = \frac{1}{\sqrt{2}}\begin{pmatrix} 0 & v \end{pmatrix}^T$, the mass

term in Eq. (2.11),

$$\begin{aligned}\mathscr{L}^{\text{Lep}}_{\text{Yukawa}} &= -\bar{L}\mathrm{Y}_\ell H \ell_R - \bar{\ell}_R \mathrm{Y}_\ell H^\dagger L \\ &= -\frac{Y_\ell}{\sqrt{2}}\left(\begin{pmatrix} \bar{\nu}_L & \bar{\ell}_L \end{pmatrix}\begin{pmatrix} 0 \\ v \end{pmatrix}\ell_R + \bar{\ell}_R \begin{pmatrix} 0 & v \end{pmatrix}\begin{pmatrix} \nu_L \\ \ell_L \end{pmatrix}\right) \\ &= -\frac{1}{\sqrt{2}} Y_\ell v \left(\bar{\ell}_L \ell_R + \bar{\ell}_R \ell_L\right).\end{aligned} \tag{2.29}$$

It is discussed in previous section, there are three generations of fermions in the SM. In case of leptons, they are e, μ and τ defined in the weak interaction basis, or flavour basis, as defined in Eq. (2.25). The flavour basis is not necessarily the same as the mass basis of leptons since the kinetic term and the mass term are two separate parts in the Lagrangian. It is alway possible to find a biunitary transformation $U\mathrm{M}_\ell V = \mathrm{M}_m$ which diagonalises M_ℓ, where M_ℓ is the lepton mass matrix in flavour basis and M_m is the diagonal lepton mass matrix. The transformation takes leptonic fields from the flavour basis to the mass eigenstate basis due to the misalignment between the two sets of bases. The term Y_ℓ is a 3×3 Yukawa coupling matrix between the leptons and Higgs field.

It can be seen from Eq. (2.29), there is no mass for neutrinos.The same mechanism can be applied to the quark sector by replacing the lepton doublets and singlets with the quark fields.This type of mass generated by the left-handed and right-handed fields is called a Dirac mass.

The charge conjugation of a spinor ψ is defined as

$$\psi^c \equiv C\overline{\psi}^T, \quad (\psi_\mathrm{L})^c \equiv C\overline{\psi_\mathrm{L}}^T, \quad (\psi_\mathrm{R})^c \equiv C\overline{\psi_\mathrm{R}}^T, \tag{2.30}$$

the charge conjugation operator follows the rules of

$$C\gamma_\mu^T C^{-1} = -\gamma_\mu, \quad C\gamma_5^T C^{-1} = \gamma_5, \quad C^{-1} = C^\dagger = C^T = -C. \tag{2.31}$$

Gamma matrices help the mass term in Eq. (2.11) to be Lorentz invariant. If the relation $\psi^c = \psi$ holds, the field ψ is said to be Majorana, otherwise it is Dirac.

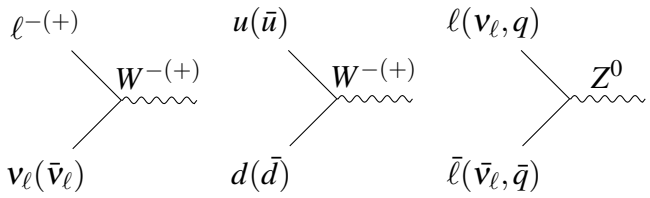

Figure 2.1: Charged (left and middle) & neutral (right) current vertices for leptons ℓ and ν_ℓ and quarks q, u, d.

A Lorentz invariant mass term of $-\frac{1}{2}m\bar{\psi_L}^c\psi_L$ can be then generated for Majorana fermion fields by using the gamma matrices. This type of mass is called the Majorana mass.

It will be discussed in next chapter, a neutrino itself can in principle have Majorana mass. It can also have Dirac mass through Yukawa coupling if a right-handed neutrino is added.

There will be right-handed singlets for both u type and d type quark fields. All generations of u and d type quarks get masses from their couplings to Higgs as shown in Eq. (2.32).

$$\mathscr{L}_{\mathrm{Y}} = -\bar{u}_R \mathrm{Y}_u \widetilde{H}^\dagger Q - \bar{d}_R \mathrm{Y}_d H^\dagger Q + \text{ h.c. }, \tag{2.32}$$

where $\widetilde{H} \equiv i\tau^2 H^*$ with τ^2 is the second Pauli matrix under $SU(2)_L$.

The charged current with leptons and hadrons has been seen in Eq. (2.13). The weak current vertices are shown in Fig.2.1. The charged current involves $W^\pm$, whereas the neutral current involves Z. The weak processes contain only left-handed fermionic fields due to parity violation.

As discussed in Sec. 2.2, the difference from the lepton sector is the misalignment between the flavour and mass states. In the flavour basis or weak interaction basis, unitary matrices can be defined V_L^u, V_L^d, V_L^ℓ which take the u quark fields, d quark fields and charged lepton fields from the mass basis ψ_L^{mass} to the flavour basis ψ_L^{flavour}, such as $\psi_L^{\text{flavour}} = V_L^f \psi_L^{\text{mass}}$. A charged current Lagrangian can be written

correspondingly,

$$\mathscr{L}_{W^\pm} = -\frac{g}{\sqrt{2}}\bar{\nu}_L W^\mu \gamma_\mu V_L^\ell \ell'_L - \frac{g}{\sqrt{2}}\bar{u}'_L W^\mu \gamma_\mu \left(V_L^{u\dagger} V_L^d\right) d'_L + \text{ h.c. }. \tag{2.33}$$

The flavour-mass mixing matrix for quarks is called the Cabibbo-Kobayashi-Maskawa (CKM) matrix [52, 53],

$$V_{\text{CKM}} \equiv V_L^{u\dagger} V_L = \begin{pmatrix} V_{ud} & V_{us} & V_{ub} \\ V_{cd} & V_{cs} & V_{cb} \\ V_{td} & V_{ts} & V_{tb} \end{pmatrix}, \tag{2.34}$$

which in the standard parameterisation is given by

$$V_{\text{CKM}} = \begin{pmatrix} c_{12}c_{13} & s_{12}c_{13} & s_{13}e^{-i\delta_{CP}} \\ -s_{12}c_{23} - c_{12}s_{13}s_{23}e^{i\delta_{CP}} & c_{12}c_{23} - s_{12}s_{13}s_{23}e^{i\delta_{CP}} & c_{13}s_{23} \\ s_{12}s_{23} - c_{12}s_{13}c_{23}e^{i\delta_{CP}} & -c_{12}s_{23} - s_{12}s_{13}c_{23}e^{i\delta_{CP}} & c_{13}c_{23} \end{pmatrix}. \tag{2.35}$$

This matrix contains three Cabibbo mixing angles $(\theta_{12}, \theta_{13}, \theta_{23})$ of $s_{ij} = \sin\theta_{c,ij}, c_{ij} = \cos\theta_{c,ij}$ and one complex phase δ_{CP} and it describes how different types of quarks mix with each other.

2.5 Beyond The Standard Model

Apart from the gauge symmetries discussed above, there are two other symmetries of the SM namely baryon number B and lepton number L. Each quark has a baryon number of $+1/3$ (-1/3 for anti-quarks) in order to give an overall +1 for a baryon (-1 for anti-baryons). Each lepton has a lepton number of +1 (-1 for anti-lepton), but in addition, there are lepton numbers L, or, flavour numbers for each generation (e, μ, τ). These symmetries are accidental global symmetries in the SM. Accidental means they emerge due to the gauge symmetry and the particle content in the SM, and, small violation in these symmetries will lead to new physics, eg. L is violated if a right-handed Majorana neutrino is added. Lepton flavour violation has already been observed in neutrino oscillation [54–56], it must happen for charged leptons

as well, but the rate is small.

As discussed in Sec. 2.4, fermion fields must have both left-handed and right-handed components in order to generate masses via Yukawa coupling with the Higgs boson. Neutrinos were assumed to be massless in the SM, are now observed to be massive due to neutrino oscillations. It is discussed that mixing is a consequence of mismatch of the flavour states and the mass states. Mixing between the states can cause change in flavour during the propagation of neutrinos and it requires at lest two massive neutrinos out of three. The origin of neutrino masses cannot be understood in the SM since there is only the left-handed neutrino fields. There may be sterile right-handed neutrinos, or other mass generation mechanisms. This work focuses on neutrino mass generation via sterile right-handed neutrino or HNL in the non-standard seesaw scenarios.

The matter-antimatter asymmetry in the Universe is not explained well in the SM. The *CP* violation in the quark sector is not sufficient to create sufficient matter over antimatter as observed. Sakharov [57] gave the conditions to create the amount of asymmetry in the Universe. The asymmetry will require most crucially baryon number violation in the quark sector. Secondly, *C* and *CP* violation would give difference between the forward and backward rates in baryon number violation processes. Lastly, the baryon number violation process should happen out of thermal equilibrium. Baryogenesis may be facilitated by extra *CP* violation effects from neutrino sector since the *CP* violation effect in the neutrino sector is larger than the effect in the quark sector. Additionally, sterile right-handed neutrino may also contribute to *CP* violation significantly.

The SM explains many phenomena well, but there is tension between the matter observed electromagnetically and the excess gravitational effect observed from rotation of galaxies [58], galactic cluster [59], CMB [60, 61] and many other indirect evidence. This is the well-known dark matter problem. There is no particle in the SM which can be used to explain dark matter and exotic particles are needed to explain the phenomenon.

The Axion is a pseudo-scalar boson, which was initially proposed to solve

the strong CP problem in QCD [62]. The first proposed axion type is therefore called the QCD axion, which not only interacts with quarks and gluons, but also with other SM particles such as the photon, at tree or loop level. QCD axion will give an additional contribution to Maxwell's equations in electromagnetism, and the corresponding axion-photon coupling is tightly constrained experimentally [63–65]. Astrophysical observations such as active galactic nuclei and supernovae also put strong bounds on the axion-photon coupling strength [66]. The coupling between the axion and SM particles should be generally small because axions have not been detected so far. The coupling strengths are expected to be inversely proportional to a symmetry breaking scale f_a, with a high f_a therefore giving a weak coupling. The QCD axions, mix with neutral pions, with mass m_π and decay constant f_π, and the axion mass m_a should obey the relation $m_a f_a \simeq m_\pi f_\pi$ if they have the same quantum number. The QCD axion mass is therefore inversely proportional to its coupling strength. The QCD axion is a type of ALP, which is more general pseudo-scalar particle not necessarily related to the strong CP problem. ALPs therefore do not necessarily interact with quarks and gluons. Also, their masses do not need to be related to their coupling strengths. ALPs were latterly found to be a potential candidate for dark matter [67, 68]. They can not only explain the observed dark matter relic density in the Universe. This thesis will discuss one scenario of ALPs, which can be produced by HNLs.

There are many more issues in the SM, for example, the strong CP problem in the quark sector, the self-coupling of Higgs field, the naturalness of the SM generations, etc.. This work only focuses on the problems of neutrino mass and lepton number, and will not discuss these issues in detail. This thesis will focus on probing the properties of HNLs and ALPs in different phenomenological scenarios.

Chapter 3

Neutrino Physics

This chapter aims to discuss our understanding of neutrinos and recent experimental and theoretical developments in neutrino physics. This chapter will start with neutrino mixing and oscillations and progress to Dirac and Majorana masses of neutrinos. Secondly, the seesaw mechanism and a brief introduction to heavy neutral leptons (HNL) is given. Finally, the basic phenomenology of neutrinoless double beta decay and cosmology is introduced.

3.1 Neutrino Mixing & Oscillation

In the SM, neutrinos are assumed to be massless because of their left-handed nature. One can add right-handed partners to acquire neutrino masses via the Higgs mechanism just like what is done in the quark and charged lepton sector and these neutrinos are therefore Dirac type.

The three corresponding right-handed neutrinos N_R are singlets under $SU(2)_L$ and there will be an additional term in the SM Lagrangian,

$$\mathscr{L}_{\text{Yukawa}} \supset - \sum_{\substack{\ell=e,\mu,\tau \\ i=1,2,3}} \mathrm{y}^{\nu}_{\ell i} \bar{L}^{\ell} \tilde{H} N^{i}_{R} + \text{ h.c.} \tag{3.1}$$

Here, $\mathrm{y}^{\nu}_{\ell i}$ is the Yukawa couplings for neutrinos. The mass obtained after symmetry breaking will be $m^{\nu}_{\ell i} = \mathrm{y}_{\ell i} v/\sqrt{2}$.

A similar diagonalisation matrix as in Eq. (2.34) can be given in the neutrino

sector,

$$\begin{pmatrix} \nu_e \\ \nu_\mu \\ \nu_\tau \end{pmatrix} = U_{\rm PMNS} \begin{pmatrix} \nu_1 \\ \nu_2 \\ \nu_3 \end{pmatrix} = \begin{pmatrix} V_{e1} & V_{e2} & V_{e3} \\ V_{\mu 1} & V_{\mu 2} & V_{\mu 3} \\ V_{\tau 1} & V_{\tau 2} & V_{\tau 3} \end{pmatrix} \begin{pmatrix} \nu_1 \\ \nu_2 \\ \nu_3 \end{pmatrix}. \tag{3.2}$$

The Pontecorvo-Maki-Nakagawa-Sakat (PMNS) unitary matrix [12, 15] $U_{\rm PMNS}$ which diagonalises the Yukawa matrix y^ν is introduced due to the misalignment between the weak flavour eigenstates and the mass eigenstates of neutrinos as stated in Eq. (2.33),

$$\begin{aligned} \nu_L^m &= U_L^\dagger \nu_L, \\ N_R^m &= U_R^\dagger N_R. \end{aligned} \tag{3.3}$$

Here, ν_L are the left-handed neutrinos in the SM and the index m indicates the mass eigenstates of the neutrinos. The matrices U_L and U_R are the mixing matrices for the left-handed and right-handed parts of the neutrino fields, respectively.

According to the charged weak Lagrangian in Eq. (2.33), the charged current can be written as

$$j^\mu_{\ell,\rm W}/2 = \overline{\nu_L}\gamma^\mu \ell_L = \overline{\nu_L^m} U_L^\dagger \gamma^\mu V_L \ell_L^m = \overline{\nu_L^m} U^\dagger_{\rm PNMS} \gamma^\mu \ell_L^m. \tag{3.4}$$

Here, the PMNS matrix is defined in terms of the neutrino mixing matrix U_L^ℓ and charged lepton mixing matrix V_L^ℓ which takes the charged flavour states to the mass states,

$$U_{\rm PNMS} = V_L^{\ell\dagger} U_L. \tag{3.5}$$

The parameterisation of the PMNS matrix follows that of the CKM matrix constructed in Eq. (2.34),

$$\begin{aligned} U_{\rm PMNS} &= U_{23}(\theta_{23}) U_{13}(\theta_{13}, \delta) U_{12}(\theta_{12}) \\ &= \begin{pmatrix} c_{12}c_{13} & s_{12}c_{13} & s_{13}e^{-i\delta} \\ -s_{12}c_{23} - c_{12}s_{23}s_{13}e^{i\delta} & c_{12}c_{23} - s_{12}s_{23}s_{13}e^{i\delta} & s_{23}c_{13} \\ s_{12}s_{23} - c_{12}c_{23}s_{13}e^{i\delta} & -c_{12}s_{23} - s_{12}c_{23}s_{13}e^{i\delta} & c_{23}c_{13} \end{pmatrix}. \end{aligned} \tag{3.6}$$

All mixing angles take values from 0 to $\pi/2$ and the δ phase goes from 0 to 2π. If neutrinos are Majorana particles, there will be additional Majorana CP phases ϕ_1 and ϕ_2 and the mixing matrix will be [69]

$$V_{\text{PMNS}}^{\text{Majorana}} = V_{\text{PMNS}}^{\text{Dirac}} \begin{pmatrix} 1 & 0 & 0 \\ 0 & e^{i\phi_1} & 0 \\ 0 & 0 & e^{i\phi_2} \end{pmatrix}. \tag{3.7}$$

Following from Eq. (3.7), the neutrino flavour states can be written in terms of the mass states,

$$\nu_\ell(x) = \sum_{i=1}^{3} U_{\ell i}^* \nu_i(x), \ell = e, \mu, \tau. \tag{3.8}$$

The flavour state is a superposition of all the mass states the neutrino has. By using a standard quantum mechanical framework for simplicity, the time-dependent superposition is expressed as

$$|\nu_\ell(t)\rangle = \sum_{i=1}^{3} U_{\ell i}^* e^{-iE_i t} |\nu_i(0)\rangle . \tag{3.9}$$

Here, E_i is the energy of the neutrino and $|\nu_i(0)\rangle$ is the initial state of the neutrino. The neutrino transition amplitude is constructed as

$$A_{\nu_\alpha \to \nu_\beta}(t) \equiv \langle \nu_\beta \mid \nu_\alpha(t) \rangle = \sum_{i=1}^{3} U_{\alpha i}^* U_{\beta i} e^{-iE_i t}, \tag{3.10}$$

and the transition probability is written as

$$P_{\nu_\alpha \to \nu_\beta}(t) = \left| A_{\nu_\alpha \to \nu_\beta}(t) \right|^2 = \sum_{i,j} U_{\alpha i}^* U_{\beta i} U_{\alpha j} U_{\beta j}^* e^{-i\left(E_i - E_j\right)t}. \tag{3.11}$$

The formula gives the probability of a neutrino of type α to be converted to type β as time progresses. Due to the small neutrino masses, neutrinos are usually ultra-relativistic during propagation. The dispersion relation of neutrinos can be approximated as $E_i \simeq E + \frac{m_i^2}{2E}$ with the kinetic energy of the neutrino and momentum $E = p$. The energy difference in Eq. (3.11) becomes $E_i - E_j \simeq \frac{\Delta m_{ij}^2}{2E}$ with the

definition $\Delta m^2_{ij} \equiv m^2_i - m^2_j$. Also, the relativistic neutrinos travel at nearly the speed of light and the time dependence can be replaced by the distance they traveled with $L = t$ (for $c = 1$),

$$P_{\nu_\alpha \to \nu_\beta} = \sum_{i,j} U^*_{\alpha i} U_{\beta i} U_{\alpha j} U^*_{\beta j} \exp\left(-i \frac{\Delta m^2_{ij} L}{2E}\right). \tag{3.12}$$

Although the probability contains four mixing matrix element, the probability does not depend on the Majorana phases since the quartic term is invariant under rephasing transformation $U_{ij} \to e^{i\alpha_i} U_{ij} e^{i\phi_j}$, where α_i is a global phase factor [70]. Another version of the oscillation formula can be constructed,

$$\begin{aligned} P_{\nu_\alpha \to \nu_\beta} = \delta_{\alpha\beta} &- 4 \sum_{k>j} \mathfrak{Re}\left[U^*_{\alpha k} U_{\beta k} U_{\alpha j} U^*_{\beta j}\right] \sin^2\left(\frac{\Delta m^2_{kj} L}{4E}\right) \\ &+ 2 \sum_{k>j} \mathfrak{Im}\left[U^*_{\alpha k} U_{\beta k} U_{\alpha j} U^*_{\beta j}\right] \sin\left(\frac{\Delta m^2_{kj} L}{2E}\right). \end{aligned} \tag{3.13}$$

If $\alpha = \beta$, the probability is called survival probability and the formula will be the first line of Eq. (3.13). If $\alpha \neq \beta$, it is a transition (or appearance) probability. Both real and imaginary terms depend on the CP phase and the CP phase makes independent transition probabilities different for neutrinos and anti-neutrinos. The transition probabilities for neutrinos and anti-neutrinos are equal only if CP symmetry is preserved (i.e. real mixing matrix). An example can be given if the mixing matrix U is real, in the simplified two neutrino (e, μ only) oscillation scenario,

$$U = \begin{pmatrix} \cos\theta & -\sin\theta \\ \sin\theta & \cos\theta \end{pmatrix}, \tag{3.14}$$

The transition probability for ν_e to ν_μ conversion is

$$P\left(\nu_e \to \nu_\mu\right) = P\left(\bar{\nu}_e \to \bar{\nu}_\mu\right) = P\left(\nu_\mu \to \nu_e\right) = \sin^2(2\theta) \sin^2\left(\frac{\Delta m^2 L}{4E}\right). \tag{3.15}$$

There is only one mixing angle θ and one mass splitting Δm^2 between the two neutrinos. In addition, the survival probability can be written correspondingly

$$P(\nu_e \to \nu_e) = P\left(\nu_\mu \to \nu_\mu\right) = 1 - P\left(\nu_e \to \nu_\mu\right).$$

A more rigorous way to study neutrino oscillations by using wave packet model [71, 72]. The effective interaction Hamiltonian can be written as

$$\mathscr{H}_I(x) = \frac{G_F}{\sqrt{2}} \sum_a U^*_{\alpha a} \bar{\nu}_a(x) \gamma^\rho \left(1 - \gamma_5\right) \ell_\alpha(x) J^P_\rho(x), \tag{3.16}$$

where G_F is the Fermi constant and J^P_ρ is the charged weak current. The time ordered transition amplitude in the quantum field theory framework will be [72]

$$i\mathscr{A}_{\alpha\to\beta}(T,\vec{L}) = \langle P_F, D_F | \hat{T} \left\{ \int d^4x_1 \int d^4x_2 \mathscr{H}^P_I(x_1) \mathscr{H}^D_I(x_2) \right\} | P_I, D_I \rangle, \tag{3.17}$$

where P_I, D_I, P_F, D_F are the initial and final particle states at production and detection, correspondingly. The amplitude will be a function of the propagation time T and propagation baseline $\mathbf{L}$. By assuming the saddle point approximation and a Gaussian momentum distribution, the wave packet for neutrinos is

$$\begin{aligned} |\nu_\alpha\rangle \propto & \sum_a U^*_{\alpha a} \int \mathrm{d}^3 p \sum_h A^i_a(\vec{p},h) \, |\nu_a(\vec{p},h)\rangle \\ & \times \int \mathrm{d}^4 x \exp\left[-i\left(E_i - E_{\nu_a}(\vec{p})\right) t + i\left(\vec{p}_i - \vec{p}\right)\vec{x} - \frac{(\vec{x} - \vec{v}t)^2}{4\sigma^2_{xi}} \right]. \end{aligned} \tag{3.18}$$

Here the index i stands for the neutrinos in production P or detection D. E_i is the average energy, p_i is the average momentum and v_i is the group velocity. σ_{xi} is defined as the spatial width of the wave packet. It satisfy the uncertainty relation,

$$\sigma_{xi}\sigma_{pi} = 1/2, \tag{3.19}$$

where σ_{pi} is the momentum width. The amplitude for production or detection is

$$A^i_a(\vec{p},h) \equiv \bar{u}_{\nu_a}(\vec{p},h) \gamma^\rho \left(1 - \gamma_5\right) v_{\ell_\alpha}\left(\vec{p}_{\ell_\alpha}, h_{\ell_\alpha}\right) J^P_\rho\left(\vec{p}'_{i,I}, h_{i,I}; \vec{p}'_{i,F}, h_{i,F}\right). \tag{3.20}$$

This amplitude can be made for production or detection process and the charged current should be a function of all initial and final state momenta p and helicity states h.

The neutrino transition amplitude inserting the neutrino states into Eq. (3.17) and integrating over space-time,

$$\begin{aligned}\mathscr{A}_{\alpha\to\beta}(T,\vec{L}) \propto \sum_a U^*_{\alpha a} U_{\beta a} \sum_h \int \mathrm{d}^3 p A^P_a(\vec{p},h) A^D_a(\vec{p},h) e^{-S_a(\vec{p})} \\ \times \exp\left[-iE_{\nu_a}(\vec{p})T + i\vec{p}\cdot\vec{L}\right].\end{aligned} \tag{3.21}$$

Here, S_a is defined as

$$S_a(\vec{p}) \equiv \sum_{i=P,D} \frac{(\vec{p}_i - \vec{p})^2}{4\sigma^2_{pi}} + \frac{[(E_i - E_{\nu_a}(\vec{p})) - (\vec{p}_i - \vec{p})\cdot\vec{v}_i]^2}{4\sigma^2_{pi}\lambda_i}, \tag{3.22}$$

where λ is defined as

$$\lambda_i \equiv \sigma^2_{xi}\left(\frac{\vec{v}^2_{iI}}{\sigma^2_{xi_I}} + \frac{\vec{v}^2_{i_F}}{\sigma^2_{xi_F}} + \frac{\vec{v}^2_{\ell\alpha}}{\sigma^2_{x\ell\alpha}}\right) - \vec{v}^2_i. \tag{3.23}$$

$\vec{k}_a$ is defined as the momentum which is the stationary point of S_a so that $\mathscr{A}_{\alpha\to\beta}$ is not suppressed. $\vec{v_{iI}}$ and $\vec{v_{iF}}$ are the velocities for initial and final state neutrinos at detection or production, respectively. $\vec{v_{\ell}}\alpha$ is the charged lepton velocity. $\sigma_{xi(I,F)}$ and $\sigma_{x\ell\alpha}$ are the spatial width of the wave packets of initial or final state neutrinos at detection or production and for charged leptons, correspondingly. The energy and momentum at the stationary point of S_a can be then given under the relativistic approximation,

$$\begin{aligned}\varepsilon_a &\simeq E + \rho\frac{m_a^2}{2E}, \\ k_a &\simeq E - (1-\rho)\frac{m_a^2}{2E},\end{aligned} \tag{3.24}$$

with ρ as the suppression factor,

$$\rho = \frac{\frac{1}{\sigma^2_p} - \frac{\vec{\ell}\cdot\vec{v}_P\left(1-\vec{\ell}\cdot\vec{v}_P\right)}{\sigma^2_{PP}\lambda_P} - \frac{\vec{\ell}\cdot\vec{v}_D\left(1-\vec{\ell}\cdot\vec{v}_D\right)}{\sigma^2_{pD}\lambda_D}}{\frac{1}{\sigma^2_P} + \frac{\left(1-\vec{\ell}\cdot\vec{v}_P\right)^2}{\sigma^2_{pP}\lambda_P} + \frac{\left(\vec{\ell}\cdot\vec{v}_D-1\right)^2}{\sigma^2_{pD}\lambda_D}}, \tag{3.25}$$

and

$$\frac{1}{\sigma^2_p} = \frac{1}{\sigma^2_{pP}} + \frac{1}{\sigma^2_{pD}}. \tag{3.26}$$

Eq. (3.17) can be further approximated by aligning $\vec{k}_a$ with $\vec{L}$ and the localisations of the production and detection are much smaller than L,

$$\mathscr{A}_{\alpha\beta}(T,\vec{L}) \propto \sum_a U^*_{\alpha a} U_{\beta a} \exp\left[-i\varepsilon_a T + ik_a L - \frac{(L-u_a T)^2}{4\eta^2}\right], \tag{3.27}$$

where velocity $u_a \simeq 1 - \frac{m_a^2}{2E^2}$ and $\eta^2 = \omega\sigma_x^2 = \omega(\sigma_{xP}^2 + \sigma_{xD}^2)$ is the total spatial coherence widths with

$$\begin{aligned}\omega = &\left\{1 + \sigma_p^2\left[\frac{(v_P^x-1)^2 + \left(v_P^y\right)^2 + (v_P^z)^2}{\sigma_{pP}^2\lambda_P} + \frac{(v_D^x-1)^2 + \left(v_D^y\right)^2 + (v_D^z)^2}{\sigma_{pD}^2\lambda_D}\right] + \right.\\ &\left.\sigma_p^4 \frac{\left[(v_P^x-1)\,v_D^y - (v_D^x-1)\,v_P^y\right]^2 + \left[(v_P^x-1)\,v_D^z - (v_D^x-1)\,v_P^z\right]^2 + \left(v_P^y v_D^z - v_P^z v_D^y\right)^2\right\}}{\sigma_{pP}^2\lambda_P\sigma_{pD}^2\lambda_D}\right\}\\ &\times\left\{1 + \sigma_p^2\left[\frac{\left(v_P^y\right)^2 + (v_P^z)^2}{\sigma_{pP}^2\lambda_P} + \frac{\left(v_D^y\right)^2 + (v_D^z)^2}{\sigma_{pD}^2\lambda_D}\right] + \sigma_p^4\frac{\left(v_P^y v_D^z - v_P^z v_D^y\right)^2}{\sigma_{pP}^2\lambda_P\sigma_{pD}^2\lambda_D}\right\}^{-1}.\end{aligned} \tag{3.28}$$

The transition probability can be computed from the amplitude as

$$\begin{aligned}P_{\alpha\beta}(T,\vec{L}) = &\sum_a |U_{\alpha a}|^2 \left|U_{\beta a}\right|^2 + 2\,\mathrm{Re}\sum_{a>b} U^*_{\alpha a} U_{\beta a} U_{\alpha b} U^*_{\beta b}\\ &\times\exp\left[-2\pi i\frac{L}{L^{\mathrm{osc}}_{ab}} - \left(\frac{L}{L^{\mathrm{coh}}_{ab}}\right)^2 - 2\pi^2\rho^2\omega\left(\frac{\sigma_x}{L^{\mathrm{osc}}_{ab}}\right)^2\right],\end{aligned} \tag{3.29}$$

where the oscillation length L^{osc} and the coherent length L^{coh} are defined as following,

$$\begin{aligned}L^{\mathrm{osc}}_{ab} &= \frac{4\pi E}{\left|\Delta m^2_{ab}\right|},\\ L^{\mathrm{coh}}_{ab} &= \frac{4\sqrt{2\omega}E^2}{\left|\Delta m^2_{ab}\right|}\sigma_x.\end{aligned} \tag{3.30}$$

It can be seen clearly in Eq. (3.29) that oscillations will be the dominant if the localisations σ_x of production and detection processes are much smaller than the oscillation length. The oscillation will not be observable if the propagation length is much greater than the coherence length of the neutrinos. Therefore, oscillationary effect will depend on the give source of neutrinos.

Mass Order	Parameters	Values
Normal Ordering	θ_{12}	$33.41^{+0.75\circ}_{-0.72}$
	θ_{23}	$42.2^{+1.1\circ}_{-0.9}$
	θ_{13}	$8.58^{+0.11\circ}_{-0.11}$
	δ	$232^{+36\circ}_{-26}$
	Δm^2_{12}	$7.41^{+0.21}_{-0.20} \times 10^{-5}$ eV^2
	Δm^2_{23}	$2.507^{+0.026}_{-0.027} \times 10^{-3}$ eV^2
Inverted Ordering	θ_{12}	$33.41^{+0.75\circ}_{-0.72}$
	θ_{23}	$49^{+1.0\circ}_{-1.2}$
	θ_{13}	$8.57^{+0.11\circ}_{-0.11}$
	δ	$276^{+22\circ}_{-29}$
	Δm^2_{12}	$7.41^{+0.21}_{-0.20} \times 10^{-5}$ eV^2
	Δm^2_{23}	$-2.486^{+0.025}_{-0.028} \times 10^{-3}$ eV^2

Table 3.1: Current fitted results for neutrino oscillation data [73].

Neutrino oscillation experiments showed that neutrinos are massive and therefore are one of the first fundamental disagreements with the SM predictions. Super-Kamiokande [54] was the first oscillation experiment which measured atmospheric neutrinos in a 33 ktons pure water tank with an exposure time of 535 days. Final state charged leptons are produced in the neutrino-nucleus interaction in water, resulting in Cherenkov radiation to be observed. The experiment measures the ν_μ to ν_τ conversion and therefore the θ_{23} mixing angle.

The Sudbury Neutrino Observatory [55] used pure heavy water to detect solar neutrinos. It has been firmly confirmed electron neutrino disappearance by results from both charged current and neutral current detections. The Double Chooz reactor neutrino experiment [25] first announced that there is a non-zero but small θ_{13} mixing angle, which was subsequently measured by the Daya Bay experiment [56].

Different experiments are needed to study different oscillation types since the oscillation probability is dependent on their baseline. The measurements from oscillation data also depends on the mass ordering of the neutrinos. The neutrino mass ordering could be normal $m_1 < m_2 < m_3$ or Inverted $(m_3 < m_1 < m_2)$. Which cannot be determined by oscillation experiments since they are only sensitive to the mass difference saquares. Tab. 3.1 shows the current global fitted data for neutrino oscillation parameters [73].

3.2 Neutrino Mass & Heavy Neutral Leptons

It is useful to introduce a Majorana field ψ_M based on the chiral Weyl fields defined previously,

$$\psi_M = \psi_L + e^{i\theta}\psi_L^C. \tag{3.31}$$

The phase θ is refered to a Majorana phase since the conjugate of the Majorana field is [74]

$$\psi_M^C = \psi_L^C + e^{-i\theta}\psi_L = e^{-i\theta}\psi_M. \tag{3.32}$$

The Majorana field coincides with its conjugate and the Majorana phase becomes an overall phase for the field. A four-component fermion field can be described by Dirac, Weyl and Majorana fields and neutrino fields can also be described by all three types of fields if they are of the Dirac type. The Majorana neutrinos are described by a left-handed field ν_L with the right-handed neutrinos being $N_R = C\bar{\nu}_L^T$. The four-component neutrino field can be constructed $\nu = \nu_L + N_R$ and it can be seen that the neutrino field ν is equivalent to its conjugate field.

There are two solutions. Firstly, neutrinos can acquire their masses through lepton number violating Majorana mass terms. In the purely (or mostly) Dirac scenarios, neutrinos acquire masses via Higgs mechanism. For $m_\nu \sim 0.1$ eV neutrino masses, we require Yukawa couplings to be $y^\nu \sim 10^{-12}$. The mixing angles between the left-handed and right-handed neutrinos are small in this sense and the left-handed neutrinos are therefore called active neutrinos and the right-handed neutrinos are called sterile neutrinos. Secondly, there are sterile right-handed neutrinos to give the Dirac masses to neutrinos via Yukawa couplings. Both mechanisms can be in play as well. For purely Majorana neutrinos, there is no need of right-handed neutrinos. A non-renormalisable dimension-5 Weinberg operator can be added to the SM Lagrangian.

The introduction of Majorana mass breaks the U(1) lepton number symmetry. A Majorana mass only breaks the gauge symmetry in the left-handed neutrino sector. An effective Weinberg operator may be introduced instead of the Majorana

mass term [75],

$$\mathscr{L}_{\text{Weinberg}} = \frac{1}{2}\sum_{i,j=1}^{3}\frac{c^{\nu}_{ij}}{\Lambda_{NP}}\left(L^{i}H\right)^{T}\left(L^{j}H\right) + \text{ h.c. }. \tag{3.33}$$

This operator is of dimension-5 which includes two lepton and two Higgs doublets, and it breaks lepton number by two units. c^{ν} is defined as a matrix of the Wilson coefficients and Λ_{NP} these have the energy scale for new physics which can give rise to lepton number violation.

We discussed the scenarios of Dirac and Majorana neutrinos. The most popular mechanism to explain light neutrino masses actually contains both, namely the See-saw mechanism. More precisely, there are the type I [31, 33, 34, 76], type II [77–79] and type III [80] seesaw mechanisms.

The type I seesaw model has the Higgs and lepton doublets to couple with a right-handed fermion singlet N_R. In the most general cases, it requires three generations of right-handed neutrinos to generate the masses for each generation of SM neutrino via Higgs mechanism. There is also a bare Majorana masses for N_R since they are completely decoupled from the SM particles apart from the left-handed neutrinos and the Higgs. The extended SM Lagrangian then becomes

$$\mathscr{L}_{\text{Seesaw}} = -\sum_{i,j=1}^{3} m^{D}_{ij}\bar{\nu_L}^{i}N_R^{c,j} - \frac{1}{2}\sum_{i,j=1}^{3} M_{ij}\left(N_R^{c,j}\right)^{T}N_R^{c,j} + \text{ h.c..} \tag{3.34}$$

m^D is the Dirac mass matrix and M is the Majorana mass matrix. The neutrino mass can be written in a matrix form as

$$\mathscr{L}_{\text{Seesaw}} = -\begin{pmatrix} \nu_L^{i} \\ N_R^{c,j} \end{pmatrix}^{T} \mathscr{M}_{\nu} \begin{pmatrix} \nu_L^{i} \\ N_R^{c,j} \end{pmatrix}. \tag{3.35}$$

For an arbitrary number $\mathscr{N}$ of right-handed neutrinos N_R, the Dirac mass matrix is $3\times\mathscr{N}$, the Majorana mass matrix is $\mathscr{N}\times\mathscr{N}$ and $\mathscr{M}_{\nu}$ is a $(3+\mathscr{N})\times(3+\mathscr{N})$ matrix. The mass spectrum of the neutrinos can be calculated by diagonalising the

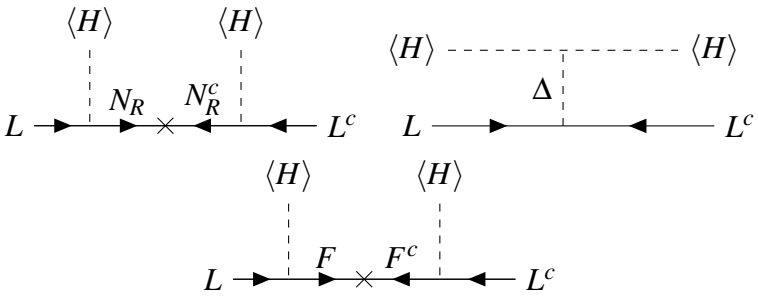

Figure 3.1: Feynman diagrams demonstrates the active neutrino mass generations for type I (top left), type II (top right) and type III (bottom) seesaw mechanisms. Here, L is the SM lepton doublet, N_R is a right-handed neutrino singlet, Δ is a $SU(2)_L$ scalar triplet and F is a $SU(2)_L$ fermion triplet.

mass matrix with a single unitary matrix,

$$\mathscr{M}_\nu = U_\nu D_m U_\nu^T. \tag{3.36}$$

Here D_m is a diagonal matrix which contains $3+\mathscr{N}$ mass eigenvalues. The unitary matrix U_ν can be represented in parts such as

$$U_\nu = \begin{pmatrix} V_{\nu\nu} & U_{\nu N} \\ U_{N\nu} & V_{NN} \end{pmatrix}. \tag{3.37}$$

The matrix $V_{\nu\nu}$ and V_{NN} give the mixing within the active neutrinos and right-handed neutrinos, respectively. Matrices $U_{\nu N}$ and $U_{N\nu}$ give the mixing between active neutrinos and right-handed neutrinos and vice-versa. The diagonalisation and resulting small Majorana mass for the active neutrinos can also be represented diagrammatically in Fig. 3.1 (top left).

Assuming, for simplicity, a single generation of ν_L and N_R, both m_D and M are just numbers. The two eigenvalues, they are

$$m_\pm = \frac{1}{2}\left(M \pm \sqrt{M^2+4m_D^2}\right). \tag{3.38}$$

Taking the seesaw limit $M \gg m_D$, the masses can approximated as

$$m_+ \simeq M + \frac{m_D^2}{M}, \quad m_- \simeq -\frac{m_D^2}{M}. \tag{3.39}$$

Recalling Eq. (3.33), the active neutrino mass can be expressed as

$$m_\nu = \frac{v^2}{2\Lambda_{\rm NP}} c^\nu, \tag{3.40}$$

which can be identified with the lighter mass. Likewise, the heavy mass scale $\Lambda_{\rm NP}$ can be matched to the right handed neutrino mass or HNL mass. It is clear that, for a 0.1 eV neutrino mass, we require a $M = 10^{14}$ GeV (setting $c^\nu = 1$).

A mixing matrix U can be found which diagonalises the seesaw mass matrix,

$$U = \begin{pmatrix} \cos\theta & \sin\theta \\ -\sin\theta & \cos\theta \end{pmatrix}. \tag{3.41}$$

By requiring the (1,2) and (2,1) elements in Eq. (3.35) to be zero, the mixing angle is obtained as

$$\tan(2\theta) = 2m_D/M. \tag{3.42}$$

This simplified one-generation version gives an approximated scale for canonical seesaw active-sterile mixing. The mixing angle is small under the limit taken and the heavy state is almost decoupled from the neutrino sector. The heavy state is therefore also called a sterile neutrino.

The lighter mass is negative as can be seen from the approximation in Eq. (3.38). To recover positive masses, a diagonal phase matrix can be multiplied $U \to U \cdot D_\phi$,

$$D_\phi = \begin{pmatrix} e^{i\phi_1} & 0 \\ 0 & e^{i\phi_2} \end{pmatrix}, \tag{3.43}$$

with $\phi_1 = \pi$ and $\phi_2 = 0$. This is equivalent to the Majorana phases to PMNS matrix.

As a result of active-sterile mixing, the SM charged current introduces interactions of the heavy neutral leptons (sterile neutrinos),

$$\begin{aligned} \sum_{i=e,\mu,\tau} \frac{g_W}{\sqrt{2}} W_\mu^+ \bar{\ell}_L^i \gamma^\mu \nu_L^i = &\sum_{m=1}^{3}\sum_{n=1}^{3} \frac{g_W}{\sqrt{2}} (U_{\rm PMNS})_{mn} W_\mu^+ \bar{\ell}_L^m \gamma^\mu \nu_L'^n \\ &+ \sum_{m=1}^{3}\sum_{n=3}^{3+\mathcal{N}} \frac{g_W}{\sqrt{2}} (U_{\nu N})_{mn} W_\mu^+ \bar{\ell}_L^m \gamma^\mu \nu_L'^n, \end{aligned} \tag{3.44}$$

where $\mathscr{N}$ is the the number of sterile neutrinos and U_{PMNS} is contained in U_ν as defined earlier.

The type II seesaw [77–79] can lower down the heavy mass scale of the theory naturally by introducing a heavy scalar triplet in $SU(2)_L$ as shown in Fig. 3.1(top right). The scalar modifies the Yukawa term in the following way,

$$\mathscr{L}_{\Delta-\text{ Yukawa}} = \sum_{\substack{\ell=e,\mu,\tau \\ \ell'=e,\mu,\tau}} \mathrm{y}^{\Delta}_{\ell\ell'} L^{\ell^T} C\left(i\tau^2\right) \Delta_L L^{\ell^{\ell'}} + \text{h.c.}. \tag{3.45}$$

Where Δ_L is the heavy scalar triplet under $SU(2)_L$,

$$\Delta_L = \Delta_L \cdot \tau = \begin{pmatrix} \frac{1}{\sqrt{2}}\Delta^+ & \Delta^{++} \\ \Delta^0 & -\frac{1}{\sqrt{2}}\Delta^+ \end{pmatrix}, \tag{3.46}$$

and $\mathrm{y}^{\Delta}_{\ell\ell'}$ is the Yukawa coupling strength between the scalar and the SM lepton doublets. The scalar can interact with the Higgs and acquire a VEV as

$$\langle \Delta_L \rangle \simeq \begin{pmatrix} 0 & 0 \\ \frac{\mu v^2}{2M_\Delta^2} & 0 \end{pmatrix}, \tag{3.47}$$

where M_Δ is the scalar mass, μ is the coupling strength with the Higgs doublets and v is the SM Higgs VEV. For $M_\Delta \gg v$, a small active neutrino mass of type II seesaw is achieved as

$$m_\nu^{\text{II}} = \frac{\mu v^2}{M_\Delta^2} \mathrm{y}^{\Delta}. \tag{3.48}$$

There is also another possible way to generate a seesaw model which is called the type III seesaw [80]. It introduces a fermion triplet under $SU(2)_L$, the triplet couples with the SM lepton and the Higgs doublets in a similar way as the right-handed fermion fields. The extension to the SM Lagrangian is

$$\mathscr{L}_F = \sum_{\substack{\ell=e,\mu,\tau \\ j=1,2,3}} \mathrm{y}^{FT}_{\ell j} L^{\ell^T} C\left(i\tau^2\right) \left(\mathbf{F}^j \cdot \tau\right) H + \sum_{\substack{i=1,2,3 \\ j=1,2,3}} \mathrm{M}^F_{ij} \left(\mathbf{F}^i\right)^T C \mathbf{F}^j + \text{h.c.}, \tag{3.49}$$

where **F** are the new fermion triplets and M^F is the mass matrix for these fields. For $M^F \gg y^F v$, she small active neutrino mass of type III seesaw is

$$\mathrm{M}_{\nu}^{\mathrm{III}} = \left(\mathrm{y}^F\right)^T v^2 \frac{1}{\mathrm{M}^F} \mathrm{y}^F . \tag{3.50}$$

With a focus of the type I seesaw model, the heavy mass scale can be lowered by adding two sterile neutrinos. The simplified mass model for the one-generation mass matrix can be written as,

$$\mathscr{M}_{\mathrm{Inverse}} = \begin{pmatrix} 0 & m_D & 0 \\ m_D & 0 & M \\ 0 & M & \mu \end{pmatrix}, \tag{3.51}$$

where m_D is the Dirac mass term and M is a heavy mass scale. This mass model has a lower lepton number violation mass scale μ. This form of mass matrix is the inverse seesaw mass matrix [81–83]. In the limit $\mu \to 0$, lepton number is conserved. This model can naturally give a small active neutrino mass due to small μ and the heavy mass scale M can be therefore significantly lower than the standard seesaw scenario. It can be seen that the active neutrino mass scale is approximately

$$m_\nu \simeq \frac{m_D^2 \mu}{M^2}, \tag{3.52}$$

and the HNL masses are

$$m_{N_{2/1}} \simeq M \pm \frac{1}{2}\left(\frac{m_D^2}{M} + \mu\right). \tag{3.53}$$

There is a mass splitting $\frac{1}{2}\left(\frac{m_D^2}{M} + \mu\right)$ between the lighter HNL mass m_{N_1} and the heavier mass m_{N_2}. The mass term μ naturally gives a small neutrino mass accroding to Eq. (3.51) and lepton number is conserved if $\mu \to 0$. The mass spectrum of this model is shown in Fig. 3.2 as a function of μ. It is clear from the Fig. 3.2 that the neutrino mass becomes infinitesimally small when μ tends to zero and the inverse-seesaw assumption breaks down when μ overcomes the heavy mass scale

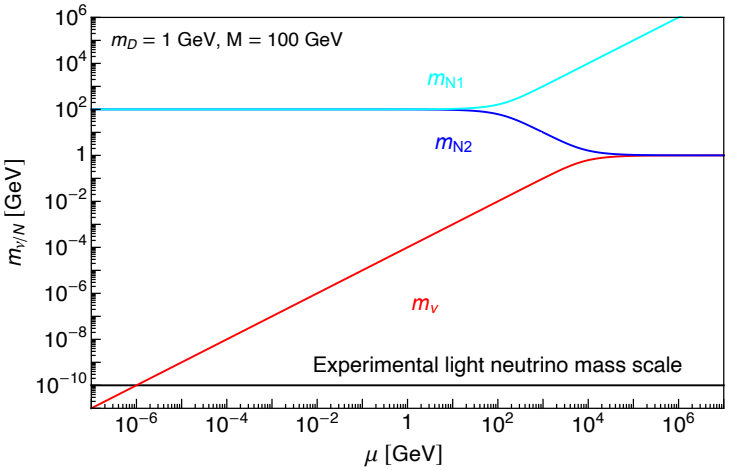

Figure 3.2: Neutrino mass eigenvalues as a function of the μ mass term in the inverse seesaw matrix calculated numerically for M = 100 GeV and m_D = 1 GeV.

$M = 100$ GeV. The light neutrino mass grows logarithmically and the heavy masses stay almost constantly with a negligible mass splitting for μ below 10 GeV.

Another scenario is the so-called linear seesaw [84–87]. In one generation, the mass matrix is

$$\mathscr{M}_{\text{Linear}} = \begin{pmatrix} 0 & m_D & m_2 \\ m_D & 0 & M \\ m_2 & M & 0 \end{pmatrix}. \tag{3.54}$$

This model has an extra lepton number violation mass term m_2. By applying a rotation between the sterile states,

$$\mathscr{U} = \begin{pmatrix} 1 & 0 & 0 \\ 0 & \cos\theta & \sin\theta \\ 0 & -\sin\theta & \cos\theta \end{pmatrix}, \tag{3.55}$$

the mass matrix transforms as

$$\mathscr{U}^T \mathscr{M}_{\text{Linear}} \mathscr{U} = \begin{pmatrix} 0 & m_D/\cos\theta & 0 \\ m_D/\cos\theta & M\sin 2\theta & M\cos 2\theta \\ 0 & M\cos 2\theta & -M\sin 2\theta \end{pmatrix} = \begin{pmatrix} 0 & m'_D & 0 \\ m'_D & m_R & M' \\ 0 & M' & m_L \end{pmatrix}. \tag{3.56}$$

It can be seen that the generalised inverse-seesaw mechanism with a small (2,2)

entry ($m_R \ll M$) is the most general model of its kind [88].

Our current best direct measurement of neutrino mass is done with single beta decay experiment, the observable m_β is defined as

$$m_\beta = \sum_i |U_{ei}|^2 m_{\nu_i}^2. \tag{3.57}$$

An upper bound of $m_\beta < 0.45$ eV with at 90 % CL is given by KATRIN [89]. KATRIN is an upper limit of the effective beta decay mass m_β. There is also an upper limit $\sum_i m_{\nu_i} < 0.1$ eV from cosmology. Oscillation experiments are evidence for the neutrino mass splitting Δm^2.

Another question is the mass ordering. The mass differences are measured to a good precision by oscillation experiments, but there are two possibilities, normal ordering (NO) and inverted ordering (IO). Combined analysis from oscillation, beta decay and cosmological observations will be needed to confirm neutrino mass ordering. Although precise analyses have been done in neutrino oscillation experiments, a direct measurement of neutrino masses is still needed to confirm the result. The current data for different neutrino mass ordering is shown in Tab. 3.1.

3.3 Neutrinos in Double Beta Decay

The process of inverse beta decay resulted in the discovery of neutrinos and it is still the leading way to measure absolute neutrino masses [90]. In some isotopes, it is discovered that the nucleus undergoes two beta decay to reach an energetically stable state as shown in Fig. 3.3 (left) [91]. This simultaneous process is called double beta decay or two-neutrino double beta decay ($2\nu\beta\beta$),

$$(A,Z) \to (A,Z+2) + 2e^- + 2\bar{\nu}_e. \tag{3.58}$$

Double beta decay is a rare process in nature. The life times of double beta decay isotopes usually ranges from $10^{18} - 10^{22}$ years [92–95].

In the Majorana neutrino scenario, the two emitted neutrinos can become an internal propagator as shown in Fig. 3.3 (right), this is called neutrinoless double

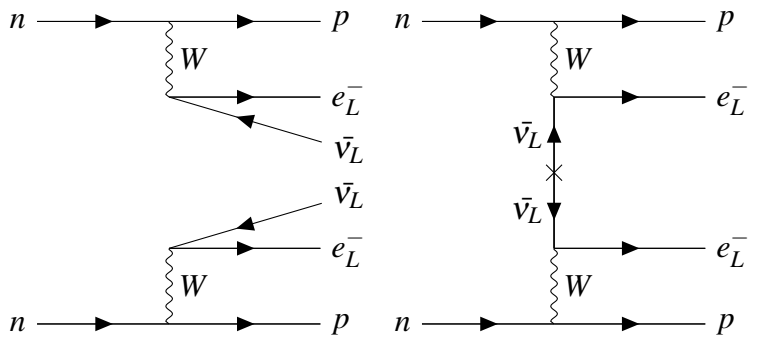

Figure 3.3: Feynman diagrams for double beta decay (left) and neutrinoless double beta decay (right).

beta decay ($0\nu\beta\beta$),

$$(A,Z) \rightarrow (A,Z+2) + 2e^- . \tag{3.59}$$

There is a clear experimental difference between $0\nu\beta\beta$ and $2\nu\beta\beta$ to distinguish between the two processes shown in Fig. 3.4. It is clear that neutrinoless double beta decay experiments are looking for the end point energy peak in the these decays and two-neutrino double beta decay acts as background.

The half life of a $2\nu\beta\beta$ isotope is already long, it makes the detection of $0\nu\beta\beta$ even harder. Large amount of high purity isotopes and long exposure time are therefore needed for the experiments. The number of observed $0\nu\beta\beta$ events N in a $0\nu\beta\beta$ experiment is parameterised by

$$N = \frac{\ln 2 \cdot N_A \cdot \mathscr{E}}{m_A \cdot T_{1/2}^{0\nu}}, \tag{3.60}$$

where $\mathscr{E}$ is the sensitivity exposure of the detector used in the experiment, N_A is Avogadro's number, m_A is the molar mass of the isotope used and $T_{1/2}^{0\nu}$ is the $0\nu\beta\beta$ decay half life. There are two parts which contribute to the decay rate [97],

$$T_{1/2}^{-1} = G_{0\nu} \left|\mathrm{M}_{lep}\right|^2 \left|\mathrm{M}_{nuc}\right|^2 . \tag{3.61}$$

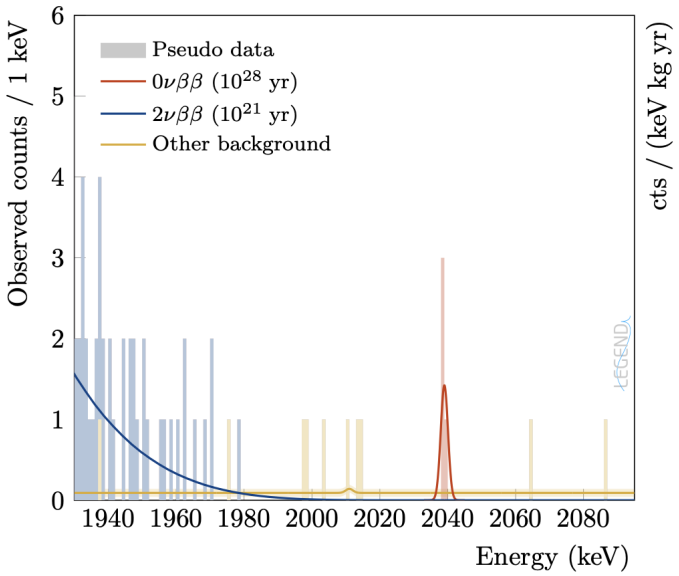

Figure 3.4: An illustrative Monte-Carlo pseudo-dataset of LEGEND-1000 for two-neutrino double beta decay (blue curve) and neutrinoless double beta decay (red curve) in a observed counts versus electron energy plot normalised to exposure. The full background model is implemented over 10 t yr of exposure, and a $0\nu\beta\beta$ decay half life of 10^{28} yr is assumed.The $2\nu\beta\beta$ decays do not leak in the $0\nu\beta\beta$ decay signal region, and their contribution is shown separately from the rest of the background sources. The yellow background model curve shows a small peak from ^{214}Bi decay as the nearest γ line within the displayed energy range. The uncertainty on the overall background model is covered by the yellow band [96].

The leptonic matrix element can be expressed as [98–100]

$$\begin{aligned} M_{\text{lep}}^{\mu\nu} &\propto g_W^2 \sum_{i=1}^{3} \overline{e_2} \left[(U_{ei}\gamma^\mu P_L) \frac{q^\rho \gamma_\rho + m_{\nu_i}}{q^2 - m_{\nu_i}^2} (U_{ei} P_L \gamma^\nu) \right] e_1^c \\ &\propto \frac{g_W^2}{q^2} \left[\sum_{i=1}^{3} U_{ei}^2 m_{\nu_i} \right] \overline{e_2} \left[\gamma^\mu \gamma^\nu P_R \right] e_1^c, \end{aligned} \tag{3.62}$$

where g_W is the weak coupling, e_1, e_2 are the spinors for the first and second electron emitted and U_{ei} is a PMNS mixing matrix element. The momentum $q \sim 100$ MeV is for the neutrino internal propagator which is much greater than the neutrino mass. The product of the PMNS matrix element and the neutrino mass left is defined as the effective $0\nu\beta\beta$ mass

$$m_{\beta\beta} = \sum_{i=1}^{3} U_{ei}^2 m_i.$$

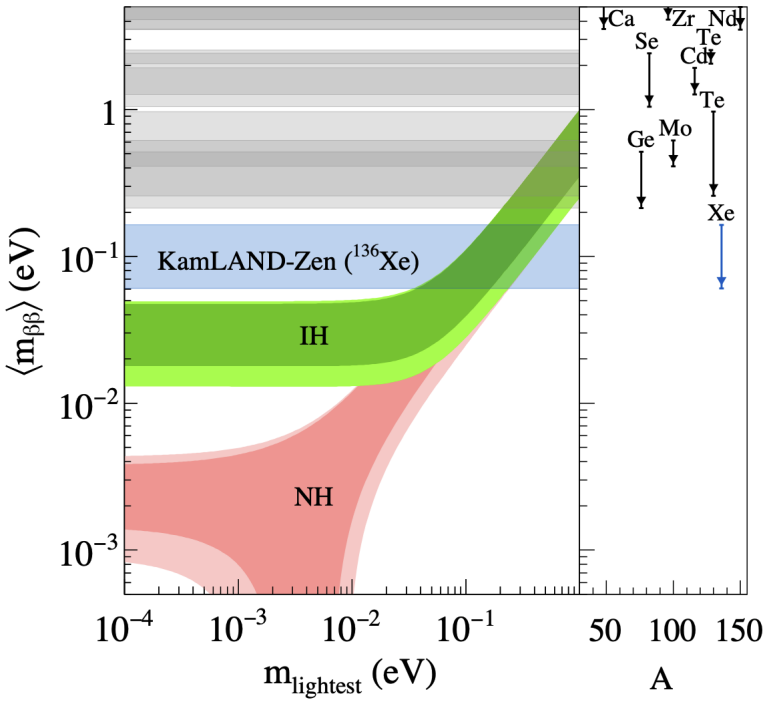

Figure 3.5: The effective $0\nu\beta\beta$ mass $m_{\beta\beta}$ versus the lightest neutrino mass m_{lightest} [101]. The dark shaded regions are the predictions based on best-fit values of neutrino oscillation parameters for the normal hierarchy (NH) and the inverted hierarchy (IH), and the light shaded regions indicate the 3σ from oscillation parameter uncertainties [102, 103]. The blue band shows the 90% C.L. upper sensitivity in ^{136}Xe of Kamland-Zen. The impact of different isotopes [104–106] on $m_{\beta\beta}$ is also given. Recent results of improved phase space factor [107, 108] and NMEs [109–115] are implemented. The right part shows the limit on $m_{\beta\beta}$ for different NMEs of isotopes versus the mass number of the isotopes.

The decay half life can also be expressed through the decay rate $\Gamma_{0\nu}/\ln 2 = T_{0\nu}^{-1}$,

$$\Gamma_{0\nu} = \ln 2 \frac{G_{0\nu} g_A^4}{m_e^2} \left| m_{\beta\beta} \mathcal{M}_{\text{nuc}} \right|^2, \tag{3.63}$$

where $G_{0\nu}$ is the kinematic phase space factor for $0\nu\beta\beta$ in the given isotope, g_A is the axial coupling strength, m_e is electron mass and $\mathcal{M}_{\text{nuc}}$ is the nuclear matrix element (NME) for $0\nu\beta\beta$ in the given isotope. The $0\nu\beta\beta$ decay can also be used as a tool to probe neutrino mass ordering due to its inclusion in $m_{\beta\beta}$. Fig. 3.5 shows the allowed parameter space as a function of the lightest neutrino mass and the mass ordering. The green region is for inverted mass ordering (IO) and the red region is for normal ordering (NO). The allowed parameter spaces are band shaped, be-

Experiment	Isotope	Status	$T^{0\nu}_{1/2}/[yr]$	$m_{\beta\beta}/[meV]$
LEGEND-200	construction	^{76}Ge	1.5×10^{27}	27-63
LEGEND-1000	proposed	^{76}Ge	1.3×10^{28}	9-21
NEXT-100	construction	^{136}Xe	7×10^{25}	66-281
NEXT-HD	proposed	^{136}Xe	2.2×10^{27}	12-50
PandaX-III-200	construction	^{136}Xe	1.5×10^{26}	45-194
LZ-nat	construction	^{136}Xe	7.2×10^{25}	64-277
LZ-enr	proposed	^{136}Xe	7.1×10^{26}	20-87
Darwin	proposed	^{136}Xe	1.1×10^{27}	17-72
KL2Z	proposed	^{136}Xe	1.1×10^{27}	17-71
SNO+I	construction	^{130}Te	1.8×10^{26}	31-144
SNO+II	proposed	^{130}Te	5.7×10^{26}	17-81

Table 3.2: Summary of future $0\nu\beta\beta$ decay searches. The table includes current status, expected sensitivity to the $0\nu\beta\beta$ half life and corresponding $m_{\beta\beta}$ [116].

cause all possible CP phase and Majorana phase values are considered. There is an overlapping region between the two orderings for the lightest neutrino mass greater than 10^{-2} eV and $m_{\beta\beta} > 10^{-2}$ eV. The effective mass has already been excluded to $m_{\beta\beta} \lesssim 10^{-1}$ eV by KamLAND-Zen and other recent experiments with inclusion of the NME calculation uncertainties. Future experiments will be able to probe the whole IH region down to the sensitivity of 10^{-2} eV with a greater precision in NME calculations. Tab. 3.2 shows some of the future $0\nu\beta\beta$ experiments with the future sensitivity to the half life for corresponding isotopes and the sensitivity to $m_{\beta\beta}$.

Fig. 3.3 gives a simplified Feynman diagram for $0\nu\beta\beta$ decay via light neutrino exchange. Theoretically, the internal neutrino propagator can involve unknown process which contains complicated loops and exotic interactions. It is needed to clarify whether the observation of $0\nu\beta\beta$ process is equivalent to being Majorana neutrinos. In the effective field theory (EFT) point of view, the whole $0\nu\beta\beta$ process can be described as a dimension-9 operator by counting all the external legs. The equivalence of Majorana nature of neutrino and $0\nu\beta\beta$ observation is proved by previous work [117–119], neutrinos are Majorana no matter what diagram induces $0\nu\beta\beta$. The seesaw typed heavy neutral lepton contributions in $0\nu\beta\beta$ will be discussed in chapter 4.

3.4 Neutrino Cosmology

The observation of the dark matter problem [58, 59, 67, 68] leads to the proposal of a wide range of dark matter particle candidates including HNLs and axion-like particles (ALPs). The properties of these potential candidates will affect the evolution of the Universe. All new physics theory (e.g. seesaw mechanisms) must also be consistent with cosmological and astrophysical observations, cosmology therefore becomes an important probe to BSM theories.

In the standard model of cosmology, the Universe after Big Bang is considered to be homogeneous and isotropic. This ideal system can be described by the Friedmann–Robertson–Walker (FRW) metric,

$$g_{\mu\nu}dx^{\mu}dx^{\nu} = -dt^2 + a^2(t)\left(\frac{dr^2}{1-kr^2} + r^2\left(d\theta^2 + \sin^2\theta d\phi^2\right)\right), \tag{3.64}$$

where r, θ, ϕ are the radial and angular components for the comoving polar spherical coordinate. The scale factor $a(t)$ encodes information from the Einstein Equation and describes the expansion of the Universe. The parameter k describes the spatial curvature of the Universe and it takes values from $+1$ to -1 corresponding to positively curved space $(+1)$, flat space (0) and negatively curved space (-1). The scaling factor $a(t)$ appears in the component of metric $g_{\mu\nu}$ and it can be calculated from the Einstein equation,

$$R_{\mu\nu} - \frac{1}{2}g_{\mu\nu}R = 8\pi G T_{\mu\nu} - \Lambda g_{\mu\nu}, \tag{3.65}$$

where $R_{\mu\nu}$ and R are the Ricci tensor and Ricci scalar which encode the curvature of the space-time. G is Newton's gravitational constant, usually expressed in term of the Planck mass $m_{\rm Pl} = G^{-1/2} = 1.22 \times 10^{19}$ GeV. $T_{\mu\nu}$ is the energy-stress tensor which encodes the energy content of the Universe in terms of the energy density ρ and pressure P, $T_{\mu\nu} = \mathrm{diag}(\rho, -P, -P, -P)$ for prefect fluid. Λ is the cosmological constant which gives an additional contribution to the energy-stress tensor. The energy-stress tensor is conserved in curved space-time, $\nabla_{\mu}T^{\mu}_{\nu} = 0$, given ∇_{μ} is the covariant derivative. By solving Eq. (3.65) and Eq. (3.64), one obtains the 0-0

component of the equation [120],

$$\frac{\dot{a}^2}{a^2} + \frac{k}{a^2} = \frac{8\pi G}{3}\rho + \frac{\Lambda}{3}. \tag{3.66}$$

It is convenient to define the Hubble parameter

$$H \equiv \frac{\dot{a}}{a}. \tag{3.67}$$

It is clear to see that there are three parts (Λ, k and matter) which contribute to the expansion of the Universe. Each part will dominate in different cosmological eras. In the early Universe after an accelerated expansion period - inflation, radiation or more generally, relativistic particles will dominate at the high temperature. The energy-stress relation can be calculated from $p = \rho/3$ and the conservation of energy-stress tensor,

$$\rho_{\rm R} = g_* \frac{\pi^2}{30} T^4 = 3P_{\rm R}, \tag{3.68}$$

where g_* is defined as the number of light particle degrees of freedom in the Universe. There are contributions from number of bosonic degrees g_i and number of fermionic degrees g_j respectively,

$$g_* = \sum_{i,\,\text{boson}} g_i \left(\frac{T_i}{T}\right)^4 + \frac{7}{8} \sum_{j,\,\text{fermion}} g_j \left(\frac{T_j}{T}\right)^4, \tag{3.69}$$

the factor $7/8$ in front of the fermion term is from the integral of Fermi-Dirac distribution over momentum space. The Hubble parameter can be then derived by approximating Eq. (3.66) as

$$H = \sqrt{\frac{4\pi^3}{45 m_{\rm Pl}^2} g_*} T^2. \tag{3.70}$$

During radiation domination, the number density of a light particle species i with degree of freedom g_i follows,

$$n_i = \frac{\zeta(3)}{\pi^2} g_i T^3, \tag{3.71}$$

where $\zeta(3) = 1.20206$ is the zeta function. The temperature-time relation for radiation domination can also be computed,

$$\left(\frac{t}{s}\right) \sim g_*^{-1/2} \left(\frac{1\ \text{MeV}}{T}\right)^2. \tag{3.72}$$

3.4.1 Neutrino Decoupling

The Universe can be modeled by statistical mechanics, particles were initially in a plasma environment and the plasma is cooled down as the Universe expands. When particles are in thermal equilibrium, for all decay and scattering processes, the rates of forward interactions are equal to the rates of backwards interactions, which makes particles are in dynamical equilibrium. The particles will be out of equilibrium when the temperature of the Universe is insufficient to support the backward interaction to happen as the Universe cools down. The neutrinos will decouple from the thermal plasma of the Universe if [38]

$$\Gamma_{\text{int}}(T) \lesssim H(T). \tag{3.73}$$

The neutrino interaction rate Γ_{int} can be approximated from the weak interaction cross-section,

$$\Gamma_{int} = \langle \sigma_W n_\nu v \rangle \sim G_F^2 T^5, \tag{3.74}$$

where the weak interaction cross-section is σ_W, n_ν is the neutrino number density and v is the relative velocity between interacting particles. The bracket denotes thermal averaging of the physical quantities inside. The cross-section is of the order $G_F^2 T^2$ from Fermi theory and the other 3 powers of temperature are from the number density in Eq. (3.71). Together with the expression of the Hubble parameter in Eq. (3.70), the neutrinos will decouple from the thermal plasma at the temperature,

$$T_D \simeq \left(\frac{\sqrt{g_*}}{G_F^2 m_{\text{Pl}}}\right)^{1/3}. \tag{3.75}$$

Taking the SM value $g_* = 10.75$ (including electron and positron, three neutrinos and the photon), the decoupling temperature will be around $T_D \sim 1$ MeV which is equivalent to 1 s after the Big Bang according to Eq. (3.72).

3.4.2 Big Bang Nucleosynthesis (BBN)

Light nuclei (^{2}H, ^{3}He, ^{4}He, ^{7}Li) were formed shortly after neutrino decoupling [39]. Nuclear and electromagnetic interactions dominated during the nuclear equilibrium period. Free neutrons and protons became the main baryonic species in the Universe when the excess of photons around a few MeV energy, it is because the photon energy will be sufficient to produce neutrons from the protons in the plasma. The density ratio between the proton and neutron product and the second lightest nucleus ^2H is given by Saha equation,

$$\frac{n_{^2\mathrm{H}}}{n_p n_n} = \frac{3}{4}\left(\frac{2\pi\left(m_n + m_p - B_{^2H}\right)}{m_n m_p T}\right)^{3/2} \exp\left(\frac{B_{^2\mathrm{H}}}{T}\right). \tag{3.76}$$

Here, m_n and m_p are the mass for neutron and proton, respectively. $B_{^2H}$ is the binding energy for deuterium which is around 2.2 MeV. In the MeV regime, the neutron and proton numbers have approximately the same value n_B, the ratio can be approximated to

$$\frac{n_{^2\mathrm{H}}}{n_\mathrm{B}} \sim \eta_\mathrm{B}\left(\frac{T}{m_{\mathscr{N}}}\right)^{3/2} \exp\left(\frac{B_{^2\mathrm{H}}}{T}\right), \tag{3.77}$$

given that the baryon density $n_B = \eta_B n_\gamma$ with the photon density n_γ and a baryon to photon number ratio η_B. $m_{\mathscr{N}}$ is the nuclear mass of the nucleus of interest. For heavier isotopes ($A > 7$), the density ratio becomes [121]

$$\frac{n_{\mathscr{N}(A,Z)}}{n_\mathrm{B}} \sim A^{3/2}\eta_\mathrm{B}^{A-1}\left(\frac{2\zeta(3)}{\pi^2}\right)^{A-1}\left(\frac{2\pi T}{m_{\mathscr{N}}}\right)^{3(A-1)/2} \exp\left(\frac{B(A,Z)}{T}\right), \tag{3.78}$$

where A and Z are the mass and atomic numbers of the isotope. ζ is the Apery's constant with the value $\zeta(3) \simeq 1.20$. Below the neutrino decoupling temperature, the photon energy is insufficient to break with deuterium to produce neutrons and protons. The synthesis of deuterium starts to dominate at about $T \simeq 0.07$ MeV. The production of ^{4}He marks the end of BBN since its binding energy is the highest

in the light isotope regime. A Helium-4 to baryon density ratio $Y_p \equiv \frac{4n_{^4\mathrm{He}}}{n_B}$ can be defined to measure the effect of BBN and the ratio can be approximated as [122]

$$Y_p \sim \frac{2}{1+\exp\left(\Delta m/T_{\mathrm{D}}\right)\exp\left(t\left(T_{\mathrm{BBN}}\right)/\tau_n\right)}, \tag{3.79}$$

where τ_n is the life time for neutrons and Δm is the proton-neutron mass difference. T_D denotes the neutrino decoupling temperature and T_{BBN} is the temperature at BBN. The value is $Y_p \simeq 0.25$ in the standard model scenario.

HNLs can affect the BBN via its mixing with active neutrinos through the following processes,

$$\begin{aligned} &N \to e^- \ell_2^+ \nu_{\ell_2}, \qquad && N \to \nu_e \nu_{\ell_2} \bar{\nu}_{\ell_2}, \\ &N \to P \nu_e, && N \to P^+ e^-, \\ &N \to V \nu_e, && N \to V^+ e^-. \end{aligned} \tag{3.80}$$

HNLs will decay to neutrinos and other SM particles. The decay products have very different energies from the thermal plasma particles, they will modify the spectra and production of ^{4}He (i.e. mesons produced lead to over-production of ^{4}He) at BBN and slow down the cooling of the Universe. The excessive neutrinos produced will also change the light degrees of freedom at BBN. The BBN observations therefore put a tight constraint on HNL mass and mixing with active neutrinos [123,124].

3.4.3 Cosmic Microwave Background (CMB)

The Cosmic Microwave Background (CMB) is the residual thermal radiation from the Big Bang, permeating the universe and observable in all directions. Approximately 380,000 years after the Big Bang, the universe cooled sufficiently for protons and electrons to combine into neutral hydrogen atoms, allowing photons to travel freely. This recombination process resulted in the release of the CMB, which has since cooled to a temperature of about 2.725 K due to the universe's expansion.

The cosmic mircowave background was first discovered in 1965 [125] and it was the first evidence for the Big Bang theory of cosmology. The photon temperature of the CMB was observed to be $T_{\mathrm{CMB}} = 2.73$ K [126]. At recombination,

electrons and protons bind together and the Universe started to be transparent to electromagnetic radiation. The rate of Compton scattering became negligible compared to the Hubble parameter after recombination. The CMB photons were from the last compton scattering between electrons and photons such that $\Gamma_{\rm Comp} = H(T)$. Similar to synthesis of deuterium in Eq. (3.76), a ratio between the product of proton and electron number densities to hydrogen density can be computed as [121]

$$\frac{n_p n_e}{n_{\rm H}} = \left(\frac{m_e T}{2\pi}\right)^{3/2} \exp\left(-\frac{m_e + m_p - m_{\rm H}}{T}\right). \tag{3.81}$$

Here, $n_e, n_{\rm H}$ are the electron and hydrogen number densities, and $m_e, m_{\rm H}$ are the electron and hydrogen masses. The binding energy for hydrogen atom has the value of $B_{\rm H} = 13.6$ eV. An ionised fraction can be defined correspondingly as

$$X_e \equiv \frac{n_e}{n_e + n_{\rm H}}. \tag{3.82}$$

A similar Saha equation can also be written for recombination in term of Y_p defined in Eq. (3.79),

$$\frac{X_e^2}{1 - X_e} = \frac{1}{\eta_{\rm B}\,(1 - Y_p)} \left(\frac{m_e}{T}\right)^{3/2} \frac{\sqrt{\pi}}{2^{5/2}\zeta(3)} \exp\left(-\frac{B_{\rm H}}{T}\right). \tag{3.83}$$

For $Y_p = 0.25$ and $\eta_B = 6 \times 10^{-10}$, X_e will have a dramatic decline at $T = 0.3$ eV. At later times, neutrinos become the free streaming and neutrinos show the Fermi-Dirac distribution better because the temperature is lower. The neutrino to photon temperature ratio can be inferred from electron positron and photon entropies after neutrino decoupling. When the temperature drops below the electron-positron pair creation rate $T_{\rm ann} \sim m_e$, pair production is insufficient and most electrons and positrons disappear. The photons are still in the thermal plasma due to the electromagnetic interactions and neutrinos remain almost unaffected by the pair annihilation. Photon is always relativistic because it is massless, the photon energy density

is the proportional to T^4 from Planck distribution and the entropy density is

$$S_\gamma = \frac{2\pi^2}{45} T^3 g_s(T), \tag{3.84}$$

where $g_s(T)$ is the entropy relativistic degrees of freedom which is the same way as Eq. (3.69). $g_s(T \gg m_e)$ takes the value of 11/2 and becomes 2 after $T \ll m_e$. After pair annihilation, the effective number of neutrino species $N_{\rm eff}$ is contained in the radiation density,

$$\rho_{\rm R} = \rho_\gamma \left(1 + 3\frac{7}{8} \left(\frac{4}{11} \right)^{4/3} N_{\rm eff} \right), \tag{3.85}$$

where ρ_γ is the photon energy density and it is proportional to T^4 according to Eq. (3.68). The factor $7/8$ is given by the phase-space integral of the fermi-Dirac distribution. There will be a factor of 1 for bosons. $4/11$ gives the neutrino to photon temperature ratio because neutrino temperature evolves differently from photon temperature after neutrino decoupling. $N_{\rm eff}$ is the effective number of light particle degrees of freedom which includes neutrinos and other non-relativistic species. $N_{\rm eff,SM} = 2.99^{+0.34}_{-0.33}$ is measured by cosmological and astrophysical observations [30]. The number 3 corresponds to there are three types of neutrinos in the SM. There will be additional contributions if there are more light exotic particles in the Universe.

3.4.4 Leptogenesis

The observation of a negligible amount of anti-matter in the Universe [30],

$$\eta_B = \frac{n_B - n_{\bar{B}}}{n_\gamma} \approx 6 \times 10^{-10}, \tag{3.86}$$

which requires a novel mechanism beyond SM. The origin of this asymmetry should satisfy the Sakharov conditions [57] : (a) Baryon number is violated. (b) C and CP are violated in order to differentiate matter and anti-matter. (c) the generation mechanism is not in thermal equilibrium.

One possibility to explain the matter-antimatter asymmetry is through leptogenesis [127, 128]. It is a process which generates firstly a lepton asymmetry, and the

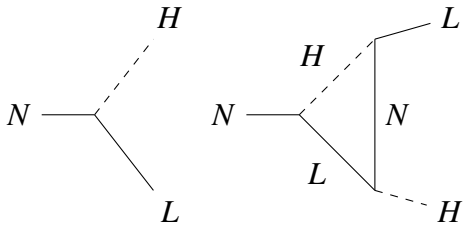

Figure 3.6: Feynman diagrams for HNL decays to a lepton and a Higgs at tree level (left) and one-loop level (right).

baryon asymmetry is then generated from the lepton sector. The decay of HNLs N is one possible way to generate a lepton asymmetry in the early Universe [129]. In the early Universe, HNL can decay to a lepton L and a Higgs H via two channels as shown in Fig. 3.6,

$$\begin{aligned} N &\to L + H, \\ N &\to \bar{L} + \bar{H}. \end{aligned} \tag{3.87}$$

CP violation will make one decay channel more efficient than the other. Then, it generates an asymmetry in the lepton number. The decay asymmetry ε generated by the HNLs is given by

$$\varepsilon_i = \frac{\sum_j \left(\Gamma\left(N_i \to L^j H\right) - \Gamma\left(N_i \to \bar{L}^j \bar{H}\right)\right)}{\sum_j \left(\Gamma\left(N_i \to L^j H\right) + \Gamma\left(N_i \to \bar{L}^j \bar{H}\right)\right)}, \tag{3.88}$$

This parameter is for the i-th HNL in the model with more than 1 HNL. It sums all the lepton flavours j and will deviate from zero if *CP* is violated.

The expansion of the Universe causes the departure from thermal equilibrium. Interaction rates that are slower than the Hubble expansion rate cannot maintain the equilibrium of the particle distribution in the Universe. Considering one-HNL scenario, The non-equilibrium process is described by Boltzmann equations for the expanding Universe,

$$\begin{aligned} Hz\frac{\mathrm{d}n_N}{\mathrm{d}z} &= -\left(\Gamma_D + \Gamma_S\right)\left(n_N - n_N^{\mathrm{eq}}\right), \\ Hz\frac{\mathrm{d}n_L}{\mathrm{d}z} &= \varepsilon\Gamma_D\left(n_N - n_N^{\mathrm{eq}}\right) - \Gamma_W n_L, \end{aligned} \tag{3.89}$$

where H is the Hubble parameter and $z = m_N/T$ is the mass of the HNL over the

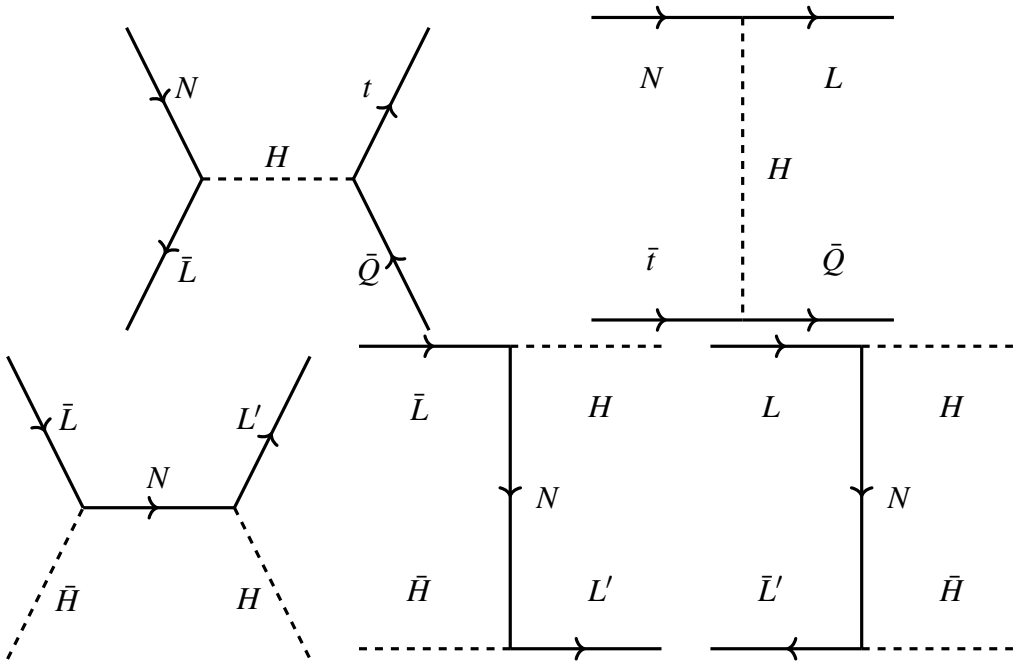

Figure 3.7: The $\Delta L = 1$ (top panel) and $\Delta L = 2$ (bottom panel) scattering processes which contribute to washout of lepton number asymmetry.

temperature of the Universe. n_N and $n_N^{\rm eq}$ are the number density and the equilibrium number density for the HNL, respectively. n_L stands for the number density of leptons. Γ_D is the rate for both decay and inverse decay of the HNL as Fig. 3.6. Γ_S is the total rate that sums all 2-2 scattering processes of HNL mediated by the Higgs, which violates the lepton number by 1 unit ($\Delta L = 1$),

$$\begin{aligned} N\ell^i &\leftrightarrow t\bar{Q}, \quad N\bar{\ell}^i \leftrightarrow t\bar{Q}, \\ Nt &\leftrightarrow \bar{\ell}^i Q, \quad N\bar{t} \leftrightarrow \ell^i \bar{Q}, \end{aligned} \tag{3.90}$$

where t stands for the top quark and Q is the SM quark doublets. The $\Delta L = 2$ scattering proceses contribute to the washout rate Γ_W,

$$L^\ell H \leftrightarrow \bar{L}^\ell \bar{H}, \quad L^\ell L^\ell \leftrightarrow \bar{H}\bar{H}, \quad \bar{L}^\ell \bar{L}^\ell \leftrightarrow HH, \tag{3.91}$$

these processes are mediated by the HNL N and are demonstrated in Fig. 3.7. The lepton asymmetry is then translated to baryon asymmetry via sphaleron processes [130]. These non-perturbative processes, which violate baryon number, are

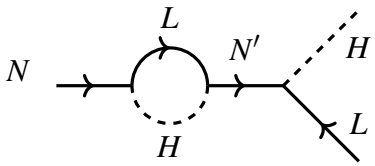

Figure 3.8: Diagram for HNL decay via one-loop HNL self-energy.

described within thermal field theory. They correspond to tunneling between two topologically distinct energy minima (vacua) of the field configurations, which cannot be connected through continuous gauge transformations. The sphaleron processes work for a range of energy from 100 to 10^{12} GeV.

Apart from the standard leptogenesis processes, leptogenesis can also occur resonantly [131, 132] as Fig. 3.8 shows. Leptonic asymmetries are resonantly amplified through the mixing of nearly degenerate HNLs, with mass differences on the order of their decay widths. Resonant leptogenesis can reduce the mass scale for HNLs from $\sim 10^{12}$ TeV for the standard leptogenesis to ~ 1 TeV. This makes low-scale seesaw models possible for explaining matter-antimatter asymmetry.

Chapter 4

Probing Heavy Neutral Leptons in $0\nu\beta\beta$ & Direct Searches

4.1 Current Status of HNL Searches

As mentioned in the last chapter, the standard seesaw mechanism results in a very high mass scale of HNLs such that $m_\nu \sim (100\,\text{GeV})^2/\Lambda < 0.1$ eV [30, 133], it requires $\Lambda \sim 10^{15}$ GeV which is close to the Grand Unified Scale. The realisation of low-scale leptogenesis scenarios as Sec. 3.4.4 mentioned and recent developments for long-lived exotic particle searches, enables a strong interest to look for HNLs at much lower scales. The active-sterile neutrino mixing $|U_{\alpha N}|$ is expected to be small in order to satisfy the small active neutrino masses such that

$$|U_{\alpha N}| \sim \sqrt{\frac{m_\nu}{m_N}} \approx 10^{-6}\sqrt{\frac{100\,\text{GeV}}{m_N}}, \tag{4.1}$$

for one-generation of HNL with mass m_N. This describes a seesaw floor that needs to be probed experimentally to test low-scale type-I seesaw scenarios, through weaker strengths are allowed by assuming other sources of light neutrino mass and stronger strengths are possible by employing specific textures [134–146] or symmetries [137,138,144,147–149] in a three-generation framework. An additional sterile neutrino decouples the scale of lepton number violation from the sterile neutrino mass scale. The large active-sterile mixing strengths are allowed for low-scale sterile neutrino masses, as proposed in the inverse [81,83,150], linear [85,87,151,152]

and generalised inverse seesaw [88, 153, 154]. The main feature of such scenarios is that the Majorana sterile neutrinos form quasi-Dirac pairs with opposite CP phases and a small mass splitting which suppresses their joint contribution to the light neutrino masses and other lepton number violating observables such as neutrinoless double beta decay.

Following the analysis [155], a general phenomenological parametrisation is used which is agnostic to the nature of the sterile neutrinos with the assumption that active neutrinos only receive their masses at tree level. The parametrisation is extended to include three generations of active neutrinos and two sterile states, all initially described as Weyl fermions. The 3+2 scenario is the minimal model in which two of the three active neutrinos acquire mass, while the lightest active neutrino remains massless. The parametrisation is compared with the Casas-Ibarra approach and other formulations focusing on quasi-Dirac sterile neutrinos as described in [156, 157]. Motivated by the fact that both future $0\nu\beta\beta$ decay and direct searches are starting to probe the seesaw floor, we make a complementary analysis between the two types of experiments, with a focus on near GeV mass range. Fig. 4.1 shows the projected sensitivity of select future searches. Considering the constraints from BBN and existing searches, HNL masses must be larger than 300 MeV, and DUNE, SHiP and LEGEND-1000 can probe HNLs near the seesaw floor. The latter is highly sensitive to the nature of HNLs, i.e., whether they are Majorana or quasi-Dirac, with a potential interference with the light neutrino mass contribution. On the other hand, direct searches are largely independent of this, mainly probing the strength of the induced SM-like charged and neutral currents. We thus use the potential of DUNE and LEGEND-1000 to probe the properties of sterile neutrinos, namely the mass splitting of a quasi-Dirac HNL, and its CP phase relative to that of the active neutrinos. These properties are crucial in understanding the role of HNLs in generating the matter-antimatter asymmetry of the universe through leptogenesis [127, 158–161].

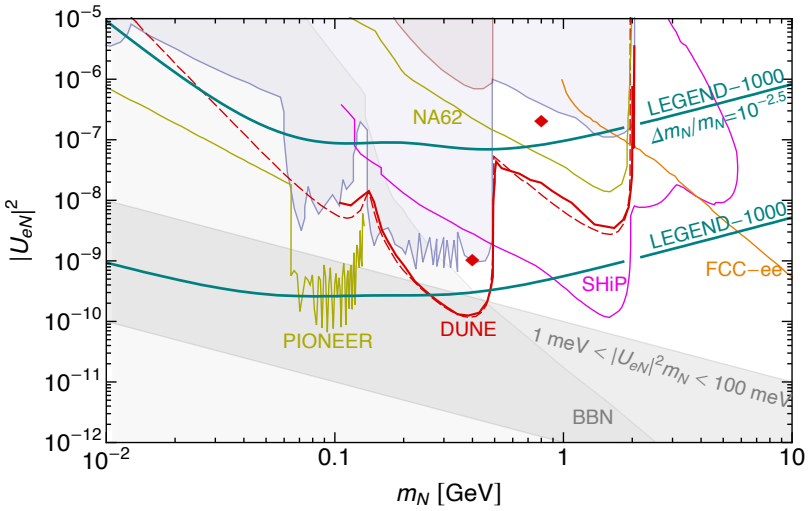

Figure 4.1: Projected sensitivities of future HNL searches on the electron active-sterile mixing strength $|U_{eN}|^2$ as a function of the HNL mass m_N [162]. Shown are projections for the direct searches at PIONEER [163], NA62 [164], DUNE (red dashed from [165], red solid from this work), SHiP [166], FCC-ee [167] and the $0\nu\beta\beta$ decay experiment LEGEND-1000 [96]. The latter is shown for the contribution of a single Majorana HNL and a pair of quasi-Dirac HNL with a mass splitting of $\Delta m_N/m_N = 10^{-2.5}$ generating a light neutrino mass of $m_\nu = 10^{-2.5}$ eV. The shaded region is excluded from existing searches [155, 162] and the impact of the HNL on Big Bang Nucleosynthesis (BBN) [123]. The diagonal band indicates the seesaw floor with the notional neutrino mass $|U_{eN}|^2 m_N$ in the given range. The diamonds indicate benchmark scenarios used in the analysis.

4.2 Phenomenological Model

In this section we will discuss the effect of two additional fermion singlets on the SM. Based on the work of [162], a useful phenomenological parametrisation which can describe the Majorana nature in quasi-Dirac limits of the HNL pair and their mixing with the light active neutrinos. In another word, The neutrino sector looks almost Dirac, but there is still a small LNV effect. The relations between the active-sterile mixing and CP phases that are necessary for the observed light neutrino oscillation parameters are derived. For most of our analysis, the number of active generations N_A is set to one. It will be extended to the minimal 3+2 scenario in the results section for comparison.

4.2.1 HNL Lagrangian

A general SM Lagrangian which includes N_S SM-singlet Weyl fermion fields N_{iR} is written as

$$\mathscr{L} = \mathscr{L}_{\rm SM} + i\bar{N}_{iR}\partial\!\!\!/ N_{iR} - (Y_\nu)_{\alpha i}\bar{L}_\alpha \tilde{H} N_{iR} - \frac{1}{\sigma}(\mathscr{M}_S)_{ij}\bar{N}^c_{iR}N_{jR} + \text{ h.c. }, \tag{4.2}$$

where $L_\alpha = (\nu_{\alpha L}, \ell_{\alpha L})^T$ is the SM doublet with $\alpha = e, \mu, \tau$ and $H = \left(H^0, H^-\right)^T$ is the SM Higgs field, Y_ν is the Yukawa coupling matrix for the neutrino sector. $\mathscr{M}_S$ stands for the Majorana mass term in the HNL states. The additional terms in the Lagrangian are the renormalisable terms for arbitrary numbers of HNL states. Here, $\mathscr{M}_\nu$ is an $\mathscr{N} \times \mathscr{N}$ complex symmetric matrix,

$$\mathscr{M}_\nu = \begin{pmatrix} 0 & \mathscr{M}_D \\ \mathscr{M}_D^T & \mathscr{M}_S \end{pmatrix}, \tag{4.3}$$

where $\mathscr{M}_D = \frac{v}{\sqrt{2}}Y_\nu$ and $v = \langle H^0 \rangle \approx 246$ GeV is the Higgs vacuum expectation value. Without loss of generality, it is possible to perform an unitary rotation among the sterile states so that $V^T \mathscr{M}_S V$ is diagonal, where V is an $\mathscr{N}_S \times \mathscr{N}_S$ unitary matrix. Alternatively, by exploiting the singular value decomposition of $\mathscr{M}_D$, the rotation among sterile states can be chosen such that $\mathscr{M}_D V = W^* \Sigma_D$, where W is an $\mathscr{N}_A \times \mathscr{N}_A$ unitary matrix and Σ_D is an $\mathscr{N}_A \times \mathscr{N}_S$ matrix with non-negative real numbers along the diagonal [88].

More generally, it is possible to rotate the active and sterile states to the mass basis by performing a unitary rotation on n_L, i.e.,

$$n_L = P_L U (\underbrace{\nu_1, \ldots}_{\mathscr{N}_A}, \underbrace{N_1, \ldots}_{\mathscr{N}_S})^T, \tag{4.4}$$

where $\nu_i = \nu_i^c$ and $N_\kappa = N_\kappa^c$ are Majorana fields and U is the $\mathscr{N} \times \mathscr{N}$ unitary matrix that diagonalises the mass matrix $\mathscr{M}_\nu$. We are interested in the limit where the ν_i are *mostly-active* states and N_κ are *mostly-sterile* states (or HNLs). The former states have masses set by the neutrino oscillation data and mix primarily with active neu-

trino fields $\nu_{\alpha L}$, while the latter states have arbitrary masses and mix predominantly with the sterile fields N^c_{kR}.

In the $\mathcal{N}_S = 2$ case, we can express the mass matrix as

$$\mathscr{M}_\nu = \begin{pmatrix} 0 & \mathscr{M}_{D,1} & \mathscr{M}_{D,2} \\ \mathscr{M}^T_{D,1} & \mu_R & m_S \\ \mathscr{M}^T_{D,2} & m_S & \mu_S \end{pmatrix} = U \begin{pmatrix} m_\nu & 0 & 0 \\ 0 & m_N & 0 \\ 0 & 0 & m_N(1+r_\Delta) \end{pmatrix} U^T, \tag{4.5}$$

where $(\mathscr{M}_{D,1})_\alpha = (\mathscr{M}_D)_{\alpha 1}$ and $(\mathscr{M}_{D,2})_\alpha = (\mathscr{M}_D)_{\alpha 2}$. Here, m_ν is an $\mathcal{N}_A \times \mathcal{N}_A$ diagonal matrix containing the observed light neutrino masses, m_N is the mass of the lighter HNL, and $r_\Delta = \Delta m_N / m_N$ (where Δm_N is the mass splitting between the HNL pair). We make the usual observation that for $\mathcal{N}_A + \mathcal{N}_S = 3 + 2$, the rank of the matrix $\mathscr{M}_\nu$ is 4, and therefore one of the light neutrinos is massless. This scenario is still compatible with the neutrino oscillation data for the normal and inverted neutrino mass orderings.

A non-zero mixing between the active neutrinos and possible sterile states is felt by the SM charged- and neutral-current interactions. For example, taking the charged lepton Yukawa matrix Y_ℓ to be diagonal, the charged-current can be written as

$$\begin{aligned} \mathscr{L}_{W^\pm} &= -\frac{g}{\sqrt{2}} \bar{\ell}_{\alpha L} \not{W}^\dagger \nu_{\alpha L} + \text{h.c.} \\ &= -\frac{g}{\sqrt{2}} U_{\alpha i} \bar{\ell}_{\alpha L} \not{W}^\dagger P_L \nu_i - \frac{g}{\sqrt{2}} U_{\alpha N_\kappa} \bar{\ell}_{\alpha L} \not{W}^\dagger P_L N_\kappa + \text{h.c.}, \end{aligned} \tag{4.6}$$

where we see that the mixing $U_{\alpha N_\kappa}$ couples charged leptons to HNLs. This interaction allows HNLs to mediate $0\nu\beta\beta$ decay and be produced via meson decays.

It is conventional to express an $\mathcal{N} \times \mathcal{N}$ unitary matrix in terms of $\mathcal{N}(\mathcal{N}-1)/2$ mixing angles and $\mathcal{N}(\mathcal{N}+1)/2$ phases. For the mixing matrix U, $\mathcal{N}_A$ phases can be eliminated through a rephasing of the charged lepton fields in Eq. (4.6). Note that only the upper $\mathcal{N}_A \times \mathcal{N}$ sub-block of U appears in Eq. (4.6), and so all mixing angles and phases that do not appear in this sub-block are unphysical. This freedom is equivalent to the arbitrary rotation among the sterile states discussed

below Eq. (4.5). The mixing matrix U can be expressed as a combination of real and complex Euler rotations; for example, in the $3+2$ scenario, a useful parametrisation of U is [168, 169]

$$U = W_{N_1N_2} W_{3N_2} W_{2N_2} W_{1N_2} W_{3N_1} W_{2N_1} W_{1N_1} R_{23} W_{13} R_{12} D\,. \tag{4.7}$$

Here, W_{ij} (R_{ij}) is a unitary, unimodular matrix describing a complex (real) rotation in the i-j plane, which can be written as

$$[W_{ij}]_{rs} = \delta_{rs} + (\cos\vartheta_{ij} - 1)(\delta_{ir}\delta_{is} + \delta_{jr}\delta_{js}) + \sin\vartheta_{ij}(e^{-i\eta_{ij}}\delta_{ir}\delta_{js} - e^{i\eta_{ij}}\delta_{ir}\delta_{js})\,, \tag{4.8}$$

with $\vartheta_{ij} \in [0, \pi/2]$ and $\eta_{ij} \in [0, 2\pi]$, while R_{ij} is given by Eq. (4.8) with $\eta_{ij} = 0$. The angles ϑ_{12}, ϑ_{13} and ϑ_{23} and phase η_{13} contained in R_{12}, W_{13} and R_{23} are taken to be the mixing angles and Dirac CP phase in the PMNS mixing matrix. The matrices W_{iN_κ} in Eq. (4.7) contain six angles ϑ_{iN_κ}, which control the active-sterile mixing strengths, and six Dirac CP phases η_{iN_κ}; for convenience, we introduce the notation $\vartheta_{i\kappa} \equiv \vartheta_{iN_\kappa}$, $c_{i\kappa} \equiv \cos\vartheta_{iN_\kappa}$, $s_{i\kappa} \equiv \sin\vartheta_{iN_\kappa}$ and $\eta_{i\kappa} \equiv \eta_{iN_\kappa}$. Finally, four (Majorana) CP phases which are defined to lie in the range $[0, 4\pi]$ are contained in the diagonal matrix

$$D = \mathrm{diag}(1, e^{i\alpha_{21}/2}, e^{i\alpha_{31}/2}, e^{i\phi_1/2}, e^{i\phi_2/2})\,, \tag{4.9}$$

where α_{21} and α_{31} correspond to the usual Majorana phases in the PMNS mixing matrix. In the $3+2$ model where $m_{\mathrm{lightest}} = 0$, only a single Majorana phase appearing in the PMNS mixing matrix is physically relevant; this is the combination $(\alpha_{21} - \alpha_{31})$ in the normal ordering (NO) scenario, where $m_1 = 0$, and α_{21} in the inverted ordering (IO) scenario, where $m_3 = 0$. Both scenarios are covered by setting $\alpha_{31} = 0$.

In the neutrino mass matrix $\mathscr{M}_\nu$ in Eq. (4.5), the upper-left $\mathscr{N}_A \times \mathscr{N}_A$ sub-block is zero because a mass term of the form $\bar{\nu}_{\alpha L}\nu^c_{\beta L}$ violates $\mathrm{SU}(2)_L$. Equating the two sides of Eq. (4.5) gives the following relation between the light neutrino masses m_i

and HNL masses m_{N_κ},

$$(\mathscr{M}_\nu)_{\alpha\beta} = 0 \quad \Rightarrow \quad 0 = \sum_{i=1}^{\mathscr{N}_A} m_i U_{\alpha i} U_{\beta i} + \sum_{k=1}^{\mathscr{N}_S} m_{N_\kappa} U_{\alpha N_\kappa} U_{\beta N_\kappa} \,. \tag{4.10}$$

However, this relation is only valid at tree level. The light neutrino masses also acquire a contribution at one-loop from self-energy diagrams involving Higgs and Z bosons [134, 170, 171]. For HNL masses $m_{N_\kappa} \lesssim 1$ GeV and active-sterile mixing $|U_{eN_\kappa}|^2 \lesssim 10^{-6}$ probed by $0\nu\beta\beta$ decay and DUNE, such one-loop corrections can be safely neglected [155].

In the limit $s_{i\kappa} \approx \vartheta_{i\kappa} \ll 1$ and $c_{i\kappa} \approx 1$, the upper-left $\mathscr{N}_A \times \mathscr{N}_A$ sub-block of U is approximately the PMNS mixing matrix, i.e. $U_{\alpha i} \approx (U_{\rm PMNS})_{\alpha i}$. Deviations from the unitarity of U_ν are controlled by the size of the angles $\vartheta_{i\kappa}$, but it is safe to ignore this effect in the regime probed by $0\nu\beta\beta$ decay and DUNE. The active-sterile mixing in Eqs. (4.6) and (4.10) is now given by

$$U_{\alpha N_\kappa} \approx \Theta_{\alpha\kappa} = |\Theta_{\alpha\kappa}| e^{i\phi_{i\kappa}/2} \equiv s_{i\kappa} e^{i\phi_{i\kappa}/2} \,, \tag{4.11}$$

where $\phi_{i\kappa} \equiv \phi_\kappa - 2\eta_{i\kappa}$. In the limit $\vartheta_{i\kappa} \ll 1$, there is a correspondence between the mass index i and the flavour index α, i.e. $e, \mu, \tau \Leftrightarrow 1, 2, 3$, and so in the remainder of this work we use $s_{\alpha k}$ and $\phi_{\alpha k}$. The phase $\phi_{\alpha\kappa}$ controls the CP-violating nature of the charged-current interaction between ℓ_α and N_κ in Eq. (4.6)[1]. With these simplifications, the relation in Eq. (4.10) can be written in the $\mathscr{N}_S = 2$ case as

$$m^\nu_{\alpha\beta} + m_N \Theta_{\alpha 1} \Theta_{\beta 1} + m_N (1 + r_\Delta) \Theta_{\alpha 2} \Theta_{\beta 2} = 0 \,, \tag{4.12}$$

where $m^\nu_{\alpha\beta} \equiv \sum_i^3 m_i U_{\alpha i} U_{\beta i}$. In the next subsection, we will use this result to derive relations between the active-sterile mixing strengths $s_{\alpha k}$ to reproduce the light

[1] Enforcing the diagonalised neutrino mass matrix to be invariant under CP, the HNL mass eigenstate N_κ transforms as $\mathrm{U_{CP}} N_\kappa \mathrm{U_{CP}^{-1}} = \pm i\gamma^0 N_\kappa^c$. The charged-current between ℓ_α and N_κ in Eq. (4.6) then transforms as $\mathrm{U_{CP}} \mathscr{L}_{W^\pm} \mathrm{U_{CP}^{-1}} \supset \mp \frac{g}{\sqrt{2}} i (\xi^{\rm CP}_{\ell_\alpha})^* \bar{N}_\kappa \not{W} P_L U_{\alpha N_\kappa} \ell_{\alpha L} + \mathrm{h.c.}$, where $(\xi^{\rm CP}_{\ell_\alpha})^*$ is the CP parity of ℓ_α. Taking $\xi^{\rm CP}_{\ell_\alpha} = i$ implies that CP is conserved for $U^*_{\alpha N_\kappa} = \pm U_{\alpha N_\kappa}$, or equivalently for $e^{i\phi_{\alpha\kappa}} = \pm 1$. The arbitrariness of $\xi^{\rm CP}_{\ell_\alpha}$ is eliminated when considering relative phase differences, e.g. $\Delta\phi_\alpha = \phi_{\alpha 2} - \phi_{\alpha 1}$. CP is conserved for $e^{i\Delta\phi_\alpha} = \pm 1$.

neutrino masses, mixing angles and phases contained in $m^{\nu}_{\alpha\beta}$.

4.2.2 Active-Sterile Mixing Ratio Formulae

If a pair of HNLs exists in nature, their masses (m_N, r_Δ), active-sterile mixing ($|\Theta_{\alpha 1}|$, $|\Theta_{\alpha 2}|$) and CP phases ($\phi_{\alpha 1}$, $\phi_{\alpha 2}$), for the flavour $\alpha = e, \mu, \tau$ can in principle be measured experimentally. Furthermore, if the HNL pair is the sole (or dominant) contribution to the light neutrino masses and mixing, Eq. (4.12) implies that there are correlations among these measurable quantities. If an HNL pair is found that does not follow Eq. (4.12), it cannot be the only contribution to the light neutrino masses. For example, there may exist more than two HNLs; we generalise Eq. (4.12) and the results derived below to the $3 + \mathscr{N}_S$ model in Appendix A.

We can insert into the neutrino mass matrix $m^{\nu}_{\alpha\beta}$ the light neutrino masses, mixing angles and Dirac CP phase inferred from the neutrino oscillation data; however, the Majorana phases α_{21} and α_{31} remain unconstrained. Taking the lightest neutrino to be massless, as implied in the $3+2$ model, we have

$$m^{\nu}_{\alpha\beta} = m_i U_{\alpha i} U_{\beta i} + m_j U_{\alpha j} U_{\beta j}\,, \tag{4.13}$$

where $(i, j) = (2, 3)$ and $(1, 2)$ in the NO and IO scenarios, respectively. Now only a single unconstrained Majorana phase is physically relevant, which we can choose to be α_{21}.

We first consider the constraint $(\mathscr{M}_\nu)_{\alpha\beta} = 0$ for $\alpha = \beta$, i.e. the constraints along the diagonal of Eq. (4.5). The expression in Eq. (4.12) can be rearranged to give

$$\frac{\Theta^2_{\alpha 2}}{\Theta^2_{\alpha 1}} = -\frac{1 + x^{\alpha}_{\alpha\alpha}}{1 + r_\Delta}\,; \quad x^{\rho}_{\alpha\beta} \equiv \frac{m^{\nu}_{\alpha\beta}}{m_N \Theta^2_{\rho 1}}\,. \tag{4.14}$$

Using $\Theta_{\alpha\kappa} = |\Theta_{\alpha\kappa}| e^{i\phi_{\alpha\kappa}/2} \equiv s_{\alpha\kappa} e^{i\phi_{\alpha\kappa}/2}$, it is now straightforward to find

$$\frac{|\Theta_{\alpha 2}|^2}{|\Theta_{\alpha 1}|^2} = \frac{|1 + x^{\alpha}_{\alpha\alpha}|}{1 + r_\Delta}\,, \quad \cos\Delta\phi_\alpha = -\frac{\mathrm{Re}[1 + x^{\alpha}_{\alpha\alpha}]}{|1 + x^{\alpha}_{\alpha\alpha}|} = \frac{|x^{\alpha}_{\alpha\alpha}|^2 - 1 - |1 + x^{\alpha}_{\alpha\alpha}|^2}{2|1 + x^{\alpha}_{\alpha\alpha}|}\,, \tag{4.15}$$

where $\Delta\phi_\alpha = \phi_{\alpha 2} - \phi_{\alpha 1}$ is the CP phase difference. Written in this way, we see that in order to reproduce the light neutrino data in $m^\nu_{\alpha\alpha}$ (up to a value of the Majorana phase α_{21}), the values of $|\Theta_{\alpha 2}|$ and $\cos\Delta\phi_\alpha$ are fixed by m_N, r_Δ, $|\Theta_{\alpha 1}|$ and $\phi_{\alpha 1}$.

If we instead consider $(\mathscr{M}_\nu)_{\alpha\beta} = 0$ for $\alpha \neq \beta$, i.e., the off-diagonal constraints of Eq. (4.5), we obtain

$$\frac{\Theta_{\beta 1}}{\Theta_{\alpha 1}} = \frac{x^\alpha_{\alpha\beta} \pm \sqrt{(x^\alpha_{\alpha\beta})^2 - x^\alpha_{\alpha\alpha} x^\alpha_{\beta\beta}}\sqrt{1 + x^\alpha_{\alpha\alpha}}}{x^\alpha_{\alpha\alpha}} \equiv y^\alpha_{\alpha\beta}\,, \tag{4.16}$$

which can be used to find

$$\frac{|\Theta_{\beta 1}|^2}{|\Theta_{\alpha 1}|^2} = |y^\alpha_{\alpha\beta}|^2\,, \quad \cos(\phi_{\beta 1} - \phi_{\alpha 1}) = \frac{\mathrm{Re}\left[(y^\alpha_{\alpha\beta})^2\right]}{|y^\alpha_{\alpha\beta}|^2}\,. \tag{4.17}$$

Combining Eqs. (4.14) and (4.16), it is also possible to write,

$$\frac{\Theta_{\beta 2}}{\Theta_{\alpha 1}} = \pm i\sqrt{\frac{(y^\alpha_{\alpha\beta})^2 + x^\alpha_{\beta\beta}}{1 + r_\Delta}}\,, \tag{4.18}$$

and therefore all active-sterile mixing strengths $|\Theta_{\beta i}|$ and CP phases $\phi_{\beta i}$ (for $\alpha \neq \beta$) can be written in terms of $m^\nu_{\alpha\beta}$ (containing the light neutrino masses, mixing angles and Dirac CP phase from the neutrino oscillation data and a single Majorana phase α_{21} for $m_{\text{light}} = 0$), the HNL masses m_N and $m_N(1 + r_\Delta)$, a single active-sterile mixing $|\Theta_{\alpha 1}|$ and CP phase $\phi_{\alpha 1}$ for a particular flavour α. We note that this approach is very similar to the Casas-Ibarra parametrisation [172], which splits the mixing matrix U into sub-blocks and uses the relation $(\mathscr{M}_\nu)_{\alpha\beta} = 0$ to express the active-sterile mixing strengths in terms of the light neutrino masses, mixing angles and phases, HNL masses and arbitrary angles in a complex orthogonal matrix R. In Appendix B, we compare the phenomenological approach summarised in this section to the minimal $3+2$ parametrisation of [173].

An interesting limit to consider for Eqs. (4.14) and (4.16) is $|x^\alpha_{\alpha\beta}| \ll 1$, or equivalently $|\Theta_{\alpha 1}|^2 \gg |m^\nu_{\alpha\beta}|/m_N$, which is exactly the *inverse seesaw* limit as discussed in Sec. 3.2. With the lightest neutrino being massless in the $3+2$ model, we

obtain

$$|\Theta_{\alpha 2}|^2 \approx \frac{|\Theta_{\alpha 1}|^2}{1+r_\Delta}, \quad \cos\Delta\phi_\alpha = -1\,, \quad \frac{\Theta_{\beta 1}}{\Theta_{\alpha 1}} \approx \frac{\sqrt{m_i}U_{\beta i} \mp i\sqrt{m_j}U_{\beta j}}{\sqrt{m_i}U_{\alpha i} \mp i\sqrt{m_j}U_{\alpha j}}\,, \tag{4.19}$$

where $(i,j) = (2,3)$ and $(1,2)$ in the NO and IO scenarios, respectively. As discussed in Appendix A, the choice of sign in Eqs. (4.16) and (4.18), and therefore $y^\nu_{\alpha\beta}$ in Eq. (4.19), is arbitrary. In Eqs. (4.18) and (4.19), we choose the positive sign and allow the physically-relevant Majorana phase α_{21} in the $U_{\alpha i}$ to lie in the range $[0, 4\pi]$, which takes into account both values of of the sign.

In Fig. 4.2 (left), we depict two regions in the $(|\Theta_{e1}|^2, |\Theta_{e2}|^2)$ plane that are compatible with the $(\mathscr{M}_\nu)_{ee} = 0$ constraint for fixed $m_N = 400$ MeV and $r_\Delta = 10^{-0.5}$, but allowing α_{21} and ϕ_{e1} to vary. The blue and green shaded regions are for the NO and IO scenarios, respectively. We see that the regions can tend to small $|\Theta_{e1}|^2$ or $|\Theta_{e2}|^2$ values while the other mixing strength remains constant. To the upper right, the region can also tend to large values of both mixing strengths; here, the ratio $|\Theta_{e2}|^2/|\Theta_{e1}|^2$ follows the relation in Eq. (4.19). These limits will be discussed in more detail in the next subsection.

4.2.3 Approximate Ratio Formulae

We will now examine Eq. (4.14) in the simple $1+2$ model, with the active neutrino flavour $\alpha = e$. These results will allow a broad strokes comparison of $0\nu\beta\beta$ decay and DUNE in the following sections. The light neutrino mass matrix element $m^\nu_{\alpha\beta}$ is simply replaced by m_ν, which gives the expression

$$|\Theta_{e2}|^2 = \frac{|r_\nu + |\Theta_{e1}|^2 e^{i\phi_{e1}}|}{1+r_\Delta} = \frac{\sqrt{r_\nu^2 + |\Theta_{e1}|^4 + 2r_\nu|\Theta_{e1}|^2\cos\phi_{e1}}}{1+r_\Delta}\,, \tag{4.20}$$

where we have defined $r_\nu \equiv m_\nu/m_N$. In Fig. 4.2 (right), we use Eq. (4.20) to plot the combination $|\Theta_{e2}|^2(1+r_\Delta)/r_\nu$ as a function of $|\Theta_{e1}|^2/r_\nu$ for different values of $\cos\phi_{e1}$. The blue region formed for $\cos\phi_{e1} \in [-1,1]$ indicates the parameter space that is compatible with $(\mathscr{M}_\nu)_{ee} = 0$. Every point in the parameter space has an associated value of $\cos\phi_{e1}$ and $\cos\phi_{e2}$; in Fig. 4.2 (right), the values of these phases

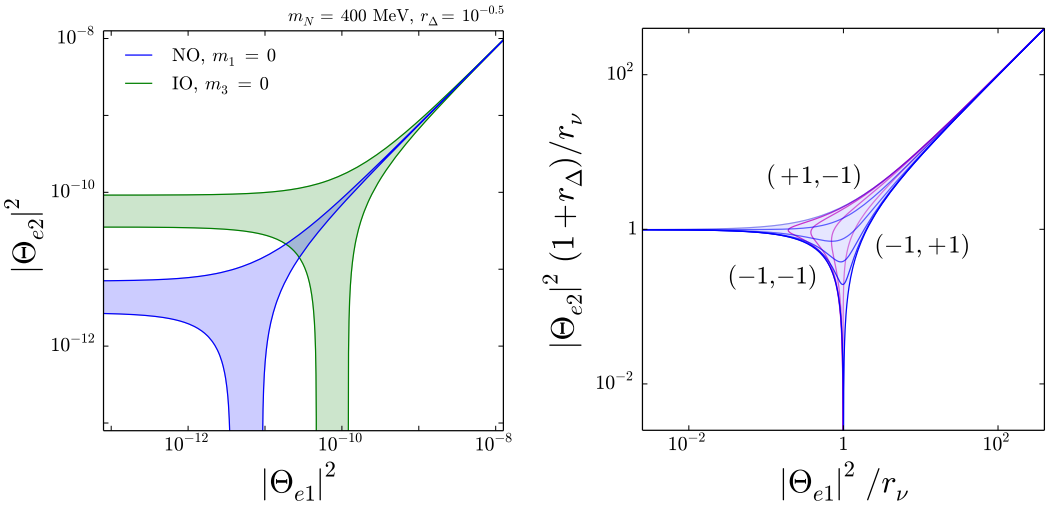

Figure 4.2: (Left) Regions in the $(|\Theta_{e1}|^2, |\Theta_{e2}|^2)$ plane that are compatible with Eq. (4.14) in the $3+2$ model, showing the NO (blue) and IO (green) cases for $m_N = 400$ MeV, $r_\Delta = 10^{-0.5}$ and $m_{\text{lightest}} = 0$. (Right) Region in the $(|\Theta_{e1}|^2/r_\nu, |\Theta_{e2}|^2(1+r_\Delta)/r_\nu)$ plane that is compatible with Eq. (4.14) in the simple $1+2$ model. The blue and magenta lines are contours of constant $\cos\phi_{e1}$ and $\cos\phi_{e2}$, respectively; their values on the edges of the allowed region are shown in parentheses.

on the extremities of the allowed region are shown. Likewise, the value of $\cos\Delta\phi_e$ is given by

$$\cos\Delta\phi_e = \frac{r_\nu^2 - |\Theta_{e1}|^4 - (1+r_\Delta)^2|\Theta_{e2}|^4}{2(1+r_\Delta)|\Theta_{e1}|^2|\Theta_{e2}|^2} = \frac{r_\nu^2 - |\Theta_{e1}|^4 - ||\Theta_{e1}|^2 + r_\nu e^{-i\phi_{e1}}|^2}{2|\Theta_{e1}|^2||\Theta_{e1}|^2 + r_\nu e^{-i\phi_{e1}}|}$$
$$= -\frac{|\Theta_{e1}|^2 + r_\nu\cos\phi_{e1}}{\sqrt{r_\nu^2 + |\Theta_{e1}|^4 + 2r_\nu|\Theta_{e1}|^2\cos\phi_{e1}}}\,. \tag{4.21}$$

The relevant limits of Eq. (4.20) are made clear in the figure; firstly, the thin extensions to the left and bottom of the allowed region indicate that the active-sterile mixing strengths tend to constant values when the other mixing is much smaller than r_ν, i.e.,

$$|\Theta_{e1}|^2 = r_\nu\,,\ \cos\phi_{e1} = -1 \qquad (|\Theta_{e2}|^2 \ll r_\nu/(1+r_\Delta))\,, \tag{4.22}$$

$$|\Theta_{e2}|^2 = \frac{r_\nu}{1+r_\Delta}\,,\ \cos\phi_{e2} = -1 \quad (|\Theta_{e1}|^2 \ll r_\nu)\,. \tag{4.23}$$

This is exactly the *standard seesaw* scenario as discussed in Sec. 3.2, where one of the HNL states generates the light neutrino mass at tree level, while the other decouples. In each case, the value of one phase is constrained, while the phase difference can take any value. Secondly, the thin extension to the upper right of the allowed region suggests that the active-sterile mixing can also tend to values much larger than r_ν. In this limit,

$$|\Theta_{e2}|^2 = \frac{|\Theta_{e1}|^2}{1+r_\Delta}, \cos\Delta\phi_e = -1 \quad (|\Theta_{e1}|^2 \gg r_\nu). \tag{4.24}$$

This is the *inverse seesaw* scenario, where both HNL states have a large active-sterile mixing, but a cancellation ensures that their combined contribution to the tree level neutrino mass is small.

4.3 Neutrinoless Double Beta Decay

In this section we will examine the $0\nu\beta\beta$ decay process in the phenomenological parametrisation set out in Sec. 4.2. Firstly, we will provide a general formula for the $0\nu\beta\beta$ decay half-life in the $3+2$ model, examining how an experimental measurement of $0\nu\beta\beta$ decay can be used to constrain the active-sterile mixing and phases for a given HNL mass m_N and mass splitting ratio r_Δ. We will then simplify to the $1+2$ scenario, considering only the first generation. Various limits of the resulting formulae will be investigated.

4.3.1 In the Phenomenological Model

The $0\nu\beta\beta$ decay rate $\Gamma_{0\nu}$ and half-life $T^{0\nu}_{1/2}$, taking into the account the exchange of $\mathcal{N}_A$ active neutrinos and $\mathcal{N}_S$ sterile neutrinos, can be written as

$$\frac{\Gamma_{0\nu}}{\ln 2} = \frac{1}{T^{0\nu}_{1/2}} = \frac{G_{0\nu} g_A^4}{m_e^2} \left| \sum_i^{\mathcal{N}_A} U_{ei}^2 m_i \mathcal{M}^{0\nu}(m_i) + \sum_\kappa^{\mathcal{N}_S} U_{eN_\kappa}^2 m_{N_\kappa} \mathcal{M}^{0\nu}(m_{N_\kappa}) \right|^2, \tag{4.25}$$

where $G_{0\nu}$ is the kinematical phase space factor for the $0\nu\beta\beta$ decay isotope, g_A is the axial coupling strength, m_e is the electron mass, and $\mathcal{M}^{0\nu}(m_i)$ is the nuclear matrix element (NME) of the process, which depends on the mass m_i of the exchanged

NME	$\mathscr{M}_F$	$\mathscr{M}_{GT}^{AA}$	$\mathscr{M}_{GT}^{\prime AP}$	$\mathscr{M}_{GT}^{\prime\prime PP}$	$\mathscr{M}_{GT}^{\prime WW}$	$\mathscr{M}_{T}^{\prime AP}$	$\mathscr{M}_{T}^{\prime\prime PP}$	$\mathscr{M}_{T}^{\prime WW}$	$\mathscr{M}_{\nu}^{0\nu}$	$\mathscr{M}_{N}^{0\nu}$
$\mathscr{M}_X$	−0.780	6.062	0.036	0.00034	0.089	−0.010	−0.00014	−0.035	−5.28	–
$\mathscr{M}_{X,\mathrm{sd}}$	−48.89	170.0	2.110	0.028	2.945	−1.310	−0.022	−6.541	–	−194

Table 4.1: Standard and short-distance Fermi, Gamow-Teller and tensor NMEs of ^{76}Ge and the resulting *light* and *heavy* NMEs [175] used in the simple interpolation formula of Eq. (4.30).

neutrino and encodes the non-trivial transition between initial and final-state nuclei. The values of NME are taken from existing computational results as shown in Tab. 4.1.

The typical energy scale of $0\nu\beta\beta$ decay, $k_F \sim 100$ MeV (the Fermi momentum of a nucleus), is much smaller than the electroweak scale. The first step in deriving Eq. (4.25) is therefore to write the interactions between the quarks, outgoing electrons and exchanged neutrino as the effective Fermi interaction, i.e., the low-energy limit of the charged-current interaction in Eq. (4.6). Due to the non-perturbative nature of QCD, this description of $0\nu\beta\beta$ decay in terms of quarks and gluons breaks down below the GeV scale. It becomes necessary to use chiral perturbation theory to characterise pions and nucleons as degrees of freedom below the chiral symmetry breaking scale $\Lambda_\chi \sim 1$ GeV. In turn, chiral effective field theory (EFT) and the non-relativistic limit must be used to describe the many-nucleon initial and final states. These steps go into calculating the NMEs in Eq. (4.25); this has been performed numerically using many-body methods such as the quasi-particle random phase approximation (QRPA), shell model and interacting boson model (IBM-2). More recently, *ab initio* methods have been used to calculate the NMEs directly from the chiral EFT [174].

The mass of the exchanged neutrino has a large impact on the above discussion. For $m_i \lesssim Q_{\beta\beta}$, where $Q_{\beta\beta} = E_I - E_F - 2m_e \sim \mathcal{O}(\mathrm{MeV})$ is the Q-value of the isotope (E_I and E_F are the energies of the initial and final nuclei, respectively), the $0\nu\beta\beta$ decay rate is dominated by the exchange of *potential* neutrinos, with $(p^0, \mathbf{p}) \sim (0, k_F)$, and *hard* neutrinos, with $p^0 \sim \mathbf{p} \sim \Lambda_\chi$ [176, 177]. In this limit,

the NMEs can be written as

$$\mathscr{M}^{0\nu}(m_i \lesssim Q_{\beta\beta}) = \frac{g_V^2}{g_A^2}\mathscr{M}_F - \frac{2m_e m_p g_\nu^{NN}}{g_A^2}\mathscr{M}_{F,\mathrm{sd}} - \mathscr{M}_{GT} + \mathscr{M}_T\,, \tag{4.26}$$

where $\mathscr{M}_F$ is the Fermi NME, while

$$\mathscr{M}_{GT} = \mathscr{M}_{GT}^{AA} - \frac{g_P}{6g_A}\mathscr{M}_{GT}^{\prime AP} + \frac{(g_V+g_W)^2}{6g_A^2}\mathscr{M}_{GT}^{\prime WW} + \frac{g_P^2}{48g_A^2}\mathscr{M}_{GT}^{\prime\prime PP}\,, \tag{4.27}$$

$$\mathscr{M}_T = \frac{g_P}{6g_A}\mathscr{M}_T^{\prime AP} + \frac{(g_V+g_W)^2}{12g_A^2}\mathscr{M}_T^{\prime WW} - \frac{g_P^2}{48g_A^2}\mathscr{M}_T^{\prime\prime PP}\,, \tag{4.28}$$

are the Gamow-Teller and tensor NMEs. In Eq. (4.26), m_p is the proton mass and $g_V = 1$, $g_W = 3.7$ and $g_P = 231$ are the vector, magnetic and pseudoscalar charges, respectively [178]. The potential neutrinos contribute to $\mathscr{M}_F$, $\mathscr{M}_{GT}$ and $\mathscr{M}_T$, while the hard neutrinos induce the term proportional to $g_\nu^{NN} \sim 1/(2F_\pi)^2$, $F_\pi = 92.2$ MeV, which is a low-energy constant (LEC) describing the short-range nucleon-nucleon coupling. This term contains the *short-range* Fermi NME $\mathscr{M}_{F,\mathrm{sd}}$, which is found by replacing the long-range neutrino potential in the calculation of the Fermi NME with a short-range potential (we use the normalisation factor of $m_e m_p$ similar to [178, 179] instead of m_π^2 used by [177]). All NMEs in Eqs. (4.26)-(4.28) are given in Table 4.1 for ^{76}Ge.

If the exchanged neutrinos are instead much heavier than the chiral symmetry breaking scale, $m_{N_\kappa} \gg \Lambda_\chi$, they must be integrated out before matching onto the chiral perturbation theory; the exchange of such states is then described by a dimension-nine operator [177, 180, 181]. Neutrinos in the intermediate mass region $Q_{\beta\beta} \lesssim m_{N_\kappa} \lesssim \Lambda_\chi$ are more difficult to describe, as loop corrections scaling as $\sim m_{N_\kappa}/\Lambda_\chi$ become large. Nevertheless, it is possible to approximate this intermediate region by applying an interpolating formula between the well-understood low- and high-mass regions. In the treatment of [177], this involves constructing an interpolating formula for each NME $\mathscr{M}_X$ appearing in Eqs. (4.26)-(4.28), for

example,

$$\mathscr{M}^{\rm int}_{X(,{\rm sd})}(m_{N_\kappa}) = \mathscr{M}_{X(,{\rm sd})}\,\frac{\langle \mathbf{p}_X^2\rangle}{\langle \mathbf{p}_X^2\rangle + m_{N_\kappa}^2}\,; \quad \langle \mathbf{p}_X^2\rangle \equiv m_e m_p \left|\frac{\mathscr{M}_{X,{\rm sd}}}{\mathscr{M}_X}\right|, \tag{4.29}$$

where $\langle \mathbf{p}_X^2\rangle \sim k_F^2$. An interpolating formula can also be formulated for g_ν^{NN}, which connects the LEC for hard neutrino exchange to other LECs from dimension-nine operators. Rather than using an interpolation formula for each NME in Eqs. (4.26)-(4.28), a more naive approach is to interpolate between the low- and high-mass limits of the whole NME $\mathscr{M}^{0\nu}$. For example,

$$\widetilde{\mathscr{M}}^{\rm int}_{0\nu}(m_{N_\kappa}) = \mathscr{M}^{0\nu}_\nu\,\frac{\langle \mathbf{p}^2\rangle}{\langle \mathbf{p}^2\rangle + m_{N_\kappa}^2}\,; \quad \langle \mathbf{p}^2\rangle \equiv m_e m_p \left|\frac{\mathscr{M}^{0\nu}_N}{\mathscr{M}^{0\nu}_\nu}\right|, \tag{4.30}$$

where the *light* NME $\mathscr{M}^{0\nu}_\nu$ is the expression in Eq. (4.26) and the *heavy* NME $\mathscr{M}^{0\nu}_N$ is given by Eq. (4.26) with $g_\nu^{NN} \to 0$ and $\mathscr{M}_X \to \mathscr{M}_{X,{\rm sd}}$. Inserting the interpolation formula in Eq. (4.30) into Eq. (4.25), it is now possible to write the inverse $0\nu\beta\beta$ decay half-life as

$$\frac{1}{T^{0\nu}_{1/2}} = \frac{G_{0\nu} g_A^4 |\mathscr{M}^{0\nu}_\nu|^2}{m_e^2}\left|m^{\rm eff}_{\beta\beta}\right|^2, \tag{4.31}$$

where the effective Majorana neutrino mass from $0\nu\beta\beta$ decay is

$$\left|m^{\rm eff}_{\beta\beta}\right| = \left|\sum_i^{\mathscr{N}_A} U_{ei}^2 m_i + \sum_\kappa^{\mathscr{N}_S} U_{eN_\kappa}^2 m_{N_\kappa}\frac{\langle \mathbf{p}^2\rangle \mathscr{F}(m_{N_\kappa})}{\langle \mathbf{p}^2\rangle + m_{N_\kappa}^2}\right|. \tag{4.32}$$

Here, $\mathscr{F}(m_{N_\kappa}) = \mathscr{M}^{\rm int}_{0\nu}(m_{N_\kappa})/\widetilde{\mathscr{M}}^{\rm int}_{0\nu}(m_{N_\kappa})$ is a correction function to the naive interpolation formula in Eq. (4.30). As mentioned above, a more accurate approach would be to include in $\mathscr{M}^{\rm int}_{0\nu}(m_{N_\kappa})$ an interpolating formula for g_ν^{NN} and each NME in Eqs. (4.26)-(4.28).

In the $3+2$ model we have $U_{eN_1} \approx |\Theta_{e1}|e^{i\phi_{e1}/2}$ and $U_{eN_2} \approx |\Theta_{e2}|e^{i\phi_{e2}/2}$. Inserting these into Eq. (4.33), it is then possible to use Eq. (4.14) to eliminate $|\Theta_{e2}|^2$ and

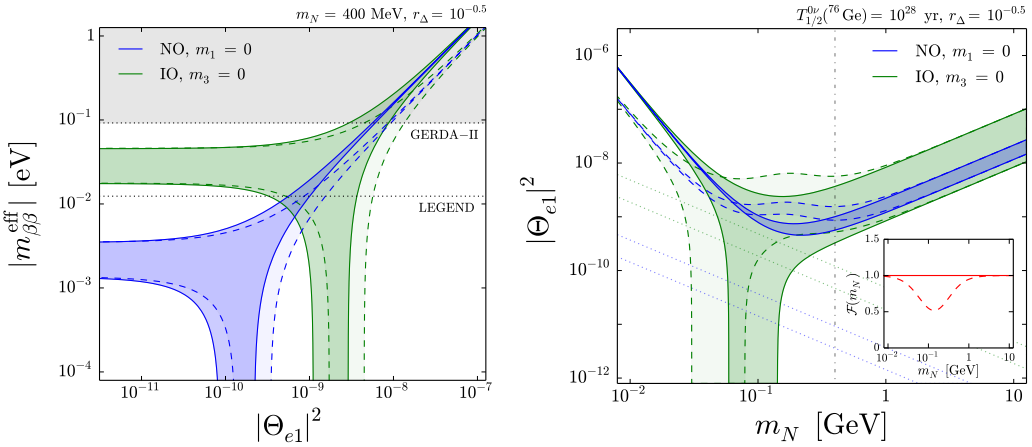

Figure 4.3: (Left) In the $3+2$ model, the effective Majorana mass $\left|m^{\rm eff}_{\beta\beta}\right|$ from the $0\nu\beta\beta$ decay of ^{76}Ge as a function of the active-sterile mixing $|\Theta_{e1}|^2$ for $m_N = 400$ MeV, $r_\Delta = 10^{-0.5}$, marginalising over α_{21} and ϕ_{e1} in the NO (blue shaded) and IO (green shaded) scenarios with $m_{\rm light} = 0$. (Right) Regions in the $(m_N, |\Theta_{e1}|^2)$ parameter space compatible with a measured $0\nu\beta\beta$ decay half-life of $T^{0\nu}_{1/2}(^{76}\mathrm{Ge}) = 10^{28}$ yr, for a mass splitting ratio of $r_\Delta = 10^{-0.5}$ in the NO (blue) and IO (green) scenarios, marginalising over α_{21} and ϕ_{e1}. In both plots, solid lines use $\mathcal{F}(m_N) = 1$, dashed lines the more accurate NME interpolating formula (shown in the inset). The corresponding seesaw lines, $|\Theta_{e1}|^2 = |m^\nu_{ee}|/m_N$, are shown (dotted).

ϕ_{e2}, giving

$$\left|m^{\rm eff}_{\beta\beta}\right| = \left|\alpha m^\nu_{ee} + \beta m_N |\Theta_{e1}|^2 e^{i\phi_{e1}}\right|, \tag{4.33}$$

where we have introduced

$$\alpha \equiv 1 - \frac{\langle \mathbf{p}^2\rangle \mathcal{F}\left(m_N(1+r_\Delta)\right)}{\langle \mathbf{p}^2\rangle + m_N^2(1+r_\Delta)^2} \qquad \beta \equiv \frac{\langle \mathbf{p}^2\rangle \mathcal{F}(m_N)}{\langle \mathbf{p}^2\rangle + m_N^2} - \frac{\langle \mathbf{p}^2\rangle \mathcal{F}\left(m_N(1+r_\Delta)\right)}{\langle \mathbf{p}^2\rangle + m_N^2(1+r_\Delta)^2}\,. \tag{4.34}$$

In Fig. 4.3 (left), we plot the effective Majorana mass from $0\nu\beta\beta$ decay in Eq. (4.33) as a function of the active-sterile mixing $|\Theta_{e1}|^2$ for an HNL mass $m_N = 400$ MeV and mass splitting ratio $r_\Delta = 10^{-0.5}$. We assume that ϕ_{e1} and the Majorana phase α_{21} are not constrained by other means; we therefore marginalise over them, forming a band of possible $\left|m^{\rm eff}_{\beta\beta}\right|$ values. The blue and green shaded regions depict the NO and IO scenarios, respectively, with a massless lightest neutrino. The

solid lines make use of the naive interpolating formula in Eq. (4.30), i.e., setting $\mathscr{F}(m_N) = 1$ in Eq. (4.33), while the dashed lines use an interpolating formula for g_ν^{NN} and each NME in Eqs. (4.26)-(4.28). The regions are compared to the current upper limit on $\left|m_{\beta\beta}^{\rm eff}\right|$ from the GERDA-II experiment, $T_{1/2}^{0\nu}(^{76}\text{Ge}) > 1.8 \times 10^{26}$ yr, and the future sensitivity of the LEGEND-1000 experiment, $T_{1/2}^{0\nu}(^{76}\text{Ge}) > 10^{28}$ yr.

In Fig. 4.3 (right), we plot the active-sterile mixing $|\Theta_{e1}|^2$ as a function of m_N found from Eq. (4.33) for $r_\Delta = 10^{-0.5}$ and a $0\nu\beta\beta$ decay half-life of $T_{1/2}^{0\nu}(^{76}\text{Ge}) = 10^{28}$ yr. Again, we depict the NO (blue shaded) and IO (green shaded) scenarios for a massless lightest neutrino and marginalise over ϕ_{e1} and the Majorana phase α_{21}. The solid and dashed lines, respectively, use the naive and more accurate interpolating formulae; in the inset, we plot the values of $\mathscr{F}(m_N)$ over the same mass range. The blue and green dotted lines show the ranges of possible seesaw relations, $|\Theta_{e1}|^2 = |m_{ee}^\nu|/m_N$, in the NO and IO cases, respectively.

4.3.2 Approximate $0\nu\beta\beta$ Decay Rate

In the $3+2$ model, $0\nu\beta\beta$ decay is induced by the exchange of the light neutrinos and a pair of HNLs. Depending on the parameters of the model, one of these contributions may dominate over the others; alternatively, if the contributions are of similar size, constructive or destructive interference may occur in $\left|m_{\beta\beta}^{\rm eff}\right|$. In order to investigate this interplay, it is useful to use the simple $1+2$ model as in Sec. 4.2.3. Replacing m_{ee}^ν with m_ν in Eq. (4.33), we obtain the simplified effective Majorana mass

$$\left|m_{\beta\beta}^{\rm eff}\right| = \left|\alpha m_\nu + \beta m_N |\Theta_{e1}|^2 e^{i\phi_{e1}}\right| = m_N \sqrt{\alpha^2 r_\nu^2 + \beta^2 |\Theta_{e1}|^4 + 2\alpha\beta r_\nu |\Theta_{e1}|^2 \cos\phi_{e1}}\,. \tag{4.35}$$

We see that the interplay between the light neutrino and HNL pair is controlled by the active-sterile mixing $|\Theta_{e1}|^2$, light neutrino mass m_ν, HNL mass m_N, mass splitting ratio r_Δ (contained in α and β) and CP phase ϕ_{e1}.

We will now examine how $\left|m_{\beta\beta}^{\rm eff}\right|$ depends on the active-sterile mixing $|\Theta_{e1}|^2$. Firstly, in the *standard seesaw* limit, i.e., when the active-sterile mixing of the HNL

pair lies in the thin extensions to the left or bottom of the allowed region in Fig. 4.2 (right), we have

$$\left|m_{\beta\beta}^{\text{eff}}\right| \approx \begin{cases} (\alpha-\beta)m_\nu & (|\Theta_{e1}|^2 = r_\nu) \\ \alpha m_\nu & (|\Theta_{e1}|^2 \ll r_\nu) \end{cases} . \tag{4.36}$$

Here, one HNL decouples while the other has an active-sterile mixing following the seesaw relation and a CP phase $\cos\phi_{ei} = -1$, therefore adding destructively with the light neutrino contribution. Instead, in the *inverse seesaw* limit $|\Theta_{e1}|^2 \gg r_\nu$, where the active-sterile mixing strengths follow $|\Theta_{e2}|^2 = |\Theta_{e1}|^2/(1+r_\Delta)$ and the relative CP phase is $\cos\Delta\phi_e = -1$ (and therefore the HNLs add destructively with each other in $\left|m_{\beta\beta}^{\text{eff}}\right|$), there are three interesting cases. If the active-sterile mixing $|\Theta_{e1}|^2$ lies in the range $r_\nu \ll |\Theta_{e1}|^2 \ll \alpha r_\nu/\beta$ (note that $\beta < \alpha$ and therefore $\alpha/\beta > 1$ for all positive values of m_N and r_Δ), it is not large enough for the HNL pair to dominate over the light neutrino contribution, and again $\left|m_{\beta\beta}^{\text{eff}}\right| \approx \alpha m_\nu$. Instead, for $|\Theta_{e1}|^2 \approx \alpha r_\nu/\beta$, cancellations can occur between the light neutrino and HNL pair. The phase ϕ_{e1} is unconstrained in the $|\Theta_{e1}|^2 \gg r_\nu$ limit, so for $|\Theta_{e1}|^2 = \alpha r_\nu/\beta$ we may have any value between $\left|m_{\beta\beta}^{\text{eff}}\right| \approx 0$ for $\cos\phi_{e1} = -1$ and $\left|m_{\beta\beta}^{\text{eff}}\right| \approx 2\alpha m_\nu$ for $\cos\phi_{e1} = 1$. Finally, for $|\Theta_{e1}|^2 \gg \alpha r_\nu/\beta$, the HNL pair dominates over the light neutrino contribution, and

$$\left|m_{\beta\beta}^{\text{eff}}\right| \approx \beta m_N |\Theta_{e1}|^2 \quad (|\Theta_{e1}|^2 \gg \alpha r_\nu/\beta) . \tag{4.37}$$

This is nothing but the destructive interference between the HNL contributions. In this limit, $\left|m_{\beta\beta}^{\text{eff}}\right|$ is insensitive to the phase ϕ_{e1}.

We can now ask the question: what would a measurement of $0\nu\beta\beta$ decay tell us about the available parameter space of the HNL pair? We can equate $\left|m_{\beta\beta}^{\text{eff}}\right|$ in

Eq. (4.35) to the experimental value of the effective Majorana mass,

$$\begin{aligned}\left|m_{\beta\beta}^{\rm exp}\right| &\equiv \frac{m_e}{g_A^2|\mathscr{M}_\nu^{0\nu}|\sqrt{G_{0\nu}T_{1/2}^{0\nu}}} \\ &= 1.24\times10^{-2}\ {\rm eV}\left(\frac{2.36\times10^{-15}\ {\rm yr}^{-1}}{G_{0\nu}}\right)^{1/2}\left(\frac{5.28}{|\mathscr{M}_\nu^{0\nu}|}\right)\left(\frac{10^{28}\ {\rm yr}}{T_{1/2}^{0\nu}}\right)^{1/2},\end{aligned} \tag{4.38}$$

where $T_{1/2}^{0\nu}$ is the measured $0\nu\beta\beta$ decay half-life. The constraint $\left|m_{\beta\beta}^{\rm eff}\right| = \left|m_{\beta\beta}^{\rm exp}\right|$ defines a hypersurface in the $(m_\nu, m_N, r_\Delta, |\Theta_{e1}|^2, \cos\phi_{e1})$ parameter space, described by

$$\cos\phi_{e1} = \frac{\left|m_{\beta\beta}^{\rm exp}\right|^2 - \alpha^2 m_\nu^2 - \beta^2 m_N^2|\Theta_{e1}|^4}{2\alpha\beta m_\nu m_N|\Theta_{e1}|^2}. \tag{4.39}$$

We can also use the constraint $\left|m_{\beta\beta}^{\rm eff}\right| = \left|m_{\beta\beta}^{\rm exp}\right|$ to define a hypersurface in the parameter space with ϕ_{e1} replaced by the relative CP phase $\Delta\phi_e$, described by

$$\cos\Delta\phi_e = \frac{\alpha^2 m_\nu^2 - (2\alpha-\beta)\beta m_N^2|\Theta_{e1}|^4 - |m_{\beta\beta}^{\rm exp}|^2}{2\sqrt{\alpha\beta}\ m_N|\Theta_{e1}|^2\sqrt{|m_{\beta\beta}^{\rm exp}|^2 - (\alpha-\beta)(\alpha m_\nu^2 - \beta m_N^2|\Theta_{e1}|^4)}}, \tag{4.40}$$

which is found by inserting Eq. (4.39) into Eq. (4.21).

In Fig. 4.4 (left), we plot regions in the $(m_N, |\Theta_{e1}|^2)$ plane that are compatible with a measured $0\nu\beta\beta$ decay half-life of $T_{1/2}^{0\nu}(^{76}{\rm Ge}) = 10^{28}$ yr, a mass splitting ratio of $r_\Delta = 10^{-0.5}$ and three different values of the light neutrino mass: $m_\nu = 10^{-2.5}$ eV (blue), $10^{-1.9}$ eV (light blue) and $10^{-1.5}$ eV (green). We allow the phase $\cos\phi_{e1}$ to lie anywhere in the range $\cos\phi_{e1} \in [-1, 1]$, forming bands of allowed $|\Theta_{e1}|^2$ values. In Fig. 4.4 (upper right), we show the effective Majorana mass $\left|m_{\beta\beta}^{\rm eff}\right|$ as a function of $|\Theta_{e1}|^2$ for $m_N = 400$ MeV, $r_\Delta = 10^{-0.5}$ and the same three values of m_ν. The observed Majorana mass $\left|m_{\beta\beta}^{\rm exp}\right|$ for a $0\nu\beta\beta$ decay half-life of 10^{28} yr is shown as a horizontal (dotted) line; where this line intersects the $\left|m_{\beta\beta}^{\rm eff}\right|$ region indicates the allowed range of $|\Theta_{e1}|^2$ along the $m_N = 400$ MeV line (dot dashed) in the left plot of Fig. 4.4.

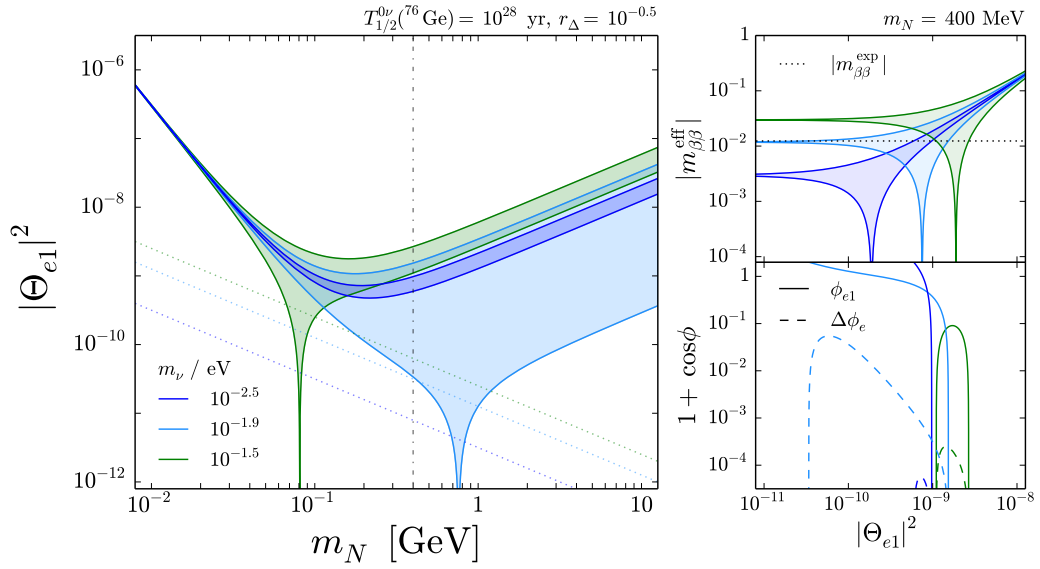

Figure 4.4: (Left) In the $1+2$ model, regions in the $(m_N, |\Theta_{e1}|^2)$ parameter space compatible with a measured $0\nu\beta\beta$ decay half-life of $T^{0\nu}_{1/2}(^{76}\mathrm{Ge}) = 10^{28}$ yr, for a mass splitting ratio of $r_\Delta = 10^{-0.5}$, an arbitrary CP phase ϕ_{e1} and a light neutrino mass $m_\nu = 10^{-2.5}$ eV (blue), $10^{-1.9}$ eV (light blue) or $10^{-1.5}$ eV (green). The corresponding seesaw lines, $|\Theta_{e1}|^2 = m_\nu/m_N$, are shown (dotted). (Upper right) For $m_N = 400$ MeV, allowed values of $|m^{\rm eff}_{\beta\beta}|$ as a function of $|\Theta_{e1}|^2$ for the same three m_ν values, compared to $|m^{\rm exp}_{\beta\beta}|$ from a $0\nu\beta\beta$ decay half-life of 10^{28} yr (black dotted). (Lower right) For $m_N = 400$ MeV, $r_\Delta = 10^{-0.5}$ and three m_ν values, $1+\cos\phi_{e1}$ (solid) and $1+\cos\Delta\phi_e$ (dashed) as a function of $|\Theta_{e1}|^2$, implied by a measured $0\nu\beta\beta$ decay half-life of 10^{28} yr.

In Fig. 4.4 (lower right), we plot the values of $1+\cos\phi_{e1}$ (solid) and $1+\cos\Delta\phi_e$ (dashed) as a function of $|\Theta_{e1}|^2$ using Eqs. (4.39) and Eqs. (4.40), respectively, given a $0\nu\beta\beta$ decay half-life of $T^{0\nu}_{1/2}(^{76}\mathrm{Ge}) = 10^{28}$ yr, for $m_N = 400$ MeV, $r_\Delta = 10^{-0.5}$ and the same three m_ν values. For $m_\nu = 10^{-2.5}$ eV, $\cos\phi_{e1}$ can lie anywhere between -1 and 1. This is made clear from Fig. 4.4 (upper right); the light neutrino mass does *not* saturate the $0\nu\beta\beta$ decay rate and so $|m^{\rm exp}_{\beta\beta}|$ intersects the $|m^{\rm eff}_{\beta\beta}|$ region where $|m^{\rm eff}_{\beta\beta}| \approx \beta m_N |\Theta_{e1}|^2$ (i.e., the HNL pair dominates), which is insensitive to ϕ_{e1}. For $m_\nu = 10^{-1.5}$ eV, we instead have $\cos\phi_{e1} \approx -1$; now, the light neutrino mass *does* saturate the $0\nu\beta\beta$ decay rate and $|m^{\rm exp}_{\beta\beta}|$ intersects the $|m^{\rm eff}_{\beta\beta}|$ region where there must be a cancellation between the light neutrino and HNL pair. For the intermediate case $m_\nu = 10^{-1.9}$ eV, the light neutrino contribution *only just* saturates the $0\nu\beta\beta$ decay rate and therefore a wider range of $|\Theta_{e1}|^2$ values are allowed.

For the relative CP phase $\Delta\phi_e$, we see that $\cos\Delta\phi_e \approx -1$ for all three m_ν values; this is because the intersection of $\left|m_{\beta\beta}^{\rm exp}\right|$ and the $\left|m_{\beta\beta}^{\rm eff}\right|$ region occurs well within the inverse seesaw regime for $m_N = 400$ MeV and $r_\Delta = 10^{-0.5}$. This is confirmed in Fig. 4.4 (left), where we see that the allowed bands of $|\Theta_{e1}|^2$ are well above the seesaw lines. Nevertheless, large values of $\cos\Delta\phi_e$ are still possible in the narrow light blue and green regions where the allowed $|\Theta_{e1}|^2$ values fall below the seesaw lines. For a light neutrino mass $m_\nu > |m_{\beta\beta}^{\rm exp}|$, this occurs when the HNL mass m_N is such that $\left|m_{\beta\beta}^{\rm exp}\right| = \alpha m_\nu$, i.e.,

$$m_N = \frac{1}{1+r_\Delta}\sqrt{\frac{|m_{\beta\beta}^{\rm exp}|\langle \mathbf{p}^2\rangle}{m_\nu - |m_{\beta\beta}^{\rm exp}|}}\,, \tag{4.41}$$

and so $\left|m_{\beta\beta}^{\rm exp}\right|$ intersects the $\left|m_{\beta\beta}^{\rm eff}\right|$ region along the thin extension to small $|\Theta_{e1}|^2$ values.

To conclude this section, we consider how the factors α and β depend on m_N and r_Δ. To do this, it is convenient to write the factors α and β (for $\mathscr{F}(m_N) = 1$) as

$$\alpha = 1 - \frac{1}{1+r_p(1+r_\Delta)^2}\,, \quad \beta = \frac{1}{1+r_p} - \frac{1}{1+r_p(1+r_\Delta)^2}\,, \tag{4.42}$$

where we have defined $r_p \equiv m_N^2/\langle \mathbf{p}^2\rangle$. The relevant limits of α and β are listed in Table 4.2. First, we can consider the scenario where the mass splitting ratio is small ($r_\Delta \ll 1$) and the HNL mass m_N is below the scale $k_F \sim 100$ MeV ($r_p \ll 1$). In this limit, $\alpha \approx r_p \ll 1$ and $\beta \approx 2r_p r_\Delta \ll 1$ and therefore the effective Majorana mass is suppressed. This can be understood from Eq. (4.33); the effective Majorana mass is approximately proportional to $(\mathscr{M}_\nu)_{ee}$ in Eq. (4.10) which is zero at tree level, and the light neutrino and HNL pair contributions exactly cancel each other. Another possible situation is that $r_p \ll 1$, i.e. the lighter HNL is less massive than ~ 100 MeV, but $r_\Delta \gg 1/r_p^{1/2}$ (or $\Delta m_N \gg \langle \mathbf{p}^2\rangle^{1/2}$), so that the heavier HNL is more massive than ~ 100 MeV. This gives $\alpha \approx \beta \approx 1$ and so the contributions from the light neutrino and lighter HNL dominate the $0\nu\beta\beta$ decay rate, while the contribution from the heavier HNL is suppressed.

α, β	$r_p \ll 1$	$r_p \gg 1$
$r_\Delta \ll 1$	r_p, $2r_p r_\Delta$	1, $2r_\Delta/r_p$
$r_\Delta \gg 1$	1, 1	1, $1/r_p$

Table 4.2: Approximate values of the factors α and β in the different limits of the ratios $r_p = m_N^2/\langle \mathbf{p}^2 \rangle$ and $r_\Delta = \Delta m_N/m_N$.

We next examine the limit in which both HNL states are heavier than $\sim$ 100 MeV ($r_p \gg 1$). This gives $\alpha \approx 1$ and $\beta \approx 2r_\Delta/r_p \ll 1$ if the mass splitting ratio is small ($r_\Delta \ll 1$) and $\alpha \approx 1$ and $\beta \approx 1/r_p \ll 1$ if the splitting is large ($r_\Delta \gg 1$). As DUNE probes HNLs in the mass range 100 MeV $\lesssim m_N \lesssim$ 2 GeV, this is the interesting regime for the comparison of $0\nu\beta\beta$ decay and DUNE. If we are in the small m_ν limit (so the HNL pair dominates $0\nu\beta\beta$ decay),

$$\begin{aligned} \left|m_{\beta\beta}^{\text{eff}}\right| &\approx \beta m_N |\Theta_{e1}|^2 \approx \frac{m_N}{r_p}\left(1 - \frac{1}{(1+r_\Delta)^2}\right)|\Theta_{e1}|^2 \\ &\approx \begin{cases} 2m_N r_\Delta |\Theta_{e1}|^2/r_p & (r_\Delta \ll 1) \\ m_N |\Theta_{e1}|^2/r_p & (r_\Delta \gg 1) \end{cases}, \end{aligned} \tag{4.43}$$

where we first approximate the factor β for $r_p \gg 1$ and then for the two different limits of r_Δ. For $r_\Delta \ll 1$, $\left|m_{\beta\beta}^{\text{eff}}\right|$ is given by the difference of the HNL contributions, which is proportional to r_Δ. The inverse $0\nu\beta\beta$ decay half-life in Eq. (4.31) therefore scales as $(T_{1/2}^{0\nu})^{-1} \propto (\Delta m_N)^2 |\Theta_{e1}|^4/m_N^4$. For $r_\Delta \gg 1$, $\left|m_{\beta\beta}^{\text{eff}}\right|$ is just the contribution of the lighter HNL, because the contribution of the heavier HNL is suppressed. The inverse $0\nu\beta\beta$ decay half-life then scales as $(T_{1/2}^{0\nu})^{-1} \propto |\Theta_{e1}|^4/m_N^2$. Equating Eq. (4.43) to $\left|m_{\beta\beta}^{\text{exp}}\right|$ and solving for $|\Theta_{e1}|^2$ (keeping an arbitrary value of r_Δ) gives

$$|\Theta_{e1}|^2 \approx \frac{m_N |m_{\beta\beta}^{\text{exp}}|}{\langle \mathbf{p}^2 \rangle} \frac{(1+r_\Delta)^2}{r_\Delta(2+r_\Delta)}. \tag{4.44}$$

This result will be used to compare $0\nu\beta\beta$ decay and direct searches at DUNE analytically in Sec. 4.5.

4.4 The Deep Underground Neutrino Experiment

Fixed target experiments are sensitive probes of HNL scenarios, which we intend to use in conjunction with $0\nu\beta\beta$ decay to explore the nature of an HNL pair. As seen in Fig. 4.4, $0\nu\beta\beta$ decay searches have the highest sensitivity to the active-sterile mixing in the 100 MeV to GeV mass range.

To explore the complementarity with direct searches, we focus on the upcoming experiment DUNE, which will be able to probe the direct production of HNLs in a similar mass range.

In this section we will first describe the production and subsequent decay of HNLs via SM channels in fixed target experiments. We will then examine in more detail the sensitivity of the DUNE near detector to HNLs produced from the decays of pions, kaons and D mesons. Using PYTHIA to simulate the momentum profiles of HNLs produced from these production channels, we will apply simplified geometric cuts on the decays of HNLs in the DUNE near detector to estimate the sensitivity of the experiment. DUNE will initially receive a 1.2 MW proton beam from the Main Injector accelerator at the Long Baseline Neutrino Facility (LBNF) at FNAL. The 120 GeV proton beam will impinge on a graphite target, which corresponds to pp collisions with the target at rest. DUNE will use two detectors; a far detector (FD) situated at a distance of 1300 km from the target and a smaller near detector (ND) at a distance of 574 m from the target [165].

For our analysis, we will model the ND with a simplified geometry; since our goal is to obtain the number of events from DUNE for a comparison with $0\nu\beta\beta$ decay, we do not include the exact geometry of the fiducial volume, which might result in $\mathcal{O}(1)$ corrections that can be obtained from a detailed analysis [165]. The basic schematic of our analysis is as follows: the proton beam hits the target, leading to the production of mesons from pp collisions, which travel and decay to SM particles and HNLs. We employ geometric cuts, where we demand that the produced HNL decays to charged tracks inside the fiducial volume, taken to have a length of 5 m along the beam axis and a cylindrical cross section. We demand that 2.44 events be detected to reject a null event rate with 90% C.L., assuming no

Meson P	π^+	K^+	$K^0_{L,S}$	D^0	D^+	D_s^+
Mesons/POT	2.8	0.24	0.18	6×10^{-5}	1.2×10^{-5}	3.3×10^{-6}

Table 4.3: Number of positively-charged and neutral pseudoscalar mesons produced per proton on target (POT) in DUNE, for a 120 GeV proton beam.

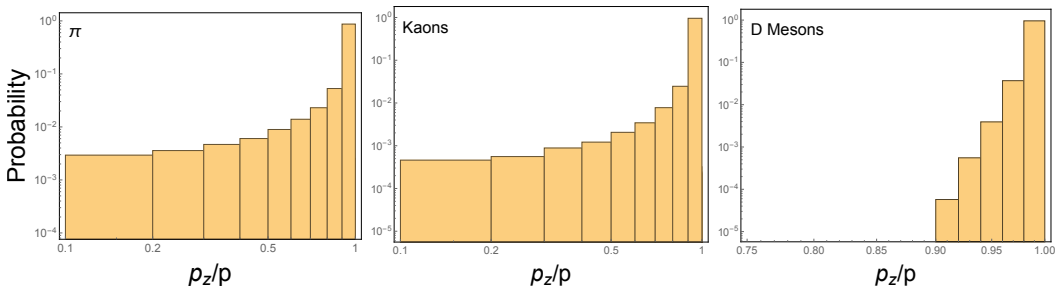

Figure 4.5: Distributions of momentum fractions along the beam axis for pions (left), kaons (centre) and D mesons (right) from PYTHIA-generated events.

background events and a Poisson-like distribution. We first limit our analysis to the case where the HNL mixes uniquely to the electron flavour ($\alpha = e$), while the more general case of mixing with all the three flavours will be explored later.

4.4.1 Meson Production at DUNE

Meson decays are the dominant source of HNLs in fixed target experiments. A variety of mesons, such as pions, kaons and D mesons are produced at DUNE via pp collisions, which we will now briefly describe in terms of their production fractions and momentum profiles.

Following the approach of Refs. [182–184], we show the production fractions of mesons at DUNE in Table 4.3, using the values given in the literature when in agreement with the values we extract from the simulation of meson production in PYTHIA (v. 8.307) [185].[2] In PYTHIA, the momentum distributions for mesons produced in DUNE are also extracted. In Fig. 4.5, we show the momentum distribution histograms for pions (left), kaons (centre) and D mesons (right), where it can be seen that the produced mesons are highly boosted along the beam direction.

[2] In the current literature, there exists a slight variation in the production fraction of pions from pp collisions at DUNE, varying roughly by an order of magnitude. A more systematic study would be needed to improve the accuracy, but it would not lead to a drastic change in the overall DUNE sensitivity (roughly at the 10% level), and would not affect our final results.

4.4.2 HNL Production from Meson Decays

After simulating the production of mesons at DUNE, we consider all possible decay modes of pions, kaons and D mesons leading to the production of HNLs. Meson decays to HNLs are calculated in the rest frame of the meson and then boosted to the lab frame using the momentum of the corresponding meson, extracted from PYTHIA.

Meson decays can be grouped into two categories, the first being purely leptonic two-body decays such as $P^+ \to e^+ N$, which have the generic branching fraction

$$\mathrm{Br}(P^+ \to e^+ N) \simeq \tau_P \frac{G_F^2 m_P^3}{8\pi} f_P^2 |U_{eN}|^2 |V_{q\bar{q}}|^2 \frac{m_N^2}{m_P^2} \left(1 - \frac{m_N^2}{m_P^2}\right)^2 , \tag{4.45}$$

where τ_P, f_P, m_P and $V_{q\bar{q}}$ correspond to the meson lifetime, decay constant, mass, and CKM mixing matrix element (depending on valence quark content of the meson), respectively [186]. The second category contains three-body semi-leptonic decays, which can be competitive to the two-body channels, as seen in Fig. 4.6. This is mainly attributed to the absence of CKM or chirality-flip suppressions, which compensates for the smaller phase space [186, 187]. The formulae for three-body decays require the use of form factors and depend on whether the daughter meson is pseudoscalar or vector. For the decay into a pseudoscalar meson, the branching fraction is given by

$$\mathrm{Br}(P^+ \to P'^0 e^+ N) \propto \tau_P \frac{G_F^2 m_P^5}{64\pi^3} |V_{qq'}|^2 |U_{eN}|^2 f(\mathscr{I}_P) . \tag{4.46}$$

For the decay into a vector meson, the branching fraction becomes,

$$\mathrm{Br}(P^+ \to V^0 e^+ N) \propto \tau_P \frac{G_F^2 m_P^7}{64\pi^3 m_V^2} |V_{qq'}|^2 |U_{eN}|^2 f(\mathscr{I}_V) , \tag{4.47}$$

where $f(\mathscr{I}_P)$ and $f(\mathscr{I}_V)$ are functions that depend on the meson coupling constants and form factors, respectively [187].

As shown in Fig. 4.6, for HNL masses below the pion threshold, $\pi^+ \to e^+ N$

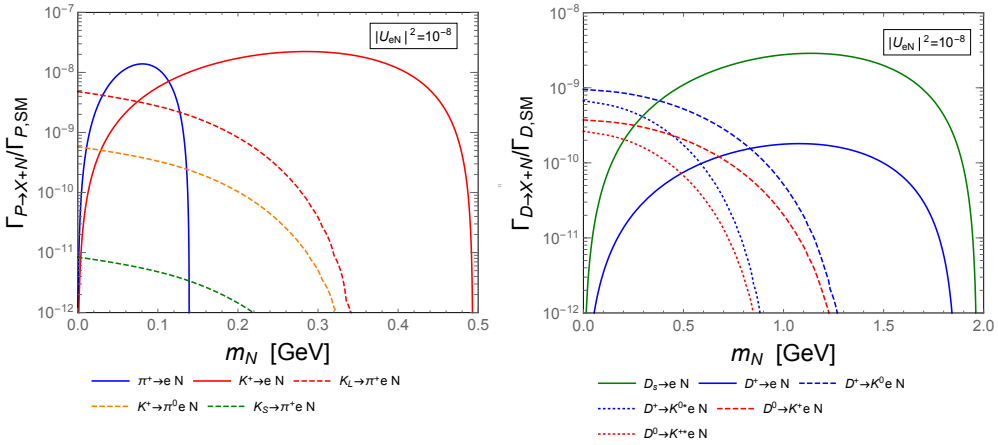

Figure 4.6: Branching fractions of decays of pions and kaons (left) and D mesons (right) to HNLs, with a value of $|U_{eN}|^2 = 10^{-8}$ for the active-sterile mixing with the electron flavour.

(solid blue) is the dominant production channel, which slowly gives way to $K^+ \to e^+N$ (solid red) up to the kaon threshold. For heavier HNLs above the kaon but below the charm threshold, production via D meson decays is dominant, with $D_s^+ \to e^+N$ (solid green) being the most important channel.

4.4.3 HNL Decays

HNLs are unstable, and will therefore decay to SM particles via charged- or neutral-current processes, suppressed via the active-sterile mixing $|U_{eN}|^2$. These decays proceed via off-shell $W^\pm/Z$ bosons, which means that they can be long-lived, with decay lengths in the tens of meters or larger, and thus are very well suited to being explored at fixed target experiments. We will briefly discuss these SM decay channels of HNLs here, a detailed discussion can be found in [183, 188]. In our framework with only one HNL species that couples with the first generation only, we have the corresponding decay channels of HNLs as:

1) $N \to \nu_e \ell_2^- \ell_2^+$: In this process, one ν_e participates. For this case, charged (only for electron flavor) as well as neutral current (for any $\ell_2 = e, \mu, \tau$) interactions are present. The corresponding decay width is (with $x_{\ell_2} = m_{\ell_2}/m_N$),

$$\Gamma^{\nu_e \ell_2^- \ell_2^+} = |U_{eN}|^2 \frac{G_F^2 m_N^5}{96\pi^3} \left[\left(C_1 + 2\sin^2\theta_w \delta_{e,\ell_2}\right) f_1(x_{\ell_2}) + \left(C_2 + \sin^2\theta_w \delta_{e,\ell_2}\right) f_2(x_{\ell_2}) \right], \tag{4.48}$$

where

$$C_1 = \frac{1}{4}(1-4\sin^2\theta_{\rm w}+8\sin^4\theta_{\rm w}), \quad C_2 = \frac{1}{2}(-\sin^2\theta_{\rm w}+2\sin^4\theta_{\rm w}), \tag{4.49}$$

and the functions defined as

$$\begin{aligned} f_1(x) &= (1-14x^2-2x^4-12x^6)\sqrt{1-4x^2}+12x^4(x^4-1)L(x) \\ f_2(x) &= 4[x^2(2+10x^2-12x^4)\sqrt{1-4x^2}+6x^4(1-2x^2+2x^4)L(x)], \end{aligned} \tag{4.50}$$

with

$$L(x) = \ln\left(\frac{1-3x^2-(1-x^2)\sqrt{1-4x^2}}{x^2(1+\sqrt{1-4x^2})}\right). \tag{4.51}$$

2) $\underline{N \to e^-\ell_2^+\nu_{\ell_2}}$: In this process, one of the participating charged lepton is e^- itself. Now, in this situation only charged current interaction is allowed and $\ell_2 = \mu, \tau$. The corresponding decay width is (with $x_M \equiv \max\{\mathrm{x_e}, \mathrm{x}_{\ell_2}\} = \mathrm{x}_{\ell_2}$),

$$\Gamma^{e^-\ell_2^+\nu_{\ell_2}} = |U_{eN}|^2\frac{G_F^2 m_N^5}{192\pi^3}(1-8x_M^2+8x_M^6-x_M^8-12x_M^4 ln(x_M^2)). \tag{4.52}$$

3) $\underline{N \to \nu_e\nu_{\ell_2}\bar{\nu}_{\ell_2}}$: Here only neutral current interaction will be present and $\ell_2 = e, \mu, \tau$. The corresponding decay width can be written as,

$$\Gamma^{\nu_e\nu_{\ell_2}\bar{\nu}_{\ell_2}} = \frac{G_F^2}{96\pi^3}|U_{eN}|^2 m_N^5. \tag{4.53}$$

4) $\underline{N \to P\nu_e}$: Here P corresponds to neutral pseudoscalar meson i.e., π^0, K^0, η, η'. The corresponding decay width is

$$\Gamma^{P\nu_e} = \frac{G_F^2 m_N^3}{32\pi} f_P^2 |U_{eN}|^2 (1-x_P^2)^2, \tag{4.54}$$

with f_P as the decay constants of the corresponding neutral meson while $x_P \equiv m_P/m_N$.

5) $\underline{N \to P^+e^-}$: Here all the relevant charged pseudoscalar mesons like $\pi^\pm, K^\pm, D^\pm, D_s^\pm$

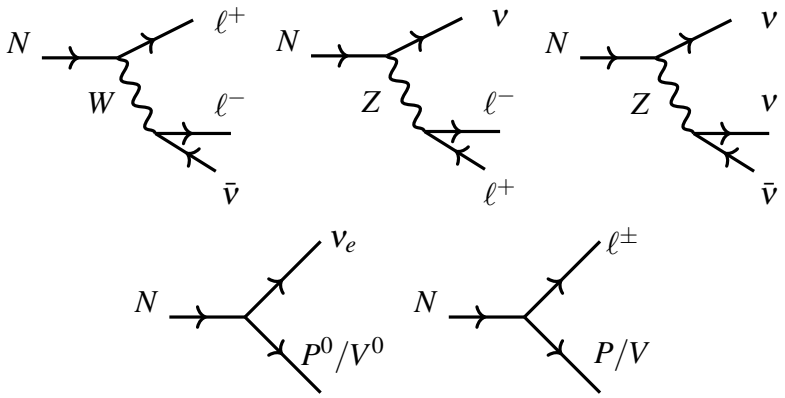

Figure 4.7: HNL decay diagrams which includes leptonic decays: $N \to e^-\ell^+\bar{\nu}_\ell$ (top left), $N \to \nu_e\ell^-\ell^+$ (top middle), $N \to \nu_e\nu_\ell\bar{\nu}_\ell$ (top right) and hadronic decays: $N \to P^0(V^0)\nu_e$ (bottom left), $N \to P(V)\ell^+(\ell^-)$ (bottom right).

will contribute. The decay width is

$$\Gamma^{P^+e^-} = \frac{G_F^2 m_N^3}{16\pi} f_P^2 |U_{eN}|^2 |V_{qq'}|^2 \lambda^{1/2}(1,x_p^2,x_e^2)[1-x_P^2-x_e^2(2+x_P^2-x_e^2)]. \quad (4.55)$$

6) $\underline{N \to V\nu_e}$: In this decay channel the neutral vector meson V like $\rho, \omega, \phi, K^{*0}$ will be present, the decay width here can be written as

$$\Gamma^{V\nu_e} = \frac{G_F^2 m_N^3}{32\pi m_V^2} f_V^2 g_V^2 |U_{eN}|^2 (1+2x_V^2)(1-x_V^2)^2. \quad (4.56)$$

7) $\underline{N \to V^+e^-}$: Here the relevant charged vector meson will be $\rho^\pm, K^{*,\pm}$, the decay width in this channel can be written as

$$\Gamma^{V^+e^-} = \frac{G_F^2 m_N^3}{16\pi m_{V^\pm}^2} f_V^2 |U_{eN}|^2 |V_{qq'}|^2 \lambda^{1/2}(1,x_V^2,x_e^2)[(1-x_V^2)(1+2x_V^2)+x_e^2(x_V^2+x_e^2-2)]. \quad (4.57)$$

All the decay diagrams are shown in Fig. 4.7 and the total decay width arising from Majorana HNL decaying into purely SM particles can be written as,

$$\Gamma^{N\to \mathrm{SM}} = \sum_{\ell_1,\ell_2} \Gamma^{\nu_e\ell_2^-\ell_2^+} + \sum_{\ell_2=\mu,\tau} 2\Gamma^{e^-\ell_2^+\nu_{\ell_2}} + \sum_{\ell_2} \Gamma^{\nu_e\nu_{\ell_2}\bar{\nu}_{\ell_2}} + \sum_P \Gamma^{P\nu_e} + \sum_P 2\Gamma^{P^+e^-} + \sum_V \Gamma^{V\nu_e} + \sum_V 2\Gamma^{V^+e^-}. \quad (4.58)$$

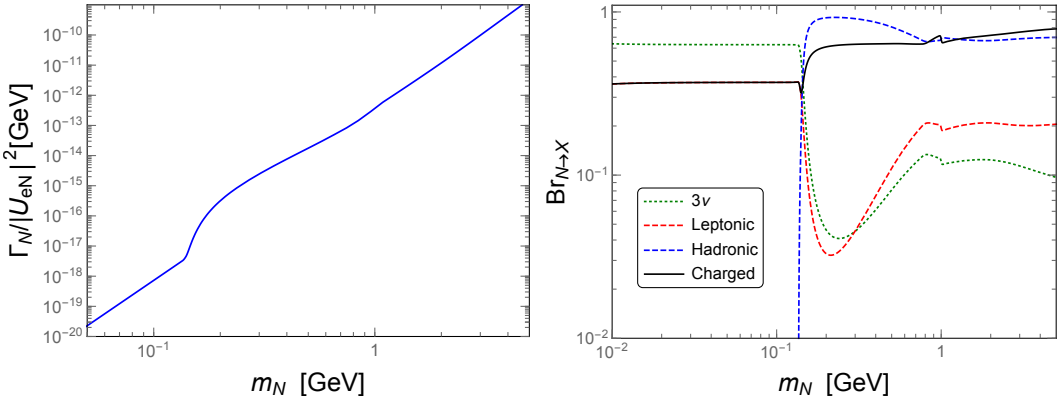

Figure 4.8: (Left) Total HNL decay width, normalised by the active-sterile mixing $|U_{eN}|^2$. (Right) branching fractions of an HNL to 3ν (dashed green), other combinations of leptons (dashed red), and hadronic states (dashed blue). The black curve corresponds to the total branching fraction of decays to charged tracks (leptonic or semi-leptonic).

For Majorana HNL, the $\Delta L = 0$ process $N \to P^+ e^-$ as well as its charge conjugate process with $|\Delta L| = 2$ i.e., $N \to P^- e^+$ are possible with same width $\Gamma^{P^+ e^-}$. That is why we have included a factor of 2 associated with this decay width. Similar argument applies for the other decay modes like $N \to e^- \ell_2^+ \nu_{\ell_2}$ and $N \to V^+ e^-$.

Schematically, the charged-current interactions result in processes such as $N \to e^+ e^- \nu$ and $N \to e^- u\bar{d}$, depending on the leptons/quarks. The neutral-current mediated decays lead to processes of the form of $N \to \nu e^+ e^-$ and $N \to \nu q\bar{q}$. Both charged-current and neutral-current mediated processes interfere for processes involving the same generations, viz. the decay modes $N \to 3\nu$ and $N \to \nu e^+ e^-$.

Below the pion threshold, the invisible decay $N \to 3\nu$ is the dominant decay mode. Above the pion threshold and below 1.5 GeV, the quarks generally confine into hadronic states, and the resultant single meson hadronic channels, corresponding to $N \to e^- P^+$ (charged-current), $N \to \nu P^0$ and $N \to \nu V^0$ (neutral-current) are important. The decay mode to a single pion makes up a large proportion of the hadronic decay modes.

In the left hand side of Fig. 4.8, we depict the total HNL decay width Γ_N, normalised to the active-sterile mixing $|U_{eN}|^2$. In Fig. 4.8 (right), we show the relevant branching fractions, including the branching fraction of invisible decays to three neutrinos (solid green) and charged final states (solid black), the latter being

a requirement to observe tracks in the DUNE ND. Both the total HNL decay width Γ_N and the branching fraction to charged tracks are needed to estimate the DUNE sensitivity.

4.4.4 Majorana vs. Quasi-Dirac HNLs at DUNE

In the literature, the distinction between Majorana and quasi-Dirac HNLs in beam dump and collider experiments has been studied in detail [189–191]. Naively, for Majorana and quasi-Dirac HNLs with the same active-sterile mixing $|U_{eN}|^2$, one would expect the rate for Majorana HNL decays to charged final-states to be twice that for a quasi-Dirac HNL in DUNE. This is because a Majorana HNL produced from the decay $K^+ \to e^+ N$ can decay via both the lepton number conserving (LNC) and LNV channels $N \to e^- \pi^+$ and $N \to e^+ \pi^-$, respectively, while a quasi-Dirac HNL with a vanishing mass splitting can only decay via $N \to e^- \pi^+$.

However, when the mass splitting is non-zero, oscillations with a frequency controlled by $\Delta m_N = m_N r_\Delta$ can occur between the Majorana pair forming the quasi-Dirac HNL. The appearance of these oscillations depends on whether the HNL decay is prompt or long-lived. If the HNL decays promptly, i.e. $\Gamma_N \tau \gg 1$, an experiment can only observe the time-integrated rates for the LNC and LNV decay modes. The ratio of LNV to LNC events in the detector is given by

$$R_{ll} = \frac{m_N^2 r_\Delta^2}{2\Gamma_N^2 + m_N^2 r_\Delta^2}\,, \tag{4.59}$$

which can range from 0 and 1 depending on the relative sizes of the HNL mass splitting and decay width [192, 193].

To decay inside the DUNE ND, however, the quasi-Dirac HNL must be long-lived. For the baseline $L = 574$ m, we require an HNL lifetime,

$$\tau = \frac{L}{\beta\gamma} \sim \frac{2 \times 10^{-6}\ \text{s}}{\beta\gamma}\,, \tag{4.60}$$

where $\beta\gamma = p_{N_z}/m_N$ is the HNL boost factor. The signal in the detector now depends on the relative sizes of $m_N r_\Delta$ and τ. If the mass splitting is such that

$m_N r_\Delta \tau \gg 2\pi$, or

$$r_\Delta \gg \frac{2\pi}{m_N}\frac{1}{\tau} \sim 10^{-17}\left(\frac{400\text{ MeV}}{m_N}\right)\left(\frac{574\text{ m}}{L}\right)\beta\gamma, \tag{4.61}$$

the oscillations must be averaged out, yielding an equal rate for LNC and LNV decays. Only when the mass splitting is extremely small will the LNV decay modes be suppressed for quasi-Dirac HNLs. For the mass splittings r_Δ required to produce an observable $0\nu\beta\beta$ decay rate, as explored in the Sec. 4.5, we must include both LNC and LNV decay modes to estimate the DUNE sensitivity. In the following, we consider the sensitivity of DUNE to a single Majorana HNL. For a quasi-Dirac HNL, we would need to add the contributions of two Majorana states.

4.4.5 DUNE Acceptance

We will now describe our approach to calculating the expected number of signal events in the DUNE ND. The detector is located at a distance of $L = 574$ m from the target, with a transverse cross-section of $A_{\text{det}} = 12\text{ m}^2$ and a depth of $\Delta\ell_{\text{det}} = 5$ m along the beam axis [194]. Instead of using the cuboidal geometry of the detector, we use a simplified cylindrical geometry to model the experimental setup. Keeping the beam axis the same and defining an angular aperture θ_{det} for the transverse cross-section,

$$\theta_{\text{det}} = \tan^{-1}\left(\frac{\langle x_{\text{det}}\rangle}{\langle L\rangle}\right) \sim \frac{3.8\text{ m}}{576.5\text{ m}} \sim 7\times 10^{-3}, \tag{4.62}$$

where $\langle x_{\text{det}}\rangle$ corresponds to the average transverse width of the fiducial volume and $\langle L\rangle$ is the mean distance along the beam axis from the target to the fiducial volume.

As described above, we first use PYTHIA (v. 8.307) [185] to simulate the production of mesons from a pp collision at $\sqrt{s} = 15$ GeV, extracting the four-momenta profile to define the lab frame for each event. The HNLs are produced from the decays of these simulated mesons at rest, and then boosted corresponding to the extracted meson momentum. The HNLs with angular distribution smaller than θ_{det} will end up in the the fiducial volume, and hence can contribute to the event rate if they decay to a charged final state. The HNLs with larger transverse angles will not

enter the fiducial volume and therefore not contribute to the event rate, regardless of the decay mode. Putting this together, the total number of signal events is

$$N_{\rm sig} = N_P \cdot {\rm Br}(P \to N) \cdot {\rm Br}(N \to {\rm charged}) \cdot \varepsilon_{\rm geo}\,, \tag{4.63}$$

where N_P is the relevant production fraction in Table 4.3 multiplied by the total number of protons on target $N_{\rm POT}$. The geometrical efficiency is given by

$$\varepsilon_{\rm geo} = \frac{1}{N_{\rm tot}} \sum_{\rm cut} e^{-\frac{m_N \Gamma_N}{p_{N_z}} \langle L \rangle} \left(1 - e^{-\frac{m_N \Gamma_N}{p_{N_z}} \Delta \ell_{\rm det}}\right), \tag{4.64}$$

where $N_{\rm tot}$ is the total number of simulated events, p_{N_z} is the lab-frame momentum of the HNL along the beam axis, and Γ_N is the total decay width of the HNL. We use $N_{\rm POT} = 6.6 \times 10^{21}$ protons on target, which corresponds to a run-time of 6 years [165]. In Eq. (4.64), 'cut' refers to the HNLs which pass through the fiducial volume, i.e., all HNLs that have an angular momenta profile smaller than the angle $\theta_{\rm det}$,

$$\frac{p_{N_T}}{p_{N_z}} < \theta_{\rm det} \sim 7 \times 10^{-3}\,, \tag{4.65}$$

where p_{N_T} is the lab-frame momentum of the HNL transverse to the beam axis. The geometic efficiency $\varepsilon_{\rm geo}$ therefore corresponds to the requirement that the HNL decays inside the fiducial volume.

The analysis above only considers HNL production and decay via the electron neutrino mixing, but this can be easily generalised to the mixing to all three active neutrinos. As an example, we consider arbitrary mixing strengths to both electron and muon neutrinos[3]. The basic schematics of the calculation are similar, with HNL production and decay proceeding via both $|U_{eN}|^2$ and $|U_{\mu N}|^2$. In our simulation, we fix $m_N = 800$ MeV as a benchmark scenario and calculate the sensitivity for arbitrary $|U_{eN}|^2$ and $|U_{\mu N}|^2$. At this HNL mass, the dominant production channels are $D_s^+ \to \ell_\alpha^+ N$ ($\alpha = e, \mu$) and HNL decays to pions have the largest branching

[3]We neglect the active-sterile mixing to tau neutrinos as HNL decays to taus are forbidden for the HNL masses considered.

Experiment	Beam type	$\Delta A_{\rm det}$ [m^2]	$\Delta \ell_{\rm det}$ [m]	$\ell_{\rm det}$ [m]	$N_{\rm POT}$
DUNE	120 GeV, p	12	5	574	6.6×10^{21}
SHiP	400 GeV, p	50	45	50	2.0×10^{20}

Table 4.4: Brief description of the upcoming fixed target experimental facilities, DUNE and SHiP, considered in our analysis. The beam type corresponds to a proton beam of given energy impinging on the target nuclei [194].

ratios, $N \to \ell_\alpha^\mp \pi^\pm$ ($\alpha = e, \mu$). As expected, the inclusion of the muon channels leads to an enhanced signal rate; the behaviour of the electron and muon channels are also similar, since both charged leptons can be considered massless compared to an HNL of mass 800 MeV. As we will explore in Sec. 4.5.7, HNL decays such as $N \to \ell_\alpha^\mp \pi^\pm$ that only proceed via one of the mixing strengths $|U_{eN}|^2$ and $|U_{\mu N}|^2$ can be used as useful observables of the phenomenological model in Sec. 4.2.

We emphasise that the methods of this analysis are not restricted to the DUNE setup, and can be extended to other fixed target experimental facilities. The generic scheme would require the relevant proton beam energy and the associated meson production fractions, as well as a new geometrical cut for the specific experimental setup. Putting these together, one can then estimate the sensitivity using Eq. (4.63). To this end, we have modified our analysis for the well-studied SHiP proposal by changing the incoming proton beam energy to 400 GeV as shown in Table 4.4, the number of protons on target to 2×10^{20} and adjusting the detector geometry to a distance of 50 m from the beam dump and a fiducial volume of length 45 m and transverse cross section of 5×10 m^2 [194]. Our estimated upper bound on $|U_{eN}|^2$ is in good agreement with the results of [166], and can be improved further by introducing an additional attenuation factor to account for the exact geometrical cut (as the fiducial volume is a much longer length compared to DUNE). The attenuation factor quantifies the intensity or amplitude of a signal diminishes before reaching the detector. This is influenced by the medium through which the signal travels and the distance between the source and the detector. Note that we do not use any ad-hoc factors for DUNE since the detector length is small and so our assumed cylindrical geometry works well.

4.5 Probing HNLs with DUNE and LEGEND-1000

We will begin this section with an analytical comparison of $0\nu\beta\beta$ decay and the direct production of HNLs in DUNE. Using the approximate results for the $0\nu\beta\beta$ decay half-life in Sec. 4.3.2 and the DUNE ND event rate, we will estimate the HNL mass splitting $r_\Delta = \Delta m_N/m_N$ implied by the observation of $0\nu\beta\beta$ decay and an HNL-like DUNE signal. This will be done in the optimistic scenario where the light neutrino mass does not saturate the observed $0\nu\beta\beta$ decay half-life and the DUNE event rate is large.

Following on from these estimates, we will perform a more detailed Bayesian analysis, using Markov chain Monte Carlo (MCMC) methods to sample the statistical likelihoods, given the HNL pair hypothesis, of positive signals in a $0\nu\beta\beta$ decay experiment and the DUNE ND. This will allow us to identify the 68% and 95% credible regions in the $1+2$ model parameter space for four benchmark scenarios. We will also consider the sensitivities in the scenario where $0\nu\beta\beta$ decay is observed but no HNL-like events are seen at DUNE, and vice versa. Finally, we will derive excluded regions in the $1+2$ model parameter space if neither $0\nu\beta\beta$ decay nor HNL-like DUNE events are seen. To extend, we will perform a Bayesian analysis implementing the current active neutrino data in the complete $3+2$ model with a massless lightest neutrino.

In the following, we will consider the upcoming search for $0\nu\beta\beta$ decay by the LEGEND experiment [195], which will use a ^{76}Ge detector to provide an excellent energy resolution and low intrinsic background. The next phase of the experiment will be LEGEND-1000 [96], which increases the mass of ^{76}Ge detector to 1 ton and an exposure leading to a sensitivity of $T^{0\nu}_{1/2} = 10^{28}$ y. We assume that DUNE collects data for 6 years in the neutrino beam mode, collecting $N_{\rm POT} = 6.6\times10^{21}$.

4.5.1 Analytical Comparison

In Fig. 4.9, we illustrate two signal scenarios in $0\nu\beta\beta$ decay and direct HNL searches. The plots on the upper (lower) row assume a $0\nu\beta\beta$ decay half-life of 10^{28} years from the LEGEND experiment and 100 (300) HNL-like events at DUNE. Considering the constraints on the simple $1+2$ model, on the upper row we take the

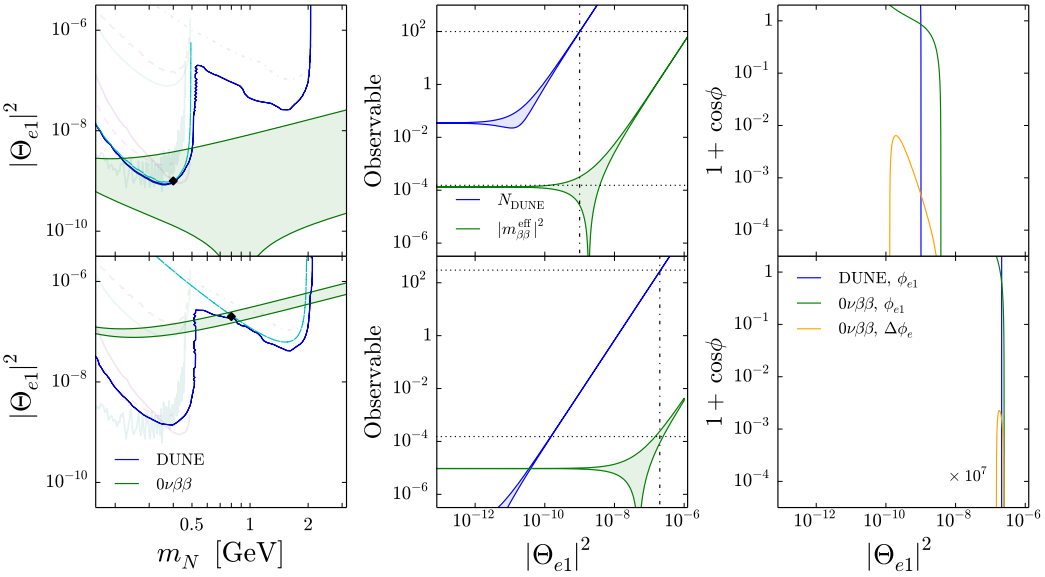

Figure 4.9: Constraints in the $1+2$ model parameter space if both $0\nu\beta\beta$ decay and HNL-like events at DUNE are observed, for $T_{1/2}^{0\nu} = 10^{28}$ yr, $N_{\rm DUNE} = 100$, $r_\Delta = 0.1$ (above) and $T_{1/2}^{0\nu} = 10^{28}$ yr, $N_{\rm DUNE} = 300$, $r_\Delta = 1.5\times10^{-3}$ (below). Left: Regions in the $(m_N, |\Theta_{e1}|^2)$ plane from signals at DUNE (blue) and $0\nu\beta\beta$ decay (green), marginalising over $\cos\phi_{e1}$. The regions roughly overlap at the benchmark HNL masses (black diamond) $m_N = 400$ MeV (above) and $m_N = 800$ MeV (below). Middle: $N_{\rm DUNE}$ (blue) and $|m_{\beta\beta}^{\rm eff}|^2$ (green) as a function of $|\Theta_{e1}|^2$. Right: Implied values of $\cos\phi_{e1}$ from DUNE (blue) and $0\nu\beta\beta$ decay (green) signals as a function of $|\Theta_{e1}|^2$. Also shown is the implied value of $\cos\Delta\phi_{e1}$ from $0\nu\beta\beta$ decay (yellow) as a function of $|\Theta_{e1}|^2$.

light neutrino mass to be $m_\nu = 10^{-1.9}$ eV, which marginally saturates the observed $0\nu\beta\beta$ decay half-life. Below, we instead take $m_\nu = 10^{-2.5}$ eV, which does not saturate the half-life and therefore implies a dominant HNL contribution, as discussed in Sec. 4.3.

The two plots to the left of Fig. 4.9 show the regions in the $(m_N, |\Theta_{e1}|^2)$ plane implied by the positive $0\nu\beta\beta$ decay (green region) and DUNE (blue region) signals, with the spread from varying $\cos\phi_{e1}$ (only visible for $0\nu\beta\beta$ decay). In the $1+2$ model, the last relevant parameter is the mass splitting r_Δ; in the upper (lower) row, we take $r_\Delta = 0.1$ ($r_\Delta = 1.5\times10^{-3}$) which results in the $0\nu\beta\beta$ decay and DUNE regions overlapping at the benchmark point of $m_N = 400$ MeV (800 MeV) and $|\Theta_{e1}|^2 = 10^{-9}$ (2×10^{-7}), just below the current upper bound from T2K (CHARM).

We also show the DUNE region using an approximate formula for the number

of signal events induced by the HNL pair in the DUNE ND (dashed cyan). For $m_N = 400$ MeV (800 MeV), the dominant HNL production channel and decay mode to charged final states are $K^+ \to e^+ N$ ($D_s^+ \to e^+ N$) and $N \to e^\mp \pi^\pm$, respectively. We can then estimate the number of events as

$$N_{\rm DUNE} \approx C_{\rm det}^P \left[\mathscr{A}_{PP'}(m_N) |\Theta_{e1}|^4 + \mathscr{A}_{PP'}\big(m_N(1+r_\Delta)\big) \frac{|r_\nu + |\Theta_{e1}|^2 e^{i\phi_{e1}}|^2}{(1+r_\Delta)^2} \right], \quad (4.66)$$

where we have used the expression for $|\Theta_{e2}|^2$ in the $1+2$ model in Eq. (4.20) and

$$\mathscr{A}_{PP'}(m_N) \equiv \frac{m_N \Gamma_N}{|U_{eN}|^4} {\rm Br}(P^+ \to e^+ N) {\rm Br}(N \to e^\pm P'^\mp), \quad (4.67)$$

where ${\rm Br}(P^+ \to e^+ N)$ and ${\rm Br}(N \to e^\pm P'^\mp)$ are given in section 4.4.3. For convenience, we have introduced the factor

$$C_{\rm det}^P \equiv N_P \varepsilon_{\rm geo} \frac{\Delta \ell_{\rm det} \varepsilon_{\rm det}}{\langle p_{N_z} \rangle} = N_P \frac{\langle p_{N_z} \rangle}{\langle p_{N_T} \rangle^2} \frac{V_{\rm det} \varepsilon_{\rm det}}{L^2}, \quad (4.68)$$

where $V_{\rm det}$ is the fiducial volume and we use the estimate $\varepsilon_{\rm geo} = \langle p_{N_z} \rangle^2 / \langle p_{N_T} \rangle^2 \times A_{\rm det}/L^2$ for the geometric efficiency, with $\langle p_{N_z} \rangle$ and $\langle p_{N_T} \rangle$ the average longitudinal and transvese HNL momenta. For $N_{\rm DUNE}^{\rm exp} = 100$ (300), we use Eq. (4.66) to plot the dashed cyan lines in Fig. 4.9. The expressions above are simplified if we consider the limit $|\Theta_{e1}|^2 \gg r_\nu$, i.e., the *inverse seesaw* regime. This allows to pull out a factor of $|\Theta_{e1}|^4$ in Eq. (4.66) and write

$$|\Theta_{e1}|^2 = \sqrt{\frac{N_{\rm DUNE}}{C_{\rm det}^P \mathscr{B}_{PP'}}} \quad (|\Theta_{e1}|^2 \gg r_\nu), \quad \mathscr{B}_{PP'} \equiv \mathscr{A}_{PP'}(m_N) + \frac{\mathscr{A}_{PP'}\big(m_N(1+r_\Delta)\big)}{(1+r_\Delta)^2}. \quad (4.69)$$

In the limit of small mass splitting between the HNL pair, $r_\Delta \ll 1$, the function simplifies to $\mathscr{B}_{PP'} \approx 2\mathscr{A}_{PP'}(m_N)$. We see that Eq. (4.69) is effectively independent of ϕ_{e1}.

The two plots in the centre of Fig. 4.9 show the value of $N_{\rm DUNE}$ (using the approximate formula in Eq. (4.66)) and $|m_{\beta\beta}^{\rm eff}|^2$ as a function of $|\Theta_{e1}|^2$, for

$m_N = 400$ MeV (800 MeV) and allowing the value of $\cos\phi_{e1}$ to vary. The two horizontal dashed lines indicate the measured experimental values $N_{\rm DUNE}^{\rm exp}$ and $|m_{\beta\beta}^{\rm exp}|^2$, while the vertical dot-dashed line shows the value of $|\Theta_{e1}|^2$ compatible with the two measurements. Finally, the two plots to the right of Fig. 4.9 show the values of $1+\cos\phi_{e1}$ determined from the $0\nu\beta\beta$ decay and DUNE signals using Eqs. (4.39) and (4.66). It is evident that DUNE has little sensitivity to the value of $\cos\phi_{e1}$. The crossing point of these curves indicates the compatible values of $|\Theta_{e1}|^2$ and ϕ_{e1} (for given values of m_ν, m_N and r_Δ). We also show the values of $1+\cos\Delta\phi_e$, in the lower plot being multiplied by a factor of 10^7 to be visible. We see that $\cos\Delta\phi_e \approx -1$ is being probed in both scenarios.

In the scenario where the light neutrino mass does not saturate $0\nu\beta\beta$ decay and the HNL-like event rate in DUNE is large, we will now show that the value of r_Δ being probed by both experiments is approximately insensitive to the value of $\cos\phi_{e1}$. Using Eq. (4.69), the active-sterile mixing implied by an observation at DUNE is given approximately by

$$|\Theta_{e1}|^2 \approx 2\times10^{-7}\left(\frac{N_{\rm DUNE}^{\rm exp}}{300}\right)^{1/2}\left(\frac{6.6\times10^{21}}{N_{\rm POT}}\right)^{1/2}\left(\frac{5\text{ m}}{\Delta\ell_{\rm det}}\right)^{1/2}\left(\frac{7.3\times10^3\text{ MeV}^2}{\mathscr{A}_{PP'}(m_N)}\right)^{1/2}, \tag{4.70}$$

where we have used $\mathscr{A}_{D_s\pi}(800\text{ MeV}) = 7.3\times10^3$ MeV^2. With this active-sterile mixing, we can then solve Eq. (4.44) for r_Δ. If the value of $N_{\rm DUNE}^{\rm det}$ is large, and therefore the implied value of r_Δ small, we obtain the approximate result:

$$r_\Delta \sim 1.5\times10^{-3}\left(\frac{2\times10^{-7}}{|\Theta_{e1}|^2}\right)\left(\frac{m_N}{800\text{ MeV}}\right)\left(\frac{10^{28}\text{ yr}}{T_{1/2}^{0\nu}}\right)^{1/2}. \tag{4.71}$$

This estimate is not possible if the light neutrino mass *does* almost saturate the observed $0\nu\beta\beta$ decay half-life, because there is then much more freedom in the value of $\cos\phi_{e1}$. To better understand this region of the parameter space, we perform a statistical analysis of the experimental likelihoods in the next section.

4.5.2 General Statistical Analysis

To incorporate statistical uncertainties, we perform a simple Bayesian analysis based on a combined likelihood for DUNE and LEGEND-1000. We treat both as simple counting experiments and to avoid running an ensemble of mock experiments, we take the continuous version of the Poisson distribution,

$$\text{Poisson}\left(n_{\text{obs}} \mid \lambda_{\text{sig}}(\theta)+\lambda_{\text{bkg}}(\theta)\right) \propto \frac{\left(\lambda_{\text{sig}}(\theta)+\lambda_{\text{bkg}}(\theta)\right)^{n_{\text{obs}}} e^{-\left(\lambda_{\text{sig}}(\theta)+\lambda_{\text{bkg}}(\theta)\right)}}{\Gamma\left(n_{\text{obs}}+1\right)}. \tag{4.72}$$

Here, n_{obs} is the 'observed' number of events, expected in a hypothetical benchmark scenario (or $n_{\text{obs}} = 0$, if the experiment is assumed to see no signal). The expected number of signal and background events given a theoretically-predicted parameter choice θ are $\lambda_{\text{sig}}(\theta)$ and λ_{bkg}, respectively.

For $0\nu\beta\beta$ decay, the number of signal events in the $1+2$ model, with the parameters $\theta = \{m_\nu, m_N, r_\Delta, |\Theta_{e1}|^2, \phi_{e1}\}$, can be calculated as

$$\lambda^{0\nu}_{\text{sig}}(\theta) = \frac{\ln 2 \cdot N_A \cdot \mathscr{E}}{m_A \cdot T^{0\nu}_{1/2}(\theta)}, \tag{4.73}$$

where N_A is Avogadro's number, m_A is the average molar mass of the $0\nu\beta\beta$ decaying material ($m_A = 75.74$ g/mol for ^{76}Ge), and $\mathscr{E}$ is the sensitive exposure of the detector, with $\mathscr{E} = 6632$ kg·yr for LEGEND-1000 [116, 196]. The half-life is calculated from Eq. (4.25) using the full interpolating formula discussed in Sec. 4.3. The background event rate is $\lambda^{0\nu}_{\text{bkg}} = \mathscr{E} \cdot \mathscr{B}$, where $\mathscr{B}$ is the sensitive background, giving $\lambda^{0\nu}_{\text{bkg}} = 0.4$ events for LEGEND-1000. Although the $0\nu\beta\beta$ decay NMEs have considerable discrepancies between different nuclear structure calculations and it may be possible that the nuclear axial coupling is quenched [197], we assume that there are no theoretical uncertainties to explore the full potential of future $0\nu\beta\beta$ decay searches.

For DUNE, we use the sensitivity formula derived in Sec. 4.4. For the expected number of signal events in the $1+2$ model, we incoherently add up the contribution

Scenario	m_N [MeV]	$\lvert\Theta_{e1}\rvert^2$	r_Δ	m_ν [eV]	$\lambda_{\rm DUNE}$	$\lambda_{0\nu}$	$T^{0\nu}_{1/2}$ [yr]
1	400	$10^{-9.0}$	$10^{-0.5}$	$10^{-1.9}$	76.7	5.94	$10^{27.8}$
2	400	$10^{-9.0}$	$10^{-0.5}$	$10^{-2.5}$	76.7	2.73	$10^{28.1}$
3	800	$10^{-6.7}$	$10^{-2.5}$	$10^{-1.9}$	325	15.5	$10^{27.4}$
4	800	$10^{-6.7}$	$10^{-2.5}$	$10^{-2.5}$	325	12.3	$10^{27.5}$

Table 4.5: Benchmark scenarios for the light neutrino mass m_ν, the HNL mass m_N, the active-sterile mixing strength $|\Theta_{e1}|^2$ and the HNL mass splitting r_Δ adopted in our statistical analysis. In all cases, the HNL phase parameter is $\cos\phi_{e1} = 0$. Also given are the expected number of signal events at DUNE, $\lambda_{\rm DUNE}$, and LEGEND-1000, $\lambda_{0\nu}$, as well as the corresponding half-life for the latter, $T^{0\nu}_{1/2}$.

Eq. (4.63) from each HNL separately, i.e.,

$$\lambda^{\rm DUNE}_{\rm sig}(\theta) = N_{\rm sig}(m_N, |\Theta_{e1}|^2) + N_{\rm sig}\left(m_N(1+r_\Delta), |\Theta_{e2}|^2\right) , \tag{4.74}$$

where $|\Theta_{e2}|^2$ is given by Eq. (4.20) as a function of m_ν, m_N, r_Δ $|\Theta_{e2}|^2$ and $\cos\phi_{e1}$. We assume a negligible background for HNL-like events in the DUNE ND ($\lambda^{\rm DUNE}_{\rm bkg} = 0$), because the primary background for this search arises from neutrino interactions within the detector volume and active neutrino events exhibit a topology that differs significantly from that of HNL decays. [165]

In our analysis, we consider four benchmark scenarios, listed in Table 4.5. The first two benchmarks are chosen for an HNL mass $m_N = 400$ MeV with an active-sterile mixing strength just below the current bound from T2K. The third and fourth benchmarks are at $m_N = 800$ MeV with an active-sterile mixing strength well below the current bound from CHARM. The benchmark points are indicated in Fig. 4.1. The light neutrino mass is chosen to be either $m_\nu = 10^{-1.9}$ eV or $10^{-2.5}$ eV. These roughly correspond to the smallest and largest possible effective Majorana masses for the light neutrinos in the inverted ordering and normal ordering, respectively. The benchmark scenarios are further distinguished by having a rather large HNL mass splitting $r_\Delta = \Delta m_N/m_N = 10^{-0.5}$ in scenarios 1 and 2 (being close to the seesaw line, the HNLs are not required to form a quasi-Dirac pair) and a small splitting $r_\Delta = 10^{-2.5}$ in scenarios 3 and 4. The benchmark scenarios are chosen to represent different parameter regions of interest that yield appreciable number of

events, both at DUNE and LEGEND-1000, also listed in Table 4.5. As expected, the DUNE event rate is not affected by the light neutrino mass, being only sensitive to the incoherent sum of the HNL contributions. On the other hand, the $0\nu\beta\beta$ decay event rate is affected by m_ν, as well as the HNL phase parameter $\cos\phi_{e1}$, which is chosen to be $\cos\phi_{e1} = 0$ in all scenarios, as the light neutrino and HNL contributions are coherently added.

In the following, we discuss four hypothetical experimental outcomes, namely, (A) both DUNE and LEGEND-1000 observe a signal, (B) DUNE observes signal events but not LEGEND-1000, (C) LEGEND-1000 observes signal events but not DUNE and (D) both DUNE and LEGEND-1000 see no signal events. We sample the parameter space using an MCMC to find the posterior parameter distribution for a given likelihood formed by the Poisson-Lambda distribution in Eq. (4.72), for DUNE and LEGEND-1000. We scan over the parameters $\log_{10}(|\Theta_{e1}|^2)$, $\log_{10}(r_\Delta)$ and $\cos\phi_{e1}$ in the range $[-12,-6]$, $[-4,0]$ and $[-1,1]$, respectively, using a flat prior, in analysis (a) and (b), i.e., m_N is fixed, assumed to be determined from kinetic information at DUNE to sufficient accuracy. In (c) and (d), m_N is also scanned over the range $[0.1,1.0]$ MeV.

For each benchmark point, we insert the expected event rate for LEGEND-1000 and DUNE, following the Asimov data set approach [198], setting the number of observed events $n_{\rm obs}$ for each experiment equal to the number of expected events $\lambda_{\rm sig}(\theta)+\lambda_{\rm bkg}$ in a benchmark scenario. In the case of no signal, we set $n_{\rm obs} = \lambda_{\rm bkg}$. In Sec. 4.5.7, we extend our analysis to the full $3+2$ model using the currently measured active neutrino data, under the assumption that the lightest active neutrino is massless. The free parameter in the active neutrino sector becomes the light Majorana phase α_{21} instead of the active neutrino mass m_ν in the simplified $1+2$ scenario.

4.5.3 (A) Signals at both

In Fig. 4.10, we illustrate the posterior distributions resulting from the MCMC, marginalized to the $(|\Theta_{e1}|^2, r_\Delta)$ parameter plane. Here, we assume an observation of the expected number of events at DUNE (near vertical blue points) and LEGEND-

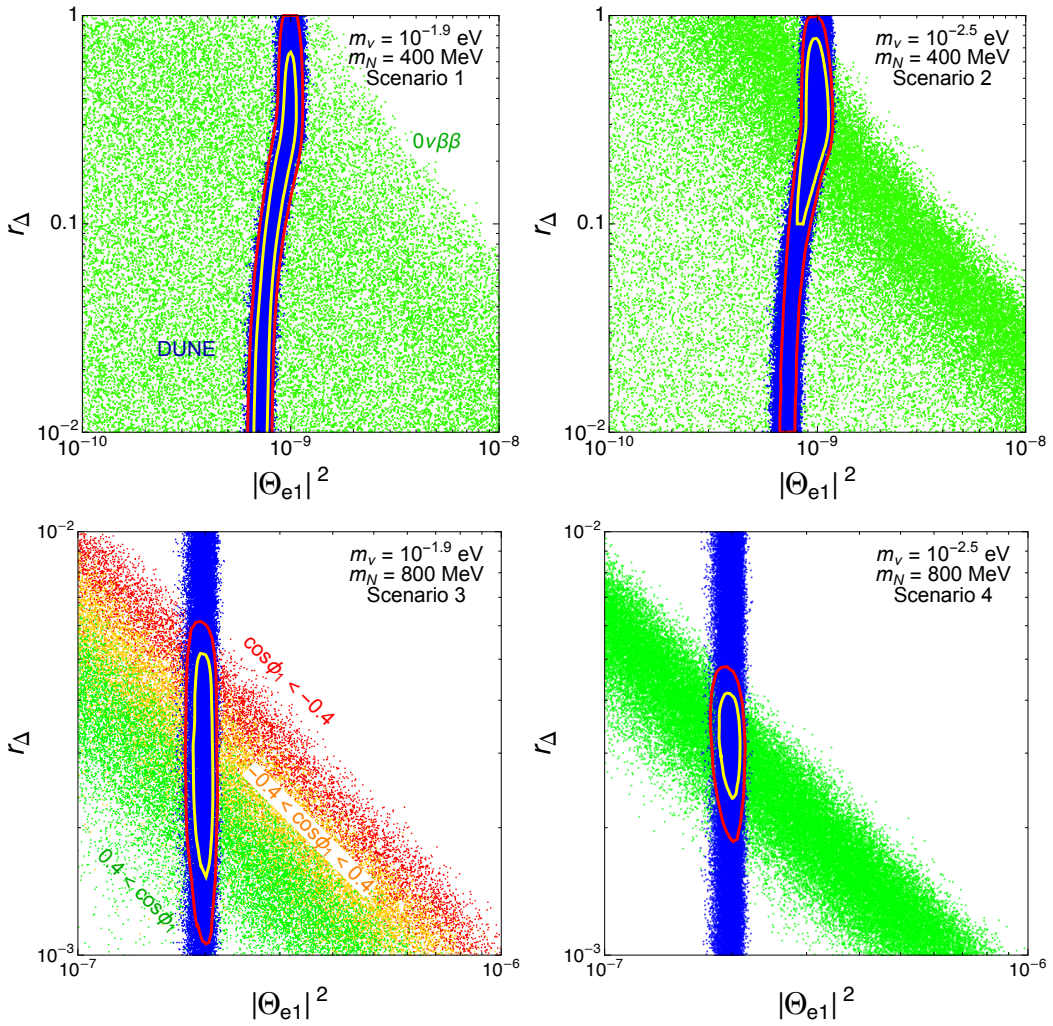

Figure 4.10: Posterior distribution marginalized to the $(|\Theta_{e1}|^2, r_\Delta)$ parameter plane assuming an observation at DUNE (blue points), LEGEND-1000 (diagonal green or coloured points) or both simultaneously (yellow and red contours representing the 68% and 95% credible regions) in the four benchmark scenarios. In the bottom plots, the LEGEND-1000 points are colour-coded according to the value of the HNL phase parameter $\cos\phi_{e1}$ as indicated.

1000 (diagonal green or coloured points) as per Table 4.5 for the four benchmark scenarios. In the top plots, the red, orange and green points for observed $0\nu\beta\beta$ decay are filtered according to the value of the HNL phase parameter $\cos\phi_{e1}$, namely $\cos\phi_{e1} < -0.4$, $-0.4 \leq \cos\phi_{e1} \leq 0.4$ and $\cos\phi_{e1} > 0.4$, respectively. The points thus indicate the posterior distributions assuming observation in either DUNE or LEGEND-1000 but not both. The combined posterior assuming observation in both is illustrated by the red and yellow contours indicating the 68% and 95% credible

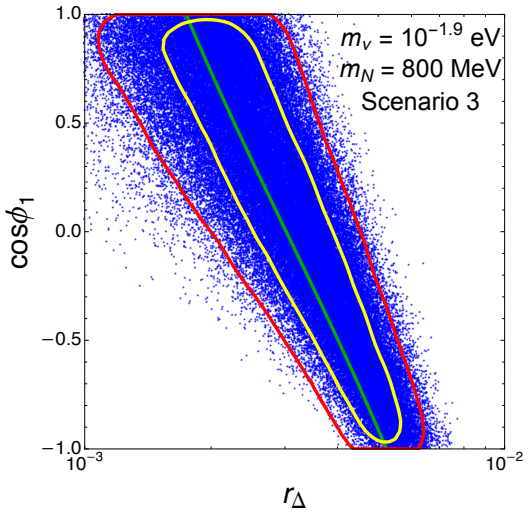

Figure 4.11: Posterior distribution (blue points and yellow/red contours) marginalized to the $(\cos\phi_{e1}, r_\Delta)$ plane assuming observations at both DUNE and LEGEND-1000 in benchmark Scenario 3. The green line shows the analytic relation in Eq. (4.39).

regions.

In all benchmark scenarios, the number of DUNE events is fairly large, resulting in a narrow, near vertical band, essentially fixing the value of $|\Theta_{e1}|^2$. The deviation from vertical in the top plots is due to the large mass splitting $r_\Delta \gtrsim 0.1$ and the resulting dependence on the mass of the second HNL N_2. In Scenarios 1 and 2 with $m_N = 400$ GeV (top plots), the number of events at LEGEND-1000 is, on the other hand, small, near the detection limit. This does not allow a definite determination of the model parameters, only setting a weak limit $r_\Delta \lesssim 1$ on the mass splitting. In Scenarios 3 and 4 (bottom plots), the number of expected LEGEND-1000 events is, instead, much larger, constraining the parameter space to a diagonal band. This reflects the fact that the contribution of the HNLs is constrained to be sufficiently small, either due to a small active-sterile mixing or a small mass splitting with a resulting quasi-Dirac nature of the HNLs. In combination with the DUNE observation this would allow a measurement of the mass splitting $r_\Delta \approx 10^{-2.5}$, with a higher precision in Scenario 4, where the light neutrino contribution is not saturating the $0\nu\beta\beta$ decay half life.

As can be seen in Fig. 4.10, DUNE is effectively insensitive to the light neu-

trino mass and HNLs with $r_\Delta < 0.1$, whereas $0\nu\beta\beta$ decay is sensitive to both the HNL mass splitting ratio and the active-sterile mixing. In addition, $0\nu\beta\beta$ decay is also sensitive to the HNL phase ϕ_{e1}, namely, the interference term proportional to $\cos\phi_{e1}$ in Eq. (4.35) is important if the light and heavy neutrino contributions are of a similar size. In Fig. 4.10 (bottom), the widths of the $0\nu\beta\beta$ bands depends on the light neutrino mass; when the light neutrino contribution saturates the $0\nu\beta\beta$ decay half-life, as in Scenario 3, the band of allowed points is much wider. This is in agreement with the analytical behaviour discussed in Sec. 4.5.1. Increasing the HNL mass can be seen to shift the allowed region to smaller $|\Theta_{e1}|^2$ and r_Δ values. The resulting degeneracy between $\cos\phi_{e1}$ and r_Δ is displayed in Fig. 4.11, showing the posterior distribution in Scenario marginalized to this parameter plane. The points and contours both illustrate the combined distribution assuming observation at both DUNE and LEGEND-1000. The central green line results from the analytical relation in Eq. (4.39).

4.5.4 (B) Signal at DUNE — No Signal at LEGEND-1000

In Fig. 4.12, we analogously display the posterior distribution in $(|\Theta_{e1}|^2, r_\Delta)$, assuming an observation at DUNE (blue points) but no events at LEGEND-1000 (green points), for the four benchmark scenarios. The yellow and red contours show the 68% and 95% credible regions combining both observations. As mentioned earlier, in this case the number of $0\nu\beta\beta$ decay signal events is not set according to Table 4.5 but $\lambda_{0\nu}^{\rm sig} = 0$ is imposed. With regard to DUNE the assumptions are identical to (A) above and thus the blue point distributions are the same.

With no $0\nu\beta\beta$ decay events, the corresponding regions extend to arbitrarily small values of r_Δ but they also partially overlap with those in Fig. 4.10 where $0\nu\beta\beta$ decay is assumed to be observed. This is due to the inherent statistical uncertainties but also because cancellations in the $0\nu\beta\beta$ decay rate can occur, especially for a large light neutrino mass m_ν.

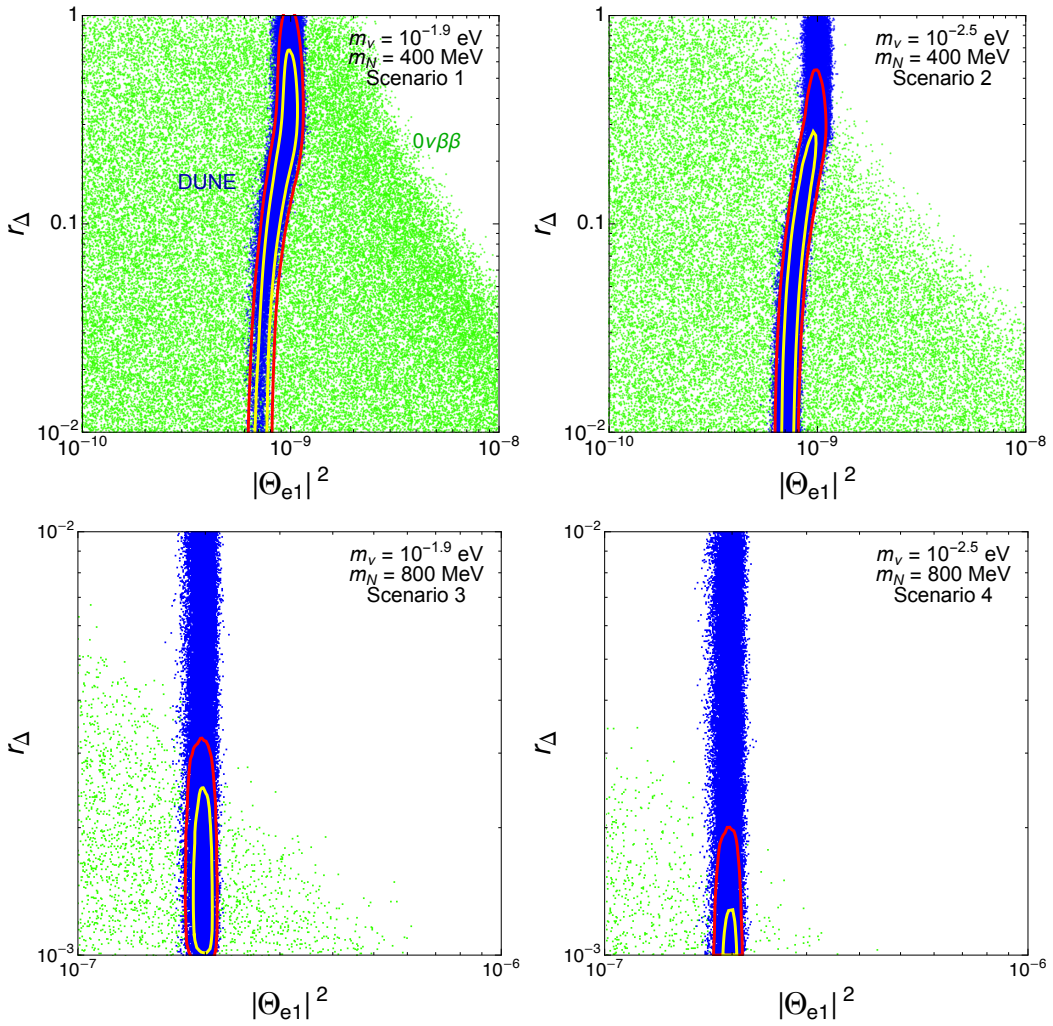

Figure 4.12: As Fig. 4.10, but assuming a signal at DUNE with no events at LEGEND-1000 in the four benchmark scenarios. Top-left: use r_Δ range 10^{-2} to 1. Bottom-right: use r_Δ range 10^{-3} to 10^{-2}.

4.5.5 (C) No Signal at DUNE — Signal at LEGEND-1000

In Figs. 4.13 and 4.14, we show the points generated in the MCMC scans in the $(m_N, |\Theta_{e1}|^2)$ and $(|\Theta_{e1}|^2, r_\Delta)$ planes, respectively, assuming no HNL-like DUNE events (blue points) and a positive $0\nu\beta\beta$ decay signal (green points), for the four benchmark scenarios. In Fig. 4.13, it can be seen that increasing the HNL mass shifts the $0\nu\beta\beta$ decay points to larger values of $|\Theta_{e1}|^2$. This is to be expected from the approximate formula of Eq. (4.44), where the active-sterile mixing is linearly proportional to the HNL mass. We see that the light neutrino mass does not change the results of the MCMC scan significantly in the $(m_N, |\Theta_{e1}|^2)$ plane. The region

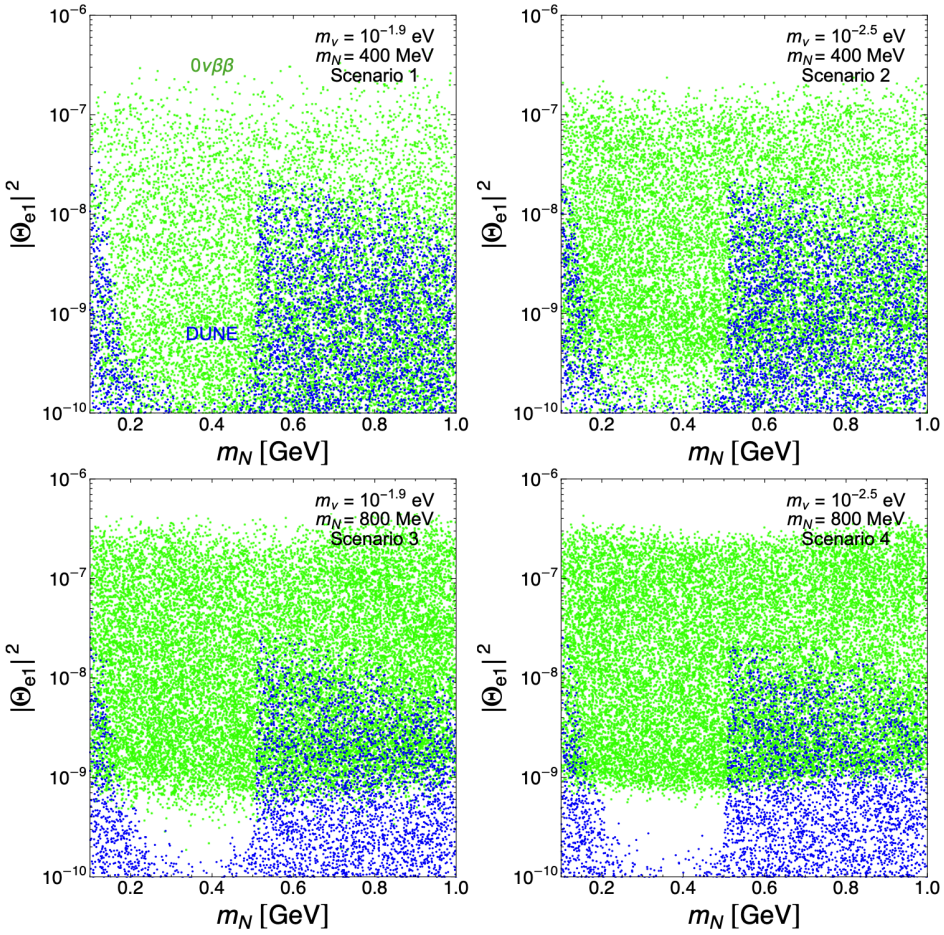

Figure 4.13: Posterior distribution marginalised in the $(m_N, |\Theta_{e1}|^2)$ plane assuming an observation at LEGEND-1000 but no signal for DUNE for the four benchmark scenarios. The green points represent the distribution for LEGEND-1000, the blue points for no signal at DUNE.

compatible with an observation of $0\nu\beta\beta$ decay but not HNL-like events at DUNE is mostly determined by $0\nu\beta\beta$ decay for large HNL masses.

If there is no observation of HNL-like events at DUNE, there is still the chance to observe $0\nu\beta\beta$ decay for the benchmark points in the red 68% credible contour regions in the $(|\Theta_{e1}|^2, r_\Delta)$ plane, shown in Fig. 4.14. The combined regions are now mostly determined by $0\nu\beta\beta$ decay, since a positive DUNE signal is no longer placing a stringent constraint on the parameter space. The combined regions are situated at large HNL mass splittings and relatively large active-sterile mixing, $|\Theta_{e1}|^2 \gtrsim 10^{-9}$.

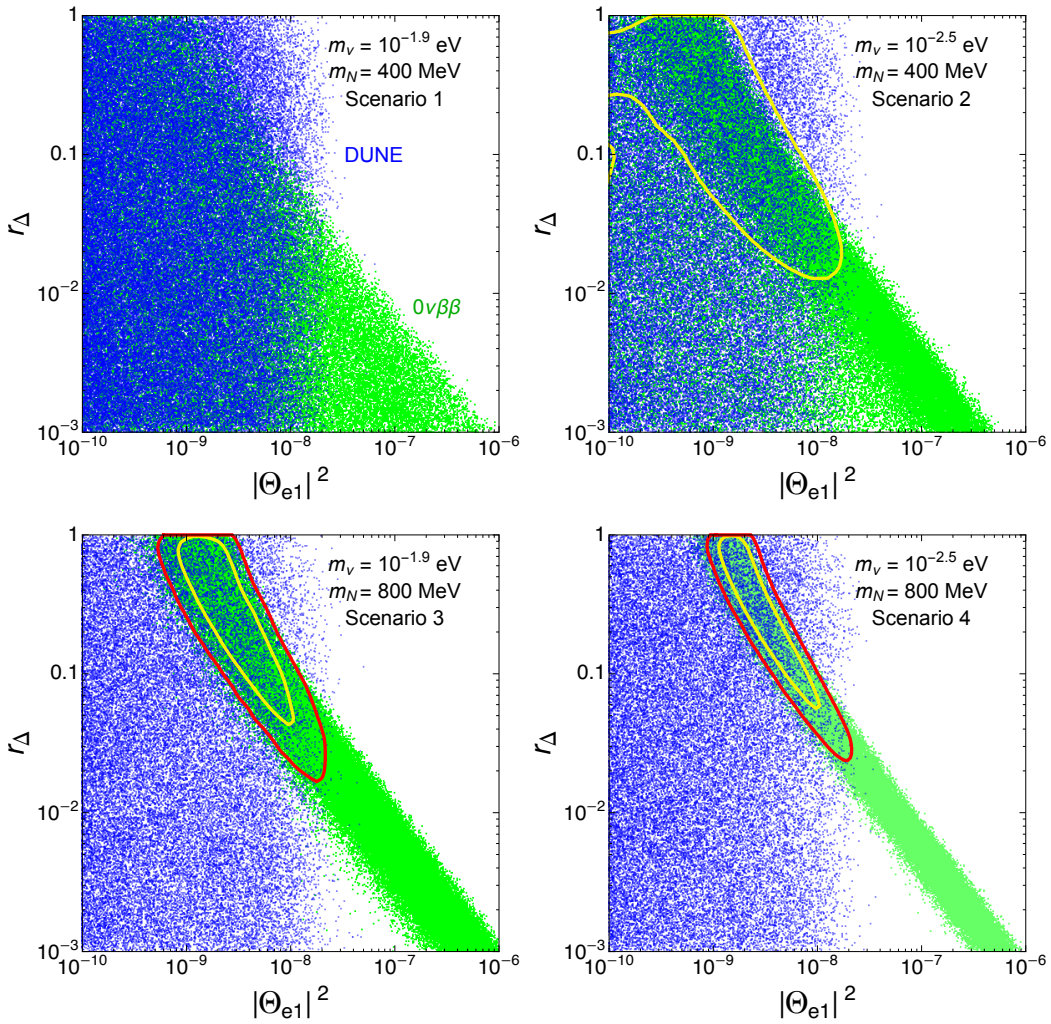

Figure 4.14: The same data set as Fig. 4.13 shows, but in the $(|\Theta_{e1}|^2, r_\Delta)$ plane for the four benchmark scenarios. The green points represent the distribution for LEGEND-1000, the blue points for no signal at DUNE. The yellow and red contours are the 68% and 95% credible regions combining both measurements respectively.

4.5.6 (D) No signals at neither

In Fig. 4.15, we display the points produced in the MCMC scans in the $(m_N, |\Theta_{e1}|^2)$ plane (left) and $(|\Theta_{e1}|^2, r_\Delta)$ plane (right), assuming no DUNE (blue points) or $0\nu\beta\beta$ decay (green points) signals. In the top left-hand plot, where the light neutrino mass $m_\nu = 10^{-1.9}$ eV only just saturates a $0\nu\beta\beta$ decay half-life of 10^{28} yr, we indicate the value of the HNL mass splitting r_Δ for each point; green for $r_\Delta < 10^{-2}$, orange for $10^{-2} < r_\Delta < 10^{-1}$, and red for $10^{-1} < r_\Delta < 1$. It can be seen that the points with larger active-sterile mixing correspond to larger values of r_Δ. The points with small

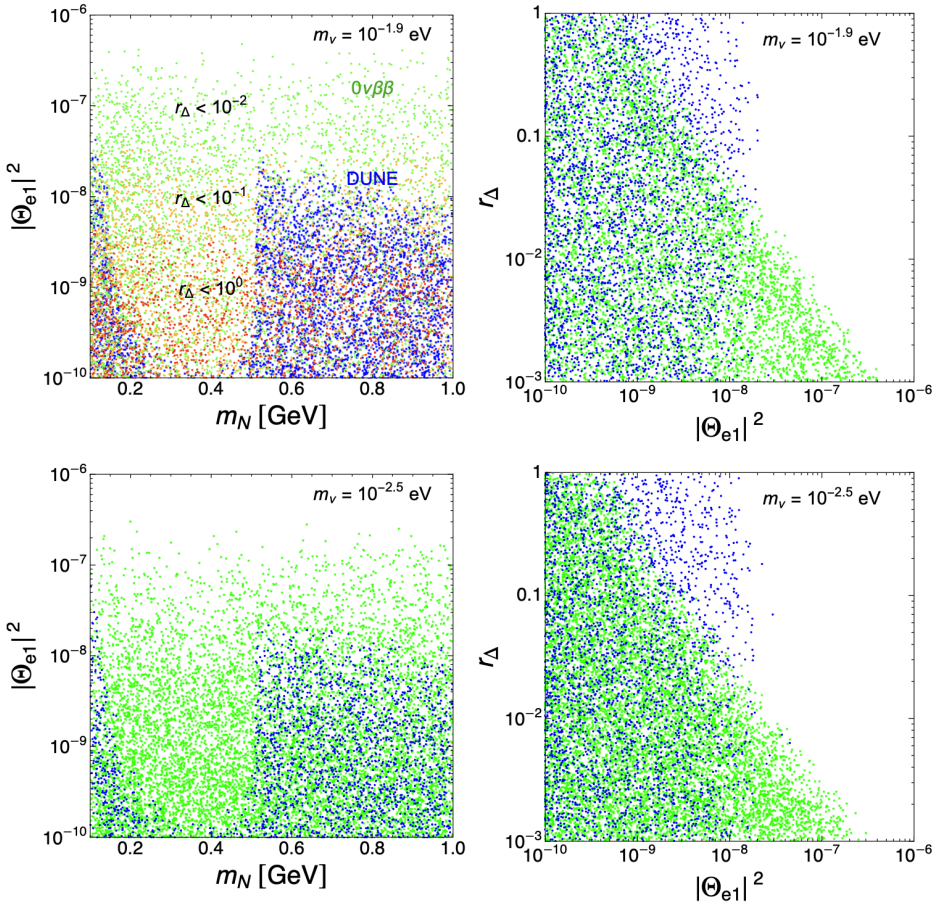

Figure 4.15: Posterior distribution marginalised in the $(m_N, |\Theta_{e1}|^2)$ plane (left) and $(|\Theta_{e1}|^2, r_\Delta)$ plane (right) assuming no observation at LEGEND-1000 nor DUNE for the four benchmark scenarios. The blue points represent the distribution for no signal at DUNE and the green points for no signal at LEGEND-1000. In the top left-hand plot, the points for no observation at LEGEND-1000 are colour-coded according to the value of the HNL mass splitting r_Δ, as indicated.

r_Δ (red) cover the whole region in which no $0\nu\beta\beta$ decay signal is seen, while points with large r_Δ (red) only occupy the region where the active-sterile mixing is small. In the plots to the right, it can be seen that the regions compatible with no DUNE or $0\nu\beta\beta$ decay signals extend from arbitrarily small $|\Theta_{e1}|^2$ values up to an upper limit determined by r_Δ. For $0\nu\beta\beta$ decay, these upper limits are shifted slightly by the value of m_ν.

Comparing the plots in the $(m_N, |\Theta_{e1}|^2)$ plane in Figs. 4.10 and 4.15, it can be seen that in some regions of the parameter space, $0\nu\beta\beta$ decay can either be observed or not observed. It is due to the fine-tuned nature of cancellations between

the light neutrino and HNL pair needed to suppress the $0\nu\beta\beta$ decay rate; nevertheless, the specific arrangement of the parameters in the model needed for this cancellation are possible over much of the parameter space.

4.5.7 (E) Signals at both in the $3+2$ scenario

In this final subsection, we further investigate the $m_N = 800$ MeV scenario, but now in the $3+2$ model with $m_{\text{light}} = 0$. We now include HNL production and decay in DUNE via the muon neutrino mixing, as discussed at the end of Sec. 4.4. Events involving HNL mixing with the tau neutrino are neglected for $m_N = 800$ MeV, as it is not kinematically possible to produce $\tau^{\pm}$ from the considered meson decay channels. The expected number of DUNE signal events is given by

$$\lambda_{\text{sig}}^{\text{DUNE}}(\theta) = N_{\text{sig}}(|\Theta_{e1}|^2, |\Theta_{\mu 1}|^2) + N_{\text{sig}}\left(|\Theta_{e2}|^2, |\Theta_{\mu 2}|^2\right), \tag{4.75}$$

where $|\Theta_{e2}|^2$, $|\Theta_{\mu 1}|^2$ and $|\Theta_{\mu 2}|^2$ are written in terms of $|\Theta_{\mu 1}|$ and ϕ_{e1} using Eq. (4.16). In Fig. 4.16, we plot $|\Theta_{e2}|^2$ and $|\Theta_{\mu 1}|^2$ as a function of α_{21} in the NO (left) and IO (right) for $|\Theta_{e1}|^2 = 10^{-6.7}$ and $r_\Delta = 10^{-2.5}$. This is in the regime $|\Theta_{e1}|^2 \gg |m_{ee}^\nu|/m_N$, where the ratio of mixing strengths is given by Eq. (4.19); in the NO and IO scenarios, the only freedom is the Majorana phase α_{21}. For small mass splittings r_Δ, it is also the case that $|\Theta_{e1}|^2 \simeq |\Theta_{e2}|^2$ and $|\Theta_{\mu 1}|^2 \simeq |\Theta_{\mu 2}|^2$.

To perform the analysis, we consider the two benchmark scenarios shown in Table 4.6; for the HNL mass $m_N = 800$ MeV, the active-sterile mixing strengths $|\Theta_{e1}|^2$ and $|\Theta_{\mu 1}|^2$ are chosen to lie just below the current experimental bounds. The light neutrino Majorana phase is chosen to be either $\alpha_{21} = 0$. These give the upper bounds on the effective Majorana masses for the light neutrinos in the inverted ordering and normal ordering, respectively. $|\Theta_{e1}|^2$ can no longer be chosen as the same value since it is further constrained by current muon-sterile mixing strength bound and the mixing strengths can be one order of magnitude different between $|\Theta_{eN}|^2$ and $|\Theta_{\mu N}|^2$ as Figs. 4.16 shows. With the choice of different values of $r_\Delta = 10^{-2.5}$ and $r_\Delta = 10^{-1.5}$ to keep observable LEGEND-1000 sensitivity (10^{28} years), $|\Theta_{e1}|^2 = 10^{6.70}$ and $|\Theta_{e1}|^2 = 10^{7.64}$ are chosen to make the scenarios just below

Ordering	α_{21}	m_N [MeV]	$\lvert\Theta_{e1}\rvert^2$	$\lvert\Theta_{\mu 1}\rvert^2$	r_Δ	ϕ_{e1}
IO	0	800	$10^{-6.70}$	$10^{-7.05}$	$10^{-2.50}$	$\pi/2$
NO	0	800	$10^{-7.50}$	$10^{-6.58}$	$10^{-1.50}$	$\pi/2$

Ordering	$T_{1/2}^{0\nu}$ [yr]	$\lambda_{0\nu}$	$\lambda_{\rm DUNE}$	$\lambda_{\rm DUNE\,(e)}$	$\lambda_{\rm DUNE\,(\mu)}$
IO	$10^{26.7}$	65.2	192	71.5	28.1
NO	$10^{27.1}$	28.2	193	12.3	95.4

Table 4.6: Default values for the light neutrino Majorana phase α_{21}, the HNL mass m_N, the active-sterile mixing strengths $|\Theta_{e1}|^2$ and $|\Theta_{\mu 1}|^2$ and the HNL mass splitting r_Δ adopted in the benchmark scenarios of our statistical analysis in the inverted and normal mass ordering scenarios respectively under the 3 + 2 model. In all cases, the HNL phase parameter is $\phi_{e1} = \pi/2$. Also given are the total expected number of events at DUNE, $\lambda_{\rm DUNE}$, and DUNE electron and muon only events, $\lambda_{\rm DUNE\,(e)}$ and $\lambda_{\rm DUNE\,(\mu)}$,and LEGEND-1000, $\lambda_{0\nu}$, as well as the corresponding half-life $T_{1/2}^{0\nu}$.

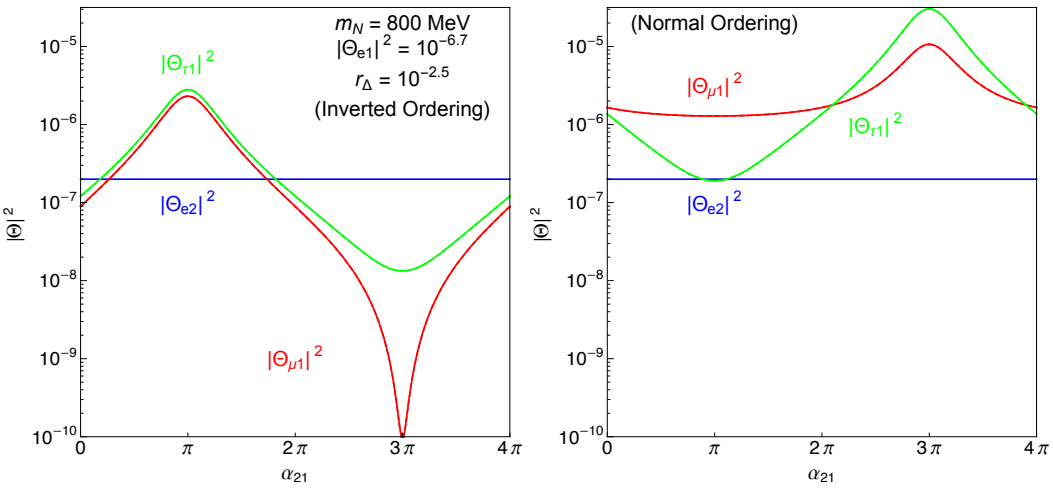

Figure 4.16: Different mixing angles $(|\Theta_{e2}|^2, |\Theta_{\mu 1}|^2, |\Theta_{\tau 1}|^2)$ versus the Majorana phase α_{21} in the 3 + 2 model for inverted ordering (left) and the normal ordering (right). The mixing strengths have the relations that $|\Theta_{e1}|^2 \simeq |\Theta_{e2}|^2$ and $|\Theta_{\mu 1}|^2 \simeq |\Theta_{\mu 2}|^2$.

the active-sterile mixing constraints and give similar number of total DUNE events for IO and NO, respectively. The electron (DUNE(e)) and muon (DUNE(μ)) only events can be made as separate observales to constrain the HNL phase parameter ϕ_{e1}, which is chosen to be $\phi_{e1} = \pi/2$ in both scenarios, to match previous $\cos\phi_{e1} = 0$ benchmark value.

Figs. 4.17 shows the MCMC scans in the $(|\Theta_{e1}|^2, \alpha_{21})$,$(r_\Delta, |\Theta_{e1}|^2)$,$(\phi_{e1}, r_\Delta)$

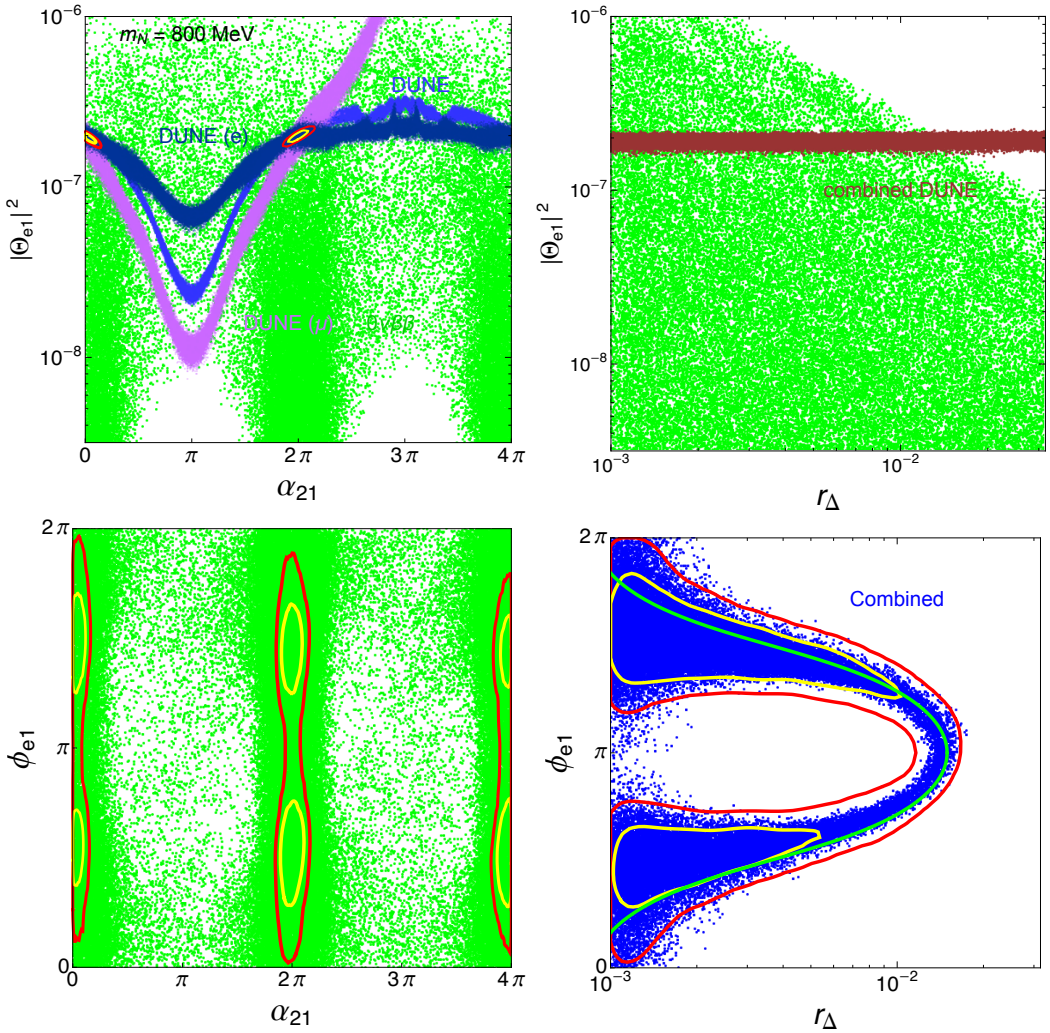

Figure 4.17: Posterior distribution marginalised in the $(\alpha_{21}, |\Theta_{e1}|^2)$ plane (top left), $(r_\Delta, |\Theta_{e1}|^2)$ plane (bottom left), (α_{21}, ϕ_{e1}) plane (top right) and (r_Δ, ϕ_{e1}) plane (bottom right) by assuming observations at both LEGEND-1000 and DUNE for the benchmark scenario 3 in inverted mass ordering. The blue points represent the total DUNE event, the pink points are for electron only observations and purple points for muon only observations at DUNE. The green points stand for LEGEND-1000 observations, the blue points for total DUNE observations, the purple points are muon only DUNE events and the dark blue points represent the electron only DUNE events.The blue points stand for combined DUNE and LEGEND-1000 likelihood events and the brown points show the combined total, muon only and electron only DUNE events. The green curve is the predicted relation between r_Δ and ϕ_{e1} by using Eq. (4.39) given the IO scenario in Table 4.6. The red contour is for 95% for combined measurement and the purple (yellow) stands for 68% likelihood.

and (α_{21}, ϕ_{e1}) planes assuming combined observations of HNL-like events at both DUNE (dark blue points) and LEGEND-1000 (green points) with additional con-

straints from electron only (pale blue points) and muon only (purple points) events at DUNE, respectively. The red contour again represents the combined likelihood at 95% and the purple for 68%.

In the parameter space studied, DUNE is still sensitive to the mixing strengths but insensitive to the light Majorana phase α_{21}, whereas $0\nu\beta\beta$ decay is really sensitive to α_{21} with a periodic feature but not to the mixing strengths. Both experiments are not effectively sensitive to the HNL Majorana phase ϕ_{e1}. In the top left plot, the combined analysis constrains the allowed space within two small circle which is the benchmark point and one of the periodic identical points of α_{21}. The reason for no observation at $\alpha_{21} = 4\pi$ is clearly due to the constraint from muon only DUNE events. The top right plot illustrates that the electron only events constrain the space dominantly alongside with additional narrow down from the total DUNE event and muon only events and LEGEND-1000 only excludes the very large HNL mass splitting region. Also, the three DUNE lines show the same behaviour Fig. 4.16 presented. The bottom right plot shows a tightly constrained space in high mass splitting regime, which is due to nearly equal amount contributions from all 4 observable HNL-like events.

In Figs. 4.18, the MCMC scans are presented in the $(r_\Delta, |\Theta_{e1}|^2)$ and $(\alpha_{21}, |\Theta_{e1}|^2)$ planes under the same analysis as Figs. 4.17 in the normal ordering scenario. The left plot demonstrates a similar feature at DUNE as the right plot in Figs. 4.16 indicates. In comparison with the inverted ordering case, the left plot gives a band for $0\nu\beta\beta$ rather than three strips for the IO, it is due to the saturation of the light effective mass in IO which enhances the impact of the Majorana phase in the light neutrino sector. The right plot agrees with the bottom right plot in Figs. 4.10, the allowed band is narrowed down to a circle from the IO effective mass regime to the NO regime since less chance for the cancellation between the light and heavy neutrino contributions to occur in $0\nu\beta\beta$ for given LEGEND-1000 sensitivity. In the NO scenario, LEGEND-1000 become less sensitive to α_{21} and the sensitivity is completely lost for ϕ_{e1}.

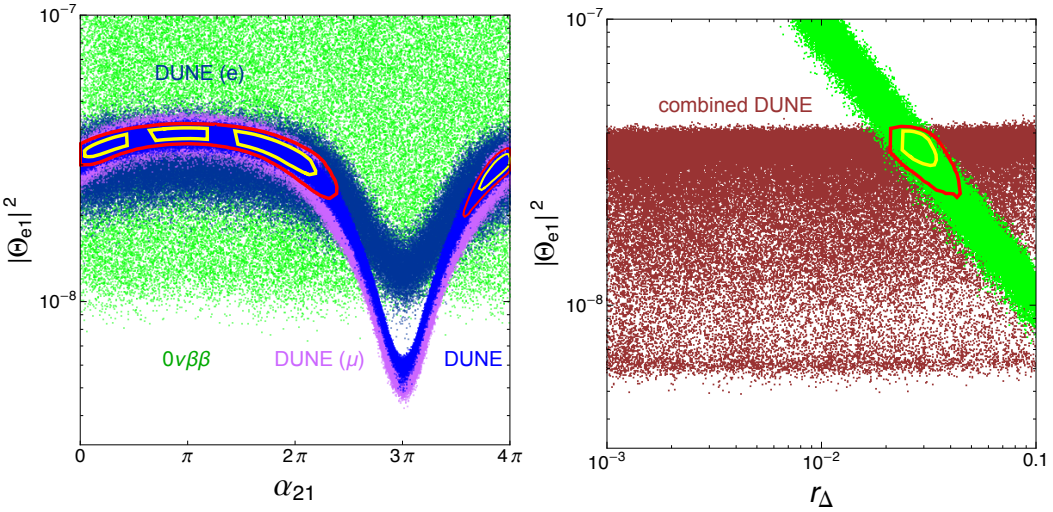

Figure 4.18: The parameter planes as the plots in Fig. 4.17, but for the normal mass ordering. The blue points represent the total DUNE event, the pale blue points are for electron only observations and purple points for muon only observation at DUNE. The green points stand for LEGEND-1000 observations, the blue points for total DUNE observations, the purple points are muon only DUNE events and the dark blue points represent the electron only DUNE events. The left plot shows the $(\alpha_{21}, |\Theta_{e1}|^2)$ plane. The right plot shows the $(r_\Delta, |\Theta_{e1}|^2)$ plane with brown points represent the combined DUNE analysis.The yellow contour is for 95% for combined measurement and the red stands for 68% likelihood.

4.6 Conclusions

In this chapter, we have investigated the phenomenology of a pair of heavy neutral leptons (HNLs) in the MeV to GeV mass range, which can generate the observed masses and mixing of the light active neutrinos but also impact neutrinoless double beta ($0\nu\beta\beta$) decay and direct searches for HNLs at fixed target experiments. In particular, we have shown how the combination of a positive $0\nu\beta\beta$ decay signal at LEGEND-1000 and HNL-like events in the DUNE near detector (ND) can constrain the active-sterile mixing and mass splitting of the HNL pair. Additionally, we have considered the model implications of only one or neither of the signals being observed.

In Sec. 4.2, we introduced a phenomenological parametrisation of the $3+2$ model, which adds a gauge-singlet Weyl fermion pair to the SM and is sufficient to generate masses for two light neutrinos at tree level. Using the tree level relations between the light neutrino and HNL parameters in the limit of small active-sterile

mixing, we derived useful ratio formulae making it possible to express all active-sterile mixing parameters in terms of a single active-sterile mixing and CP phase (in addition to the light neutrino data and HNL masses). This is in contrast to the Casas-Ibarra parametrisation, which uses a complex angle as the free parameter. This parametrisation is generalised for an arbitrary number $\mathcal{N}_S$ of additional HNL states in Appendix A, with the number of free parameters increasing accordingly. We also illustrated the behaviours of the active-sterile mixing parameters in the simple $1+2$ model, which covers the relevant limits of the $3+2$ model. We saw how either of the HNL pair can effectively decouple, with one HNL giving a mass to the light neutrino via the standard seesaw, and how both active-sterile mixing strengths to the HNLs can become large in the inverse seesaw limit.

Using the phenomenological model, in Sec. 4.3 we examined the $0\nu\beta\beta$ decay process, carefully taking into account the exchange of HNLs in the 100 MeV to 1 GeV mass range. In this mass region, around the Fermi momentum k_F, the exchange of HNLs is difficult to treat using chiral effective field theory methods. However, the low and high-mass regions are well understood and so a carefully chosen interpolation formula can be used to good approximation in the intermediate region. In the simple $1+2$ model, we gave a schematic illustration of how the HNL pair can either interfere constructively or destructively with the light neutrino contribution. Thus, given a precise knowledge of the neutrino masses and whether they have a normal or inverted ordering, the observation of a $0\nu\beta\beta$ decay half-life $T^{0\nu}_{1/2}$ that is incompatible with the light neutrino contribution could be used to put stringent constraints on the HNL pair. Conversely, if the light neutrino contribution *just* saturates the observed half-life, the $1+2$ model parameter space is less constrained.

In Sec. 4.4, we covered the production and decay of long-lived HNLs in the DUNE experiment in the phenomenological model. Using PYTHIA, we performed a simulation of mesons produced from 120 GeV protons on target, generating their production fractions and momentum profiles. All possible decays of these mesons to HNLs via the active-sterile mixing $|U_{eN}|^2$ are used to simulate the production

of HNLs in the rest frame of the mesons. The HNLs are then boosted to the lab frame and required to decay to charged tracks inside the ND, which we take to have a cylindrical cross-section. This analysis allows us to estimate the sensitivity of DUNE to Majorana HNLs, which can either be detected via LNC or LNV decay modes. This is also relevant for quasi-Dirac neutrinos; for the mass splittings of interest, the oscillations between the HNL pair are averaged out and the quasi-Dirac pair appears to be a pair of Majorana states.

In Sec. 4.5, we finally examined the complementary of $0\nu\beta\beta$ decay and DUNE in constraining the HNL paramater space. We first compared a measurement of $0\nu\beta\beta$ decay and HNL-like events at DUNE analytically, finding the implied mass splitting r_Δ in the limit where the light neutrino mass does not saturate the observed $0\nu\beta\beta$ decay half-life and the HNL event rate is large, so the HNL contribution is tightly constrained. We then explored in more detail the parameter space of the simple $1+2$ model by performing a Markov chain Monte Carlo scan over the statistical likelihoods of signals at LEGEND-1000 and DUNE, given the HNL pair hypothesis. We found that if both signals are seen, the mass splitting between the HNL pair is well constrained, with values $r_\Delta \sim 0.1$ implied for HNL masses around $m_N = 400$ MeV and $r_\Delta \sim 3 \times 10^{-3}$ for $m_N = 800$ MeV, shown in Fig. 4.10 as contours at the 68% and 95% confidence levels. If one signal is observed but not the other, we showed how the mass splitting is generally less constrained in Figs. 4.12 and 4.14. Finally, we found the regions of the parameter space in Fig. 4.15 where neither $0\nu\beta\beta$ decay nor HNL-like events are observed.

In this work, we have demonstrated how two very different probes of HNLs can constrain an intriguing region of the HNL parameter space where the active-sterile mixing is just above or touching the seesaw floor, $|U_{\alpha N}|^2 = m_\nu/m_N$. We therefore have the exciting prospect for $0\nu\beta\beta$ decay and DUNE to not only confirm (as their principal experimental aims) the mass ordering of the light neutrinos and their Majorana nature, but also that their masses are generated by the presence of a HNL pair with a small mass splitting.

Chapter 5

Probing Heavy Neutral Leptons in Astrophysics & Cosmology

There are numerous past, current and planned future searches for HNLs based on BBN constraint, over a wide range of HNL masses m_N; from the eV-scale where HNLs can be tested in oscillations, over keV and MeV scales mainly probed in nuclear processes such as β decay, MeV to GeV in beam dump and meson decays, to electroweak scale masses and above probed in colliders. A recent overview of current and future searches is provided in [155]. There has especially be an increased effort to search for HNLs in the mass range 100 MeV $\lesssim m_N \lesssim$ 100 GeV. The reason for this is that in this mass range, HNLs are naturally long-lived for the small active-sterile mixing strengths expected for successful neutrino mass generation. This results in macroscopic decay lengths and thus displaced decay vertices that can be looked for with a high sensitivity.

Being long-lived, HNLs also affect the early history of the Universe. If HNLs had been in thermal equilibrium, and they decay around or later than about a second after the big bang, the produced particles affect Big Bang Nucleosynthesis (BBN) [123]. HNLs decay to SM products with very different energies to the thermal plasma. The rates of the expansion of the Universe and the rate of weak interaction are therefore altered. This leads to different light element abundances we observe today. Such considerations disfavour HNLs with masses $m_N \lesssim 1$ GeV, for small active-sterile mixing strengths required by current constraints and expected for light

neutrino mass generation. Even lighter and longer-lived N are likewise disfavoured as they will act as additional degrees of freedom, or inject them through their decays, and may overclose the universe.

We here explore such a scenario where the HNL couples to a light, exotic pseudoscalar a, akin to an axion-like particle (ALP). We will refer to this dark scalar as ALP in the following, and it is dark in the sense that it couples only to the HNL in the first instance, with interactions to the SM suppressed by the active-sterile mixing and through loops. Our motivation is to explore the cosmological consequences of changing the HNL decay width due to the additional channel $N \to a\nu$ in the scenario. While suppressed by both the active-sterile neutrino mixing and the ALP decay constant f_a, it is a two-body decay that can compete with the three-body (at parton level) decays to SM particles only. This will enlarge the region of interest constrained by BBN, i.e., where HNLs decay earlier and motivate direct searches with such an additional invisible HNL decay. At the same time, the production of ALPs and their own decays will themselves lead to constraints on the viable parameter space by ensuring the cosmological history, especially until the time of the formation of the cosmic microwave background (CMB), is not affected.

This chapter is organized as follows. In Section 5.1, we describe the model and determine the HNL and ALP decay widths as important quantities for our later considerations. In Section 5.2, we describe our modelling of the cosmological history in our scenario by setting up the Boltzmann equations which we separate into a regime before and after BBN. The relevant constraints from cosmology and astrophysics are then discussed in Section 5.3, and they are applied in Section 5.5 where we present our results in terms of the viable parameter space. We briefly sketch expectations for direct searches in Section 5.4.

5.1 Phenomenological Model

In this chapter, we have extended the existing SM particle spectrum by adding SM gauge singlet Heavy Neutral Lepton (HNL) or Right-Handed Neutrino (RHN) and an Axion-Like Patricle (ALP) to it.

Axions are weakly interacting pseudo-scalar particles for solving strong CP problem in QCD [62, 199, 200]. It is also considered as one of the most popular candidates of cold dark matter (CDM) [201]. Axion-like particles (ALPs) are pseudo-scalar particles which do not necessarily solve the strong CP problem, but can still be dark matter candidates. In this context, as the mass of this ALP is not strictly tied to the QCD phase transition scale, $\Lambda_{\rm QCD}$, this particle can be quite light in the framework. With this extension, we will outline a phenomenological framework which can describe the coupling between HNL and ALP and its implications on current phenomenological, cosmological and astrophysical constraints from other complimentary studies.

5.1.1 Lagrangian and Particle Spectrum

In order to generate at least two non-degenerate active neutrino masses, as confirmed by the results from various neutrino oscillation experiments, it is necessary to introduce at least two HNLs. In general, we can extend the SM to include $\mathscr{N}$ HNLs as SM gauge-singlet Weyl fermion fields N_{iR} ($i = 1,..,\mathscr{N}$) and we include the pseudoscalar ALP a where the most general, renormalisable terms added to the SM Lagrangian are

$$\mathscr{L} = \mathscr{L}_{\rm SM} + i\bar{N}_{iR}\partial\!\!\!/ N_{iR} - (Y_\nu)_{\alpha i}\bar{L}_\alpha \tilde{H} N_{iR} - \frac{1}{2}(\mathscr{M}_R)_{ij}\bar{N}^c_{iR}N_{jR} + \mathscr{L}_{aNN} + \text{h.c.}. \quad (5.1)$$

Here, $L_\alpha = (\nu_{\alpha L}, \ell_{\alpha L})^T$ and $H = (H^0, H^-)^T$ are the SM lepton doublet with flavor index $\alpha = e, \mu, \tau$ and Higgs doublet, with $\tilde{H} \equiv i\sigma_2 H$ as the dual of H, respectively.

Recalling the SM decay modes of HNLs in Section 4.4.3, we also assume that the ALPs a couples with the HNL N, but not with other SM particles directly. Hence, due to the pseudoscalar nature of ALPs, the Lagrangian for the ALP-HNL interaction is given by the derivative coupling [202] in the mass basis as,

$$\mathscr{L}_{aNN} = \sum_{\kappa=1}^{\mathscr{N}} \frac{1}{f_a}(\partial_\mu a)\bar{N}_\kappa \gamma^\mu \gamma_5 N_\kappa = -\sum_{\kappa=1}^{\mathscr{N}} \frac{2i}{f_a} m_{N_\kappa} a \bar{N}_\kappa \gamma_5 N_\kappa, \quad (5.2)$$

where f_a is the ALP decay constant and m_{N_κ} are the eigenvalues of M_N. The second

equality holds by applying the equation of motion for the HNLs and removing a total derivative after integration by parts [203]. Due to the small active-sterile mixing $U_{\nu N} = U_{N\nu} \equiv \sqrt{m_\nu M_N^{-1}}$, an interaction between the ALP and the active neutrinos ν_α is induced. In the mass bases of active neutrinos and HNLs, we can write the interaction Lagrnagian between ALP and two active neutrinos as (also considering the HNLs to be almost degenerate),

$$\begin{aligned}\mathscr{L}_{a\nu\nu} &= -\sum_{\lambda,\lambda'=1}^{3}\sum_{\kappa=1}^{\mathscr{N}}\frac{2i}{f_a}m_{N_\kappa}a(U_{\nu\nu}^{\dagger}U_{N\nu}^{T})_{\kappa\lambda}(U_{N\nu}^{*}U_{\nu\nu})_{\kappa\lambda'}\bar{\nu}_\lambda\gamma_5\nu_{\lambda'} \\ &\approx -\sum_{\lambda,\lambda'=1}^{3}\frac{2i}{f_a}m_N a|U_{N\nu}U_{\nu\nu}^{*}|^2_{\lambda\lambda'}\bar{\nu}_\lambda\gamma_5\nu_{\lambda'} \end{aligned} \tag{5.3}$$

where λ,λ' denote the mass eigenstates for active neutrinos. Furthermore, the interaction Lagrangian for $aN\nu$ vertex can be written similarly as,

$$\mathscr{L}_{aN\nu} = -\sum_{\lambda'=1}^{3}\sum_{\kappa=1}^{\mathscr{N}}\frac{2i}{f_a}m_{N_\kappa}a(U_{N\nu}^{*}U_{\nu\nu})_{\kappa\lambda'}\bar{N}_\kappa\gamma_5\nu_{\lambda'}. \tag{5.4}$$

While at least two HNLs are needed to explain all active neutrino masses and mixing, we are mainly interested in elucidating the principle effects in our framework. For simplicity, we consider a single HNL only, $N_1 \equiv N$, we can acquire all the important information from the framework using this simplified viewpoint. Furthermore, we consider the active-sterile mixing of N_1 with a single active neutrino ν_1 which is mostly electron-type neutrino i.e., $\nu_1 \equiv \nu_e$, without loss of generality. From now on, we take $|U_{\nu\nu}|^2 \sim \mathscr{O}(1) \gg |U_{\nu N}|^2 = |U_{N\nu}|^2$ and $U_{\nu N} = U_{eN}$. Equations (5.2) and (5.3) then take the form

$$\begin{aligned}\mathscr{L}_{aNN} &= -\frac{2i}{f_a}m_N a\bar{N}\gamma_5 N, \\ \mathscr{L}_{aN\nu} &= -\frac{2i}{f_a}m_N U_{eN}a\bar{N}\gamma_5\nu_e, \\ \mathscr{L}_{a\nu\nu} &= -\frac{2i}{f_a}m_N|U_{eN}|^2 a\bar{\nu}_e\gamma_5\nu_e = -\frac{2i}{f_a}m_\nu a\bar{\nu}_e\gamma_5\nu_e, \end{aligned} \tag{5.5}$$

with the light neutrino mass $m_\nu = |U_{eN}|^2 m_N$ induced by the seesaw mechanism.

5.1.2 HNL Decays

Apart from the model for neutrinos and HNLs as mentioned in Section 4.2.1, the interaction in Eq. (5.5) gives a new decay channel for HNLs in this framework, where the HNL decays into an ALP and an active neutrino via active-sterile mixing at tree level. The decay width, in the limit where $m_\nu \ll m_N$, can be written as

$$\Gamma^{N\to a\nu} = \frac{U_{eN}^2 m_N^3}{4\pi f_a^2}\sqrt{1+\left(\frac{m_a}{m_N}\right)^2}\left(1-\left(\frac{m_a}{m_N}\right)^2\right)^{3/2} \simeq \frac{U_{eN}^2 m_N^3}{4\pi f_a^2}, \tag{5.6}$$

where the last equality holds in the limit where $m_a, m_\nu \ll m_N$. Hence the lifetime of the HNL considering only this decay mode, calculated in its rest frame, can be expressed as

$$\begin{aligned}\tau_{N\to a\nu} = \frac{1}{\Gamma^{N\to a\nu}} &\simeq 8.6\times 10^{-4}\ \text{sec}\times\left(\frac{\mathrm{f_a}}{1\ \text{TeV}}\right)^2\times\left(\frac{10^{-14}}{\mathrm{U_{eN}^2}}\right)\times\left(\frac{1\ \text{GeV}}{\mathrm{m_N}}\right)^3 \\ &= \frac{4\pi f_a^2}{U_{eN}^2 m_N^3}.\end{aligned} \tag{5.7}$$

The total decay width of HNL to SM particles only can be approximately written as [155],

$$\Gamma^{N\to\text{SM}} \sim \left(30\,\Gamma^{2-\text{body}} + 10\,\Gamma^{3-\text{body}}\right)|U_{eN}|^2 \sim \left(30\,\frac{G_F^2 f_M^2 m_N^3}{5\pi} + 10\,\frac{G_F^2 m_N^5}{200\pi^3}\right)|U_{eN}|^2 \tag{5.8}$$

where $f_M \sim \mathcal{O}(0.1)$ GeV, corresponds to the typical decay constant of the produced pseudoscalar or vector meson. The factors 30 and 10 are from the numerical results of chosen region of parameter space. Comparing this with Eq. (5.6), it is clear that the $N \to a\nu$ channel will be dominant over the SM decay channels if,

$$m_N > \frac{\sqrt{5|1-24G_F^2 f_M^2 f_a^2|}\pi}{f_a G_F}. \tag{5.9}$$

Moreover, all the SM as well as ALP decay channels have similar dependency on active-sterile mixing, so the above equation is completely independent of $|U_{eN}|^2$.

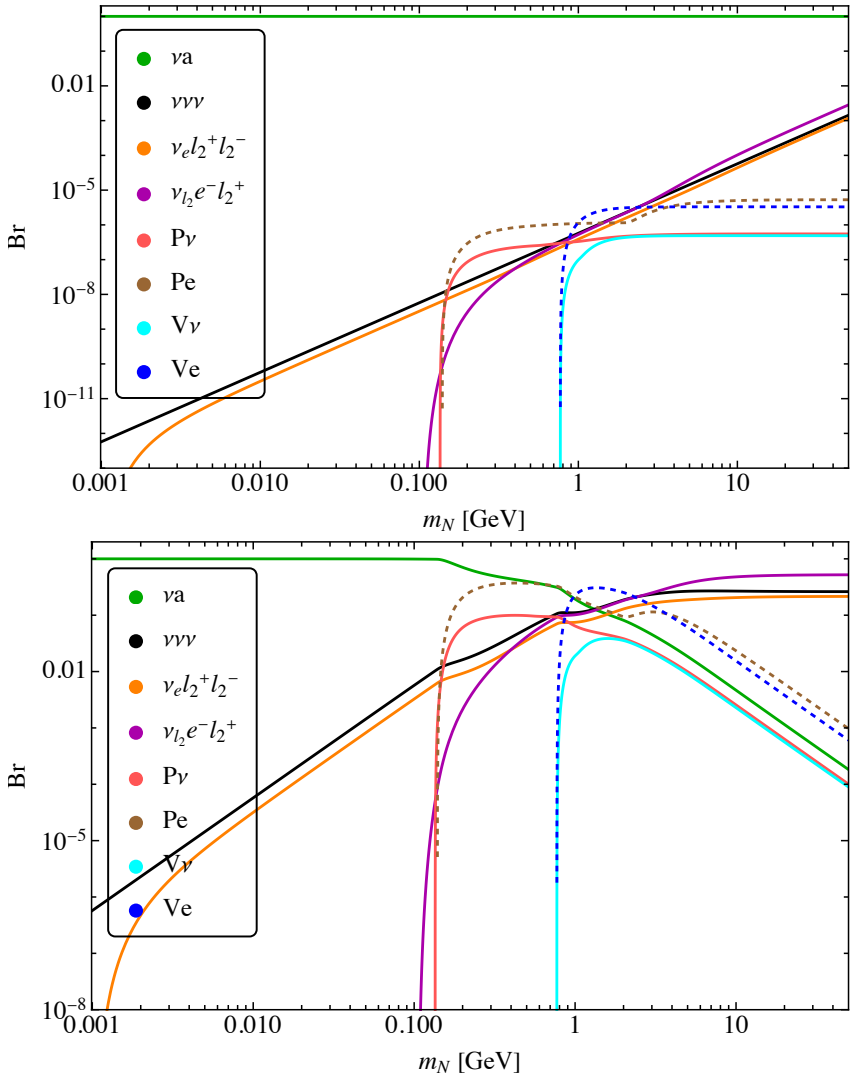

Figure 5.1: Branching ratios of HNL to axionic as well as various SM channels as a function of m_N for $m_a = 1$ keV and two different values of f_a: 1 TeV (top) and 10^3 TeV (bottom)

The branching ratios of the HNL to as a function of mass of the HNL for two different values of f_a are shown in Fig. 5.1. In this work, as we are mostly interested in the regime where $m_a \ll m_N$, correspondingly we have chosen $m_a = 1$ keV and varied $m_N \in [10^{-3} - 50]$ GeV range. In the top panel, we have considered $f_a = 1$ TeV where the $\mathrm{Br}(N \to a\nu) \approx 100\%$ (*solid green*) throughout the entire mass range of HNL, while the behaviour of different SM decay channels are shown as, $N \to 3\nu$ (*solid black*), $N \to \nu_e(e^+e^- + \mu^+\mu^- + \tau^+\tau^-)$ (*solid orange*), $N \to e^-(\nu_\mu\mu^+ + \nu_\tau\tau^+)$ (*solid magenta*), different pseudoscalar (P) and vector (V) mesonic channels

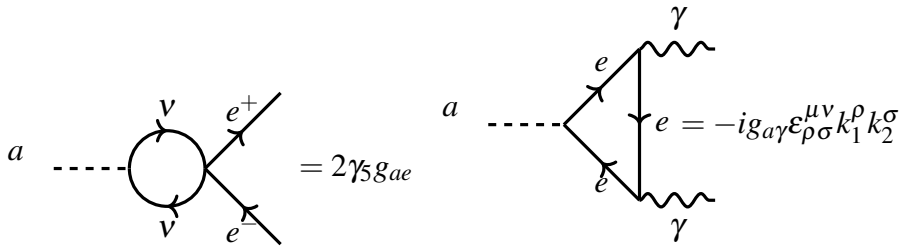

Figure 5.2: Effective couplings of the ALP to electrons (left) and photons (right).

(which become relevant as $m_N \geq m_\pi$) as $N \to P\nu$ (*solid red*), $N \to Pe$ (*dashed brown*), $N \to V\nu$ (*solid cyan*), $N \to Ve$ (*dashed blue*). In the bottom panel of the figure we have taken $f_a = 10^3$ TeV, for which the coupling of the ALP to HNL significantly decreases. Here, for lower mass of HNL the axionic decay channel still dominates the scenario, while for $m_N > m_\pi$, as the mesonic channels come into picture, the BR to axionic channel drops significantly as compared to the SM decay channel BRs.

5.1.3 ALP Decays

The interaction between the ALPs and active neutrinos in Eq. (5.3) causes the ALP to decay. This decay channel occurs at tree level, thus dominating the ALP decay width, and it is given by

$$\Gamma^{a\to\nu\nu} = \frac{1}{f_a^2}\frac{m_N^2 m_a U_{eN}^4}{2\pi}\sqrt{1-\frac{4m_\nu^2}{m_a^2}}\left(1-\frac{2m_\nu^2}{m_a^2}\right) \simeq \frac{m_N^2 m_a U_{eN}^4}{2\pi f_a^2}, \tag{5.10}$$

where we have considered $m_a \gg m_\nu$ to arrive at the last expression.

No other decay channels are available at tree level. However, as it will be seen below (see Section 5.3), most of the constraints on axion-like particles come from their interactions with electrons and photons. Though the Lagrangian in Eq. (5.5) does not produce axion-electron or axion-photon interactions at tree level, such couplings can be induced at 1-loop and 2-loop respectively, as shown in Fig. 5.2.

These effective axion-electron and axion-photon couplings, g_{ae} and $g_{a\gamma}$, can cause the ALP to decay to a pair of electrons or photons and, in the limit where

$m_a, m_\nu, m_e \ll m_N$, are given by

$$g_{ae} \approx \frac{\sqrt{2} G_F g_{aN} |U_{eN}|^4 m_e m_N}{16\pi^2} = \frac{\sqrt{2} G_F |U_{eN}|^4 m_e m_N^2}{16\pi^2 f_a},$$
$$g_{a\gamma} \approx \frac{e^2 g_{ae}}{2\pi^2 m_e}\left(1 + \frac{1}{12}\frac{m_a^2}{m_e^2}\right) = \frac{\sqrt{2} e^2 G_F |U_{eN}|^4 m_N^2}{32\pi^4 f_a}\left(1 + \frac{1}{12}\frac{m_a^2}{m_e^2}\right), \tag{5.11}$$

where $g_{aN} = m_N / f_a$.

Nevertheless, for light ALPs, $m_a \leq 1$ keV, which is the focus of this study, the only open decay channels for the ALPs are either a pair of active neutrinos or a pair of photons. But, as seen in Fig. 5.2, the diphoton decay happens at 2-loop and thus it is significantly suppressed with respect to the decay to active neutrinos. For example, the decay width to photons of a 1 keV ALP with decay constant of 1 TeV will be of order 10^{-46} GeV, negligible compared to decay width to active neutrinos [204, 205].

The ALP lifetime can thus be computed from its decay width to two active neutrinos. So in ALP rest frame,

$$\tau_a = 1 \text{ sec} \times \left(\frac{1 \text{ GeV}}{\mathrm{m_N}}\right)^2 \times \left(\frac{10 \text{ keV}}{\mathrm{m_a}}\right) \times \left(\frac{6 \times 10^{-7}}{|\mathrm{U_{eN}}|^2}\right)^2 \times \left(\frac{\mathrm{f_a}}{1 \text{ TeV}}\right)^2. \tag{5.12}$$

For HNLs and ALPs in the mass range of interest, $m_N \sim 1$ GeV and $m_a \sim 1$ keV, the lifetime of the ALPs, and hence the scenario that is realised, depends on the ALP-HNL interaction $1/f_a$ and the active-sterile mixing U_{eN}. For example, an ALP that is stable compared to the age of the universe would require $f_a \sim 1$ TeV and $|U_{eN}|^2 \leq 10^{-13}$.

5.1.4 Benchmark Scenarios

There are four benchmark points we choose to study, given in Tab. 4.5. The allowed parameter space is investigated for all four scenarios in active-HNL mixing versus HNL mass planes in Sec. 5.5. The number density evolutions and interaction rates are studied explicitly through cosmological history for scenarios 1 and 2 as examples. These benchmark points satisfy the requirements that HNL decays before the start of BBN and ALP decays before the start of CMB. The reason for these choice

Scenario	m_N [GeV]	$\lvert U_{eN}\rvert^2$	f_a [GeV]	m_a [keV]
1	10^{-1}	10^{-10}	10^{3}	1
2	$10^{-0.4}$	$10^{-9.2}$	$10^{5.5}$	1
3	-	-	10^{3}	10^{-2}
4	-	-	$10^{5.5}$	10^{-2}

Table 5.1: Benchmark scenarios labelled by the red squares on Fig.5.6. For fixed ALP mass $m_a = 1$ keV, they are $m_N = 10^{-1}$ GeV and $|U_{eN}|^2 = 10^{-10}$ for $f_a = 10^3$ GeV and $m_N = 10^{-0.4}$ GeV and $|U_{eN}|^2 = 10^{-9.2}$ for $f_a = 10^{5.5}$ GeV respectively. The last two scenarios are given at fixed $m_a = 10$ eV for $f_a = 10^3$ GeV and $f_a = 10^{5.5}$ GeV, respectively.

is explained in Sec. 5.2 and the points are also deliberately chosen in (or close to) the seesaw region in order to explain massive neutrinos.

5.2 Cosmological History of HNLs and ALPs

In the hot dense plasma of the early Universe, it is expected that the interactions between the HNLs and SM particles are strong enough to maintain thermal and chemical equilibrium between the two sectors. HNLs with masses around the GeV scale typically do not have time to freeze-out as their decays into SM particles, and in our framework into ALPs, will deplete their abundance sufficiently fast. On the other hand, the interactions of HNLs and SM particles with ALPs are typically weak, and hence we assume that that ALPs do not start in thermal equilibrium with the SM and HNLs, and that their initial abundance is negligible (freeze-in production). The scattering between ALPs and HNLs might briefly bring the ALPs in thermal equilibrium, for small enough f_a, but they would soon freeze out, and eventually decay into active neutrinos. All of these decay channels and scattering rates play an important role in the evolution of the energy and number densities of HNLs and ALPs throughout the history of the universe. The most relevant processes that determine the abundances of HNLs and ALPs can be seen in Fig.5.3.

The change on the energy and number densities of the various particle species due to the expansion of the universe and the processes in Fig. 5.3 can be computed with the Boltzmann equations for the expanding Universe [206, 207]

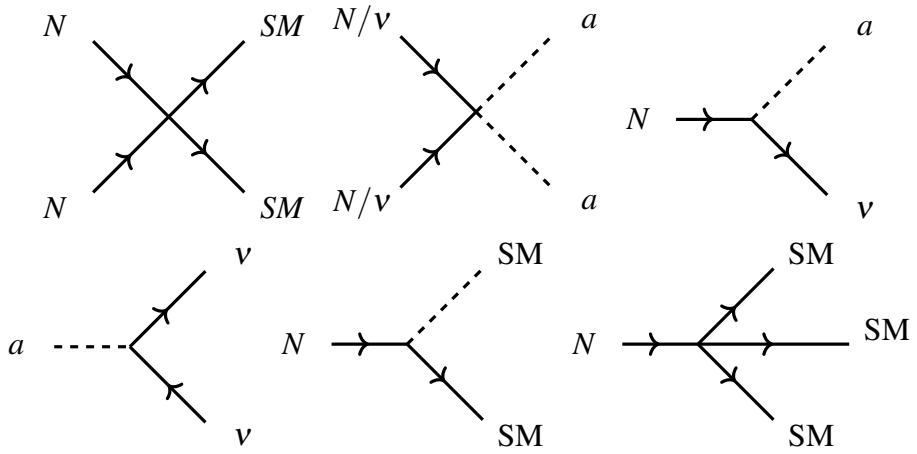

Figure 5.3: Relevant processes for the scattering of HNLs, ALPs and SM particles, responsible for determining their abundances. The diagrams on the top describe the scattering of HNLs with SM particles ($NN \leftrightarrow$ SM), and the scattering of HNLs or active neutrinos with ALPs ($NN \leftrightarrow aa$). The diagrams on the right and second row depict the decays of HNLs ($N \to a\nu$ and $N \to SM$) and ALPs ($a \to \nu\nu$).

$$\begin{aligned} \frac{d\rho_i}{dt} + 3H(\rho_i + p_i) = \frac{\delta\rho_i}{\delta t} &= \int g_i E \frac{d^3p}{(2\pi)^3} \mathscr{C}[f] \\ \frac{dn_i}{dt} + 3Hn_i = \frac{\delta n_i}{\delta t} &= \int g_i \frac{d^3p}{(2\pi)^3} \mathscr{C}[f] \end{aligned} \tag{5.13}$$

where ρ_i, p_i and n_i are energy density, pressure and number density of particle i, H the Hubble parameter, g_i its internal degrees of freedom and $\delta\rho_i/\delta t$ and $\delta n_i/\delta t$ the energy and number density transfer rates, computed with the collision operator $\mathscr{C}[f]$, which takes into account all energy and number changing processes.

As mentioned earlier, the addition of the ALPs to this model has the intended consequence of forcing the HNLs to decay faster than in vanilla HNL models. Consequently, even for HNL masses of the order of 10-100 MeV, HNLs decay fast enough to avoid affecting the BBN abundances. In contrast, the ALPs should not decay before BBN, otherwise they would in turn modify BBN. Therefore, we study the HNL and ALP abudances in two different time epochs, before BBN and between BBN and recombination[1]. After recombination the ALPs may or may not be

[1]We should mention that we here consider the onset of BBN to occur at the time of neutrino decoupling, i.e. $t \sim 1$ s. This approximation holds as long as none of the number changing processes involved are active between that time and the end of BBN, $t \sim 10^4$ s.

stable, and that will have some astrophysical consequences that will discussed in Section 5.3.

5.2.1 Abundances before BBN

We start by assuming that after some inflationary epoch and subsequent reheating, the SM particles are in equilibrium in the early Universe. The actual value of the reheating temperature is no importance, since most particles will be at their equilibrium densities, but it must be low enough to ensure that the ALPs are not strongly coupled after reheating. The HNLs are thus assumed to be in thermal and kinetical equilibrium with the SM, but the ALPs are not. The evolution of the densities of HNL and ALP can be described by coupled Boltzmann equations, as in Eq. (5.13). Before neutrino decoupling, the HNL number density is given by

$$\begin{aligned}\frac{dn_N}{dt}+3Hn_N =& -\langle\sigma_{NN\to SM}\,v\rangle\left(n_N^2-n_N^{\mathrm{eq},2}\right)-\langle\sigma_{NN\to aa}\,v\rangle\left(n_N^2-n_N^{\mathrm{eq},2}\frac{n_a^2}{n_a^{\mathrm{eq},2}}\right)\\ &-\langle\Gamma_{N\to SM}\rangle\left(n_N-n_N^{\mathrm{eq}}\right)-\langle\Gamma_{N\to a\nu}\rangle\left(n_N-n_N^{\mathrm{eq}}\frac{n_a}{n_a^{\mathrm{eq}}}\right)\end{aligned} \tag{5.14}$$

where $\langle\sigma_{NN\to\mathrm{SM}}v\rangle$, $\langle\sigma_{NN\to aa}v\rangle$, $\langle\Gamma_{N\to\mathrm{SM}}\rangle$ and $\langle\Gamma_{N\to a\nu}\rangle$ are the thermally-averaged scattering cross-sections of HNL annihilation to SM particles and ALPs, and the thermally-averaged decay widths of HNLs into light SM particles and ALP-active neutrino pairs, respectively. The quantities n_X^{eq} denote the equilibrium number density of any species ($X=N,a$). Similarly the Boltzmann equation for ALPs is

$$\begin{aligned}\frac{dn_a}{dt}+3Hn_a =& -\langle\sigma_{aa\to\nu\nu}\,v\rangle\left(n_a^2-n_a^{\mathrm{eq},2}\right)-\langle\sigma_{aa\to NN}\,v\rangle\left(n_a^2-n_a^{\mathrm{eq},2}\frac{n_N^2}{n_N^{\mathrm{eq},2}}\right)\\ &-\langle\Gamma_{a\to\nu\nu}\rangle\left(n_a-n_a^{\mathrm{eq}}\right)+\langle\Gamma_{N\to a\nu}\rangle\left(n_N-n_N^{\mathrm{eq}}\frac{n_a}{n_a^{\mathrm{eq}}}\right)\end{aligned} \tag{5.15}$$

which also contains various contributions from the scattering of ALPs with the HNLs and neutrinos and the thermally averaged ALP decay width $\langle\Gamma_{a\to\nu\nu}\rangle$. The solution of these Boltzmann equations will give the evolution of the number densities of HNLs and ALPs between some unspecificed reheating time and the time of neutrino decoupling, $t\sim 1$ s. The solve the Boltzmann equations we make a vari-

able transformation, to the comoving yield $Y_X = n_X/s$ for any species X, where s is the entropy density given by

$$s = \frac{2\pi^2}{45} g_* T^3. \tag{5.16}$$

where g_* are the number of relativistic degrees of freedom and T the temperature of the thermal bath of SM particles. The Boltzmann equations for the yield Y_X are therefore

$$\begin{aligned} zHs\frac{dY_N}{dz} &= -\gamma^{\rm eq}_{NN\to SM}\left(\frac{Y_N^2}{Y_N^{\rm eq,2}} - 1\right) + \gamma^{\rm eq}_{aa\to NN}\left(\frac{Y_a^2}{Y_a^{\rm eq,2}} - \frac{Y_N^2}{Y_N^{\rm eq,2}}\right) \\ &\quad - \gamma_{N\to SM}\left(\frac{Y_N}{Y_N^{\rm eq}} - 1\right) - \gamma_{N\to a\nu}\left(\frac{Y_N}{Y_N^{\rm eq}} - \frac{Y_a}{Y_a^{\rm eq}}\right), \\ zHs\frac{dY_a}{dz} &= -\gamma^{\rm eq}_{aa\to \nu\nu}\left(\frac{Y_a^2}{Y_a^{\rm eq,2}} - 1\right) - \gamma^{\rm eq}_{aa\to NN}\left(\frac{Y_a^2}{Y_a^{\rm eq,2}} - \frac{Y_N^2}{Y_N^{\rm eq,2}}\right) \\ &\quad - \gamma_{a\to \nu\nu}\left(\frac{Y_a}{Y_a^{\rm eq}} - 1\right) + \gamma_{N\to a\nu}\left(\frac{Y_N}{Y_N^{\rm eq}} - \frac{Y_a}{Y_a^{\rm eq}}\right), \end{aligned} \tag{5.17}$$

where $z = m_N/T$ and the thermally averaged decay/scattering density $\gamma_{X\to Y}$ is defined as

$$\gamma_{X\to Y} = n_X^{eq}\frac{K_1(z)}{K_2(z)}\Gamma_{X,0}, \tag{5.18}$$

with $\Gamma_{X\to Y,0}$ the rest frame decay with / scattering rate for the given process at zero temperature, and $K_{1(2)}(z)$ are the Bessel function of first (second) kind. The relation between the thermally averaged cross-section, the interaction rate and the thermally averaged interaction density,

$$\langle\sigma_{X\to Y}v\rangle n_X^{eq,2} = \langle\Gamma_{X\to Y}\rangle n_X^{eq} = \gamma_{X\to Y} \tag{5.19}$$

The decay and scattering rates, normalised to the equilibrium number density of the parental particles, are shown in the bottom plots of Fig. 5.4 and 5.5 as a function of the inverse temperature $z = m_N/T$, from some arbitrary initial reheating temperature $T_R = 10^6$ GeV until the formation of the CMB. The bottom panels in Fig. 5.4 and 5.5 use benchmark values of the model parameters of scenario 1 (Fig. 5.4) or scenario 2 (Fig. 5.5) according to Tab. 5.1. These values are chosen

to showcase a scenario where the dominant decay channel of HNLS is via ALPs and also the ALPS enter briefly into thermal equilibrium before BBN (top), and a scenario where the HNLs decay with almost equal likelihood to ALPS and SM particles, and also the ALPs are never in equilibrium (bottom).

As the universe cools down from the reheating era ($z \sim 10^{-6}$) to the time of neutrino decoupling ($10^2 < z < 10^3$), the annihilation processes for the HNLs become inefficient, $\gamma^{\rm eq}_{NN\to \rm SM}, \gamma^{\rm eq}_{NN\to aa} \ll H$, and the HNLs would undergo thermal freeze-out in the absence of decays. However, the decays of HNLs to ALPs (and SM particles if not-negligible) kick in sufficiently before BBN so as to deplete the abundance of HNLs early enough and not affect the formation of nuclei. It is worth noting that in either scenario depicted in the bottom panels Fig. 5.4 and 5.5, the decay of ALPs is extremely inefficient for most of the temperature range, only becoming efficient after BBN. Because of this, for the solution of the Boltzmann equations in eq. (5.17) until the time of neutrino decoupling, we neglect the contribution from ALP decays.

The evolution of the number densities of HNLs and ALPs can be seen in the top panels of Fig. 5.4 and 5.5, for the same benchmark scenarios as before. As expected, the abundance of HNLs depletes very fast once their decays becoming efficient. In the panel on the top, the HNL starts decaying before falling out of thermal equilibrium and thus follows the equilibrium density, whereas the bottom panel shows that the HNLs freeze-out for a short time, only decreasing with the expansion and Boltzmann suppression, before the decays completely overtake them and destroy the HNL abundance. If the ALPs are sufficiently strongly coupled to the HNLs, they would enter in thermal equilibrium for a short period of time before BBN, as seen in the top panel of Fig. 5.4, where their number density follows the equilibrium number density of relativistic particles. Conversely, for weakly coupled ALPs (bottom panel), the ALPs are never in thermal equilibrium, their number density increases while their production via scattering or decays of HNLs is efficient, and ultimately they undergo freeze-in some time before the beginning of BBN.

5.2.2 Abundance of ALPs after BBN and temperature evolution

As we saw before, in all scenarios we consider, the abundance of HNLs depletes very fast before BBN. As a consequence, the main production mechanisms for ALPs, which were HNL-ALP scattering and HNL decays, are really inefficient after BBN and thus the ALP abundance only decreases at late times. Even the process $\nu\nu \to aa$ falls out of thermal equilibrium significantly before BBN. Therefore, the abundance of ALPs after the end BBN is solely determined by their decays. Their Boltzmann equation is therefore given by [208]

$$zHs\frac{dY_a}{dz} = -\gamma_{a\to\nu\nu}\left(\frac{Y_a}{Y_a^{\rm eq}} - 1\right), \qquad z > z_{\rm BBN}. \tag{5.20}$$

If the ALP decays are fast enough, as in the top panel of Fig. 5.4, the ALPs decay shortly after the end of BBN, and their number density completely disappears. Conversely, the abundance of long-lived ALPs becomes frozen-out after BBN as the top panel of Fig. 5.5 shows, and will only deplete slowly, depending on their lifetime.

Before neutrino decoupling, the temperatures of the photon and neutrino baths evolved together, changing only via adiabatic cooling since ALP decays are negligible before BBN [209]. After the end of BBN, however, the decays of ALPs to neutrinos, $a \to \nu\nu$ become relevant, which will introduce energy into the neutrino bath and thus increase its temperature. An increase on the neutrino temperature relative with the photon temperature at the time of recombination has a strong impact on the number of effective neutrino degrees of freedom $N_{\rm eff}$. Because of this, we need to track separately the evolution of the photon and neutrino temperatures from the end of BBN until the formation of the CMB. Neglecting chemical potentials and effects from neutrino oscillations, the evolution of the temperatures with time

is given by [207, 210]

$$\begin{aligned}\frac{dT_\gamma}{dt} &= -\frac{4H\rho_\gamma + 3H(\rho_e + p_e)}{\frac{\partial\rho_\gamma}{\partial T_\gamma} + \frac{\partial\rho_e}{\partial T_\gamma}} \\ \frac{dT_\nu}{dt} &= -\frac{12H\rho_\nu + 3H(\rho_a + p_a) + \delta\rho_a/\delta t}{3\frac{\partial\rho_\nu}{\partial T_\nu} + \frac{\partial\rho_a}{\partial T_\nu}}\end{aligned} \tag{5.21}$$

where ρ_i and p_i are the energy density and pressure of particle species i, and $\delta\rho_a/\delta t$ is the energy exchange rate from ALPs to neutrinos, given by the collision operator in eq. (5.13). Eq. (5.21) takes into account the decoupling of the electrons from the photon bath when they become non-relativistic, as well as the decoupling of the ALP from the neutrino bath when $T_\nu \gtrsim m_a$.

5.2.3 Abundance and Interaction Rate Evolution

Fig. 5.4 and 5.5 show the evolution of the thermally averaged scattering and decay rates (bottom row) and the number density of various species (top row) for two different scenarios from Table 4.5. Scenario 1 has $m_N = 10^{-1}$ GeV, $|U_{eN}|^2 = 10^{-10}$, $f_a = 10^3$ GeV and $m_a = 1$ keV. Scenario 2 has $m_N = 10^{-0.4}$ GeV, $|U_{eN}|^2 = 10^{-9.2}$, $f_a = 10^{5.5}$ GeV and $m_a = 1$ keV.

The rate evolution plots (bottom) show how the various rates compare to the Hubble parameter (red). In scenario 1 in Fig. 5.4, the thermally averaged scattering rate $aa \to NN$ (solid blue) begins becomes efficient for a short period of time at around $z \sim 1$, which brings the ALPs and HNLs close to thermal equilibrium. Other scattering rates, such as $aa \to \nu\nu$, with either N (dotted blue) or ν (dashed blue) mediation, are negligible. Once the ALP-HNL scattering rate becomes inefficient shortly before the onset of BBN, HNL decays to ALPs (green) become the primary source of ALP production while the HNLs are abundant enough. Other HNL decays to SM particles (orange) only become efficient in scenario 1 much after all HNLs have decayed away to ALPs, and thus have to effect on the evolution. Lastly, a long time after BBN, but before recombination, the decays of ALPs, $aa \to \nu\nu$ (pink) become efficient and make the ALPs decay completely before the formation of the CMB. On the other hand, in scenario 2 in Fig. 5.5, the scattering rates are never

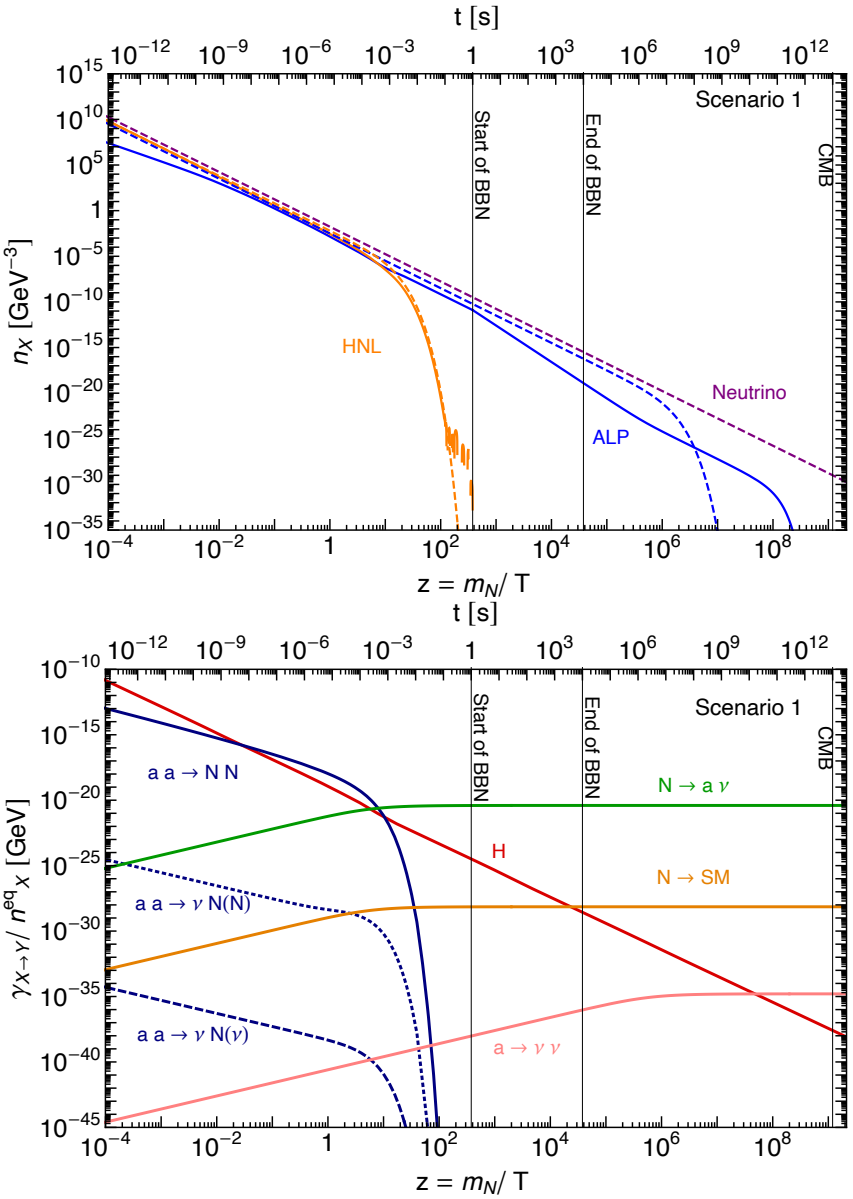

Figure 5.4: Evolution of the number densities (top) and the rates for relevant processes (bottom) for benchmark scenario 1 as given in Tab. 4.5. The blue lines on the rate plots show the ALP to HNL annihilation rates (solid), ALP to a neutrino and a HNL annihilation rates via HNL exchange (dotted) and ALP to a neutrino and a HNL annihilation rates via light neutrino exchange (dashed). The green curves give the thermally averaged decay rates for HNL to ALP and a neutrino and the yellow curve give the rates for SM HNL decay channel. There is also the di-neutrino decay rates for ALP which is represented by the pink curves. Finally, the red curves give the evolution of Hubble parameter. The blue and orange lines represent the number densities for ALP and HNL respectively. The dashed lines denote the equilibrium number densities for the corresponding species and neutrinos (purple line).

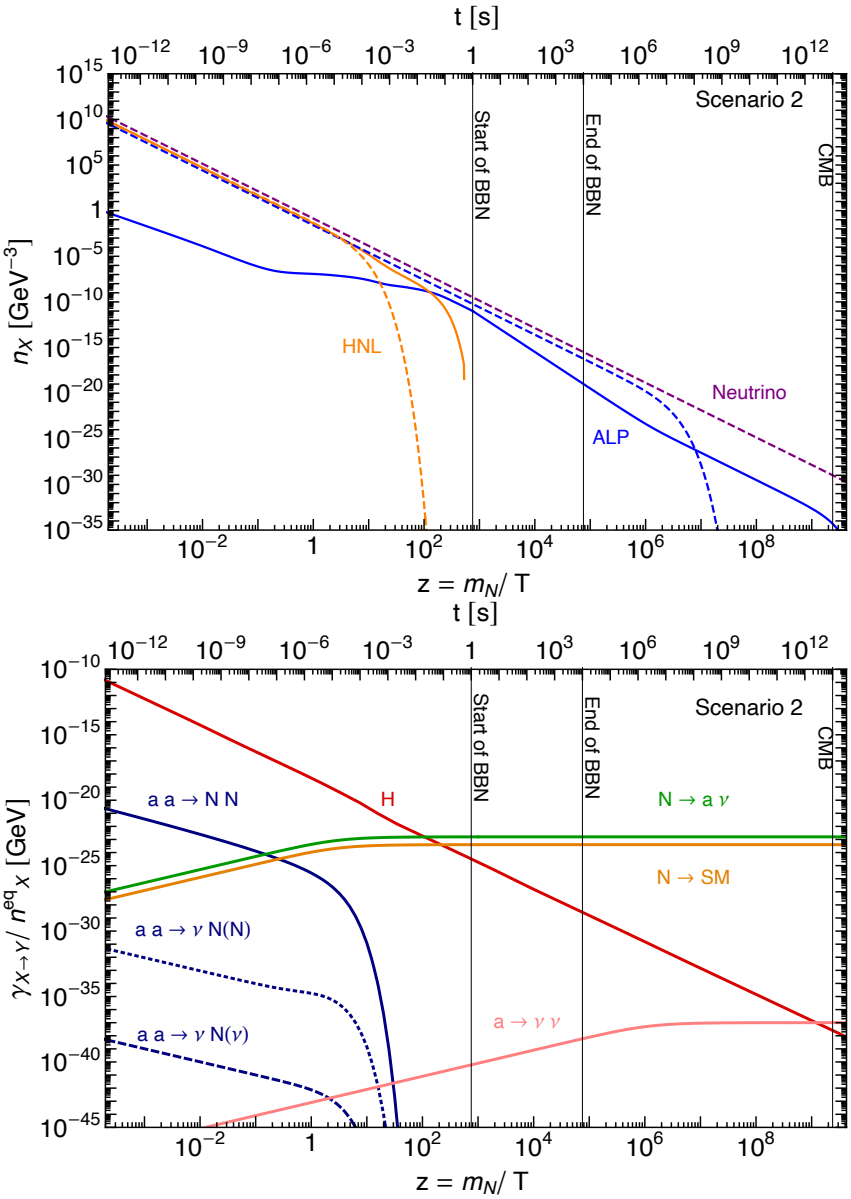

Figure 5.5: As Fig. 5.4 but for benchmark scenario 2.

efficient enough, so the HNLs and ALPs are never in thermal equilibrium. The decay of HNLs to ALPs (green) is thus the only source of ALP production, but in this scenario it is comparable to the HNLs decays to SM particles (orange), and thus not all HNLs decay to ALPs. Since the ALP-neutrino interaction rate is weaker compared to scenarion 1, larger f_a, ALPs do not decay efficiently in scenario 2, as their decay rate only becomes efficient around or after the formation of the CMB, which causes the ALPs to survive after recombination.

In the number density plots (top), the orange curves show the actual (solid)

and equilibrium (dashed) number density for HNL, the blue curves shgow the actual (solid) and equilibrium (dashed) number density for ALP and the dashed purple curve gives the equilibrium density for neutrinos. In scenario 1, the strong scattering between HNLs and ALPs brings them close to thermal equilibrium at around $z \sim 1$. Shortly after, the HNLs become non-relativistic and thus their actual and equilibrium abundances are Boltzmann suppressed, thereby falling rapidly before BBN. Since the ALPs and HNLs are close to equilibrium already, the incrasing effect of HNL decays on the ALP abundance is small, and in fact causes the ALP abundance to decrease as inverse decays tend to dominate when the ALP population is high. Lastly, after BBN the ALPs become non-relativistic, but initially there are no equilibrium processes that can deplete their abundance, and thus they freeze-out, i.e. their real abundance (solid blue) overshoots their equilibrium abundance (dashed blue). Finally, shortly before recombination, ALPs decay to light neutrinos, depleting their abundance completely. In scenario 2, the ALPs are never in thermal equilibrium, and are only efficiently produced by HNL decays, so they freeze-in after the HNLs become non-relativistic and disappear. In this scenario, ALPs are longer lived, and thus their abundance freezes-out, as before, but only depletes slowly before the formation of the CMB.

5.3 Astrophysical and Cosmological Constraints

In this work we have introduced two new particles, a HNL and an ALP. that modify very significantly the evolution of the early Universe compared to ΛCDM. The cosmological and astrophysical implications of both of these species are well known separately [211, 212]. However, their combination has a somewhat different effect, as the HNLs are allowed to be lighter than in most previous scenarios, due to the weakening of the BBN bound (see below), and also due to the ALPs coupling exclusively to neutrinos via the HNL portal. Consequently we need to evaluate the predictions of our model towards known cosmological and astrophysical observables and hence assess whether their strong constraints render the model invalid or there are still parameter combinations that are unconstrained. For this purpose

we study how this model affects the formation of primordial elements (BBN), the observations of the CMB, as well as astrophysical constraints such as those from the observation of the supernova SN1987A, and others such as Extragalactic background light (EBL) or X-ray constraints.

5.3.1 Big Bang Nucleosynthesis

The predictions of ΛCDM with regards to the formation of the primordial elements match very well with their observed present abundances[2] These predictions are, however very sensitive to the cosmological state of the Universe at any time between neutrino decoupling and the CMB. Any modification of the temperature of neutrino decoupling, the rate of expansion of the Universe or energy injection in the primordial plasma, may cause a catastrophic change on the formation of light elements. This is specially true in our scenario, where the decays of HNLs into mesons disturb the $p \leftrightarrow n$ conversion processes that set the initial proton and neutron abundances for BBN [215]. If the HNLs decay fast enough, however, the abundances of protons and neutrons have time to restore to the expected values from ΛCDM, and thus there is no effect on BBN. Hence, we set a conservative limit on the HNL lifetime of $\tau_N < 0.023$ s [215], beyond which the decays will disturb the BBN abundances too much and is therefore marked as excluded in our scenario.

In addition to the decays of the HNLs, the decays of ALPs may also modify the primordial plasma and affect BBN. If the ALPs decay before neutrino decoupling, since their primary decay channel is $a \to \nu\nu$, they would modify the neutrino spectrum and increase the temperature of the neutrino bath, thereby delaying neutrino decoupling and the formation of primordial elements. Consequently, we do not consider scenarios where the ALPs have short lifetimes, and to ensure that they do not directly affect BBN, we only consider ALPs decaying after the end of BBN, i.e $\tau_a > 10^4$ s. Subsequent decays of the ALPs may also dissociate the formed elements and modify their abundance [209], however this dissociation is mostly caused

[2]The present-day abundance of ^7Li is currently is disagreement with the predictions from standard cosmology. Attempts have been made to provide an explanation in modified cosmologies, with varying degrees of success. Therefore, it remains unclear whether this is caused by modifications over ΛCDM or an inaccurate measurement of their present abundance [213, 214].

by electromagnetic cascades, which are rare in our scenario since the decay rate of $a \to \gamma\gamma$ is negligible.

Even if the ALPs do not decay before BBN, they may still affect the formation of the primordial elements if they are too abundant. Since ALPs are relativistic before neutrino decoupling, a sufficient abundance would act as dark radiation and thus modify the Hubble rate during radiation domination. This effect can be understood as increase in the neutrino temperature and therefore results in a modification on the value of $N_{\rm eff}$ at the time of BBN [216]. Since the contribution from dark radiation is only relevant when the ALPs are close to thermal equilibrium, we can parametrise the deviation from ΛCDM as

$$\Delta N_{\rm eff}^{\rm BBN} \approx \frac{\rho_a}{\rho_\gamma} \approx \frac{\rho_a^{eq} n_a}{n_a^{eq} \rho_\gamma} \tag{5.22}$$

where ρ_γ is the energy density in photons at BBN. Though $N_{\rm eff}$ is not directly measured at BBN, it can inferred from the measured value at recombination by Planck [30], to be [217] $N_{\rm eff}^{\rm BBN} = 2.86 \pm 0.15$, hence we set an upper bound on the ALP abundance at BBN by requiring $\Delta N_{\rm eff}^{\rm BBN} \lesssim 0.2$.

BBN is one of the most important probes to early Universe which can be tested and measured by both laboratory experiments and cosmological observations [218–220]. In the ΛCDM model, the primordial abundance of light nuclei such as ^{2}H, ^{4}He and ^{7}He, can be calculated directly from the SM. The light element abundance nowadays can be therefore predicted with the aid of simulated galactic chemical evolution [221]. The abundance of light nuclei is parameterised by the baryon to photon ratio η_B as mentioned in Section 3.4 or baryon density $\omega_B = \Omega_B h^2$. The current best observed data is $\omega_B = 0.02236 \pm 0.00029$ [30] which agrees with theoretical predictions [213, 222–225]. The presence of new non-relativistic particles at BBN will increase the light nucleus abundances due to the increase in energy density compared to relativistic particles. MeV-GeV HNLs as super-weakly interacting particles can decay to the SM particles via active-sterile mixing $U_{\nu N}$ which is $|U_{\nu N}| \ll 1$ due to the seesaw relation $m_\nu = m_N |U_{\nu N}|^2$. The decay products of HNLs will inject energy to the SM thermal plasma of the Universe and therefore increase

the temperature and shift chemical equilibrium of the weak processes. This restricts the HNL life time to be $\lesssim 1$ sec [123]. Furthermore, mesons from HNL decay can also increase the production of ^{4}He and further constrain the HNL life time to be $\lesssim 0.02$ sec [215].

5.3.2 Cosmic Microwave Background

After the end of BBN, any particle that injects energy in the primordial plasma will modify to some extent the observations of the CMB. The impact of energy injected before recombination would work to heat up the plasma and hence cause changes to the observed anisotropies in the CMB power spectrum. However, since the major source of energy injected is via ALP decays to neutrinos, the energy injected into the photon bath is negligible, and thus we not expect constraints arising from CMB anisotropies. Late time decays of ALPs could also cause spectral distortions in the black body spectrum of the CMB if the decays heat up the photon batch significantly [226]. Fortunately, as before, the decay rate from ALPs to photons is neglibile and we assume that secondary energy injected into the photon spectrum from the decays to neutrinos can be safely ignored.

The most significant impact of the decays of ALPs for recombination is the modification of the neutrino temperature. Since neutrino decoupling, the photon and neutrino temperatures evolved independently which, even in ΛCDM, causes a value of the effective neutrino degrees of freedom as $N_{\rm eff} = 3.044 \pm 0.384$ [30]. ALP decays before the formation of the CMB increase the neutrino temperature, as in eq.(5.21). This increase of the temperature of the neutrino bath with respect to that of the photon bath, causes the value of $N_{\rm eff}$ to increase from the expectations of ΛCDM, as

$$N_{\rm eff}^{\rm CMB} = N_{\rm eff}^{\rm BBN} \left(\frac{11}{4}\right)^{\frac{4}{3}} \left(\frac{T_\nu}{T_\gamma}\right)^4 \tag{5.23}$$

which strongly constraints the decay rate of ALPs.

Lastly, from observations of the CMB, the abundance of non-baryonic matter (dark matter) was observed to be around $\Omega_{\rm DM} \sim 0.12$. ALPs that become non-relativistic before recombination, and they have lifetimes larger than $\tau_a > 10^{13}$ s,

would survive long enough to contribute their abundance to that of dark matter. Therefore this also sets a strong constraint on the total abundance of ALPs at the time of recombination, which is partially complementary to the constraint on N_{eff}.

5.3.3 SN1987A

The core of supernovae (SN) are very hot and dense systems, with temperatures of the order of $T \sim 30$ MeV. Most of the particles created in such energetic medium are trapped and contribute to the energy transfer inside the SN core. Weakly coupled particles, however, can free-stream and escape the core, contributing to the cooling of the SN. The primary source of cooling for SNs are neutrinos, which can escape as long as they have energies $E_\nu \lesssim 30$ MeV. This neutrino burst was observed for SN1987A by various water Cherenkov detectors, including Kamiokande-II [227, 228]. Besides neutrinos, the HNLs and ALPs in our model could also escape the SN core as they interact very weakly with the SN inner medium, and contribute to SN cooling [229–234]. This additional source of cooling is very constrained by measurements of the luminosity of SN1987A. Secondary decays of HNLs and ALPs into neutrinos produce a high-energetic additional flux of active neutrinos that could have been detected alongside the normal neutrino burst [232,233]. The combination of SN cooling and the additional neutrino flux can impose strong constraints on our model for high couplings.

For both HNLs and ALPs, the constraint on the secondary neutrino flux is much stronger than the constraint from SN cooling [233, 234], and hence we only include the former in our study. Typical constraints on the secondary neutrino flux from HNL decays assume decay rates for HNLs in the absence of additional channels, so the $N \to \pi\nu$ and $N \to 3\nu$ decays dominates [231]. Other studies involving SN constraints on lighter HNLs can be found in [229, 235–237]. In our model the primary decay channel for HNLs is to ALPs, which consecutively decay to a pair of neutrinos. Hence, neglecting resonant effects, the secondary neutrino flux from HNLs can be approximated to that arising from the 3-body decay of the HNLs to neutrinos. Even though the 2-body decay branching ratio is around 7 times larger than the 3-body decays for HNL masses in the 100 MeV range, Cherenkov detec-

tors are more sensitive to the 3-body decays, since the interaction cross section of antineutrinos, only produced in 3-body decays, is around 100 times larger than that of neutrinos from our numerical result [227]. Therefore, SN limits on traditional HNL decays can be directly applied to our scenario. We thus use the limits on HNL masses and mixing from Fig. 2 of [234] to constrain the large mixing angle regions in our model.

In addition to HNLs, ALPs can also be produced in the core of SN. The expected secondary neutrino flux from decaying ALPs with masses below the keV scale is smaller than that from HNL decays that can escape the SN core. However, heavy HNLs cannot escape and thus SN constraints from the production of ALPs are stronger for $m_N \gtrsim 400$ MeV. From Fig. 5 of [234], we can see that the coupling between the ALP and the electron-neutrino g_{ae} must be $g_{ae} \lesssim 10^{-7}$ for keV-scale ALPs. In our model, g_{ae} is given by Eq. (5.11), which imposes only weak limits for heavy HNLs and large HNL-ALP couplings, beyond the ranges considered in our study.

Lastly, there could be additional constraints from secondary decays of HNLs and/or ALPs to photons [66, 238–242]. However, these are negligible as the photonic branching ratios of both particles are very small for the masses considered.

5.3.4 Other Astrophysical Constraints

In addition to the astrophysical constraints from SN cooling and its secondary fluxes, there is a plethora of possible astrophysical probes of ALPs. The production of ALP in the core of white dwarfs or RGB stars can lead to strong cooling, and even provide an explanation for the observed cooling hints [243,244]. In fact, it has been shown that an ALP with a coupling to electrons of the order $g_{ae} \sim 10^{-13}$ provides a good fit to stellar cooling data [244]. However, in our model the ALP-electron coupling is very small, so much that the value $g_{ae} \sim 10^{-13}$ can only be reached for mixings $U_{eN}^2 \sim 10^{-1}$ and HNL masses $m_N \sim 1$ TeV. Since this parameter region is beyond our scope, and anyways disfavoured by various cosmological constraints, as we will see later, we neglect the constraints from stellar cooling in our study.

Long-lived ALPs that survive after recombination may still be observable to-

day through their decay products. The photons injected by ALP decays are the most detectable candidates, as they can be probed in observations of the extragalactic background light (EBL) or via X-rays [245]. For ALP masses below the keV scale, the constraints on the ALP-photon coupling from X-ray and EBL surveys require that $g_{a\gamma} \lesssim 10^{-15}$ GeV^{-1} [226, 245]. In our model, however, the ALP-photon coupling is derived at two-loop order, and therefore extremely small. As above, only for very large mixings $U^2_{eN} \sim 10^{-3}$ and large HNL masses $m_N \sim 1$ TeV, has this constraint any effect. Consequently, we also ignore any astrophysical constraints from late-time photonic decays of ALPs.

5.4 Impact on Direct HNL Searches

Future HNL searches, especially those based on long-lived signatures, will probe small active-sterile mixing strengths approaching the seesaw expectation. Prominent examples of proposed and planned searches are PIONEER [163], NA62 [164, 246], DUNE [165], SHiP [166], FCC-ee [167] and Faser [247]. A dedicated analysis is needed to present a study of the sensitivity in our scenario depending on the specific search strategy. Such a detailed analysis is beyond the scope of this chapter and will be considered in future work. In this section, we will assess how the sensitivity is modified in the presence of new HNL-ALP coupling in the context of DUNE. We qualitatively describe the approach for calculating the expected number of signal events in the DUNE near detector (ND) based on the analysis [248]. The ND is located at a distance of $L = 574$ m from the HNL production point, with a transverse cross-section of $A = 12$ m^2 and a depth of $\Delta L = 5$ m along the beam axis. Following [248], we write the expected number of signal events as

$$N_{\text{sig}} = N_P \times \text{Br}(\text{P} \to \text{N}) \times \text{Br}(\text{N} \to \text{charged}) \times \varepsilon_{\text{geo}}, \tag{5.24}$$

where N_P is the relevant production fraction of positively charged and neutral pseudoscalar mesons multiplied by the total number of protons on target $N_{\text{POT}} = 6.6 \times 10^{21}$ for a 120 GeV proton beam at DUNE, $\text{Br}(\text{P} \to \text{N})$ are the branching fractions of HNL production from the meson P, $\text{Br}(\text{N} \to \text{charged})$ is the branching

fraction of produced HNL decaying into charged lepton pairs and ε_{geo} corresponds to the geometric efficiency,

$$\varepsilon_{\text{geo}} = e^{-\frac{m_N \Gamma_N}{p_{N_z}} L} \left(1 - e^{-\frac{m_N \Gamma_N}{p_{N_z}} \Delta L}\right). \tag{5.25}$$

Here, p_{N_z} is the momentum of the HNL along the beam axis in the lab frame, where we have considered $p_{N_z} = 7.5$ GeV, following the simulation of meson production from a pp collision at $\sqrt{s} = 15$ GeV [248]. As we have not explicitly simulated any events and analysed with respect to detector level cuts, for simplicity, we will consider, in our analysis, that all produced HNL events will be accepted at detector level.

In the presence of the HNL-ALP coupling as well as the new HNL decay channel $N \to a\nu$ in our scenario, the corresponding total decay width will also be affected. Correspondingly, the partial decay width of HNLs decaying into visible final states as well as the geometrical efficiency factor will change. In contrast, the production rate N_P as well as the branching ratio of the HNL production from mesons is unaffected. We thus consider the relative change in the number of events,

$$\frac{N'_{\text{sig}}}{N_{\text{sig}}} = \frac{\text{Br}'(\text{N} \to \text{charged})}{\text{Br}(\text{N} \to \text{charged})} \frac{\varepsilon'_{\text{geo}}}{\varepsilon_{\text{geo}}} \tag{5.26}$$

where the unprimed and primed quantities correspond to $\Gamma_N \equiv \Gamma^{N \to \text{SM}}$ and $\Gamma'_N \equiv \Gamma^{N \to \text{SM}} + \Gamma^{N \to a\nu}$, respectively, as discussed in Sec. 4.4.3 and Sec. 5.1.2. From Fig. 5.1, we can notice that for $(m_a, f_a) = (1\text{ keV}, 1\text{ TeV})$, the total decay width of the HNL is dominated by $N \to a\nu$ throughout the mass range considered, while for $(1\text{ keV}, 10^{2.5}\text{ TeV})$, up to $m_N \sim m_\pi$, $N \to a\nu$ dominates the scenario and beyond this point, it drops significantly. Furthermore, as the decay widths for $N \to a\nu$ and $N \to \text{SM}$ have the same U_{eN} dependence, the branching fractions are independent of U_{eN}.

Likewise, the ratio of the geometric efficiencies can be approximated by

$$\frac{\varepsilon'_{\rm geo}}{\varepsilon_{\rm geo}} = \exp\left[-\frac{m_N}{p_{N_z}}\Gamma(N\to a\nu)L\right]\frac{\Gamma'_N}{\Gamma_N}, \tag{5.27}$$

for a shallow detector depth ΔL, i.e., for $(m_N/p_{N_z})\Gamma'_N\Delta L \ll 1$. The ratio of decay rates in this expression is equal to $\Gamma'_N/\Gamma_N = {\rm Br}(N\to{\rm charged})/{\rm Br}'({\rm N}\to{\rm charged})$, thus canceling the corresponding ratio in Eq. (5.26) in this limit. Thus, we have

$$\frac{N'_{\rm sig}}{N_{\rm sig}} = \exp\left[-\frac{m_N}{p_{N_z}}\Gamma(N\to a\nu)L\right], \tag{5.28}$$

which approaches unity for long decay lengths, $(m_N/p_{N_z})\Gamma(N\to a\nu)L \ll 1$. Thus, for small $|U_{eN}|^2$ and m_N where $\Gamma(N\to a\nu) \ll p_{N_z}/(m_N L)$, we expect that DUNE will have the same sensitivity to the active-sterile mixing strength $|U_{eN}|^2$ in our HNL-ALP scenario as in the standard HNL case. For shorter decay lengths, the sensitivity will be reduced.

As another example for a direct search experiment we consider the existing NA62 experiment which uses a different search strategy as compared to DUNE. The NA62 experiment [246] used a secondary 75 GeV hadron beam containing a fraction of kaons, and has been able to probe the decays $K^+\to\ell^+N$. For small active-sterile mixing the decay length of HNL is much larger than the 75 m detector size and the process is characterised by a single detected track, that of the charged lepton – a positive signal is a peak in its missing mass distribution. As this experiment is currently insensitive to the decay of the HNLs, the presence of the $N\to a\nu$ decay channel will not affect the search as long as the decay length remains large.

5.5 Results and Discussion

The aim of this chapter is to find valid scenarios where the traditional BBN bound on HNLs [215] is relaxed due to the primary decays to ALPs. For this purpose we have performed some small scale parameter scans around the benchmark scenarios in Table 4.5 to illustrate this effect[3]. Figure 5.6 shows the results of these parameter

[3]We performed a grid scan on two parameters of the model, m_N and $|U_{eN}|^2$. This simplification is enough for our purposes as we only intend to highlight the crucial features of the model, but do not

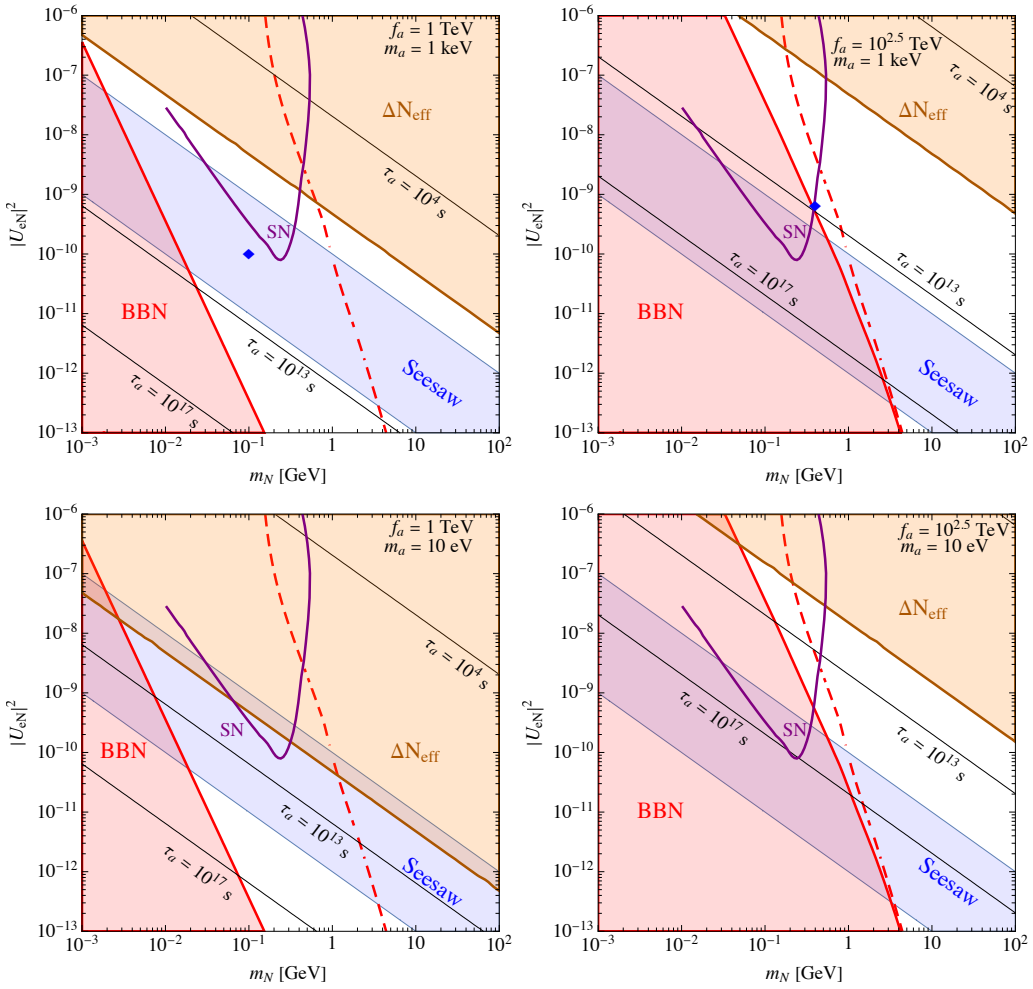

Figure 5.6: Allowed parameter regions in the m_N vs $|U_{eN}|^2$ plane for the four benchmark scenarios in Table 5.1: Upper left panel : $f_a = 1$ TeV, $m_a = 1$ keV, Upper right panel : $f_a = 10^{2.5}$ TeV, $m_a = 1$ keV, Lower left panel : $f_a = 1$ TeV, $m_a = 10$ eV, Lower right panel : $f_a = 10^{2.5}$ TeV, $m_a = 10$ eV. The red region shows the space disallowed by HNL decay time after the start of BBN, while the region left to red dashed contour is disfavored if HNL decays only via SM decay channels, in absence of ALP. The most stringent bound from cosmology, $N_{\rm eff} < 3.10322\ (\Lambda{\rm CDM}) + 0.0384\ (0.1\sigma_N)$ gives the brown forbidden region of active neutrinos produced from ALP decays. The region above the purple contour is excluded due to astrophysical constraints from supernova SN1987A. The seesaw regime for active neutrinos 1 meV $\lesssim m_\nu \lesssim$ 100 meV is shown in blue. The different black lines label the ALP decay time at 10^4 s (end of BBN), 10^{13} s (CMB) and 10^{17} s (today). Benchmark values from Tab.5.1 for scenario 1 and 2 with fixed m_N and $|U_{eN}|^2$ are denoted in top panels by blue diamonds.

scans, varying the values of $m_N = [10^{-3}, 10^2]$ GeV and $|U_{eN}|^2 = [10^{-13}, 10^{-6}]$. The

attempt to map the available parameter space nor perform any statistical interpretation of the results. For more details on the rigorous treatment of inference and statistics in physics see [**?**].

top row corresponds to scans around scenarios 1 and 2, with only m_a and f_a fixed, and, where the blue diamond markers are the fixed values of m_N and $|U_{eN}|^2$ from Table 4.5. The bottom row shows scans of scenarios 3 and 4, which have a lighter ALP mass of $m_a = 10$ eV.

In all the panels of Fig. 5.6, the three different regimes of ALP decay lifetime (as discussed earlier) are shown. ALPs decaying before the end of BBN, i.e., $\tau_a < 10^4$ s, to the right of the $\tau_a = 10^4$ s line, are not considered in this study. As we will argue below, points in this region are excluded anyway due to the fast ALP decays, so in this way we are justified in neglecting scenarios with short-lived ALPs. As expected, since the lifetime of the ALP goes like $\sim f_a^2/m_a$, for the larger values of f_a in the right-hand panels and lower m_a values on the bottom panels, the excluded region for short ALP lifetimes moves to larger HNL masses and larger mixing. Additionally, the ALP lifetimes around the formation of the CMB, $\tau_a = 10^{13}$ s, and the age of the Universe, $\tau_a = 10^{17}$ s are shown.

The dashed red line corresponds to the HNL decay lifetime $\tau_N = 0.023$ s where only SM decay channels are present, i.e. in the absence of the ALP. Conversely, the solid red line denotes the same HNL lifetime limit, but in the presence of the additional decay channel $N \to a\nu$. Since HNL decays after the start of BBN would modify the abundance of primordial elements, scenarios with longer lived HNLs are also not considered, and hence shaded in red in Fig. 5.6. Consequently, whenever the HNL to ALP decays dominate, the BBN limit is relaxed as compared to the standard scenario. This effect is more evident on the left-hand side panels, with $f_a = 1$ TeV, where the BBN limit is lowered by about two orders of magnitude with respect to vanilla HNL models. For larger f_a values, on the right-hand panels, the HNL-ALP coupling, which goes like $\sim 1/f_a$, is weaker and thus the exclusion due to the HNL lifetime is stronger as the impact of the addition of the ALP to the model is less significant.

In this chapter, for simplicity, we have only considered a single HNL, which is not enough to generate non-zero masses for all active neutrinos. Nevertheless, it is useful to show the expected mass scale of active neutrino mass generation, under

the seesaw approximation. We thus show in Fig. 5.6 the blue shaded region for the seesaw mass 1 meV $\lesssim m_\nu \lesssim$ 100 meV.

The strongest cosmological constraint, shown as the shaded brown region in the panels, arises from the increase on the neutrino temperature due to ALP decays, which shows as a modification of the $N_{\rm eff}$ at the time of recombination. $N_{\rm eff}$ constrains the larger HNL masses and mixing, corresponding to shorter ALP lifetimes. $0.1\sigma_N$ has been chosen because $1\sigma_N$ did not place constraints on the parameter space studied. Consequently, ALPs decaying before the onset of BBN, or shortly after, would cause a sufficient increase of the neutrino temperature and be excluded by the Planck measurement of the $N_{\rm eff}$ value. Smaller HNL-ALP couplings cause longer ALP lifetimes, and thus the right-handed panels with larger f_a have weaker $N_{\rm eff}$ constraints. However, for the bottom panels with lower m_a, even though the lifetime is also longer and one would expect the limit to be weaken, the opposite effect occurs and the $N_{\rm eff}$ limit is significantly stronger. This happens because lighter ALPs are ultra-relativistic for a longer period between BBN and recombination, and thus have a stronger effect on the expansion rate, and thus on the neutrino temperature and value of $N_{\rm eff}$. Other cosmological constraints such as, energy injection before BBN or the relic abundance of ALPs are subleading and thus not shown. The region above the purple contour is, in principle, excluded due to the astrophysical constraints from supernova SN1987A, arising from the modified neutrino flux due to the production of HNLs in the core of the supernova. Nevertheless, the uncertainties in the calculation of the SN neutrino flux are high and depend on the choice of SN core model [249], hence we show in purple a conservative expectation of the limit, but refrain from excluding models only on the basis of this SN constraint. Supernova constraints due to ALP production, which is largely independent of m_a in the ranges of interest, only apply for large values of $|U_{eN}|^2$ and m_N, which however resides well outside of our considered region.

The combination of all the overlaid constraints still leaves a significant region of the parameter space allowed, which becomes narrower for large values of $|U_{eN}|^2$ and wider for smaller values. The most interesting section of this allowed

region corresponds to the one on the left of the BBN limit in vanilla HNL models (dashed red), which is the parameter space gained for lower HNL masses with the introduction of the additional decay channel $N \to a\nu$. The panels on the left, for $f_a = 1$ TeV, show a significant increase on the viability of HNL masses, all the way down to $m_N \sim$ MeV, at the expense of stronger constraints on the mixing $|U_{eN}|^2$ due to the stronger HNL-ALP interactions. The newly open region is much narrower in the panels on the right, with $f_a = 10^{2.5}$ TeV, as the HNL-ALP interactions are much weaker, and only slightly relevant for high $|U_{eN}|^2$ values. On the other hand, stronger HNL-ALP interactions, for $f_a < 1$ TeV, would not provide any noticeable improvement, as the ALPs would then be produced in equilibrium and the cosmological constraints would be much stronger. In conclusion, from Fig. 5.6 there is a reasonable expectation for HNLs in our model to have masses at around the MeV scale without affecting the cosmological history of the Universe.

In Fig. 5.7 we present this newly available parameter region which may be the target of future dedicated searches for HNLs. In the left panel, we show the corresponding parameter space for scenario 1 ($f_a = 1$ TeV, $m_a = 1$ keV) as described in previous section, while the right panel corresponds to the scenario 2 ($f_a = 10^{2.5}$ TeV, $m_a = 1$ keV). The gray shaded regions in both panels are disfavored from various cosmological and astrophysical constraints discussed in Sec. 5.3, and shown coloured in Figure 5.6. The gray dashed curve denotes the BBN bound from the HNL only decaying to SM decay channels i.e., in absence of the ALP. The corresponding seesaw regime is shown in blue considering 1 meV $\lesssim \mathrm{m}_\nu \lesssim$ 100 meV. The red dashed contour corresponds to the future sensitivity of DUNE HNL searches in standard HNL models (without ALPs), while the solid red contours in both panels denote the resultant sensitivity contours for observation of 6 events in presence of the new $N \to a\nu$ decay channel in respective benchmark scenarios with two different f_a values. Additionally, as described in Tab. 4.5, in blue diamonds two benchmark scenarios with fixed HNL mass and mixing $m_N = 10^{-1}$ GeV, $|U_{eN}|^2 = 10^{-10}$ and $m_N = 10^{-0.4}$ GeV, $|U_{eN}|^2 = 10^{-9.2}$, have been shown. The brown dashed contour denotes the present exclusion contour

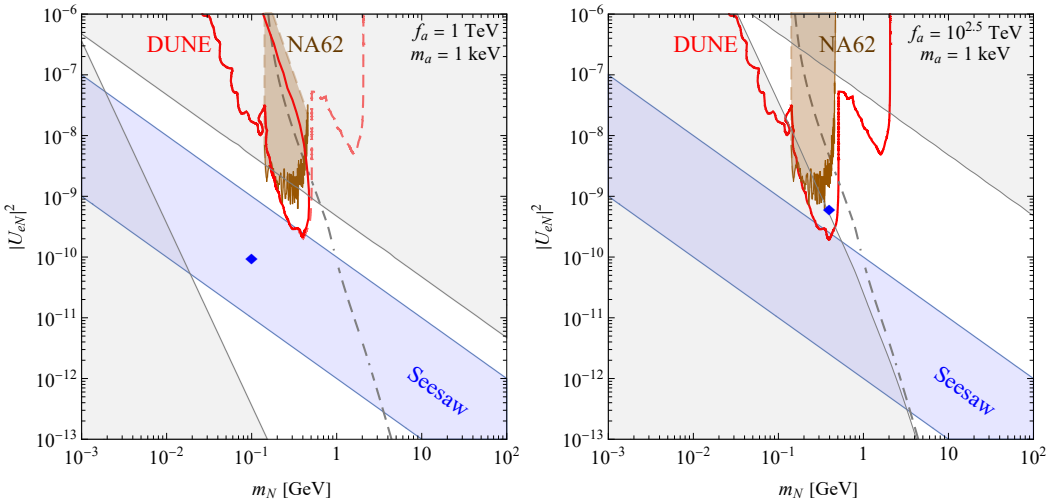

Figure 5.7: The sensitivity contours of future DUNE and current NA62 searches for observation of 6 events in newly available parameter space constrained by several astrophysical and cosmological constraints (gray shaded region) for two different benchmark scenarios i.e., left panel (f_a = 1 TeV, $m_a = 1$ keV) and right panel ($f_a = 10^{2.5}$ TeV, $m_a = 1$ keV). The region left to gray dashed contour is disfavored if HNL decays only via SM decay channels, in absence of ALP. The seesaw regime for active neutrinos 1 meV $\lesssim$ m$_\nu$ $\lesssim$ 100 meV is shown in blue. Benchmark values from Tab.4.5 for scenario 1 and 2 with fixed m_N and $|U_{eN}|^2$ are denoted in two panels by blue diamonds. The red solid (dashed) contours denote the DUNE sensitivity contours with (without) HNL to ALP decay channel. The brown contour corresponds to NA62 present sensitivity while the brown shaded region denotes the unaffected parameter space, in presence of $N \to a\nu$ channel, using the approximation discussed in subsection 5.4.

from NA62 experiment. Furthermore, considering the discussion of subsection 5.4, we have also highlighted in brown the region where the approximation holds (with $L_{\rm NA62}$ = 75 m and $p_{N_z} \sim 30$ GeV as the K^+ beams have energy ~ 75 GeV [246]), the present sensitivity contour remains unaffected by the new axion decay channel of HNL in this region. From Figure 5.7 it is evident that the available regions constrained by several astrophysical and cosmological constraints can be well probed in the future by DUNE and NA62 in presence of this new decay channel of HNLs.

Chapter 6

Conclusions

In this thesis, we have explored the nature of HNLs and active neutrinos in fixed target experiments, neutrinoless double beta decay and cosmology. We started with a review of the basics of the SM in Chapter 2. As pointed out in Section 2.5, there are still a lot of open questions in the SM which are related to neutrinos such as the neutrino mass origin, lepton number violation and the matter-antimatter asymmetry.

An introduction to neutrino physics is given in Chapter 3. It goes from the theory of neutrino mixing and neutrino oscillation experiments to the current understanding of neutrino mass. The Dirac and Majorana nature of neutrinos is discussed to facilitate the introduction of the seesaw mechanism and HNLs. The three types of seesaw mechanisms are stated with an emphasis of the type-I and type-II seesaw mechanisms. We use a simplified one-generation model to show the way to parameterise the neutrino mass matrix and how light neutrino mass is generated. The parameterisation is extended to 3 generations of active neutrinos by adding more mixing angles and phases. The simplified model is compared to the 3+2 minimal model to show the consistency. The current neutrino mass measurements are also presented for different experiments. Apart from the basic properties of neutrinos, we also give the phenomenology in the other half of this chapter. Neutrinoless double beta decay is a consequence of the Majorana nature of neutrinos since lepton number is broken by two units in this process. The formulation of $0\nu\beta\beta$ is given and the contributions from neutrinos ($m_{\beta\beta}$) and nuclear isotopes (NMEs) are demonstrated. Examples of the experimental signature are given and the current

status of $0\nu\beta\beta$ searches is discussed. We also show that neutrinos behave differently in different cosmological periods; the final part of this chapter demonstrates how neutrinos impact the Universe in neutrino decoupling, BBN and CMB.

In Chapter 4, we show the effect of a pair of near-GeV mass HNLs on observations in LEGEND-1000 ($0\nu\beta\beta$) and the near detector (ND) of DUNE (fixed target) by using a one-generation light neutrino simplification. The pair of HNLs give additional contributions to $0\nu\beta\beta$, but the contributions will be suppressed by the HNL mass. Also, the Majorana phase between the active neutrino and HNL sector can cancel the contributions from the two sectors. HNLs can be produced by and decay to SM particles via the active-sterile mixing. The HNL decay products can be captured in the ND of DUNE. DUNE can therefore measure the mass of HNLs and active-sterile mixing. We also extensively study the effect of the mass splitting between the HNL pair on these experiments. After a combined analysis in signals observed in both experiments, signal observed in one of the experiments and no observed signal at all, we demonstrate how the two different types of experiments can constrain the parameter space in HNL searches and determine the light neutrino properties. The results for the 1+2 model are also compared with a more complete 3+2 scenario.

In Chapter 5, we bring the well-studied HNLs and ALPs together in a dark sector which only interacts with the SM through the neutrino portal. We demonstrate that the $N \to a\nu$ decay channel can significantly reduce the BBN constraint for relatively low decay constants ($f_a \lesssim 10^6$ GeV) and open up a possibility for MeV-mass HNLs. All the relevant HNL and ALP processes are computed and we calculate the effective coupling between the ALP and SM particles such as the electron and the photon. Two sets of Boltzmann equations are used for the regime before and after the start of BBN. For 100 MeV - 1 GeV HNLs and an ALP mass $m_a = 1$ keV, we find that the freeze-out of HNLs will be delayed and ALPs will not be in thermal equilibrium for higher decay constants ($f_a \sim 10^6$ GeV) compared to $f_a = 10^3$ GeV. Cosmological and astrophysical observations such as N_{eff}, Ω_{CDM} and SN1987A will put constraints on the parameter space studied, but a viable region in the considered

mass range remains.

In conclusion, this thesis gives highlights for searches of HNLs through various experiments and observations, as well as the way to conduct a complementary analysis by combining observations from different types of experiments. It also demonstrates how the interaction between hypothetical particles will both constrain the parameter space for new physics searches.

In the future, the sensitivities of different types of experiments, such as neutrino oscillation, β decay, $0\nu\beta\beta$ and charged lepton flavour violation will be improved. DUNE and Hyper-Kamiokande as long baseline neutrino oscillation experiments will be able to measure the neutrino oscillation parameters with a greater sensitivity [250]. Medium baseline experiments such as JUNO will be able to determine the neutrino mass ordering and measure δ_{CP} [251]. Newly proposed experiments for long-lived particle searches such as DUNE, SHiP and PIONEER can probe the nature of HNLs in different regimes [163, 166]. Upper bounds on the absolute neutrino mass scale are expected to reach the sub-eV range with upcoming beta decay experiments, such as KATRIN and Project 8, along with cosmological surveys. As we enter this era of increased precision, the neutrino sector offers an additional avenue for exploring new physics [252]. LEGEND-1000, as an example of a future $0\nu\beta\beta$ experiment, will be able to probe the IO neutrino regime and NP can also be tested. With advancements in the precision of these and other experiments in the future, it will become increasingly feasible to investigate and place tighter constraints on the broader landscape of BSM physics.

Appendix A

Extended Phenomenological Parametrisation

In this appendix, we generalise the phenomenological parametrisation in Sec. 4.2 to the $\mathscr{N}_A + \mathscr{N}_S$ scenario, i.e., the SM with an arbitrary number $\mathscr{N}_A$ of active fields extended to include $\mathscr{N}_S$ gauge-singlet Weyl fermion fields. Now, the relation in Eq. (4.10) can be written as (at first-order in the active-sterile mixing stengths $\Theta_{\alpha\kappa}$),

$$m^{\nu}_{\alpha\beta} + m_N \Theta_{\alpha 1}\Theta_{\beta 1} + m_N(1+r^{21}_{\Delta})\Theta_{\alpha 2}\Theta_{\beta 2} + \sum_{\kappa=3}^{n} m_N(1+r^{\kappa 1}_{\Delta})\Theta_{\alpha\kappa}\Theta_{\beta\kappa} = 0\,, \quad \text{(A.1)}$$

where $\Theta_{\alpha\kappa} \equiv |\Theta_{\alpha\kappa}| e^{i\phi_{\alpha\kappa}/2}$ and $r^{\kappa 1}_{\Delta} \equiv (m_{N_\kappa} - m_N)/m_N$. It is now possible to take the diagonal elements $(\alpha = \beta)$ and rearrange the expression above to find

$$\frac{\Theta_{\alpha 2}}{\Theta_{\alpha 1}} = \pm i \sqrt{\frac{1 + x^{\alpha}_{\alpha\alpha}}{1 + r_{\Delta}}}\,, \quad \text{(A.2)}$$

where the parameter $x^{\rho}_{\alpha\beta}$ is given by

$$x^{\rho}_{\alpha\beta} \equiv \frac{m^{\nu}_{\alpha\beta}}{m_N \Theta^2_{\rho 1}} + \sum_{\kappa=3}^{n} (1+r^{\kappa 1}_{\Delta}) \frac{\Theta_{\alpha\kappa}\Theta_{\beta\kappa}}{\Theta^2_{\rho 1}}\,. \quad \text{(A.3)}$$

Additionally, it is possible to take the off-diagonal elements ($\alpha \neq \beta$) to find

$$\frac{\Theta_{\beta 1}}{\Theta_{\alpha 1}} = \frac{x^{\alpha}_{\alpha\beta} \pm \sqrt{(x^{\alpha}_{\alpha\beta})^2 - x^{\alpha}_{\alpha\alpha} x^{\alpha}_{\beta\beta}}\sqrt{1 + x^{\alpha}_{\alpha\alpha}}}{x^{\alpha}_{\alpha\alpha}} \equiv y^{\alpha}_{\alpha\beta}\,. \tag{A.4}$$

Combining these two results, we can write

$$\frac{\Theta_{\beta 2}}{\Theta_{\alpha 1}} = \pm i \sqrt{\frac{(y^{\alpha}_{\alpha\beta})^2 + x^{\alpha}_{\alpha\alpha}}{1 + r_{\Delta}}}\,, \tag{A.5}$$

which reduces to Eq. (A.2) for $\alpha = \beta$ because $y^{\alpha}_{\alpha\alpha} = 1$. Thus, for a given flavour α, it is possible to completely determine the mixing to the first and second HNL, $\Theta_{\beta 1}$ ($\alpha \neq \beta$) and $\Theta_{\beta 2}$ ($\beta = e, \mu, \tau$), in terms of $\Theta_{\alpha 1}$ (the convenient choice for $0\nu\beta\beta$ decay is $\alpha = e$).

Above, the constraint from the upper-left $\mathscr{N}_A \times \mathscr{N}_A$ sub-block of $\mathscr{M}_\nu$ has made it possible to eliminate $\mathscr{N}_A(\mathscr{N}_A - 1)$ parameters among the $(\mathscr{N}_A + \mathscr{N}_S + 1)(\mathscr{N}_A + \mathscr{N}_S)$ describing the complex symmetric mass matrix $\mathscr{M}_\nu$. Additionally, $\mathscr{N}_A$ phases can be eliminated via a redefinition of the charged lepton fields and $\mathscr{N}_S^2$ mixing angles and phases eliminated via an unphysical rotation among the sterile states. Consequently, the number of active-sterile mixing strengths and CP phases that can be eliminated is given by $\mathscr{N}_A(\mathscr{N}_A - 1) + \min(\mathscr{N}_A, \mathscr{N}_S)$, i.e., two parameters in the $1+2$ scenario ($|\Theta_{e2}|$ and ϕ_{e2}) and 10 parameters in the $3+2$ scenario ($|\Theta_{\beta 1}|$ and $\phi_{\beta 1}$ for $\beta = \mu, \tau$ and $|\Theta_{\beta 2}|$ and $\phi_{\beta 2}$ for $\beta = e, \mu, \tau$). In the $3+3$ scenario, it becomes possible to eliminate 12 parameters; i.e., an additional active-sterile mixing and CP phase such as $|\Theta_{\beta 3}|$ and $\phi_{\beta 3}$ for a single flavour.

In the $3+2$ model, the ratio in Eq. (A.2) has branch points at

$$\Theta_{\alpha 1} = |\Theta_{\alpha 1}| e^{i\phi_{\alpha 1}/2} = \pm i \sqrt{\frac{m^{\nu}_{\alpha\alpha}}{m_N}}\,. \tag{A.6}$$

This corresponds to the seesaw limit in which the heavier HNL decouples and the lighter HNL has a mixing $|\Theta_{\alpha 1}| = \sqrt{|m^{\nu}_{\alpha\alpha}|/m_N}$ and CP phase $\phi_{\alpha 1} = \phi^{\nu}_{\alpha\alpha} \pm \pi$, where we have defined $m^{\nu}_{\alpha\alpha} \equiv |m^{\nu}_{\alpha\alpha}| e^{i\phi^{\nu}_{\alpha\alpha}}$. In the $1+2$ model, with $m^{\nu}_{\alpha\alpha} \to m_\nu$,

we instead have the requirement that $\phi_{\alpha 1} = \pm\pi$. As a matter of convention, we take the positive square root in Eqs. (A.5) and (A.6) and negative square root Eq. (A.4). Having defined the Dirac phases in Eq. (4.8) and the Majorana phases in Eq. (4.9) to lie in the ranges $[0, 2\pi]$ and $[0, 4\pi]$, respectively, the CP phases $\phi_{\alpha\kappa} = \phi_\kappa - 2\eta_{\alpha i}$ are also taken to be in the range $[0, 4\pi]$. This extended range takes into account both values of the square root sign; for example, in the inverse seesaw limit of the $3+2$ model, Eq. (A.4) tends to

$$\frac{\Theta_{\beta 1}}{\Theta_{\alpha 1}} = \frac{m^\nu_{\alpha\beta} \pm \sqrt{(m^\nu_{\alpha\beta})^2 - m^\nu_{\alpha\alpha} m^\nu_{\beta\beta}}}{m^\nu_{\alpha\alpha}} = \frac{\sqrt{m_2}\, U_{\beta 2} \mp \sqrt{m_3}\, U_{\beta 3}}{\sqrt{m_2}\, U_{\alpha 2} \mp \sqrt{m_3}\, U_{\alpha 3}}\,, \tag{A.7}$$

where the second equality is valid for the normal ordering case. Both signs of the square root are taken into account by allowing the physically-relevant Majorana phase α_{21} to lie in the range $[0, 4\pi]$.

Appendix B

Phenomenological vs. Minimal Casas-Ibarra Parametrisation

In this appendix we compare the phenomenological parametrisation in Sec. 4.2 with the mininal Casas-Ibarra parametrisation used to study the $3+2$ model in [173].

Firstly, we note that in the phenomenological approach of this work, the six active-sterile mixing strengths in the $3+2$ model can be written in terms of the elements of the light neutrino mass matrix $m^{\nu}_{\alpha\beta} \equiv \sum_i m_i U_{\alpha i} U_{\beta i}$ (depending on two light neutrino masses, three mixing angles, a Dirac CP phase and single Majorana phase for $m_{\text{light}} = 0$), the masses of the two HNLs $m_{N_1} = m_N$ and $m_{N_2} = m_N(1+r_\Delta)$ with $r_\Delta = \Delta m_N / m_N$, a single active-sterile mixing $|\Theta_{\alpha 1}|$ and CP phase $\phi_{\alpha 1}$, i.e.,

$$U_{\beta N_1} \approx |\Theta_{\alpha 1}| e^{i\phi_{\alpha 1}/2} y^{\alpha}_{\alpha\beta}\,, \quad U_{\beta N_2} \approx i|\Theta_{\alpha 1}| e^{i\phi_{\alpha 1}/2} \sqrt{\frac{(y^{\alpha}_{\alpha\beta})^2 + x^{\alpha}_{\beta\beta}}{1+r_\Delta}}\,, \tag{B.1}$$

for $\beta = e, \mu, \tau$, where the factors $x^{\rho}_{\alpha\beta}$ and $y^{\rho}_{\alpha\beta}$ are functions of $|\Theta_{\alpha 1}|$ and $\phi_{\alpha 1}$ and are given in Eqs. (4.14) and (4.16), respectively. A useful choice for the comparison of $0\nu\beta\beta$ decay and direct searches at DUNE is $\alpha = e$.

In the scheme of [173], the neutrino mass matrix is diagonalised similarly (in the normal ordering case with $m_1 = 0$) as

$$U^{\dagger} \mathscr{M}_{\nu} U^{*} = \text{diag}(0, m_2, m_3, m_{N_1}, m_{N_2})\,, \quad U = \begin{pmatrix} U_{\nu\nu} & U_{\nu N} \\ U_{N\nu} & U_{NN} \end{pmatrix}\,, \tag{B.2}$$

where now the sub-blocks of the 5×5 mixing matrix U are parametrised as

$$U_{\nu\nu} = U_{\text{PMNS}} \begin{pmatrix} 1 & 0 \\ 0 & H \end{pmatrix}, \quad U_{\nu N} = -iU_{\text{PMNS}} \begin{pmatrix} 0 \\ Hm_l^{1/2} R^T m_h^{-1/2} \end{pmatrix}, \tag{B.3}$$

$$U_{N\nu} = -i \begin{pmatrix} 0 & \bar{H} m_h^{-1/2} R^* m_l^{1/2} \end{pmatrix}, \quad U_{NN} = \bar{H}. \tag{B.4}$$

Here, m_l and m_h are the 2×2 matrices,

$$m_l = \begin{pmatrix} m_2 & 0 \\ 0 & m_3 \end{pmatrix}, \quad m_h = \begin{pmatrix} m_{N_1} & 0 \\ 0 & m_{N_2} \end{pmatrix}, \tag{B.5}$$

containing the masses of the light and heavy states, respectively. The 2×2 matrix R is described by a single complex angle,

$$R = \begin{pmatrix} \cos(\theta_{45} + i\gamma_{45}) & \sin(\theta_{45} + i\gamma_{45}) \\ -\sin(\theta_{45} + i\gamma_{45}) & \cos(\theta_{45} + i\gamma_{45}) \end{pmatrix}. \tag{B.6}$$

Finally, the 2×2 matrices H and $\bar{H}$ can be written in terms of the matrices above as

$$H = \left[I_2 + m_l^{1/2} R^T m_h^{-1} R^* m_l^{1/2} \right]^{-1/2}, \quad \bar{H} = \left[I_2 + m_h^{-1/2} R^* m_l R^T m_h^{-1/2} \right]^{-1/2}, \tag{B.7}$$

where I_2 is the 2×2 identity matrix. The active-sterile mixing contained in $U_{\nu N}$ is therefore determined by the light neutrino masses, mixing angles and phases (a Dirac phase and single Majorana phase for $m_1 = 0$) contained in m_l and U_{PMNS}, the HNL masses $m_{N_1} = m_N$ and $m_{N_2} = m_N(1 + r_\Delta)$ and the two parameters θ_{45} and γ_{45}.

The difference between the two parametrisations is the choice of $(|\Theta_{e1}|, \phi_{e1})$ or $(\theta_{45}, \gamma_{45})$ as free parameters. The former, which has a direct physical interpretation, is useful for considering the experimental observation of an HNL that couples to a flavour α. In that scenario, the active-sterile mixing $|\Theta_{\alpha 1}|^2$ and HNL mass m_N are measured quantities, and all other active-sterile mixing strengths are determined for particular values of ϕ_{e1} and r_Δ.

Appendix C

Calculation of decay and scattering rates

In this appendix, we will give analytical expressions for the scattering cross-sections involving active neutrinos, HNL and ALP in all possible way. Due to the couplings presented in Eq.(5.5) one can also consider the axion-HNL scattering in early universe. The process happens via t-channel scattering. The matrix element responsible for the process $a(p_1)+a(p_2)\to N(p_3,s)+N(p_4,r)$ can be written as

$$\mathscr{M}_t = \frac{4m_N^2}{f_a^2}\left(\bar{u}_3^s \frac{\not{q}-m_N}{q^2-m_N^2} u_4^r\right) \tag{C.1}$$

where momentum exchange is $q^2 \equiv (p_1-p_3)^2 = t$. Now finding $|\mathscr{M}_t|^2$ and performing the sum over final spin states s,r of HNLs one gets

$$\sum_{r,s}|\mathscr{M}_t|^2 = \frac{64m_N^4}{f_a^4(t-m_N^2)^2}\Big[2(p_3.q)(p_4.q)-(p_3.p_4)(q.q-m_N^2)+2m_N^2(p_3.q)+2m_N^2(p_4.q) + m_N^2(q.q+m_N^2)\Big] \tag{C.2}$$

Now, putting the definitions for kinematic variables and phase space factor as well as integrating over the angular variables, we get the total cross-section as

$$\sigma_{aaNN} = \frac{4m_N^4\sqrt{s-4m_a^2}}{\pi f_a^4 s^{3/2}}\Bigg[-1-\frac{m_a^4-4m_a^2m_N^2}{m_a^4-4m_a^2m_N^2+m_N^2 s} + \frac{2(s-2m_a^2)\coth^{-1}\left(\frac{s-2m_a^2}{\sqrt{s-4m_a^2}\sqrt{s-4m_N^2}}\right)}{\sqrt{s-4m_a^2}\sqrt{s-4m_N^2}}\Bigg]. \tag{C.3}$$

Similarly, for the inverse scattering $N(p_1,s)+N(p_2,r)\to a(p_3)+a(p_4)$ we have

$$\sigma_{NNaa} = \frac{4m_N^4}{\pi f_a^4 s^{3/2}}\Bigg[-\frac{\sqrt{s-4m_N^2}(2m_a^4-8m_a^2m_N^2+m_N^2 s)}{m_a^4-4m_a^2m_N^2+m_N^2 s} + \frac{2(s-2m_a^2)\coth^{-1}\left(\frac{s-2m_a^2}{\sqrt{s-4m_a^2}\sqrt{s-4m_N^2}}\right)}{\sqrt{s-4m_a^2}}\Bigg], \tag{C.4}$$

where $s\equiv(p_1+p_2)^2=(p_3+p_4)^2$. Likewise, for $aa\to\nu\nu$ scattering with t-channel HNL mediation,

$$\begin{aligned}\sigma_{aa\nu\nu} =& \frac{4m_N^4\sqrt{s-4m_a^2}U_{eN}^4}{\pi f_a^4 s^{3/2}} \\ &\times\Bigg[-\frac{2(m_a^4+m_N^4+m_\nu^4-2m_a^2m_N^2-2m_a^2m_\nu^2-2m_N^2m_\nu^2)+m_N^2 s}{m_a^4+m_N^4+m_\nu^4-2m_a^2m_N^2-2m_a^2m_\nu^2-2m_N^2m_\nu^2+m_N^2 s} \\ &+\frac{2(2(m_a^2-m_N^2+m_\nu^2)-s)\coth^{-1}\left(\frac{2(m_a^2-m_N^2+m_\nu^2)-s}{\sqrt{s-4m_a^2}\sqrt{s-4m_\nu^2}}\right)}{\sqrt{s-4m_a^2}\sqrt{s-4m_\nu^2}}\Bigg].\end{aligned} \tag{C.5}$$

In the limit, $m_\nu\to 0$, we will get simplified expression for $aa\to\nu\nu$ scattering as

$$\sigma_{aa\nu\nu} = \frac{4m_N^4\sqrt{s-4m_a^2}U_{eN}^4}{\pi f_a^4 s^{3/2}}\Bigg[-\frac{2(m_a^4+m_N^4-2m_a^2m_N^2)+m_N^2 s}{m_a^4+m_N^4-2m_a^2m_N^2+m_N^2 s} + \frac{2(2(m_a^2-m_N^2)-s)\coth^{-1}\left(\frac{2(m_a^2-m_N^2)-s}{\sqrt{s-4m_a^2}\sqrt{s}}\right)}{\sqrt{s-4m_a^2}\sqrt{s}}\Bigg]. \tag{C.6}$$

The cross-section for $aa \to \nu N$ scattering (in the limit $m_\nu \to 0$) with t-channel HNL mediation,

$$\sigma_{aa\nu N} = \frac{2m_N^4\sqrt{s-4m_a^2}U_{eN}^2}{\pi f_a^4 s^{3/2}}\left[-\frac{2(2m_a^4-7m_a^2m_N^2+5m_N^4+m_N^2 s)}{m_a^4-2m_a^2m_N^2+m_N^4+m_N^2 s} + \frac{4(2m_a^2-4m_N^2-s)\coth^{-1}\left(\frac{2(m_a^2-m_N^2)-s}{\sqrt{s-4m_a^2}\sqrt{s}}\right)}{\sqrt{s-4m_a^2}\sqrt{s}}\right]. \quad \text{(C.7)}$$

The cross-section for $aa \to NN$ scattering (in the limit $m_\nu \to 0$) with t-channel ν mediation,

$$\sigma_{aaNN} = \frac{4m_N^4\sqrt{s-4m_a^2}U_{eN}^4}{\pi f_a^4 s^{3/2}}\left[-\frac{2m_a^4-4m_a^2m_N^2+4m_N^4-m_N^2 s}{m_a^4-2m_a^2m_N^2+m_N^4} + \frac{2(2(m_a^2+m_N^2)-s)\coth^{-1}\left(\frac{2(m_a^2+m_N^2)-s}{\sqrt{s-4m_a^2}\sqrt{s-4m_N^2}}\right)}{\sqrt{s-4m_a^2}\sqrt{s-4m_N^2}}\right]. \quad \text{(C.8)}$$

The cross-section for $aa \to \nu\nu$ scattering (in the limit of $m_\nu \to 0$) with t-channel ν mediation,

$$\sigma_{aa\nu\nu} = \frac{4m_N^4\sqrt{s-4m_a^2}U_{eN}^8}{\pi f_a^4 s^{3/2}}\left[-2+\frac{2(s-2m_a^2)\coth^{-1}\left(\frac{s-2m_a^2}{\sqrt{s-4m_a^2}\sqrt{s}}\right)}{\sqrt{s-4m_a^2}\sqrt{s}}\right]. \quad \text{(C.9)}$$

The cross-section for $aa \to \nu N$ scattering (in the limit $m_\nu \to 0$) with t-channel ν mediation,

$$\sigma_{aa\nu N} = \frac{4m_N^4\sqrt{s-4m_a^2}U_{eN}^6}{\pi f_a^4 s^{3/2}}\left[-2+\frac{m_N^2}{m_a^2}+\frac{2(s-2m_a^2)\coth^{-1}\left(\frac{s-2m_a^2}{\sqrt{s-4m_a^2}\sqrt{s}}\right)}{\sqrt{s-4m_a^2}\sqrt{s}}\right]. \quad \text{(C.10)}$$

The cross-section for $\nu\nu \to NN$ scattering (in the limit $m_\nu \to 0$) with t-channel axion mediation,

$$\sigma_{\nu\nu NN} = \frac{m_N^4 U_{eN}^4}{\pi f_a^4 s}\left[\frac{2m_a^4+2m_N^4+m_N^2 s+2m_a^2(s-2m_N^2)}{m_a^4+m_N^4+m_a^2(s-2m_N^2)} + \frac{2(s+2m_a^2-2m_N^2)\coth^{-1}\left(\frac{-2m_a^2+2m_N^2-s}{\sqrt{s-4m_N^2}\sqrt{s}}\right)}{\sqrt{s-4m_N^2}\sqrt{s}}\right]. \tag{C.11}$$

The cross-section for $a\nu \to aN$ (in the limit $m_\nu \to 0$) with s and t-channel HNL mediation,

$$\begin{aligned}\sigma_{a\nu aN} =& \frac{m_N^4 U_{eN}^2}{2\pi f_a^4 (m_N^2-s)^2 s} \\ &\times\left[\frac{1}{m_a^4-4m_a^2m_N^2+m_N^2 s}\right. \\ &\Big\{2m_a^8+m_N^2(8m_N^6-20m_N^4 s+15m_N^2 s^2+(5-2m_N^2)s^3+2s^4) \\ &+2m_a^2(3m_N^6+6m_N^4(s-1)s-6m_N^2 s^2(3+s))+2m_a^6(2m_N^2(s-3) \\ &-s(3+2s))+m_a^4(2m_N^4(7-8s)+s^2(7+2s)+m_N^2 s(29+14s))\Big\} \\ &-4\sqrt{\frac{s-m_N^2}{s-4m_a^2}}\Big\{2m_a^4+m_N^4(3-2s)-s^2+2m_N^2 s(s+3)-m_a^2(3s \\ &\left.+m_N^2(3+4s))\Big\}\coth^{-1}\left(\frac{s-2m_a^2}{\sqrt{s-4m_a^2}\sqrt{s-4m_N^2}}\right)\right].\end{aligned} \tag{C.12}$$

Bibliography

[1] S. L. Glashow. Partial Symmetries of Weak Interactions. *Nucl. Phys.*, 22:579–588, 1961.

[2] Steven Weinberg. A Model of Leptons. *Phys. Rev. Lett.*, 19:1264–1266, 1967.

[3] Abdus Salam. Weak and Electromagnetic Interactions. *Conf. Proc. C*, 680519:367–377, 1968.

[4] E. Fermi. An attempt of a theory of beta radiation. 1. *Z. Phys.*, 88:161–177, 1934.

[5] F. Reines and C. L. Cowan. Detection of the free neutrino. *Phys. Rev.*, 107:641, 1957.

[6] B. Pontecorvo. Inverse beta process. *Camb. Monogr. Part. Phys. Nucl. Phys. Cosmol.*, 1:25–31, 1991.

[7] Kan Chang Wang. A Suggestion on the Detection of the Neutrino. *Phys. Rev.*, 61(1-2):97–97, 1942.

[8] G. Danby et al. Observation of high-energy neutrino reactions and the existence of two kinds of neutrinos. *Phys. Rev. Lett.*, 9:36–44, 1962.

[9] K. Kodama et al. Observation of tau neutrino interactions. *Phys. Lett. B*, 504:218–224, 2001.

[10] T. D. Lee and Chen-Ning Yang. Question of Parity Conservation in Weak Interactions. *Phys. Rev.*, 104:254–258, 1956.

[11] C. S. Wu, E. Ambler, R. W. Hayward, D. D. Hoppes, and R. P. Hudson. Experimental Test of Parity Conservation in β Decay. *Phys. Rev.*, 105:1413–1414, 1957.

[12] B. Pontecorvo. Neutrino Experiments and the Problem of Conservation of Leptonic Charge. *Zh. Eksp. Teor. Fiz.*, 53:1717–1725, 1967.

[13] Raymond Davis, Jr., Don S. Harmer, and Kenneth C. Hoffman. Search for neutrinos from the sun. *Phys. Rev. Lett.*, 20:1205–1209, 1968.

[14] Bruce T. Cleveland et al. Measurement of the solar electron neutrino flux with the homestake chlorine detector. *Astrophys. J.*, 496:505–526, 1998.

[15] Ziro Maki, Masami Nakagawa, and Shoichi Sakata. Remarks on the unified model of elementary particles. *Prog. Theor. Phys.*, 28:870–880, 1962.

[16] V. N. Gribov and B. Pontecorvo. Neutrino astronomy and lepton charge. *Phys. Lett. B*, 28:493, 1969.

[17] P. Adamson et al. Improved search for muon-neutrino to electron-neutrino oscillations in MINOS. *Phys. Rev. Lett.*, 107:181802, 2011.

[18] M. H. Ahn et al. Measurement of Neutrino Oscillation by the K2K Experiment. *Phys. Rev. D*, 74:072003, 2006.

[19] M. A. Acero et al. New constraints on oscillation parameters from ν_e appearance and ν_μ disappearance in the NOvA experiment. *Phys. Rev. D*, 98:032012, 2018.

[20] K. Abe et al. Indication of Electron Neutrino Appearance from an Accelerator-produced Off-axis Muon Neutrino Beam. *Phys. Rev. Lett.*, 107:041801, 2011.

[21] Y. Ashie et al. A Measurement of atmospheric neutrino oscillation parameters by SUPER-KAMIOKANDE I. *Phys. Rev. D*, 71:112005, 2005.

[22] S. Fukuda et al. Solar B-8 and hep neutrino measurements from 1258 days of Super-Kamiokande data. *Phys. Rev. Lett.*, 86:5651–5655, 2001.

[23] M. G. Aartsen et al. Determining neutrino oscillation parameters from atmospheric muon neutrino disappearance with three years of IceCube DeepCore data. *Phys. Rev. D*, 91(7):072004, 2015.

[24] C. Arpesella et al. Direct Measurement of the Be-7 Solar Neutrino Flux with 192 Days of Borexino Data. *Phys. Rev. Lett.*, 101:091302, 2008.

[25] Y. Abe et al. Improved measurements of the neutrino mixing angle θ_{13} with the Double Chooz detector. *JHEP*, 10:086, 2014. [Erratum: JHEP 02, 074 (2015)].

[26] J. H. Choi et al. Observation of Energy and Baseline Dependent Reactor Antineutrino Disappearance in the RENO Experiment. *Phys. Rev. Lett.*, 116(21):211801, 2016.

[27] Xinheng Guo et al. A Precision measurement of the neutrino mixing angle θ_{13} using reactor antineutrinos at Daya-Bay. 1 2007.

[28] M. G. Aartsen et al. First observation of PeV-energy neutrinos with IceCube. *Phys. Rev. Lett.*, 111:021103, 2013.

[29] M. Aker et al. Improved Upper Limit on the Neutrino Mass from a Direct Kinematic Method by KATRIN. *Phys. Rev. Lett.*, 123(22):221802, 2019.

[30] N. Aghanim et al. Planck 2018 results. VI. Cosmological parameters. *Astron. Astrophys.*, 641:A6, 2020. [Erratum: Astron.Astrophys. 652, C4 (2021)].

[31] Peter Minkowski. $\mu \to e\gamma$ at a Rate of One Out of 10^9 Muon Decays? *Phys. Lett. B*, 67:421–428, 1977.

[32] R. N. Mohapatra and G. Senjanovic. Neutrino mass and spontaneous parity nonconservation. *Phys. Rev. Lett.*, 44:91, 1980.

[33] Murray Gell-Mann, Pierre Ramond, and Richard Slansky. Complex Spinors and Unified Theories. *Conf. Proc. C*, 790927:315–321, 1979.

[34] J. Schechter and J. W. F. Valle. Neutrino Masses in SU(2) x U(1) Theories. *Phys. Rev. D*, 22:2227, 1980.

[35] J. Schechter and J. W. F. Valle. Neutrinoless double-beta decay in su(2) x u(1) theories. *Phys. Rev.*, D25:2951, 1982.

[36] Martin Hirsch, Sergey Kovalenko, and Ivan Schmidt. Extended black box theorem for lepton number and flavor violating processes. *Phys. Lett.*, B642:106, 2006.

[37] Martin Hirsch, Rahul Srivastava, and José W. F. Valle. Can one ever prove that neutrinos are Dirac particles? *Phys. Lett. B*, 781:302–305, 2018.

[38] K. Enqvist, K. Kainulainen, and V. Semikoz. Neutrino annihilation in hot plasma. *Nucl. Phys. B*, 374:392–404, 1992.

[39] R. A. Alpher, H. Bethe, and G. Gamow. The origin of chemical elements. *Phys. Rev.*, 73:803–804, 1948.

[40] Richard P. Feynman. Very high-energy collisions of hadrons. *Phys. Rev. Lett.*, 23:1415–1417, 1969.

[41] J. D. Bjorken and Emmanuel A. Paschos. Inelastic Electron Proton and gamma Proton Scattering, and the Structure of the Nucleon. *Phys. Rev.*, 185:1975–1982, 1969.

[42] David J. Gross and Frank Wilczek. Ultraviolet Behavior of Nonabelian Gauge Theories. *Phys. Rev. Lett.*, 30:1343–1346, 1973.

[43] F. Englert and R. Brout. Broken Symmetry and the Mass of Gauge Vector Mesons. *Phys. Rev. Lett.*, 13:321–323, 1964.

[44] Peter W. Higgs. Broken symmetries, massless particles and gauge fields. *Phys. Lett.*, 12:132–133, 1964.

[45] G. S. Guralnik, C. R. Hagen, and T. W. B. Kibble. Global Conservation Laws and Massless Particles. *Phys. Rev. Lett.*, 13:585–587, 1964.

[46] Jeffrey Goldstone, Abdus Salam, and Steven Weinberg. Broken Symmetries. *Phys. Rev.*, 127:965–970, 1962.

[47] F. J. Hasert et al. Observation of Neutrino Like Interactions Without Muon Or Electron in the Gargamelle Neutrino Experiment. *Phys. Lett. B*, 46:138–140, 1973.

[48] F. J. Hasert et al. Observation of Neutrino Like Interactions without Muon or Electron in the Gargamelle Neutrino Experiment. *Nucl. Phys. B*, 73:1–22, 1974.

[49] F. J. Hasert et al. Search for Elastic ν_μ Electron Scattering. *Phys. Lett. B*, 46:121–124, 1973.

[50] G. Arnison et al. Experimental Observation of Isolated Large Transverse Energy Electrons with Associated Missing Energy at $\sqrt{s} = 540$ GeV. *Phys. Lett. B*, 122:103–116, 1983.

[51] M. Banner et al. Observation of Single Isolated Electrons of High Transverse Momentum in Events with Missing Transverse Energy at the CERN anti-p p Collider. *Phys. Lett. B*, 122:476–485, 1983.

[52] Nicola Cabibbo. Unitary Symmetry and Leptonic Decays. *Phys. Rev. Lett.*, 10:531–533, 1963.

[53] Makoto Kobayashi and Toshihide Maskawa. CP Violation in the Renormalizable Theory of Weak Interaction. *Prog. Theor. Phys.*, 49:652–657, 1973.

[54] Y. Fukuda et al. Evidence for oscillation of atmospheric neutrinos. *Phys. Rev. Lett.*, 81:1562–1567, 1998.

[55] Q. R. Ahmad et al. Direct evidence for neutrino flavor transformation from neutral current interactions in the Sudbury Neutrino Observatory. *Phys. Rev. Lett.*, 89:011301, 2002.

[56] F. P. An et al. Observation of electron-antineutrino disappearance at Daya Bay. *Phys. Rev. Lett.*, 108:171803, 2012.

[57] A. D. Sakharov. Violation of CP Invariance, C asymmetry, and baryon asymmetry of the universe. *Pisma Zh. Eksp. Teor. Fiz.*, 5:32–35, 1967.

[58] W. J. G. de Blok, Stacy S. McGaugh, Albert Bosma, and Vera C. Rubin. Mass density profiles of LSB galaxies. *Astrophys. J. Lett.*, 552:L23–L26, 2001.

[59] Steven W. Allen, August E. Evrard, and Adam B. Mantz. Cosmological Parameters from Observations of Galaxy Clusters. *Ann. Rev. Astron. Astrophys.*, 49:409–470, 2011.

[60] G. Hinshaw et al. Five-Year Wilkinson Microwave Anisotropy Probe (WMAP) Observations: Data Processing, Sky Maps, and Basic Results. *Astrophys. J. Suppl.*, 180:225–245, 2009.

[61] P. A. R. Ade et al. Planck 2015 results. XIII. Cosmological parameters. *Astron. Astrophys.*, 594:A13, 2016.

[62] R. D. Peccei and Helen R. Quinn. CP Conservation in the Presence of Instantons. *Phys. Rev. Lett.*, 38:1440–1443, 1977.

[63] Daniele S. M. Alves and Neal Weiner. A viable QCD axion in the MeV mass range. *JHEP*, 07:092, 2018.

[64] Jia Liu, Navin McGinnis, Carlos E. M. Wagner, and Xiao-Ping Wang. Challenges for a QCD Axion at the 10 MeV Scale. *JHEP*, 05:138, 2021.

[65] R. Acciarri et al. First Constraints on Heavy QCD Axions with a Liquid Argon Time Projection Chamber Using the ArgoNeuT Experiment. *Phys. Rev. Lett.*, 130(22):221802, 2023.

[66] Sebastian Hoof and Lena Schulz. Updated constraints on axion-like particles from temporal information in supernova SN1987A gamma-ray data. *JCAP*, 03:054, 2023.

[67] John Preskill, Mark B. Wise, and Frank Wilczek. Cosmology of the Invisible Axion. *Phys. Lett. B*, 120:127–132, 1983.

[68] L. F. Abbott and P. Sikivie. A Cosmological Bound on the Invisible Axion. *Phys. Lett. B*, 120:133–136, 1983.

[69] Patrick D. Bolton, Frank F. Deppisch, Lukáš Gráf, and Fedor Šimkovic. Two-Neutrino Double Beta Decay with Sterile Neutrinos. *Phys. Rev. D*, 103(5):055019, 2021.

[70] Isard Dunietz. Rephase Invariance of K^{-}m Matrices and CP Violation. *Annals Phys.*, 184:350, 1988.

[71] C. Giunti, C. W. Kim, J. A. Lee, and U. W. Lee. On the treatment of neutrino oscillations without resort to weak eigenstates. *Phys. Rev. D*, 48:4310–4317, 1993.

[72] C. Giunti. Neutrino wave packets in quantum field theory. *JHEP*, 11:017, 2002.

[73] Ivan Esteban, M. C. Gonzalez-Garcia, Michele Maltoni, Thomas Schwetz, and Albert Zhou. The fate of hints: updated global analysis of three-flavor neutrino oscillations. *JHEP*, 09:178, 2020.

[74] R. N. Mohapatra and P. B. Pal. *Massive neutrinos in physics and astrophysics*, volume 41. 1991.

[75] Steven Weinberg. Baryon and Lepton Nonconserving Processes. *Phys. Rev. Lett.*, 43:1566–1570, 1979.

[76] Rabindra N. Mohapatra and Goran Senjanovic. Neutrino Mass and Spontaneous Parity Nonconservation. *Phys. Rev. Lett.*, 44:912, 1980.

[77] G. Lazarides, Q. Shafi, and C. Wetterich. Proton lifetime and fermion masses in an so(10) model. *Nucl. Phys.*, B181:287, 1981.

[78] M. Magg and C. Wetterich. Neutrino Mass Problem and Gauge Hierarchy. *Phys.Lett.*, B94:61, 1980.

[79] R. N. Mohapatra and G. Senjanović. Neutrino masses and mixings in gauge models with spontaneous parity violation. *Phys. Rev.*, D23:165, 1981.

[80] R. Foot, H. Lew, X. G. He, and G. C. Joshi. Seesaw neutrino masses induced by a triplet of leptons. *Z. Phys.*, C44:441, 1989.

[81] R. N. Mohapatra. Mechanism for Understanding Small Neutrino Mass in Superstring Theories. *Phys. Rev. Lett.*, 56:561–563, 1986.

[82] Rabindra N. Mohapatra. Limits on the mass of the right-handed majorana neutrino. *Phys. Rev.*, D34:909, 1986.

[83] S. Nandi and U. Sarkar. A Solution to the Neutrino Mass Problem in Superstring E6 Theory. *Phys. Rev. Lett.*, 56:564, 1986.

[84] D. Wyler and L. Wolfenstein. Massless neutrinos in left-right symmetric models. *Nucl. Phys.*, B218:205, 1983.

[85] Evgeny K. Akhmedov, Manfred Lindner, Erhard Schnapka, and J. W. F. Valle. Dynamical left-right symmetry breaking. *Phys. Rev. D*, 53:2752–2780, 1996.

[86] E. K. Akhmedov. Parametric resonance of neutrino oscillations and passage of solar and atmospheric neutrinos through the earth. *Nucl. Phys.*, B538:25–51, 1999.

[87] Michal Malinsky, J. C. Romao, and J. W. F. Valle. Novel supersymmetric SO(10) seesaw mechanism. *Phys. Rev. Lett.*, 95:161801, 2005.

[88] Ernest Ma. Deciphering the Seesaw Nature of Neutrino Mass from Unitarity Violation. *Mod. Phys. Lett. A*, 24:2161–2165, 2009.

[89] M. Aker et al. Direct neutrino-mass measurement with sub-electronvolt sensitivity. *Nature Phys.*, 18(2):160–166, 2022.

[90] A. Osipowicz et al. KATRIN: A Next generation tritium beta decay experiment with sub-eV sensitivity for the electron neutrino mass. Letter of intent. 9 2001.

[91] S. R. Elliott, A. A. Hahn, and M. K. Moe. Direct Evidence for Two Neutrino Double Beta Decay in ^{82}Se. *Phys. Rev. Lett.*, 59:2020–2023, 1987.

[92] Asoka S. De Silva, M. K. Moe, M. A. Nelson, and M. A. Vient. Double beta decays of Mo-100 and Nd-150. *Phys. Rev. C*, 56:2451–2467, 1997.

[93] R. Arnold et al. Double beta decay of Se-82. *Nucl. Phys. A*, 636:209–223, 1998.

[94] V. B. Brudanin et al. Search for double beta decay of Ca-48 in the TGV experiment. *Phys. Lett. B*, 495:63–68, 2000.

[95] H. V. Klapdor-Kleingrothaus et al. Latest results from the Heidelberg-Moscow double beta decay experiment. *Eur. Phys. J. A*, 12:147–154, 2001.

[96] N. Abgrall et al. The Large Enriched Germanium Experiment for Neutrinoless $\beta\beta$ Decay: LEGEND-1000 Preconceptual Design Report. 7 2021.

[97] F. F. Deppisch. *A Modern Introduction to Neutrino Physics*. Morgan & Claypool Publishers, 2019.

[98] M. Doi, T. Kotani, H. Nishiura, K. Okuda, and E. Takasugi. Neutrino Mass, the Right-handed Interaction and the Double Beta Decay. 1. Formalism. *Prog. Theor. Phys.*, 66:1739, 1981. [Erratum: Prog.Theor.Phys. 68, 347 (1982)].

[99] M. Doi, T. Kotani, H. Nishiura, and E. Takasugi. DOUBLE BETA DECAY. *Prog. Theor. Phys.*, 69:602, 1983.

[100] T. Tomoda. Double beta decay. *Rept. Prog. Phys.*, 54:53–126, 1991.

[101] A. Gando et al. Search for Majorana Neutrinos near the Inverted Mass Hierarchy Region with KamLAND-Zen. *Phys. Rev. Lett.*, 117(8):082503, 2016. [Addendum: Phys.Rev.Lett. 117, 109903 (2016)].

[102] Stefano Dell'Oro, Simone Marcocci, and Francesco Vissani. New expectations and uncertainties on neutrinoless double beta decay. *Phys. Rev. D*, 90(3):033005, 2014.

[103] F. Capozzi, G. L. Fogli, E. Lisi, A. Marrone, D. Montanino, and A. Palazzo. Status of three-neutrino oscillation parameters, circa 2013. *Phys. Rev. D*, 89:093018, 2014.

[104] Carla Maria Cattadori. Gerda : Results and perspectives. *Nucl. Part. Phys. Proc.*, 265-266:38–41, 2015.

[105] K. Alfonso et al. Search for Neutrinoless Double-Beta Decay of ^{130}Te with CUORE-0. *Phys. Rev. Lett.*, 115(10):102502, 2015.

[106] A. S. Barabash. Double Beta Decay: Historical Review of 75 Years of Research. *Phys. Atom. Nucl.*, 74:603–613, 2011.

[107] J. Kotila and F. Iachello. Phase space factors for double-β decay. *Phys. Rev. C*, 85:034316, 2012.

[108] Sabin Stoica and Mihail Mirea. New calculations for phase space factors involved in double-β decay. *Phys. Rev. C*, 88(3):037303, 2013.

[109] Tomas R. Rodriguez and G. Martinez-Pinedo. Energy density functional study of nuclear matrix elements for neutrinoless $\beta\beta$ decay. *Phys. Rev. Lett.*, 105:252503, 2010.

[110] J. Menendez, A. Poves, E. Caurier, and F. Nowacki. Disassembling the Nuclear Matrix Elements of the Neutrinoless beta beta Decay. *Nucl. Phys. A*, 818:139–151, 2009.

[111] J. Barea, J. Kotila, and F. Iachello. $0\nu\beta\beta$ and $2\nu\beta\beta$ nuclear matrix elements in the interacting boson model with isospin restoration. *Phys. Rev. C*, 91(3):034304, 2015.

[112] Juhani Hyvärinen and Jouni Suhonen. Nuclear matrix elements for $0\nu\beta\beta$ decays with light or heavy Majorana-neutrino exchange. *Phys. Rev. C*, 91(2):024613, 2015.

[113] A. Meroni, S. T. Petcov, and F. Simkovic. Multiple CP non-conserving mechanisms of $(\beta\beta)_{0\nu}$-decay and nuclei with largely different nuclear matrix elements. *JHEP*, 02:025, 2013.

[114] Fedor Šimkovic, Vadim Rodin, Amand Faessler, and Petr Vogel. $0\nu\beta\beta$ and $2\nu\beta\beta$ nuclear matrix elements, quasiparticle random-phase approximation, and isospin symmetry restoration. *Phys. Rev. C*, 87(4):045501, 2013.

[115] M. T. Mustonen and J. Engel. Large-scale calculations of the double-β decay of ^{76}Ge,^{130}Te,^{136}Xe, and ^{150}Nd in the deformed self-consistent Skyrme quasiparticle random-phase approximation. *Phys. Rev. C*, 87(6):064302, 2013.

[116] Matteo Agostini, Giovanni Benato, Jason A. Detwiler, Javier Menéndez, and Francesco Vissani. Toward the discovery of matter creation with neutrinoless $\beta\beta$ decay. *Rev. Mod. Phys.*, 95(2):025002, 2023.

[117] J. Schechter and J. W. F. Valle. Neutrinoless Double beta Decay in SU(2) x U(1) Theories. *Phys. Rev. D*, 25:2951, 1982.

[118] Jose F. Nieves. Dirac and Pseudodirac Neutrinos and Neutrinoless Double Beta Decay. *Phys. Lett. B*, 147:375–379, 1984.

[119] Eiichi Takasugi. Can the Neutrinoless Double Beta Decay Take Place in the Case of Dirac Neutrinos? *Phys. Lett. B*, 149:372–376, 1984.

[120] Steven Weinberg. *Cosmology*. 2008.

[121] Julien Lesgourgues, Gianpiero Mangano, Gennaro Miele, and Sergio Pastor. *Neutrino Cosmology*. Cambridge University Press, 2 2013.

[122] Utpal Sarkar. Spontaneous leptogenesis. 9 1996.

[123] Oleg Ruchayskiy and Artem Ivashko. Restrictions on the lifetime of sterile neutrinos from primordial nucleosynthesis. *JCAP*, 1210:014, 2012.

[124] Oleg Ruchayskiy and Artem Ivashko. Experimental bounds on sterile neutrino mixing angles. *JHEP*, 1206:100, 2012.

[125] Arno A. Penzias and Robert Woodrow Wilson. A Measurement of excess antenna temperature at 4080-Mc/s. *Astrophys. J.*, 142:419–421, 1965.

[126] John C. Mather, D. J. Fixsen, R. A. Shafer, C. Mosier, and D. T. Wilkinson. Calibrator design for the COBE far infrared absolute spectrophotometer (FIRAS). *Astrophys. J.*, 512:511–520, 1999.

[127] M. Fukugita and T. Yanagida. Baryogenesis without grand unification. *Phys. Lett.*, B174:45, 1986.

[128] M. A. Luty. Baryogenesis via leptogenesis. *Phys. Rev. D*, 45:455–465, 1992.

[129] Sacha Davidson, Enrico Nardi, and Yosef Nir. Leptogenesis. *Phys.Rept.*, 466:105–177, 2008.

[130] V. A. Kuzmin, V. A. Rubakov, and M. E. Shaposhnikov. On the anomalous electroweak baryon number nonconservation in the early universe. *Phys. Lett.*, B155:36, 1985.

[131] Apostolos Pilaftsis and Thomas E. J. Underwood. Resonant leptogenesis. *Nucl. Phys.*, B692:303–345, 2004.

[132] Thomas Hambye, John March-Russell, and Stephen M. West. TeV scale resonant leptogenesis from supersymmetry breaking. *JHEP*, 07:070, 2004.

[133] M. Tanabashi et al. Review of Particle Physics. *Phys. Rev. D*, 98(3):030001, 2018.

[134] Apostolos Pilaftsis. Radiatively induced neutrino masses and large Higgs neutrino couplings in the standard model with Majorana fields. *Z. Phys. C*, 55:275–282, 1992.

[135] W. Buchmuller, C. Greub, and P. Minkowski. Neutrino masses, neutral vector bosons and the scale of B-L breaking. *Phys. Lett. B*, 267:395–399, 1991.

[136] Janusz Gluza. On teraelectronvolt Majorana neutrinos. *Acta Phys. Polon. B*, 33:1735–1746, 2002.

[137] Apostolos Pilaftsis. Resonant tau-leptogenesis with observable lepton number violation. *Phys. Rev. Lett.*, 95:081602, 2005.

[138] Jörn Kersten and Alexei Yu. Smirnov. Right-Handed Neutrinos at CERN LHC and the Mechanism of Neutrino Mass Generation. *Phys. Rev. D*, 76:073005, 2007.

[139] Zhi-zhong Xing. Naturalness and Testability of TeV Seesaw Mechanisms. *Prog. Theor. Phys. Suppl.*, 180:112–127, 2009.

[140] M. B. Gavela, T. Hambye, D. Hernandez, and P. Hernandez. Minimal Flavour Seesaw Models. *JHEP*, 09:038, 2009.

[141] Xiao-Gang He, Sechul Oh, Jusak Tandean, and Chung-Cheng Wen. Large Mixing of Light and Heavy Neutrinos in Seesaw Models and the LHC. *Phys. Rev. D*, 80:073012, 2009.

[142] Rathin Adhikari and Amitava Raychaudhuri. Light neutrinos from massless texture and below TeV seesaw scale. *Phys. Rev. D*, 84:033002, 2011.

[143] A. Ibarra, E. Molinaro, and S. T. Petcov. TeV Scale See-Saw Mechanisms of Neutrino Mass Generation, the Majorana Nature of the Heavy Singlet Neutrinos and $(\beta\beta)_{0\nu}$-Decay. *JHEP*, 09:108, 2010.

[144] Frank F. Deppisch and Apostolos Pilaftsis. Lepton Flavour Violation and theta(13) in Minimal Resonant Leptogenesis. *Phys. Rev. D*, 83:076007, 2011.

[145] A. Ibarra, E. Molinaro, and S. T. Petcov. Low Energy Signatures of the TeV Scale See-Saw Mechanism. *Phys. Rev. D*, 84:013005, 2011.

[146] Manimala Mitra, Goran Senjanovic, and Francesco Vissani. Neutrinoless Double Beta Decay and Heavy Sterile Neutrinos. *Nucl. Phys. B*, 856:26–73, 2012.

[147] Mikhail Shaposhnikov. A Possible symmetry of the nuMSM. *Nucl. Phys. B*, 763:49–59, 2007.

[148] Chang-Hun Lee, P. S. Bhupal Dev, and R. N. Mohapatra. Natural TeV-scale left-right seesaw mechanism for neutrinos and experimental tests. *Phys. Rev. D*, 88(9):093010, 2013.

[149] Pratik Chattopadhyay and Ketan M. Patel. Discrete symmetries for electroweak natural type-I seesaw mechanism. *Nucl. Phys. B*, 921:487–506, 2017.

[150] R. N. Mohapatra and J. W. F. Valle. Neutrino Mass and Baryon Number Nonconservation in Superstring Models. *Phys. Rev. D*, 34:1642, 1986.

[151] D. Wyler and L. Wolfenstein. Massless Neutrinos in Left-Right Symmetric Models. *Nucl. Phys. B*, 218:205–214, 1983.

[152] Evgeny K. Akhmedov, Manfred Lindner, Erhard Schnapka, and J. W. F. Valle. Left-right symmetry breaking in NJL approach. *Phys. Lett. B*, 368:270–280, 1996.

[153] P. S. Bhupal Dev and Apostolos Pilaftsis. Light and Superlight Sterile Neutrinos in the Minimal Radiative Inverse Seesaw Model. *Phys. Rev. D*, 87(5):053007, 2013.

[154] P. S. Bhupal Dev and Apostolos Pilaftsis. Minimal Radiative Neutrino Mass Mechanism for Inverse Seesaw Models. *Phys. Rev. D*, 86:113001, 2012.

[155] Patrick D. Bolton, Frank F. Deppisch, and P. S. Bhupal Dev. Neutrinoless double beta decay versus other probes of heavy sterile neutrinos. *JHEP*, 03:170, 2020.

[156] Arindam Das and Nobuchika Okada. Inverse seesaw neutrino signatures at the LHC and ILC. *Phys. Rev. D*, 88:113001, 2013.

[157] Arindam Das and Nobuchika Okada. Bounds on heavy Majorana neutrinos in type-I seesaw and implications for collider searches. *Phys. Lett. B*, 774:32–40, 2017.

[158] Sacha Davidson and Alejandro Ibarra. A lower bound on the right-handed neutrino mass from leptogenesis. *Phys. Lett.*, B535:25–32, 2002.

[159] Laurent Canetti and Mikhail Shaposhnikov. Baryon Asymmetry of the Universe in the NuMSM. *JCAP*, 09:001, 2010.

[160] Apostolos Pilaftsis. CP violation and baryogenesis due to heavy Majorana neutrinos. *Phys.Rev.*, D56:5431–5451, 1997.

[161] Nodoka Yamanaka. Unobservability of topological charge in nonabelian gauge theory. 12 2022.

[162] Patrick D. Bolton, Frank F. Deppisch, and P. S. Bhupal Dev. Probes of Heavy Sterile Neutrinos. In *56th Rencontres de Moriond on Electroweak Interactions and Unified Theories*, 6 2022.

[163] W. Altmannshofer et al. PIONEER: Studies of Rare Pion Decays. 3 2022.

[164] Marco Drewes, Jan Hajer, Juraj Klaric, and Gaia Lanfranchi. NA62 sensitivity to heavy neutral leptons in the low scale seesaw model. *JHEP*, 07:105, 2018.

[165] Peter Ballett, Tommaso Boschi, and Silvia Pascoli. Heavy Neutral Leptons from low-scale seesaws at the DUNE Near Detector. *JHEP*, 03:111, 2020.

[166] C. Ahdida et al. Sensitivity of the SHiP experiment to Heavy Neutral Leptons. *JHEP*, 04:077, 2019.

[167] A. Blondel et al. Searches for long-lived particles at the future FCC-ee. *Front. in Phys.*, 10:967881, 2022.

[168] J. Schechter and J. W. F. Valle. Comment on the Lepton Mixing Matrix. *Phys. Rev. D*, 21:309, 1980.

[169] Asmaa Abada, Alvaro Hernandez-Cabezudo, and Xabier Marcano. Beta and Neutrinoless Double Beta Decays with KeV Sterile Fermions. *JHEP*, 01:041, 2019.

[170] Walter Grimus and Luis Lavoura. One-loop corrections to the seesaw mechanism in the multi-Higgs-doublet standard model. *Phys. Lett. B*, 546:86–95, 2002.

[171] Enrique Fernandez-Martinez, Josu Hernandez-Garcia, Jacobo Lopez-Pavon, and Michele Lucente. Loop level constraints on Seesaw neutrino mixing. *JHEP*, 10:130, 2015.

[172] J. A. Casas and A. Ibarra. Oscillating neutrinos and $\mu \to e, \gamma$. *Nucl. Phys. B*, 618:171–204, 2001.

[173] A. Donini, P. Hernandez, J. Lopez-Pavon, M. Maltoni, and T. Schwetz. The minimal 3+2 neutrino model versus oscillation anomalies. *JHEP*, 07:161, 2012.

[174] V. Cirigliano et al. Towards Precise and Accurate Calculations of Neutrinoless Double-Beta Decay: Project Scoping Workshop Report. *J. Phys. G*, 49:120502, 2022.

[175] Frank F. Deppisch, Lukas Graf, Francesco Iachello, and Jenni Kotila. Analysis of light neutrino exchange and short-range mechanisms in $0\nu\beta\beta$ decay. *Phys. Rev. D*, 102(9):095016, 2020.

[176] Vincenzo Cirigliano, Wouter Dekens, Jordy De Vries, Michael L. Graesser, Emanuele Mereghetti, Saori Pastore, and Ubirajara Van Kolck. New Leading Contribution to Neutrinoless Double-β Decay. *Phys. Rev. Lett.*, 120(20):202001, 2018.

[177] Wouter Dekens, Jordy de Vries, Kaori Fuyuto, Emanuele Mereghetti, and Guanghui Zhou. Sterile neutrinos and neutrinoless double beta decay in effective field theory. *JHEP*, 06:097, 2020.

[178] F. Simkovic, G. Pantis, J. D. Vergados, and Amand Faessler. Additional nucleon current contributions to neutrinoless double beta decay. *Phys. Rev. C*, 60:055502, 1999.

[179] J. Barea, J. Kotila, and F. Iachello. Nuclear matrix elements for double-β decay. *Phys. Rev. C*, 87(1):014315, 2013.

[180] J. Menéndez. Neutrinoless $\beta\beta$ decay mediated by the exchange of light and heavy neutrinos: The role of nuclear structure correlations. *J. Phys. G*, 45(1):014003, 2018.

[181] Lukáš Gráf, Manfred Lindner, and Oliver Scholer. Unraveling the $0\nu\beta\beta$ decay mechanisms. *Phys. Rev. D*, 106(3):035022, 2022.

[182] Jeffrey M. Berryman, Andre de Gouvea, Patrick J Fox, Boris Jules Kayser, Kevin James Kelly, and Jennifer Lynne Raaf. Searches for Decays of New Particles in the DUNE Multi-Purpose Near Detector. *JHEP*, 02:174, 2020.

[183] Pilar Coloma, Enrique Fernández-Martínez, Manuel González-López, Josu Hernández-García, and Zarko Pavlovic. GeV-scale neutrinos: interactions with mesons and DUNE sensitivity. *Eur. Phys. J. C*, 81(1):78, 2021.

[184] Igor Krasnov. On DUNE prospects in the search for sterile neutrinos. 2019.

[185] Torbjörn Sjöstrand, Stefan Ask, Jesper R. Christiansen, Richard Corke, Nishita Desai, Philip Ilten, Stephen Mrenna, Stefan Prestel, Christine O. Ras-

mussen, and Peter Z. Skands. An introduction to PYTHIA 8.2. *Comput. Phys. Commun.*, 191:159–177, 2015.

[186] Brian Batell, Jared A. Evans, Stefania Gori, and Mudit Rai. Dark Scalars and Heavy Neutral Leptons at DarkQuest. *JHEP*, 05:049, 2021.

[187] Kyrylo Bondarenko, Alexey Boyarsky, Dmitry Gorbunov, and Oleg Ruchayskiy. Phenomenology of GeV-scale Heavy Neutral Leptons. *JHEP*, 11:032, 2018.

[188] Anupama Atre, Tao Han, Silvia Pascoli, and Bin Zhang. The Search for Heavy Majorana Neutrinos. *JHEP*, 0905:030, 2009.

[189] Stefan Antusch, Eros Cazzato, and Oliver Fischer. Resolvable heavy neutrino–antineutrino oscillations at colliders. *Mod. Phys. Lett. A*, 34(07n08):1950061, 2019.

[190] Jean-Loup Tastet and Inar Timiryasov. Dirac vs. Majorana HNLs (and their oscillations) at SHiP. *JHEP*, 04:005, 2020.

[191] Jean-Loup Tastet, Oleg Ruchayskiy, and Inar Timiryasov. Reinterpreting the ATLAS bounds on heavy neutral leptons in a realistic neutrino oscillation model. *JHEP*, 12:182, 2021.

[192] Simon Bray, Jae Sik Lee, and Apostolos Pilaftsis. Resonant CP violation due to heavy neutrinos at the LHC. *Nucl.Phys.*, B786:95–118, 2007.

[193] P. S. Bhupal Dev, Apostolos Pilaftsis, and Un-Ki Yang. New Production Mechanism for Heavy Neutrinos at the LHC. *Phys.Rev.Lett.*, 112(8):081801, 2014.

[194] Asli M. Abdullahi et al. The Present and Future Status of Heavy Neutral Leptons. In *2022 Snowmass Summer Study*, 3 2022.

[195] N. Abgrall et al. The Large Enriched Germanium Experiment for Neutrinoless Double Beta Decay (LEGEND). *AIP Conf. Proc.*, 1894(1):020027, 2017.

[196] Matteo Agostini, Frank F. Deppisch, and Graham Van Goffrier. Probing the Mechanism of Neutrinoless Double-Beta Decay in Multiple Isotopes. 11 2022.

[197] Frank F. Deppisch and Jouni Suhonen. Statistical analysis of β decays and the effective value of g_A in the proton-neutron quasiparticle random-phase approximation framework. *Phys. Rev. C*, 94(5):055501, 2016.

[198] Glen Cowan, Kyle Cranmer, Eilam Gross, and Ofer Vitells. Asymptotic formulae for likelihood-based tests of new physics. *Eur. Phys. J. C*, 71:1554, 2011. [Erratum: Eur.Phys.J.C 73, 2501 (2013)].

[199] Jihn E. Kim. Weak Interaction Singlet and Strong CP Invariance. *Phys. Rev. Lett.*, 43:103, 1979.

[200] Michael Dine, Willy Fischler, and Mark Srednicki. A Simple Solution to the Strong CP Problem with a Harmless Axion. *Phys. Lett. B*, 104:199–202, 1981.

[201] P. Sikivie. Experimental Tests of the Invisible Axion. *Phys. Rev. Lett.*, 51:1415–1417, 1983. [Erratum: Phys.Rev.Lett. 52, 695 (1984)].

[202] Shivam Gola, Sanjoy Mandal, and Nita Sinha. ALP-portal majorana dark matter. *Int. J. Mod. Phys. A*, 37(22):2250131, 2022.

[203] G. B. Gelmini, S. Nussinov, and T. Yanagida. Does Nature Like Nambu-Goldstone Bosons? *Nucl. Phys. B*, 219:31–40, 1983.

[204] Eric Laenen Stan Bentvelsen and Patrick Motylinski. Higgs production through gluon fusion at leading order.

[205] Michael E. Peskin and Daniel V. Schroeder. *An Introduction to quantum field theory*. Addison-Wesley, Reading, USA, 1995.

[206] Paolo Gondolo and Graciela Gelmini. Cosmic abundances of stable particles: Improved analysis. *Nucl. Phys. B*, 360:145–179, 1991.

[207] Miguel Escudero. Neutrino decoupling beyond the Standard Model: CMB constraints on the Dark Matter mass with a fast and precise $N_{\rm eff}$ evaluation. *JCAP*, 02:007, 2019.

[208] Alexey Boyarsky, Maksym Ovchynnikov, Nashwan Sabti, and Vsevolod Syvolap. When feebly interacting massive particles decay into neutrinos: The Neff story. *Phys. Rev. D*, 104(3):035006, 2021.

[209] Marco Hufnagel, Kai Schmidt-Hoberg, and Sebastian Wild. BBN constraints on MeV-scale dark sectors. Part II. Electromagnetic decays. *JCAP*, 11:032, 2018.

[210] Miguel Escudero Abenza. Precision early universe thermodynamics made simple: $N_{\rm eff}$ and neutrino decoupling in the Standard Model and beyond. *JCAP*, 05:048, 2020.

[211] David J. E. Marsh. Axion Cosmology. *Phys. Rept.*, 643:1–79, 2016.

[212] C. Antel et al. Feebly-interacting particles: FIPs 2022 Workshop Report. *Eur. Phys. J. C*, 83(12):1122, 2023.

[213] Cyril Pitrou, Alain Coc, Jean-Philippe Uzan, and Elisabeth Vangioni. Precision big bang nucleosynthesis with improved Helium-4 predictions. *Phys. Rept.*, 754:1–66, 2018.

[214] Almudena Arcones and Friedrich-Karl Thielemann. Origin of the elements. *Astron. Astrophys. Rev.*, 31(1):1, 2023.

[215] Alexey Boyarsky, Maksym Ovchynnikov, Oleg Ruchayskiy, and Vsevolod Syvolap. Improved big bang nucleosynthesis constraints on heavy neutral leptons. *Phys. Rev. D*, 104(2):023517, 2021.

[216] Janina J. Renk et al. CosmoBit: A GAMBIT module for computing cosmological observables and likelihoods. *JCAP*, 02:022, 2021.

[217] Brian D. Fields, Keith A. Olive, Tsung-Han Yeh, and Charles Young. Big-Bang Nucleosynthesis after Planck. *JCAP*, 03:010, 2020. [Erratum: JCAP 11, E02 (2020)].

[218] Brian D. Fields, Paolo Molaro, and Subir Sarkar. Big-Bang Nucleosynthesis. *Chin. Phys. C*, 38:339–344, 2014.

[219] Terry P. Walker, Gary Steigman, David N. Schramm, Keith A. Olive, and Ho-Shik Kang. Primordial nucleosynthesis redux. *Astrophys. J.*, 376:51–69, 1991.

[220] Fabio Iocco, Gianpiero Mangano, Gennaro Miele, Ofelia Pisanti, and Pasquale D. Serpico. Primordial Nucleosynthesis: from precision cosmology to fundamental physics. *Phys. Rept.*, 472:1–76, 2009.

[221] Beatrice M. Tinsley. Evolution of the stars and gas in galaxies. *Fund. Cosmic Phys.*, 5:287, 1980.

[222] Alexandre Arbey. AlterBBN: A program for calculating the BBN abundances of the elements in alternative cosmologies. *Comput. Phys. Commun.*, 183:1822–1831, 2012.

[223] E. Lisi, Subir Sarkar, and F. L. Villante. The big bang nucleosynthesis limit on n(nu). *Phys. Rev.*, D59:123520, 1999.

[224] Luis Mendoza and Craig J. Hogan. A java calculator of standard big bang nucleosynthesis. 4 1999.

[225] O. Pisanti, A. Cirillo, S. Esposito, F. Iocco, G. Mangano, G. Miele, and P. D. Serpico. PArthENoPE: Public Algorithm Evaluating the Nucleosynthesis of Primordial Elements. *Comput. Phys. Commun.*, 178:956–971, 2008.

[226] Csaba Balázs et al. Cosmological constraints on decaying axion-like particles: a global analysis. *JCAP*, 12:027, 2022.

[227] K. Hirata et al. Observation of a Neutrino Burst from the Supernova SN 1987a. *Phys. Rev. Lett.*, 58:1490–1493, 1987.

[228] Y. Totsuka et al. Observation of a neutrino burst from the supernova SN1987a. *Nucl. Phys. A*, 478:189–195, 1988.

[229] A. D. Dolgov, S. H. Hansen, G. Raffelt, and D. V. Semikoz. Cosmological and astrophysical bounds on a heavy sterile neutrino and the KARMEN anomaly. *Nucl. Phys. B*, 580:331–351, 2000.

[230] George M. Fuller, Alexander Kusenko, and Kalliopi Petraki. Heavy sterile neutrinos and supernova explosions. *Phys. Lett. B*, 670:281–284, 2009.

[231] Leonardo Mastrototaro, Alessandro Mirizzi, Pasquale Dario Serpico, and Arman Esmaili. Heavy sterile neutrino emission in core-collapse supernovae: Constraints and signatures. *JCAP*, 01:010, 2020.

[232] Damiano F. G. Fiorillo, Georg G. Raffelt, and Edoardo Vitagliano. Strong Supernova 1987A Constraints on Bosons Decaying to Neutrinos. *Phys. Rev. Lett.*, 131(2):021001, 2023.

[233] Vsevolod Syvolap. Testing heavy neutral leptons produced in the supernovae explosions with future neutrino detectors. 1 2023.

[234] Kensuke Akita, Sang Hui Im, Mehedi Masud, and Seokhoon Yun. Limits on heavy neutral leptons, Z' bosons and majorons from high-energy supernova neutrinos. *JHEP*, 07:057, 2024.

[235] K. Kainulainen, J. Maalampi, and J. T. Peltoniemi. Inert neutrinos in supernovae. *Nucl. Phys.*, B358:435–446, 1991.

[236] G. Raffelt and G. Sigl. Neutrino flavor conversion in a supernova core. *Astropart. Phys.*, 1:165–184, 1993.

[237] Bernanda Telalovic, Damiano F. G. Fiorillo, Pablo Martínez-Miravé, Edoardo Vitagliano, and Mauricio Bustamante. The next galactic supernova can uncover mass and couplings of particles decaying to neutrinos. 6 2024.

[238] J. Jaeckel, P. C. Malta, and J. Redondo. Decay photons from the axionlike particles burst of type II supernovae. *Phys. Rev. D*, 98(5):055032, 2018.

[239] Melissa Diamond, Damiano F. G. Fiorillo, Gustavo Marques-Tavares, and Edoardo Vitagliano. Axion-sourced fireballs from supernovae. *Phys. Rev. D*, 107(10):103029, 2023. [Erratum: Phys.Rev.D 108, 049902 (2023)].

[240] Melissa Diamond, Damiano F. G. Fiorillo, Gustavo Marques-Tavares, Irene Tamborra, and Edoardo Vitagliano. Multimessenger Constraints on Radiatively Decaying Axions from GW170817. *Phys. Rev. Lett.*, 132(10):101004, 2024.

[241] Andrea Caputo, Hans-Thomas Janka, Georg Raffelt, and Edoardo Vitagliano. Low-Energy Supernovae Severely Constrain Radiative Particle Decays. *Phys. Rev. Lett.*, 128(22):221103, 2022.

[242] Andrea Caputo, Georg Raffelt, and Edoardo Vitagliano. Muonic boson limits: Supernova redux. *Phys. Rev. D*, 105(3):035022, 2022.

[243] Maurizio Giannotti, Igor Irastorza, Javier Redondo, and Andreas Ringwald. Cool WISPs for stellar cooling excesses. *JCAP*, 05:057, 2016.

[244] Luca Di Luzio, Maurizio Giannotti, Enrico Nardi, and Luca Visinelli. The landscape of QCD axion models. *Phys. Rept.*, 870:1–117, 2020.

[245] Davide Cadamuro and Javier Redondo. Cosmological bounds on pseudo Nambu-Goldstone bosons. *JCAP*, 02:032, 2012.

[246] Kereibay Dias. Search for Heavy Neutral Lepton Production in NA62$^{\#}$. *Moscow Univ. Phys. Bull.*, 77(2):220–222, 2022.

[247] Akitaka Ariga et al. FASER's physics reach for long-lived particles. *Phys. Rev. D*, 99(9):095011, 2019.

[248] Patrick D. Bolton, Frank F. Deppisch, Mudit Rai, and Zhong Zhang. Probing the nature of Heavy Neutral Leptons in direct searches and neutrinoless double beta decay. *Nucl. Phys. B*, 1010:116785, 2025.

[249] Pierluca Carenza, Giuseppe Lucente, Leonardo Mastrototaro, Alessandro Mirizzi, and Pasquale Dario Serpico. Comprehensive constraints on heavy sterile neutrinos from core-collapse supernovae. *Phys. Rev. D*, 109(6):063010, 2024.

[250] Linda Cremonesi. Neutrino oscillation physics potential of Hyper-Kamiokande. *PoS*, EPS-HEP2015:054, 2015.

[251] V. Cerrone. Current status and physics prospects of the JUNO experiment. *Nuovo Cim. C*, 47(3):70, 2024.

[252] A. Ashtari Esfahani et al. Tritium Beta Spectrum Measurement and Neutrino Mass Limit from Cyclotron Radiation Emission Spectroscopy. *Phys. Rev. Lett.*, 131(10):102502, 2023.